EARLY-TYPE DISK GALAXIES

Michael J. Williams
St Anne's College

A thesis submitted in candidature for the degree of Doctor of Philosophy
Hilary Term 2011

EARLY-TYPE DISK GALAXIES

Michael J. Williams
St Anne's College

A thesis submitted in candidature for the degree of Doctor of Philosophy
Hilary Term 2011

ABSTRACT

In this thesis I investigate the dynamics and stellar populations of a sample of 28 edge-on early-type (S0–Sb) disk galaxies, 22 of which host a boxy or peanut-shaped bulge. I begin by constructing mass models of the galaxies based on their observed photometry and stellar kinematics. Subject to cosmologically motivated assumptions about the shape of dark haloes, I measure in a purely dynamical way their stellar and dark masses. I make a preliminary comparison between the dynamically determined stellar masses and those predicted by stellar population models.

I then compare the Tully-Fisher (luminosity–velocity) relations of the spirals and S0s in the sample. I show that S0s are systematically fainter at a given rotational velocity, but the amount by which they are fainter is less than expected by models in which they are the products of truncation of star formation in spirals. This raises the possibility that S0s are smaller or more concentrated than spirals of the same mass.

I then study the vertical structure of the boxy and peanut-shaped bulges of a subset of the sample. Among this sample of five galaxies, I find one example in which the stellar populations show no evidence that the bulge and the disk formed in different processes, and in which the bulge is in perfectly cylindrical rotation, i.e. its line-of-sight velocity does not change with height above the disk. This galaxy is probably a pure disk galaxy. However, even with this small sample, I also show that cylindrical rotation and homogeneous stellar populations are not ubiquitous properties of boxy and peanut-shaped bulges.

Finally I analyse central and radial trends in the stellar populations of the bulges of full sample of 28 galaxies. I find that, at a given velocity dispersion, the central stellar populations of these barred early-type disk galaxies are identical to those of elliptical galaxies, which suggests that secular evolution does not dominate the centre of these galaxies. However, the radial metallicity gradients are shallower than those of ellipticals. This is qualitatively consistent with chemodynamical models of bar formation, in which radial inflow and outflow smears out pre-existing gradients.

DECLARATION

I declare that no part of this thesis has been accepted, or is currently being submitted, for any degree or diploma or certificate or any other qualification in this University or elsewhere. This thesis is the result of my own work unless otherwise stated below.

The work in Chapter 2 and Chapter 3 was done in collaboration with Michele Cappellari. The work in Chapter 4 and Chapter 5 was done at the European Southern Observatory Headquarters under Harald Kuntschner's supervision. All work was done in collaboration with and under the supervision of Martin Bureau. I use 'we' and 'our' to reflect this.

This thesis makes use of Michele Cappellari's published implementations of the following algorithms: MGE (multi-Gaussian expansion, used to parametrize images and mass distributions), PPXF (penalized pixel fitting, used to extract the stellar kinematics from absorption line spectra of galaxies), and JAM (use to solve the Jeans equations under assumptions of axisymmetric and constant anisotropy). Chapter 4 and Chapter 5 also make use of GANDALF, Marc Sarzi's code that uses PPXF to simultaneously fit emission and absorption lines in galaxy spectra.

The material in Chapter 2 was published in Williams, Bureau & Cappellari (2009). The material in Chapter 3 was published in Williams, Bureau & Cappellari (2010). The material in Chapter 4 was submitted to MNRAS in October 2010.

ACKNOWLEDGMENTS

I am enormously grateful to Martin Bureau, my supervisor, for his invaluable guidance and good humour, a seemingly inexhaustible supply of data, and a truly inexhaustible supply of detailed comments on issues of usage, grammer and punctuation. I am lucky to have him as a mentor, and without him you would not be reading this thesis. Please don't hold that against him. Like the baby in *Three Men and a Baby* (Nimoy, 1987), I was fortunate to have the additional supervisory support of Michele Cappellari and Harald Kuntschner. Both were precious sources of astrophysical wisdom and well-tested code.

I received further scientific, practical and professional advice and support from Alejandro Bedregal, Remco van den Bosch, Aeree Chung, Eric Emsellem, Susan Kassin, Mike Merrifield, Nadine Neumayer, Marc Sarzi, Anne-Marie Weijmans and Michel Zamojski. I am in their debt. I am extremely grateful to Neville Harnew for the opportunity to teach undergraduates at St Anne's, and to that college for generous financial support throughout my academic career.

During the long but enjoyable time I spent in Oxford, and the very pleasant fifteen months I spent in Munich, I was fortunate to have housemates, officemates and tea/beer-drinking buddies, and I am grateful to them all for good times. My great friends Millie Maier, Leila Powell and Marija Vlajic deserve my particular thanks. Away from astronomy, Robin Allender, Ben Baldwin, John Robins and Alex Stewart of Dreamboat Records, and Joe Hastings, Johnny White, Oliver Irving and Justin Kelly of *How To Be* offered welcome distraction.

Finally, and above all, I would like to thank my family for their love and support.

CONTENTS

LIST OF FIGURES

LIST OF TABLES

1

INTRODUCTION

As homes to billions of stars, and the candles that light up the cosmic web, galaxies are the visible tracers of astrophysics through cosmic time. Understanding their formation and evolution is therefore one of the most basic and far-reaching questions in astronomy. There are two observational approaches available: to observe galaxies at high redshift and therefore at early times, or to study local galaxies, including our own, in detail. This thesis takes the second approach, and focusses on a sample of 28 nearby galaxies.

The areas I attempt to address are diverse. I construct dynamical models to measure the composition of the sample by mass (Chapter 2), I use a scaling relation to constrain the possible evolutionary connection between two classes of galaxy in the sample (Chapter 3), and I study the intriguing central bulges of these galaxies (Chapters 4 and 5). Each chapter has its own introduction, in which I review previous work in the area, identify gaps in the knowledge, and discuss the specific techniques I use. The overall introduction of this thesis is therefore limited in scope to that aspect which is common to all chapters: the sample.

All of the galaxies in the sample are early-type disk galaxies, and most of them host a boxy or peanut-shaped bulge. This introduction is therefore intended to introduce those terms and is structured as follows. In Section 1.1, I review the morphological classification of galaxies using the apparent properties of their bulges, disks and spiral

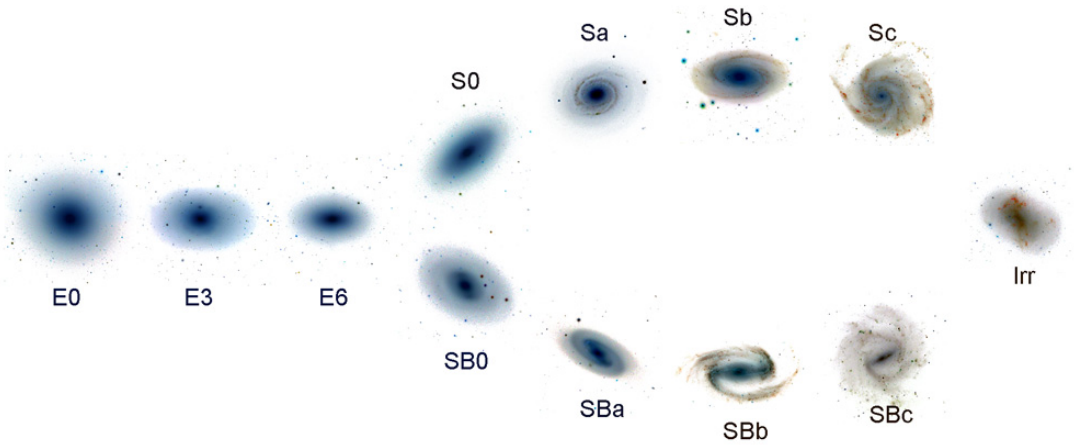

Figure 1.1: The Hubble (1936) 'tuning fork' morphological classification scheme

arms. I discuss some of the implications and limitations of the currently favoured classification scheme, and explain where my sample of early-type disk galaxies fits in. In Section 1.2, I review our knowledge of the dynamics of bars and their role in galaxy evolution. In Section 1.3, I summarize the observations, theory and simulations that lead to the conclusion that boxy and peanut-shaped bulges are the bars viewed edge-on. In Section 1.4, I give an overview of the sample that is the focus of this thesis.

1.1 THE COMPONENTS AND CLASSIFICATION OF GALAXIES

1.1.1 Historical review

The short review of the morphological classification of galaxies that follows is intended to introduce terminology and to describe an example of how one part of the scheme was (and continues to be) refined to offer more interpretative power. A more complete review is given by, e.g., Sandage (2005).

In the classification scheme of Hubble (1936, see also Sandage 1961) the two principal properties that determine the morphological classification of a galaxy are the apparent size of its central bulge with respect to the disk, and the presence or absence of spiral arms in the disk (see Fig. 1.1). Giant galaxies that are apparently without a

disk are called *ellipticals*. Galaxies whose disks have no sign of spiral arms are called *S0s* (or lenticulars). Galaxies with spiral arms are called *spiral* galaxies. Taken together, ellipticals and S0s are known as *early-type* galaxies, S0s and spirals are known as *disk galaxies*, and spirals alone are also known as *late-type* galaxies. There are similarities between bulges and ellipticals (see Sections 4.1 and 5.1) that mean they are sometimes considered together, and collectively denoted *spheroids*.

I use the term early-type disk galaxies in the title of this thesis and elsewhere to refer to the galaxies on either side of early-type/spiral boundary: S0s and Sa–Sb spirals.

Among the spirals, galaxies are arranged in a continuum from those that have relatively large bulges and/or smooth, tightly wound spiral arms, i.e. Sa galaxies (which, being placed closest to S0s on the tuning fork diagram, are the 'earliest' of the late types), through Sb galaxies, to those spirals with the smallest bulges and/or loosely wound, flocculent spiral arms, i.e. Sc galaxies (which are the 'latest' of the late types). This continuum of spirals is separated into two tines, one of unbarred galaxies, i.e. Sa, Sb and Sc, and one of barred galaxies, i.e. SBa, SBb and SBc. Bars are discussed in more detail in Section 1.2. The scheme of de Vaucouleurs (1959) augments the classification of spirals to include rings and lenses, and extends the sequence to Sd.

The detailed morphological classification of spiral galaxies is not only robust in the sense that it is reproducible, but is also interpretative in the sense that it is thought to map on to our physical understanding of the origin and evolution of spiral galaxies. The same cannot be said of the photometric classification of ellipticals in the original Hubble scheme, in which they are placed in a sequence of increasing *apparent* flatness from E0 (roundest) to E7 (flattest). This means that the morphological classification of ellipticals is a function not only of their intrinsic shape, but also the inclination with which they happen to be oriented with respect to our line of sight. The limitations of a scheme based on the apparent flatness were emphasized by van den Bergh (1990, 2009b). He showed that there is a paucity of S0 galaxies with face-on inclinations and that ellipticals of sub-types E5–E7 are, like S0s significantly fainter than apparently rounder ellipticals. This suggests that at least some ellipticals would have been classified as S0s in the Hubble scheme had an accident of their orientation

Figure 1.2: The revised classification scheme of Kormendy & Bender (1996, this figure taken from that work, ommited here for copyright reasons).

not made their featureless disk undetectable.

With the aim of classifying early-type galaxies in a more interpretative way, Kormendy & Bender (1996) replaced the round–flat continuum with one ranging from from boxy isophotes to disky isophotes. Disky systems tend to have significant net rotation about their photometric minor axis, while boxy systems have little net rotation about any axis. This scheme therefore has the significant advantage of correlating with the gross dynamics of these systems, and therefore presumably having an evolutionary origin. While not strictly a morphological classification, the recent work of the SAURON and Atlas3D projects has demonstrated that the specific angular momentum galaxies may be the observable most closely related to evolutionary history and other characteristics of early-types (de Zeeuw et al., 2002; Emsellem et al., 2007; Cappellari et al., 2011).

1.1.2 *Galaxy properties as a function morphological type*

We now briefly review the observational properties of galaxies with particular reference to their morphological type. While they are intriguing objects that may offer keys to the understanding processes that drive galaxy evolution, we do not discuss dwarf and irregular galaxies, and what appear to be outlier or transitional subpopulations such as 'red spirals' (e.g. Masters et al., 2010) and 'blue ellipticals' (e.g. Schawinski

et al., 2009).

1.1.2.1 *Morphology–density relation*

Among the key observational results concerning morphology is that early-type galaxies are more common in denser environments in the local universe (Dressler, 1980). Moreover, as clusters of galaxies gain members with increasing time, the fraction of galaxies in dense environments — and therefore the overall fraction of early-type galaxies — has increased since $z \sim 0.5$ (Dressler et al., 1997; Fasano et al., 2000).

1.1.2.2 *Composition*

The baryonic masses of most galaxies are dominated by their stars. The stellar populations of spiral galaxies are relatively young, and early-type galaxies are relatively old. This is seen most easily in global colours, which are relatively blue in spirals and red in early-types (e.g. Strateva et al., 2001; Balogh et al., 2004; Baldry et al., 2004; Driver et al., 2006; Lintott et al., 2008).

Gas is often a significant component by mass of spiral galaxies. Ongoing and recent star formation is common in spiral galaxies at all observable redshifts, and is correlated with the local gas surface density, (e.g. Kennicutt, 1998; Bigiel et al., 2008; Förster Schreiber et al., 2009). Compared to spirals, gas is generally an insignificant component by mass in early-type galaxies, which exhibit relatively little star formation (e.g. Shapiro et al., 2010). What little star formation and gas there is in early-types may, however, be significant from an evolutionary point-of-view.

Galaxies are embedded in a halo of dark matter. Our knowledge of the shape and fraction by mass of these haloes, and how they interact with baryonic material during galaxy formation, is reviewed in Section 2.1

1.1.2.3 *Photometric properties*

The radial surface brightness profiles of the disk of a galaxy may be parametrized by a exponential function (Freeman, 1970), while the profile of the axisymmetric feature that remains, i.e. the spheroid, is best described by a Sérsic (1968) profile, where the surface brightness is proportional to $e^{-r^{1/n}}$, where r is the radius. The exponential profile is a special case of the Sérsic profile with index $n = 1$. The de Vaucouleurs (1948) profile, which was originally thought to describe all spheroids, is the case $n = 4$. Improvements in the dynamical range and spatial resolution of imaging lead to the observations that the exponential profiles of disks usually break at large radii (e.g. Freeman, 1970; van der Kruit, 1979; Pohlen & Trujillo, 2006), and the observed profiles of ellipticals often contain an excess or deficit of light at small radii compared to the Sérsic profile that describes the rest of the galaxy (Kormendy et al., 2009).

In combination with the observed kinematics of galaxies, the photometric properties of galaxies reveal a number of structural scaling relations that are reviewed in Section 3.1 and in Blanton & Moustakas (2009).

1.1.3 *Galaxy morphology and galaxy evolution*

The possible modes of galaxy formation and evolution are discussed throughout this thesis. In particular, environment-driven processes and passive evolution are discussed in Chapter 3, and bar-driven secular processes in Section 1.2 and Chapters 4 and 5. We will not anticipate those discussions here. However, we must note an assumption, motivated by simulations and observations, that is implicit throughout: the physics of galaxy formation as we understand it cannot result in a population of primordial galaxies that captures the diversity seen in local galaxies. Some form of evolution is necessary and, at a minimum, that evolution must move some galaxies along the Hubble sequence.

1.2 BARS

In the previous section we mentioned that disk galaxies may be further divided into barred and unbarred systems, but we did not discuss the properties of bars or their likely significance for the evolution of their host galaxies. That is the purpose of this section.

1.2.1 *Observable photometric properties*

Bars are elongated structures found in the light distributions of disk galaxies. While the fraction of barred galaxies (and apparent strength of the bar in a given galaxy) varies with wavelength (increasing to longer wavelengths), the situation may be characterized by the statement that bars are present in approximately two thirds of local disk galaxies (Eskridge et al., 2000; Whyte et al., 2002; Marinova & Jogee, 2007). That fraction does not appear to vary strongly with environment (Marinova et al., 2009), but drops to about 20% at $z \approx 0.84$ (Sheth et al., 2008).

They typically contribute around half of the B-band light within the optical radius R_{25} (Sellwood & Wilkinson, 1993).Where present, bars in local early-type disks (S0–Sb) are typically $\approx$ 0.5–2.5 disk scale lengths. Bars in later-type disks are about half that size (Erwin, 2005). In some cases, an inner ring of stars connects the ends of the bar, while in others the spiral arms begin at the bar ends. An outer ring at larger radii may also be present, as may a plateau of slowly declining surface brightness called a lens (Kormendy & Kennicutt, 2004, and references therein).

1.2.2 *Resonances and orbits*

A bar, or indeed any non-axisymmetric feature, has resonances whose locations are fixed by the speed with which the pattern of the bar rotates and the global potential in which it resides. The reason for this is most easily understood in the limit of a weak

perturbation ϕ to the axisymmetric (i.e. unbarred) potential Φ. The argument that follows is adapted from Sellwood & Wilkinson (1993) and Kormendy & Kennicutt (2004). A star with a given angular momentum J will perform circular orbits of angular frequency Ω_c at its home radius r_c where

$$\frac{\partial \Phi}{\partial r} = r_c \Omega_c^2 = \frac{J^2}{r_c^3}. \tag{1.1}$$

If the local value of Ω_c is equal to the pattern speed Ω_p of the perturbing potential of the bar, the star will be pulled in the same direction at all times and therefore make large perturbations in its orbit. This resonance is known as corotation.

If the star has more energy than is needed to perform circular orbits (as is often the case in real galaxies), it will oscillate about the home radius. In the frame of reference of an external observer, the orbit is not closed for a realistic choice of Φ. In the inertial frame of the star, however, this oscillation appears as small (closed) ellipse. This epicycle can be shown to have the Lindblad frequency

$$\kappa = \left(4\Omega_c^2 + r \frac{\mathrm{d}\,\Omega_c^2}{\mathrm{d}\,r} \right)^{1/2}. \tag{1.2}$$

The Inner Linblad Resonances (ILRs) are located where the local value of Ω_c is such that the star completes exactly two epicycles in the rotating frame the bar for each orbit of the galaxy, i.e. where $\Omega_p = \Omega_c - \kappa/2$. There may be one or two ILRs in galaxies with relatively concentrated mass distributions, or none in galaxies with more diffuse mass distributions. The other resonances are outside the scope of this review.

Having argued qualitatively that there must be resonances, we appeal to numerical simulations, which demonstrate that two principal families of orbits are, in practice, populated within the corotation radius of a barred galaxy. The first are known as the x_1 orbits. These are elongated parallel to the bar between the ILR (if present) and corotation. Within the ILR are the small x_2 orbits, which are oriented perpendicular to the bar. Dissipation and shocking of gas is inevitable where these families cross, and results in the radial inflow of material (Athanassoula, 1992). This radial inflow is thought to be the reason for many of the observed properties of pseudobulges, the topic of the next subsection.

1.2.3 *Pseudobulges*

Pseudobulges are central excesses of light found in some disk galaxies. Their observational properties allow them to be distinguished from (classical) bulges and ellipticals (which, as we mentioned above and discuss in more detail in Section 4.1, have much in common). Those distinguishing features include some or all of the following: they are flattened; they are rotationally supported, their small velocity dispersions place them off the fundamental plane of ellipticals and classical bulges (see Section 3.1), they have embedded spiral structure or nuclear bars, they have near-exponential surface brightness profiles (in excess of the inwards extrapolation of the disk brightness profile), and they have vigorous ongoing star formation (Kormendy & Kennicutt, 2004; Athanassoula, 2005).

The fact that they occur more frequently in barred galaxies, and, as argued above, bars result in inflow of material on appropriate radial scales, has lead to the conclusion that they are the result of bar-driven *secular*, i.e. slow and internal, evolution.

1.3 BOXY AND PEANUT-SHAPED BULGES

Among edge-on disk galaxies, approximately one half contain a protuberance of light above and below the plane of the disk whose isophotes are boxy or peanut-shaped rather than elliptical (Lütticke, Dettmar & Pohlen, 2000). These are the boxy and peanut-shaped bulges. Our understanding of these features is hampered by the fact that we lack direct evidence for their intrinsic shape. One constraint comes from the observation that their kinematics differ from those of ellipticals and classical bulges in that the line-of-sight velocity does not vary with height above the disk (e.g. Kormendy & Illingworth, 1982; Howard et al., 2009). This behaviour, which is known as cylindrical rotation, is reviewed in more detail in Section 4.1.

Some of the first attempts to explain their properties used finely-tuned distribution functions to construct dynamical models (e.g Binney & Petrou, 1985; Rowley, 1988). These authors speculated that the distribution functions might be the products of the

accretion of satellite galaxies or major mergers. However, Shaw (1987) observed that there are no more satellites around galaxies with boxy and peanut-shaped bulges than around galaxies with round bulges, and the observed incidence of these bulges is uncomfortably high to be explained by major mergers.

However, Combes & Sanders (1981) had already demonstrated using N-body models that self-heating or a buckling instability in barred disks could reproduce the boxy shape when viewed in an edge-on projection. It took a more detailed analysis by Combes et al. (1990) and further work by, e.g. Raha et al. (1991) and Pfenniger & Friedli (1991) for the idea to gain its now widespread acceptance (e.g. Athanassoula & Misiriotis, 2002). The weak form of this picture, as stated by Kormendy & Kennicutt (2004), is that 'these bulges are connected to bars and owe their origin to them' and that they, like the bar itself, are 'built out of disk material'. The strong form, favoured by many others, is characterized by Kormendy & Kennicutt (2004) as the statement that they are 'nothing more nor less than bars seen edge-on'.

The strong form passes the basic sanity check that boxy and peanut-shaped bulges are approximately as common as bars in face-on galaxies. It is also consistent with the kinematic signature of such bulges when viewed in emission: the splitting of populated region of the gas position–velocity diagram within the bulge (Kuijken & Merrifield, 1995; Merrifield & Kuijken, 1999; Bureau & Freeman, 1999). It is also an explanation for the correlation between the mean and skewness h_3 of the stellar line-of-sight velocity distribution over the bar length (Chung & Bureau, 2004, anticorrelation is expected in axisymmetric systems).

If, as it seems, we now understand the origin of boxy and peanut-shaped bulges, why are they of further interest? If we want to know about bars, why not simply study barred face-on galaxies, where the structure of the galaxy is a more direct observable? Of course the answer is that edge-on galaxies are the only galaxies in which we can observe the vertical structure of bars.

1.4 THE BUREAU & FREEMAN (1999) SAMPLE

The Bureau & Freeman (1999) sample of 28 edge-on disk galaxies is the focus of this thesis. Relevant properties are tabulated in Tables 2.1, 3.1 and 5.1. It consists of galaxies at the interface between early-types and spiral galaxies. This is the crossroads of galaxy evolution and is therefore of particular interest. Not only is it one of the most prominent and discrete purely morphological transitions, but appears to be associated with a significant event or process in the lifetime of most galaxies.

The majority (22/28) host bulges that are boxy or peanut-shaped. This makes it well-suited to study the properties of these bulges. The observations include emission line optical spectroscopy (and therefore gas kinematics, Bureau & Freeman 1999), absorption line spectroscopy (and therefore stellar kinematics, Chung & Bureau 2004), and near-infrared photometry (Bureau et al., 2006).

2

MASS MODELS OF EDGE-ON EARLY-TYPE DISK GALAXIES

The material in this chapter was originally published in 'Kinematic constraints on the stellar and dark matter content of spiral and S0 galaxies', M. J. Williams, M. Bureau and M. Cappellari, 2009, MNRAS, 400, 1665. The definitive version is available at www.blackwell-synergy.com.

2.1 INTRODUCTION

In the dominant paradigm describing structure formation, initial fluctuations in density are enhanced by gravity until galaxies form in potential wells (White & Rees, 1978; Blumenthal et al., 1984). Numerical simulations and semi-analytic models of galaxy formation are able to reproduce many of the statistical characteristics of galaxies and some of their detailed features (e.g. Kauffmann, White & Guiderdoni, 1993; Cole et al., 1994; Benson et al., 2003; Baugh, 2006; Somerville et al., 2008). A detailed and consistent theory remains elusive, however, and there are apparent contradictions between the predictions of models and the observations (see, e.g. Baugh, 2006; Mayer, Governato & Kaufmann, 2008, and references therein).

The main stumbling blocks are the significant uncertainties and computational difficulties involved in capturing the baryonic physics that is dominant on sub-Mpc scales. Progress can be made in two ways. Firstly, using observational constraints

which are thought to be insensitive to baryonic physics, one can circumvent these uncertainties and directly test the predictions of large-scale structure formation, which is in itself crucially important. Alternatively, one can test formation models with galaxy-scale observations. The outcomes of these tests can be used to refine and improve the models. Perhaps one of the most useful observational constraints for either approach is an understanding of the relative distribution of dark and luminous matter. In this work we aim to measure the radial dark matter distribution in a sample of 28 edge-on disk galaxies. We make cosmologically-motivated assumptions, which allow us to lift certain modelling degeneracies.

It is well-established that, within the optical disk, the kinematics of high surface brightness spiral galaxies can be reproduced by maximal disk models, in which luminous material contributes the maximum amount consistent with the observed rotation curve (e.g. van Albada & Sancisi, 1986; Persic, Salucci & Stel, 1996; Palunas & Williams, 2000). The stellar components of maximal disk models typically contribute 75–95 per cent of the rotational velocity at $2.2\,R_{\rm disk}$, where $R_{\rm disk}$ is the scale length of the exponential disk and $2.2\,R_{\rm disk}$ is the radius where the rotational velocity of the exponential disk peaks (Sackett, 1997). This permits dark haloes that comprise 10–45 per cent of the total mass within $2.2\,R_{\rm disk}$. In a Freeman disk (Freeman, 1970), R_{25}, the radius of the $25\,{\rm mag\,arcsec^{-2}}$ isophote occurs at $\approx 3\,R_{\rm disk}$.

Side-stepping the maximal disk assumption, Ratnam & Salucci (2000) demonstrate that rotation curves can be adequately fitted without dark matter. Kassin, de Jong & Weiner (2006) avoided the maximal disk assumption entirely by using independent estimates of the stellar mass-to-light ratio inferred from a relationship with colour (Bell & de Jong, 2001; Bell et al., 2003). Most of their models were consistent with a maximal disk. Further evidence is provided by model-independent analysis of rotation curves at intermediate radii (McGaugh et al., 2007).

In the case of elliptical and S0 galaxies, evidence from dynamical modelling and gravitational lensing studies suggests that dark matter makes only a small contribution to the total mass within $R_{\rm eff}$, the radius of the elliptical isophote containing half the light. For example, from the dynamical studies, Gerhard et al. (2001) find that 10–40 per cent of the mass within $R_{\rm eff}$ is dark in their sample of 21 ellipticals, Borriello,

Salucci & Danese (2003) find 30 per cent dark matter within $R_{\rm eff}$ by constraining a sample of 221 ellipticals to lie on a fundamental plane, Cappellari et al. (2006) find a median of 30 per cent dark matter within $R_{\rm eff}$ in their sample of 25 ellipticals and S0s, Thomas et al. (2007) find 10–50 per cent dark matter within $R_{\rm eff}$ for a sample of 17 ellipticals and S0s, and Weijmans et al. (2008) find 55 per cent dark matter within $5\,R_{\rm eff}$ in NGC 2974. Lensing studies find similar results. For example, Rusin, Kochanek & Keeton (2003) find 22 per cent dark matter within 2 $R_{\rm eff}$ of 22 elliptical lenses, Koopmans et al. (2006) find 25 per cent dark matter within the Einstein radius of 15 elliptical lenses (the Einstein radius is approximately equal to the effective radius for galaxy scale lenses), and Bolton et al. (2008) find 38 per cent dark matter inside $R_{\rm eff}$ for 53 elliptical lenses.

However, the total absence of dark matter in ellipticals is sometimes excluded with only low significance due to intrinsic degeneracies in the dynamical models (see, e.g. Romanowsky et al. 2003 and the response by Dekel et al. 2005) and the lack of kinematic tracers at large radii. Moreover, in all cases $R_{\rm eff} \ll R_{25}$. The constraints on both the mass of the halo and its extent are therefore less strong for ellipticals than for spirals.

Perhaps the most compelling evidence for the dominance of stellar matter in either ellipticals or high surface brightness disk galaxies comes from the analysis of the bars and spiral arms often present in disk galaxies. These non-axisymmetric features lift the degeneracy between the contributions from luminous and dark matter. This is done by assuming that dark matter is axisymmetric, so all non-circular motions can be attributed to the non-axisymmetric luminous component. This approach has been applied to both bars (e.g. Englmaier & Gerhard, 1999; Weiner, Sellwood & Williams, 2001) and spiral arms (e.g. Kranz, Slyz & Rix, 2003) and provides results consistent with maximal disk studies. Further constraints come from N-body simulations of bars, which imply that a significant central dark component would slow or even destroy bars (e.g. Debattista & Sellwood, 2000), while observations systematically indicate that bars are fast (e.g. Aguerri, Debattista & Corsini, 2003; Gerssen, Kuijken & Merrifield, 2003).

To summarize, observational evidence indicates that the kinematics of both spiral

and elliptical galaxies can often be reproduced by mass models that include a sub-dominant contribution from dark matter in the optical or central regions. The specific amount required and correlations between halo and luminous galaxy properties are, however, unclear. Note that we have not mentioned low surface brightness and dwarf galaxies, which are dark matter-dominated at all radii (e.g. Persic, Salucci & Stel, 1996; de Blok & McGaugh, 1997; Verheijen, 1997; Swaters, 1999) and may provide the most stringent constraints on halo shapes, once observational uncertainties are resolved (e.g. de Blok, McGaugh & Rubin, 2001; Swaters et al., 2003, and references therein). Such galaxies are, however, unrepresentative and extrapolating their results to systems with greater stellar masses may introduce biases. It is therefore crucial to place accurate constraints on the dark matter content of giant, high surface brightness spiral, S0 and elliptical galaxies.

This work uses a modelling technique which is different but qualitatively similar to traditional mass decomposition and rotation curve analyses of spiral galaxies. The key differences are (1) the stellar components of our mass models are based on deep near-infrared photometry, which accurately traces the smooth stellar potential of the galaxy (see Section 2.2.1), (2) we lift a degeneracy by making assumptions about the shape of the dark halo that are motivated by the results of cosmological simulations and observational constraints (see Section 2.2.2) (3) we lift a further degeneracy (and account for pressure support) by comparing the predicted second velocity moment rather than the rotational velocity to the observed kinematics (see Section 2.2.3).

We apply this technique to a sample of 28 edge-on spiral and S0 galaxies. We use edge-on galaxies because, under the assumption of axisymmetry, the deprojection is unique. Moreover, when a galaxy is close to edge-on ($i = 90^\circ$), an inclination error does not propagate on to significant uncertainties in the kinematics in the plane of the galaxy (which is proportional to $\sin i$), and thus on to significant mass uncertainties. The mass models consist of a dark halo component and an unusually detailed parametrization of the projected light. Under justifiable assumptions, the mass model has three free parameters, the stellar mass-to-light ratio, the mass of the dark halo and the velocity anisotropy. We place constraints on these parameters by adjusting them so that the mass model predicts stellar kinematics that closely match

those observed. We hope that these simple but powerful quantitative statements will be of use in constraining models of galaxy formation and evolution.

In addition to the halo masses inferred, the constraints we place on the near-infrared stellar mass-to-light ratios are themselves of great interest. There are significant difficulties in modelling the spectral energy distribution of stellar populations in the near-infrared, due to the importance of the complex thermally pulsing asymptotic giant branch at these wavelengths (Maraston, 2005). Moreover, the normalization of the models is uncertain due to a lack of knowledge about the initial mass function of stars. Dynamical measures of the near-infrared stellar mass-to-light ratio like ours, that do not depend on population models and seek to correctly account for dark matter, therefore provide important independent tests of these models.

A final goal of the study is to provide detailed constraints on dark matter in S0 galaxies. The dark matter content of S0s is an important quantity to constrain because the dominant model of S0 formation as faded spirals predicts a simple and verifiable relation between the Tully-Fisher relations of spirals and S0s (e.g. Bedregal, Aragón-Salamanca & Merrifield, 2006, and references therein). Galaxies that lie on a single Tully-Fisher relation linking their luminosities and rotational velocities are believed to have equal dynamical mass-to-light ratios. I investigate this in more detail in Section 3.

This chapter is organised as follows: in Section 2.2 we describe the multi-Gaussian expansion used to model the luminous and dark mass distribution of the galaxies and the dark halo model adopted. We then give an overview of the Jeans modelling technique used to model the stellar kinematics. In Section 2.3 we present the sample of edge-on galaxies under consideration and describe the photometric and kinematic data. In Section 2.4 we present the results of our modelling of both the mass distribution and stellar kinematics of the sample, which we discuss in depth in Section 2.5. Finally, we summarise our conclusions in Section 2.6.

2.2 METHODS

2.2.1 *Modelling the luminous mass distribution*

We use multi-Gaussian expansions (MGEs) to create mass models that have a simple analytic form whose kinematics can easily be determined using the Jeans equations. MGE is a method of parametrizing an image of a galaxy as the sum of a finite number of two-dimensional Gaussian functions. The original application of two-dimensional Gaussians to galaxy images (Bendinelli, 1991) was extended to the non-circular case and to more general point spread functions (PSFs) by Monnet, Bacon & Emsellem (1992) and Emsellem, Monnet & Bacon (1994). Here we briefly summarize the method using a formalism due to Cappellari (2002), which we simplify for the special case of axisymmetric edge-on disk galaxies with a luminous component with a constant mass-to-light ratio.

In a coordinate system (x, y, z), where x and z are centred on the galaxy nucleus and point along the major and minor axes in the plane of the sky while the y-axis points away from the observer, $\tilde{\Sigma}_X(x,z)$ the apparent surface brightness of a galaxy at an arbitrary waveband X can be written as a sum of N two-dimensional Gaussians of apparent width $\tilde{\sigma}_i$ in the x-direction and $\tilde{\sigma}_i\tilde{q}_i$ in the z-direction:

$$\tilde{\Sigma}_X(x,z) = \sum_{i=1}^{N} \frac{L_i}{2\pi\tilde{\sigma}_i^2\tilde{q}_i} \exp\left[-\frac{1}{2\tilde{\sigma}_i^2}\left(x^2 + \frac{z^2}{\tilde{q}_i^2}\right)\right], \tag{2.1}$$

where L_i is the total luminosity of the ith Gaussian component. We further model the PSF as a circular Gaussian of width σ_{PSF} such that the intrinsic projected light distribution, deconvolved from seeing effects, is

$$\Sigma_X(x,z) = \sum_{i=1}^{N} \frac{L_i}{2\pi\sigma_i^2 q_i} \exp\left[-\frac{1}{2\sigma_i^2}\left(x^2 + \frac{z^2}{q_i^2}\right)\right], \tag{2.2}$$

where σ_i, the intrinsic width of the ith Gaussian in the x-direction, and $\sigma_i q_i$, the intrinsic width in the z-direction, are given by

$$\sigma_i^2 = \tilde{\sigma}_i^2 - \sigma_{\mathrm{PSF}}^2, \tag{2.3}$$

$$\sigma_i^2 q_i^2 = \tilde{\sigma}_i^2 \tilde{q}_i^2 - \sigma_{\mathrm{PSF}}^2. \tag{2.4}$$

Once the projected light distribution is expressed in this simple analytic form, it can be deprojected straightforwardly to give a full three-dimensional model of the light. In this work we deproject by assuming that the galaxy is axisymmetric, but other assumptions about the geometry are possible. Assuming axisymmetry and an edge-on view allows us to trivially transform from the (x, y, z) Cartesian coordinates of the Gaussians on the sky to the (R, ϕ, z) cylindrical system of the galaxy, where R is the galactocentric radius, ϕ the azimuthal angle and z the axis of symmetry of the galaxy. We also assume a constant stellar mass-to-light ratio $(M/L)_X$ to transform the stellar light at waveband X to a stellar mass distribution.

Together these assumptions of axisymmetry, an edge-on view and a constant mass-to-light ratio imply that the intrinsic mass distribution of the luminous component of the galaxy can be written as

$$\rho(R,z) = (M/L)_X \sum_{i=1}^{N} a_i \exp\left[-\frac{1}{2\sigma_i^2}\left(R^2 + \frac{z^2}{q_i^2}\right)\right], \tag{2.5}$$

where $a_i = L_i/(\sqrt{2\pi}\sigma_i)^3 q_i$.

In this work we determined an optimal MGE parametrization of the images described in Section 2.3 using the public fitting routine of Cappellari (2002)[1], which minimizes the quantity

$$\chi^2_{\mathrm{MGE}} \equiv \sum_{j=1}^{M}\left(\frac{C_j(x,z) - \tilde{\Sigma}(x,z)}{C_j(x,z)}\right)^2 \tag{2.6}$$

for a given set of σ_i, q_i and L_i, where M is the number of photometric data points C_j and $\tilde{\Sigma}$ is the apparent surface brightness of the model.

A MGE is simply a sum of Gaussians reproducing the observed surface brightness. As such, the amplitude of each individual Gaussian, L_i, is not constrained to be positive as long as the total luminosity and density are positive. Our sample consists of edge-on disk galaxies, which are particularly difficult to fit with solely positive Gaussian terms. As was demonstrated by Bureau et al. (2006), the major axis surface brightness profiles exhibit significant plateaus and secondary maxima. These cannot be fitted by a sum of concentric Gaussians with positive amplitudes, which is necessarily

[1] `http://purl.org/cappellari`

monotonically decreasing with radius. The complex rectilinear or concave two-dimensional structures visible in the isophotes of boxy and peanut-shaped (B/PS) bulges are similarly challenging.

We therefore lifted the positivity constraint on L_i when modelling the luminous mass. In doing so, we encountered numerical issues with both the accuracy and stability of the fitting algorithm when using large numbers of Gaussians (≈ 30). We solved these by reducing the maximum number of Gaussians in the sum to a relatively small number (≈ 10), enabling double precision arithmetic to avoid cancellation errors, and finally, where necessary, tweaking the minimum surface brightness level down to which the fit was constrained by the photometry. We show a typical example of the improvement that is possible when terms with negative amplitude are allowed in Fig. 2.1. These improved mass models resulted in small but systematic improvements in the accuracy of the modelled kinematics. That a more accurate description of the light gives a more accurate model of the kinematics gives us some confidence that our kinematic modelling methods and assumptions (described in Section 2.2.3) are not significantly flawed.

The pixel-by-pixel absolute deviation from the photometry of our MGEs is typically 2–4 per cent. For a given constant $(M/L)_X$ these small errors are propagated linearly into the mass model. In most previous work, the observed surface brightness distribution of disk galaxies is parametrized using fits to azimuthally averaged radial profiles (e.g. Ratnam & Salucci, 2000; Kassin, de Jong & Weiner, 2006) or two-dimensional Sérsic and/or exponential decompositions (e.g. Gentile et al., 2004). While the terms in our MGEs lack any direct physical association with intrinsic components of the galaxies (bulge, disk, etc.), they reproduce the observed surface photometry more accurately than the simpler parametrizations, and their form is mathematically convenient for Jeans modelling (see Section 2.2.3).

At large radii, where the model is only weakly constrained by photometric data, models including negative Gaussians can look a little unphysical to the eye (see, e.g., NGC 1886 in Fig. 2.5). Because there is so little light at these radii, however, we are confident that this does not affect the results significantly. We confirmed this by summing the light of all Gaussians in the MGE models, which can of course be

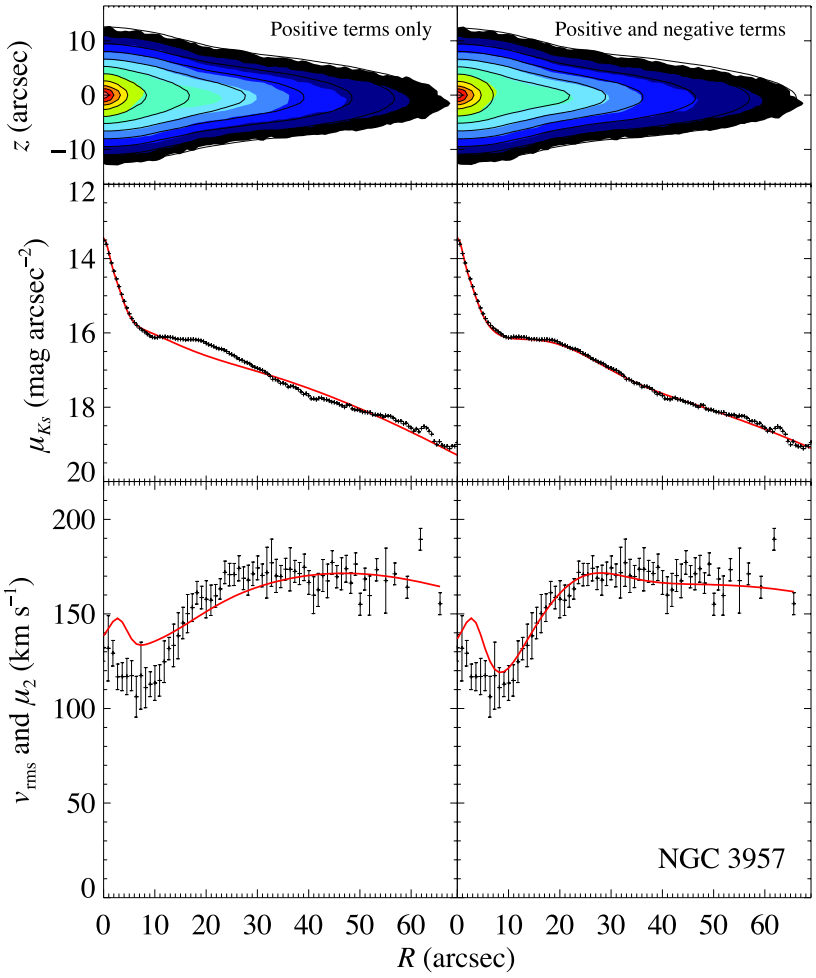

Figure 2.1: A comparison of the best MGE model with only positive amplitude Gaussians (left-hand panels) to one with both positive and negative amplitude Gaussians (right-hand panels) for the same object, NGC 3957. The top plots show the K_S-band surface brightness of the image (filled contours) and model isophotes (solid lines). Contours are separated by 0.5 mag arcsec^{-2}. The middle plots show the major axis surface brightness profiles of the image (points) and models (solid lines). The bottom panels show $v_{\rm rms}$ (points), the observed root mean square velocity, and μ_2, the best-fitting second moment found by solving the Jeans equations for the MGE model (solid lines). Note that allowing terms in the Gaussian expansion to have a negative amplitude improves both the fit to the photometry and the accuracy with which the kinematics can be reproduced. In order to make the effect clear, the mass model shown here does not include a dark halo.

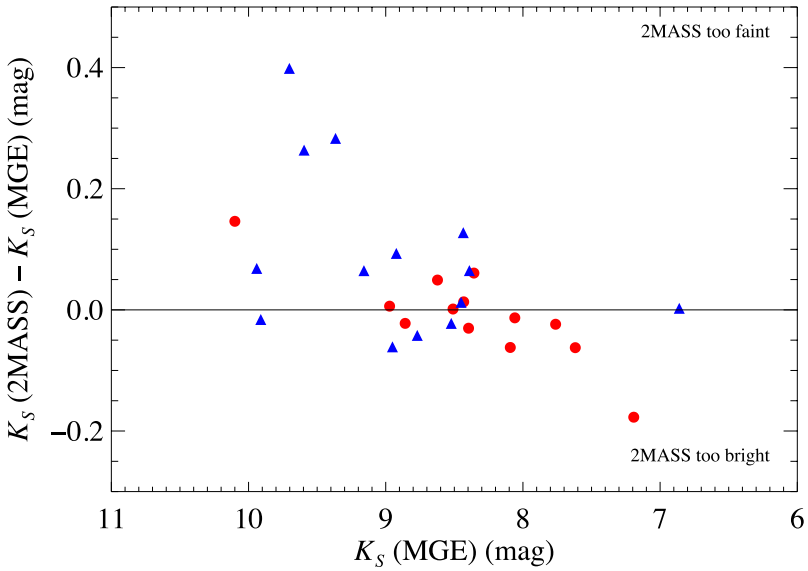

Figure 2.2: Comparison of the apparent magnitudes of the sample galaxies computed by summing the light of all Gaussians in the best-fitting MGE models with the apparent magnitudes published in the 2MASS Extended Source Catalog. The 2MASS values are derived in the usual way using a growth curve. The methods typically agree to within 0.2 mag. S0s are shown as red circles and spirals as blue triangles.

computed analytically, to derive estimates of the total apparent magnitudes of the galaxies. As is shown in Fig. 2.2, these match the total apparent magnitudes presented in the 2MASS Extended Source Catalog (Jarrett et al., 2000) to within 0.2 mag. This demonstrates that the excess light sometimes present in the outer regions of MGEs including negative terms is not significant, and that the photometric calibration described in Appendix 2.A is reliable. Fig. 2.2 also hints that the application of a growth curve method to the relatively shallow 2MASS images of faint objects results in total magnitudes that are systematically too faint (see also Noordermeer & Verheijen, 2007).

2.2.2 *Modelling the dark halo mass distribution*

If mass models are derived under the assumption that mass follows light then that implicitly assumes that dark matter is not a significant component by mass within the radius probed by the model. Strictly speaking, such models also admit the possibility

that the spatial distribution of dark matter closely matches that of the luminous matter, but we know of no physically motivated model of galaxy formation that predicts this behaviour.

We extend our models by explicitly including a dark halo. Although the long-slit kinematic data for each galaxy typically reach ≈2–3 $R_{\rm eff}$ or, equivalently, ≈0.5–1 R_{25}, they are insufficient to allow a us to constrain the shape of the halo of giant, high surface brightness galaxies like these (see, e.g. Banerjee & Jog, 2008). We therefore emphasise that we are not able to constrain the shapes of the dark haloes. Rather we attempt to probe the more limited question of what fraction by mass of each galaxy is dark *assuming* the haloes follow the particular one-parameter density profile described below.

Our halo model is motivated by the results of N-body simulations of cold dark matter (CDM) in an up-to-date cosmology. In such simulations the dark matter halo density $\rho_{\rm DM}$ is given by the spherically averaged NFW profile:

$$\rho_{\rm DM}(r) = \frac{\rho_{\rm s}}{(r/r_{\rm s})(1+r/r_{\rm s})^2} \tag{2.7}$$

(e.g. Navarro, Frenk & White, 1997; Bullock et al., 2001; Wechsler et al., 2002), were $r_{\rm s}$ is a scale radius characterising the location of the 'break' in the profile and $\rho_{\rm s}$ is a corresponding inner density.

Rewriting equation (2.7) in terms of $M_{\rm DM}$, the total dark matter mass enclosed within the virial radius $r_{\rm vir}$, and defining a concentration parameter $c_{\rm vir} \equiv r_{\rm vir}/r_{\rm s}$ implies

$$\rho_{\rm DM}(r) = \frac{M_{\rm DM}}{4\pi A(c_{\rm vir})}\frac{1}{r(r_{\rm s}+r)^2}, \tag{2.8}$$

where $M_{\rm DM} = 4\pi\rho_{\rm s} r_{\rm s}^3 A(c_{\rm vir})$ and

$$A(x) = \ln(1+x) - \frac{x}{1+x}. \tag{2.9}$$

The virial radius is defined as the radius within which the mean density is $\Delta\rho_{\rm crit}$ and $\rho_{\rm crit,0} = 3H_0^2/8\pi G$ now. Throughout this work we adopt the cosmological parameters found by the *Wilkinson Microwave Anisotropy Probe* five-year results (WMAP5), i.e. $\Delta = 95.1$ and the Hubble constant $H_0 = 100\,h\,{\rm km\,s^{-1}\,Mpc^{-1}}$ where $h = 0.70$ (Komatsu et al., 2009).

Following Napolitano et al. (2005), we use a key result from simulations of ΛCDM to eliminate one of the free parameters from equation (2.8). The simulations demonstrate that concentration and halo mass are correlated: low mass haloes are more concentrated and the concentration–mass relation is well described by a single power law with a slope ≈ -0.1 (e.g. Navarro, Frenk & White, 1997; Bullock et al., 2001; Eke, Navarro & Steinmetz, 2001; Kuhlen et al., 2005; Neto et al., 2007). We choose the fitting formula presented by Macciò, Dutton & van den Bosch (2008) that is consistent with their WMAP5 simulations over the range $10^{10}\,M_\odot < M_{\rm vir} < 10^{15}\,M_\odot$:

$$c_{\rm vir}(M_{\rm vir}) \approx 9.354 \left(\frac{M_{\rm vir}}{h^{-1}10^{12}\,M_\odot} \right)^{-0.094}, \tag{2.10}$$

where $M_{\rm vir}$ is the *total* mass enclosed within the virial radius.

We then rewrite this relationship in terms of the dark mass inside the virial radius, rather than the total mass using the equation $M_{\rm vir} = \alpha\, M_{\rm DM}$. A number of plausible choices are available to us for the constant α: to adopt the cosmological value, to neglect the contribution of baryons entirely, or to adopt some intermediate value. The cosmological value is derived from the ratios of matter density to critical density $\Omega_{\rm m} = 0.258$ and baryon density to critical density $\Omega_{\rm b} = 0.0438$, which together imply

$$\alpha = \frac{\Omega_{\rm m}}{\Omega_{\rm m} - \Omega_{\rm b}} = 1.20. \tag{2.11}$$

The most extreme 'missing baryon' scenario, which neglects the contribution of baryons to the total viral mass, implies $\alpha = 1$. An intermediate possibility is motivated by the results of observationally constrained halo occupation distribution methods and semi-analytic models, which imply that the stellar mass of a galaxy is typically around 3 per cent of that of its halo, i.e. $\alpha = 1.03$. In this work we follow Napolitano et al. (2005) and adopt the cosmological value, $\alpha = 1.20$, which gives

$$c_{\rm vir}(M_{\rm DM}) \approx 9.195 \left(\frac{M_{\rm DM}}{h^{-1}10^{12}\,M_\odot} \right)^{-0.094}. \tag{2.12}$$

However, we note that the choice of α makes almost no different to our results. This is because α is immediately raised to the power -0.094 in order to define the concentration of the halo; a 20 per cent change in α changes $c_{\rm vir}$ at the 2 per cent level. If our choice is wrong and results in the introduction of such a small systematic error

in $c_{\rm vir}$, then the consequences for the parameters of the best-fitting mass models are in any case negligible compared to the observational errors.

The dark halo density profile may therefore be written as a function of a single parameter, $M_{\rm DM}$, using equations (2.8), (2.9) and (2.12). We perform a multi-Gaussian expansion of this one-dimensional, single parameter profile to allow us to easily include it in the potential for which we derive model kinematics.

We refrain from including prescriptions for the effects of baryonic contraction on our halo model (e.g. Blumenthal et al., 1986; Gnedin et al., 2004; Abadi et al., 2010). We do this for two reasons. Firstly, our goal is not to determine the detailed shapes of dark haloes but rather the total dark and stellar masses in the optical parts of galaxies. Secondly, while our kinematic data do not allow us to constrain the halo shape, other observational evidence suggests that contracted NFW haloes do not reproduce observed kinematics. (e.g. Gentile et al., 2004; Kassin, de Jong & Weiner, 2006; Thomas et al., 2007).

2.2.3 *Modelling the stellar kinematics*

The most general dynamical methods are particle-based (e.g. de Lorenzi et al., 2007) or orbit-based (e.g. Schwarzschild, 1979; Cappellari et al., 2007; van den Bosch et al., 2008; Thomas et al., 2009). These powerful methods are so general, however, that a wide range of unrealistic models can be made to fit long-slit data, providing only weak constraints on the parameters of the mass models (see, e.g., fig. 2 of Cappellari & McDermid, 2005). In fact, the stellar kinematics of early-type fast-rotator galaxies are well-described by Jeans models with a cylindrically-aligned velocity ellipsoid with a constant flattening in the z-direction (Cappellari et al., 2007; Thomas et al., 2009). This has lead to the use of a Jeans modelling technique in which such a velocity ellipsoid is assumed. By varying the flattening of the velocity ellipsoid, the Jeans modelling approach has been shown to reproduce a wide range of two-dimensional observed kinematics in the central regions of early-type fast-rotators in the SAURON survey (Cappellari, 2008; Scott et al., 2009) and out to $5\,R_{\rm eff}$ in the case of the edge-on S0

NGC 2549 (Weijmans, 2009). The large size of our sample (28 galaxies) allows us to test whether the assumptions provide a good description of our galaxies, but we note that our galaxies are at least as rotationally supported as the SAURON galaxies, so we expect to be even less vulnerable to assumptions about anisotropy.

For convenience we provide an overview of the derivation and solution of the Jeans equations. This is essentially a summary of Sections 2 and 3.1 of Cappellari (2008). Under the assumptions required for the collisionless Boltzmann equation to hold (a smooth potential and steady state), and the further assumption of axisymmetry, the Jeans equations may be written in cylindrical coordinates as

$$\frac{\rho\overline{v_R^2} - \rho\overline{v_\phi^2}}{R} + \frac{\partial(\rho\overline{v_R^2})}{\partial R} + \frac{\partial(\rho\overline{v_R v_z})}{\partial z} = -\rho\frac{\partial\Phi}{\partial R}, \tag{2.13}$$

$$\frac{\rho\overline{v_R v_z}}{R} + \frac{\partial(\rho\overline{v_z^2})}{\partial z} + \frac{\partial(\rho\overline{v_R v_z})}{\partial R} = -\rho\frac{\partial\Phi}{\partial z} \tag{2.14}$$

(Jeans 1922; Binney & Tremaine 2008). Here ρ is the density, Φ is the gravitational potential and we use the usual notation

$$\rho\overline{v_k v_j} \equiv \int v_k v_j f \, \mathrm{d}^3\mathbf{v}. \tag{2.15}$$

Even if ρ and Φ are known (as is the case for our mass models), equations (2.13) and (2.14) are still two equations with four unknowns, $\overline{v_R^2}$, $\overline{v_z^2}$, $\overline{v_\phi^2}$ and $\overline{v_R v_z}$, so they do not specify a unique solution. In order to close the equations one can assume a particular anisotropy, i.e. a relationship between the lengths of the axes of the velocity ellipsoid. We assume here that the velocity ellipsoid is aligned with the cylindrical coordinate system of the galaxy and that the anisotropy in the meridional plane is constant ($\overline{v_R^2} = b\overline{v_z^2}$ where b is a constant). Under these assumptions, equations (2.13) and (2.14) reduce to:

$$\frac{b\,\rho\overline{v_z^2} - \rho\overline{v_\phi^2}}{R} + \frac{\partial(b\,\rho\overline{v_z^2})}{\partial R} = -\rho\frac{\partial\Phi}{\partial R}, \tag{2.16}$$

$$\frac{\partial(\rho\overline{v_z^2})}{\partial z} = -\rho\frac{\partial\Phi}{\partial z}. \tag{2.17}$$

These equations are solved for the case of a density and potential described by a sum of Gaussians in Cappellari (2008). Once the observable quantities in the solutions have been projected along the line-of-sight, a single integration gives a model of the

second velocity moment, μ_2 (see equation [28] of Cappellari 2008). We use the Jeans Anisotropic MGE (JAM) routines to perform the calculation.[1] The second velocity moment is compared to the observed root mean square velocity, $v_{\rm rms} \equiv (v^2 + \sigma^2)^{1/2}$, where v is the observed line-of-sight velocity and σ the observed line-of-sight velocity dispersion. $v_{\rm rms}$ is a good approximation to the true second moment. The second moment μ_2 is perhaps a less familiar quantity to work with than the circular or line-of-sight velocities, but it has the distinct advantage that it is not necessary to assume a particular 'splitting' between ordered and random motions. We discuss its physical meaning in more detail in Section 2.5.5.3.

The quantity b is often expressed as an anisotropy parameter $\beta_z = 1 - 1/b$, where $\beta_z = 0$ corresponds to isotropy. To give an idea of the kinds of anisotropies observed in real galaxies, Shapiro, Gerssen & van der Marel (2003) found flattened velocity ellipsoids with $0.35 \lesssim \beta_z \lesssim 0.75$ in the disks of Sa and Sb galaxies. Cappellari et al. (2007) and Thomas et al. (2009) found more circular ellipsoids for which $\beta_z \lesssim 0.4$ in fast-rotator ellipticals and S0s.

If the anisotropy β_z is free then the predicted kinematics for each galaxy are a function of three parameters: $(M/L)_{\rm X}$, $M_{\rm DM}$ and β_z. We find, however, that for our galaxies, which are rotation dominated, the predicted kinematics along the slit are not very sensitive to the particular choice of β_z. This means that we are unable to place stringent constraints on anisotropy using these data, but it also means that we are not vulnerable to serious systematic errors due to our assumptions about anisotropy.

2.2.4 *Summary of methods and assumptions*

To sum up our methods section, we find the stellar component of each mass model by assuming axisymmetry and a constant stellar mass-to-light ratio. To each model we add a dark halo that follows a spherically symmetric NFW profile and assumes the correlation between halo concentration and halo mass defined by equation (2.12). The total mass model is a function of two parameters, the stellar mass-to-light ratio $(M/L)_X$ and the dark halo mass within the virial radius $M_{\rm DM}$. It is expressed as a

sum of Gaussians.

The mass model is used to calculate an estimate of the observed stellar kinematics. This is done by solving the Jeans equations under the assumption of constant anisotropy in the meridional plane, yielding the second velocity moment, μ_2. This predicted quantity is then compared to the observed root mean square velocity $v_{\rm rms} \equiv (v^2 + \sigma^2)^{1/2}$. The two parameters of the mass model $(M/L)_X$ and $M_{\rm DM}$, and the velocity anisotropy β_z are then adjusted until the predicted stellar kinematics match the observations, placing constraints on those parameters.

Having determined the parameters for each galaxy, we also compute circular the velocities $v_{\rm c}$ of the stellar, dark and total mass distributions using the numerical techniques described in Cappellari (2002). $v_{\rm c}$ provides an intuitive measure of the mass enclosed as a function of radius, which is proportional to $v_{\rm c}^2$. The ratio of the squares of the stellar and dark circular velocities is therefore equal to the ratio of the stellar and dark mass enclosed. $v_{\rm c}$ will also be useful in Chapter 3.

All mass-to-light ratios in this work are given in solar units, i.e. the mass-to-light ratio at waveband X, $(M/L)_X$, is in units of $(M/L)_{X,\odot}$.

2.3 SAMPLE AND OBSERVATIONS

We apply the methods described above to a sample of 28 edge-on disk galaxies selected by Bureau & Freeman (1999). 14 of the 28 galaxies are classified as S0s and the remaining 14 are Sa–Sb galaxies (see Table 2.1).

The galaxies in the sample were originally selected to investigate the nature of boxy and peanut-shaped (B/PS) bulges. Of the 28 galaxies, 22 have a B/PS bulge and 6 form a control sample with spheroidal bulges. Galaxies with a B/PS bulges are edge-on disk systems with bulge isophotes above and below the centre of the disk that are either horizontal (boxy) or concave (peanut-shaped). B/PS bulges are thought to simply be bars viewed edge-on. Many N-body simulations have shown that bars buckle and thicken soon after formation, resulting in an object that appears peanut-shaped when viewed side-on and boxy when viewed at intermediate angles

(e.g. Combes & Sanders, 1981; Combes et al., 1990; Raha et al., 1991; Athanassoula & Misiriotis, 2002). Lütticke, Dettmar & Pohlen (2000) found that 45 per cent of edge-on disk galaxies have a B/PS bulge, which is roughly consistent with the fraction of bars in face-on spirals. Moreover, several studies have identified the kinematic signatures of bars in systems with a B/PS bulge (e.g. Kuijken & Merrifield, 1995; Merrifield & Kuijken, 1999; Bureau & Freeman, 1999; Chung & Bureau, 2004) and a recent study demonstrates the converse by observing kinematic evidence for a B/PS bulge in a face-on barred system (Méndez-Abreu et al., 2008). The sample therefore contains galaxies whose central regions are probably non-axisymmetric. If there is a direct correspondence between B/PS bulges and bars, then the bar fraction in our sample ($\approx$ 75 per cent) is representative of that in all disk galaxies ($\approx$ 65 per cent, e.g. Sheth et al. 2008). In fact, we will argue in Section 2.5 the these non-axisymmetries do not affect our results, despite our axisymmetric modelling techniques.

To parametrize the projected light distribution we use the relatively deep, high-resolution *K*n-band images presented by Bureau et al. (2006). In the course of this work we discovered that the photometric calibration of the images was incorrect (they were too faint by $\approx$ 0.8 mag), so we used shallower 2MASS images to recalibrate them, transforming from *K*n to K_S-band in the process. We describe this procedure in detail in Appendix 2.A. We also correct the 2MASS images and therefore our models for the effects of foreground Galactic extinction using the dust maps of Schlegel, Finkbeiner & Davis (1998). Because the apparent surface brightness distributions that we parametrize are at K_S-band, the mass-to-light ratios we measure are also at K_S-band, and therefore denoted $(M/L)_{K_S}$. Throughout this work we adopt a value for the absolute magnitude of the Sun at K_S-band of $M_{K_S,\odot} = 3.29$ (Blanton & Roweis, 2007).

Table 2.1: Galaxy sample

Galaxy	Type	D (Mpc)	R_{25} (arcsec)	$R_{\rm eff}$ (arcsec)	$R_{\rm max}/R_{25}$	$R_{\rm max}/R_{\rm eff}$	K_S (mag)	B (mag)	M_{K_s} (mag)	M_B (mag)
(1)	(2)	(3)	(4)	(5)	(6)	(7)	(8)	(9)	(10)	(11)
				B/PS bulges						
ESO 151-G004	$S0^0$	106.9	42.2	14.1	0.71	2.13	10.29	14.73	−24.85	−20.41
ESO 185-G053	SB pec	66.9	37.4	12.3	0.77	2.34	9.91	14.04	−24.22	−20.09
ESO 240-G011	Sb	41.4	167.2	41.5	0.73	2.92	8.43	11.53	−24.65	−21.56
ESO 311-G012	S0/a?	14.5	122.8	29.7	0.49	2.04	7.76	10.89	−23.05	−19.92
ESO 443-G042	Sb	35.8	84.6	35.9	0.86	2.02	9.37	12.56	−23.40	−20.21
ESO 597-G036	$S0^0$ pec	123.5	43.3	18.5	0.87	2.04	10.10	14.76	−25.36	−20.70
IC 4767	S pec	53.3	57.8	21.4	0.64	1.72	9.94	13.91	−23.69	−19.72
IC 4937	Sb	72.4	51.5	27.7	0.87	1.63	9.70	13.84	−24.60	−20.46
IC 5096	Sb	47.0	105.7	27.6	0.56	2.14	8.52	12.15	−24.84	−21.21
NGC 128	S0 pec	59.2	95.3	18.1	0.49	2.58	8.51	12.46	−25.35	−21.40
NGC 1381	SA0	16.8	76.2	20.1	0.92	3.47	8.36	12.35	−22.76	−18.77
NGC 1596	SA0	15.3	116.7	21.7	0.39	2.11	8.06	11.94	−22.86	−18.98
NGC 1886	Sab	24.5	96.2	31.1	0.71	2.20	9.16	12.22	−22.79	−19.73
NGC 2310	S0	15.2	135.6	39.2	0.64	2.21	8.43	11.48	−22.48	−19.43
NGC 3203	$SA(r)0^+$	35.4	96.6	22.1	0.64	2.80	8.86	12.76	−23.89	−19.99
NGC 3390	Sb	44.0	93.8	28.4	0.92	3.03	8.39	11.73	−24.83	−21.49
NGC 4469	SB(s)0/a?	16.5	143.3	39.1	0.60	2.21	8.09	12.07	−23.00	−19.02
NGC 4710	$SA(r)0^+$	16.5	131.6	44.0	0.73	2.19	7.62	11.69	−23.47	−19.40
NGC 5746	SAB(rs)b?	30.4	217.3	51.0	0.67	2.84	6.86	10.11	−25.55	−22.30
NGC 6722	Sb	70.9	87.9	22.4	0.81	3.19	8.95	12.28	−25.30	−21.97
NGC 6771	$SA(r)0^+$	64.6	98.7	15.5	0.52	3.29	8.97	13.24	−25.08	−20.81
PGC 44931	Sbc	61.2	91.4	32.3	0.66	1.86	9.60	12.60	−24.34	−21.33
				Control sample						
IC 5176	SAB(s)bc?	24.8	135.2	29.6	0.46	2.10	8.77	12.02	−23.20	−19.95
NGC 1032	S0/a	37.0	106.0	21.0	0.58	2.91	8.40	12.13	−24.44	−20.71
NGC 3957	$SA0^+$	24.1	100.7	31.6	0.65	2.08	8.62	12.71	−23.29	−19.20
NGC 4703	Sb	72.0	50.9	28.0	1.33	2.43	8.92	13.37	−25.36	−20.92

continued ...

Table 2.1: — continued

Galaxy	Type	D (Mpc)	R_{25} (arcsec)	$R_{\rm eff}$ (arcsec)	$R_{\rm max}/R_{25}$	$R_{\rm max}/R_{\rm eff}$	K_S (mag)	B (mag)	M_{K_S} (mag)	M_B (mag)
(1)	(2)	(3)	(4)	(5)	(6)	(7)	(8)	(9)	(10)	(11)
NGC 5084	S0	24.2	297.9	27.0	0.30	3.26	7.19	10.07	−24.73	−21.85
NGC 7123	Sa	55.3	80.2	17.1	0.60	2.83	8.45	12.90	−25.26	−20.81

Notes. (1) Galaxy name. To ensure continuity with previous studies, the sample is subdivided into B/PS bulges and control galaxies. (2) Morphological type taken from Jarvis (1986), de Souza & Dos Anjos (1987), Shaw (1987) and Karachentsev, Karachentseva & Parnovskij (1993). (3) Distance. The distance of NGC 1381 is taken from Jensen et al. (2003) and that of NGC 1596 from Tonry et al. (2001). NGC 4469 and NGC 4710 are members of the Virgo cluster so we adopt the cluster distance derived by Mei et al. (2007). For all other galaxies we use distances from the NASA/IPAC Extragalactic Database (NED) calculated assuming a WMAP5 cosmology (Komatsu et al. 2009, $H_0 = 70\,{\rm km\,s^{-1}\,Mpc^{-1}}$) and a Virgocentic flow model (Mould et al., 2000). (4) Radius of the $25\,{\rm mag\,arcsec^{-2}}$ B-band isophote taken from HYPERLEDA (Paturel et al., 2003). (5) Semi-major axis of the ellipse containing half the light at K_S-band, measured using the near-infrared photometry presented in Bureau et al. (2006) and the method described in Section 2.4. (6) and (7) Radius of the last stellar kinematic data point used in this work, expressed as a fraction of R_{25} and $R_{\rm eff}$. (8) Apparent magnitude at K_S-band derived from the MGE parametrization of the Kn-band image (Bureau et al., 2006) calibrated using the 2MASS K_S-band image (Skrutskie et al., 2006) corrected for Galactic extinction. (9) Apparent magnitude at B-band corrected for internal and Galactic extinction taken from HyperLEDA. (10) and (11) Absolute magnitudes derived from the distance and apparent magnitudes in columns (3), (8) and (9).

We compare the predicted kinematics of the mass models to major-axis long-slit stellar kinematics presented in Chung & Bureau (2004). We use stellar kinematics rather than gas kinematics because gas is not present and/or not extended in many cases. Where gas is present, it is strongly affected by non-circular motions and shocks in the inner parts of many of the objects (see Bureau & Athanassoula, 1999; Athanassoula & Bureau, 1999). Line-of-sight velocity distributions were extracted using the Fourier Correlation Quotient algorithm (Bender, 1990); the v and σ used are those of the best-fitting Gaussian.

2.4 RESULTS

2.4.1 *Exploring parameter space*

Before presenting our best models, we give an overview of how the changes in $(M/L)_{K_S}$ and $M_{\rm DM}$ affect the predicted second velocity moment μ_2, and what kinds of constraints this allows us to place on these parameters. In general, increasing $(M/L)_{K_S}$ shifts the model μ_2 to greater velocities at all radii. Increasing $M_{\rm DM}$ increases μ_2 at large radii more than it does at small radii. Fig. 2.3 demonstrates this behaviour for NGC 1381.

We define the best-fitting model for each galaxy to be the one with the combination of parameters $(M/L)_{K_S}$, $M_{\rm DM}$ and β_z that results in a predicted μ_2 that most closely matches the observed $v_{\rm rms}$. The figure of merit, χ^2, is therefore defined as

$$\chi^2 \equiv \sum \frac{\{v_{\rm rms} - \mu_2[M_{\rm DM}, (M/L)_{K_S}, \beta_z]\}^2}{\Delta v_{\rm rms}^2}, \tag{2.18}$$

where $\Delta v_{\rm rms}$ is the error in $v_{\rm rms}$ and the summation is over all kinematic data points.

We show contour plots of χ^2 as a function of these parameters for the complete sample in Fig. 2.4. For clarity, these plots are marginalized over the anisotropy β_z. This means that the value of χ^2 used at each point in $M_{\rm DM}$–$(M/L)_{K_S}$ space is set to $\min(\chi^2[M_{\rm DM}, (M/L)_{K_S}, \beta_z])$ for $0 < \beta_z < 0.75$. The contours become horizontal for $M_{\rm DM} \lesssim 10^8 M_\odot$ because very low mass haloes do not affect the dynamics of the

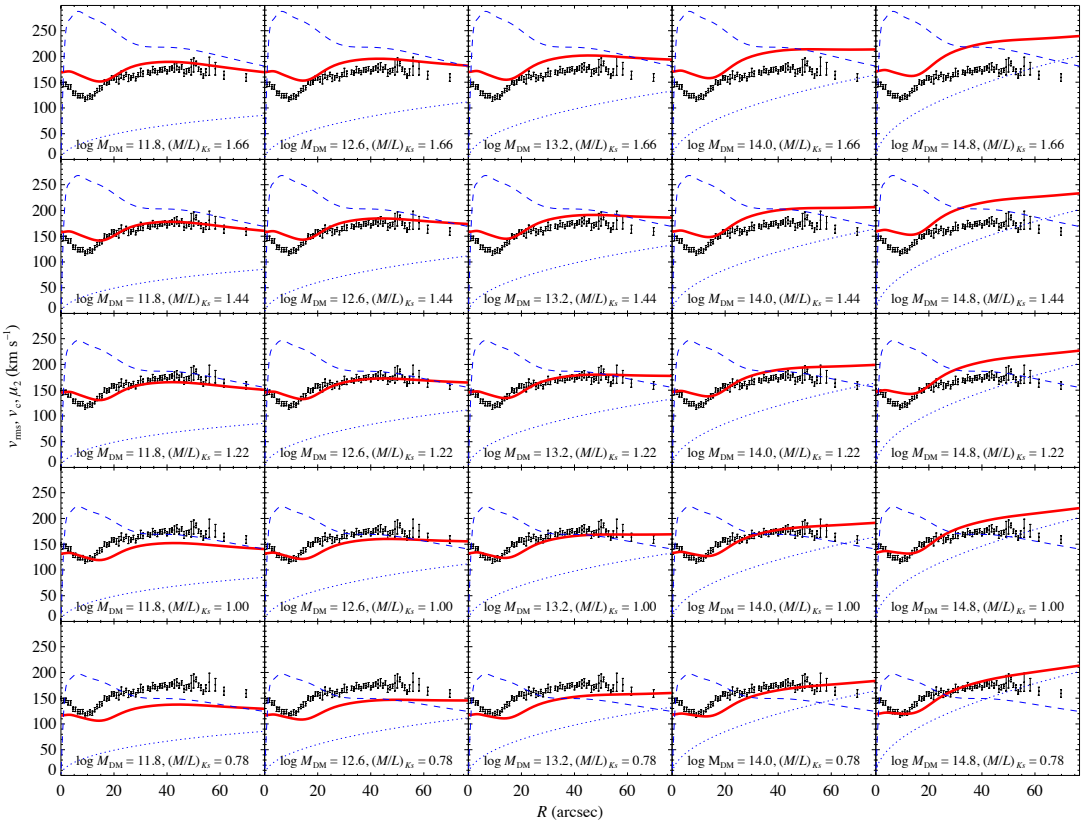

Figure 2.3: Predicted kinematics for several mass models of NGC 1381, demonstrating the effects of varying the model parameters M_{DM} and $(M/L)_{K_S}$ Each plot shows the observed v_{rms} (points with error bars) and predicted μ_2 (solid red line). We also show the circular velocity of the luminous (dashed blue line) and dark (dotted blue line) components. The text at the bottom of each plot gives the parameters of the mass model in solar units at K_S-band. The best fitting mass model for this galaxy has $(M/L)_{K_S} = 1.22$, $M_{DM} = 10^{13.21}$ and $\beta_z = 0.14$. For this figure we assumed isotropy, i.e. $\beta_z = 0.0$.

galaxies. There are two classes of χ^2 plot: those where we can rule out $M_{DM} = 0$ at at least the 3σ confidence level (i.e. where the red contour in Fig. 2.4 fully encircles the minimum in χ^2, e.g. NGC 128 and NGC 1381) and those where we cannot (where the red contour forms an open horizontal 'tongue', e.g. NGC 1886 and IC 4937). All galaxies therefore have a best-fitting combination of mass model parameters and allow us to place upper and lower bounds on $(M/L)_{K_S}$ and at least an upper limit on M_{DM}. Not all galaxies allow us to place a lower limit on M_{DM}.

Figure 2.4: χ^2 contour plots for the complete sample showing fit quality as a function of dark halo mass $M_{\rm DM}$ and stellar mass-to-light ratio $(M/L)_{K_S}$. The third parameter, the anisotropy β_z, has been marginalized out for this figure, as described in Section 2.4.1. The red contours are the $3\,\sigma$ confidence levels. The inner black contours are at $1\,\sigma$ and $2\,\sigma$. The cross in each plot shows the location of minimum χ^2. The upper horizontal axis shows the halo concentrations $c_{\rm vir}(M_{\rm DM})$ corresponding to $M_{\rm DM}$, as defined by equation (2.12). With the exception of ESO 240-G011, we arrange galaxies in the same order in which we present them in Table 2.1. The parameters of the best-fitting model for ESO 240-G011 are outliers, so this galaxy is shown over a different range of $(M/L)_{K_S}$.

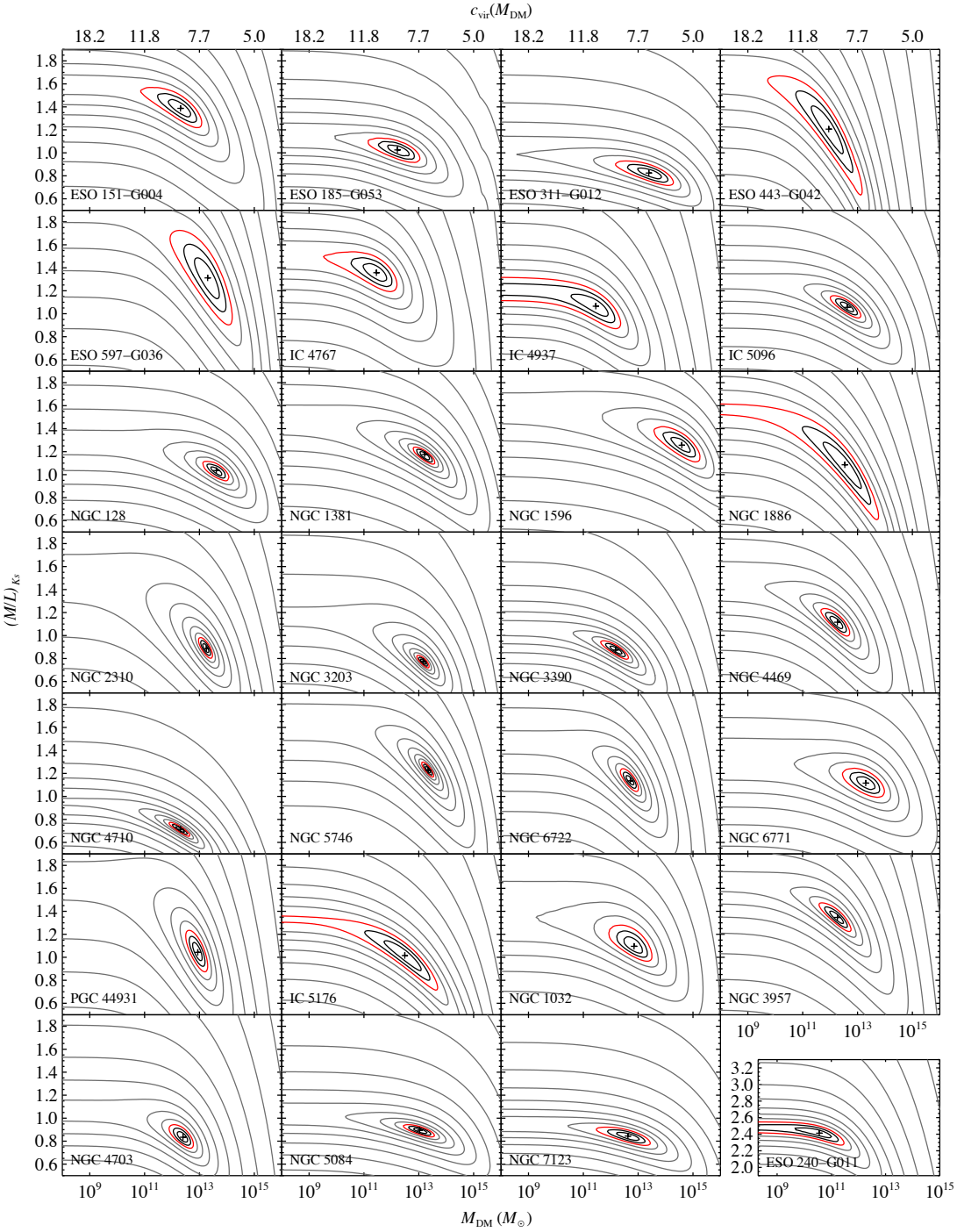
$c_{\rm vir}(M_{\rm DM})$
18.2 11.8 7.7 5.0
$(M/L)_{Ks}$
ESO 151–G004
ESO 185–G053
ESO 311–G012
ESO 443–G042
ESO 597–G036
IC 4767
IC 4937
IC 5096
NGC 128
NGC 1381
NGC 1596
NGC 1886
NGC 2310
NGC 3203
NGC 3390
NGC 4469
NGC 4710
NGC 5746
NGC 6722
NGC 6771
PGC 44931
IC 5176
NGC 1032
NGC 3957
NGC 4703
NGC 5084
NGC 7123
ESO 240–G011
$M_{\rm DM}\,(M_\odot)$

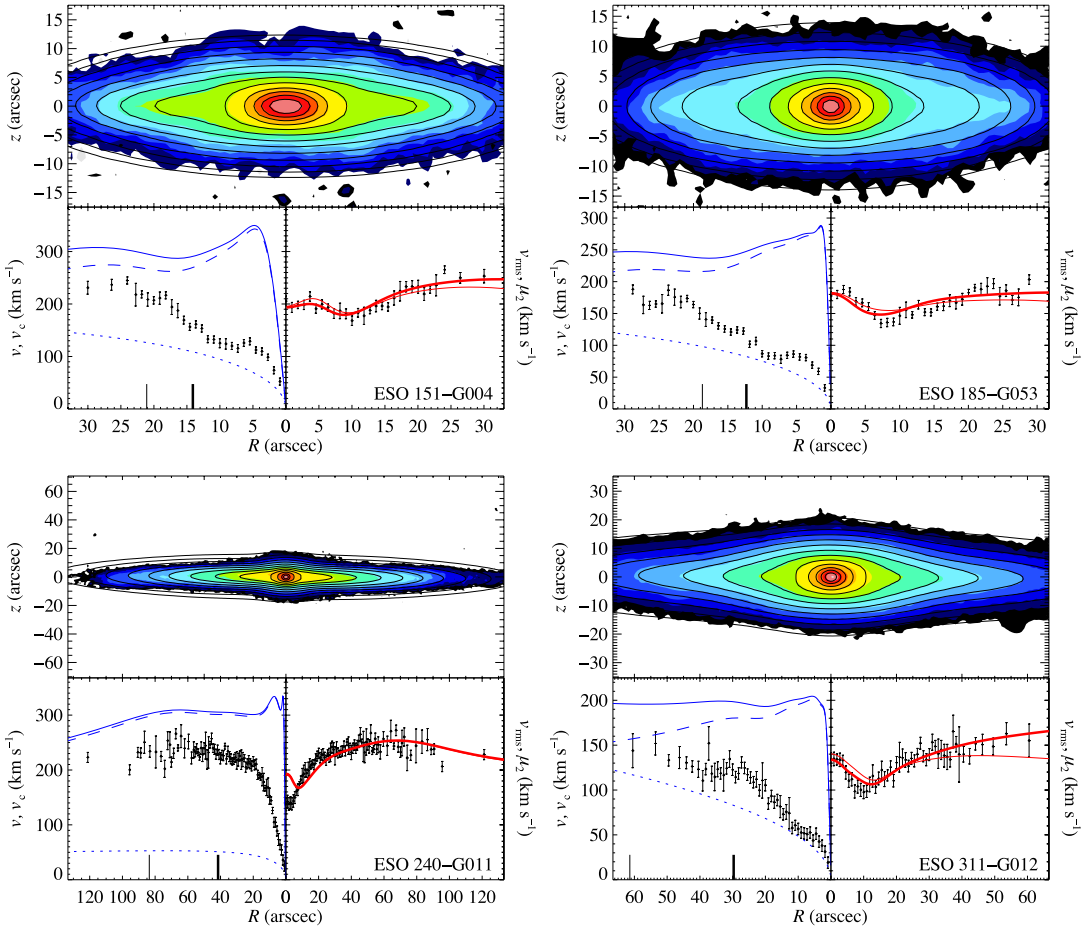

Figure 2.5: Complete results of the mass and dynamical modelling described in Section 2.2 for the sample of galaxies with a B/PS bulge. Briefly, the top plot of each panel shows the isophotes of the image (filled contours) and the MGE parametrization of this luminous component (solid black lines). The bottom left plot shows v, the observed line-of-sight velocity (points), v_c, the total circular velocity (solid blue line), and the circular velocities of the luminous component (dashed blue line) and dark halo (dotted blue line). The thick notch on the R-axis shows $R_{\rm eff}$, the K_S-band effective radius. The thin notch shows $R_{25}/2$, half the B-band optical radius. The bottom right plot shows $v_{\rm rms}$, the observed root mean square line-of-sight velocity (points), μ_2, the best-fitting model second velocity moment (thick solid red line) and the best-fitting second moment with no dark halo (thin solid red line). See Section 2.4.2 for a more detailed explanation of these figures.

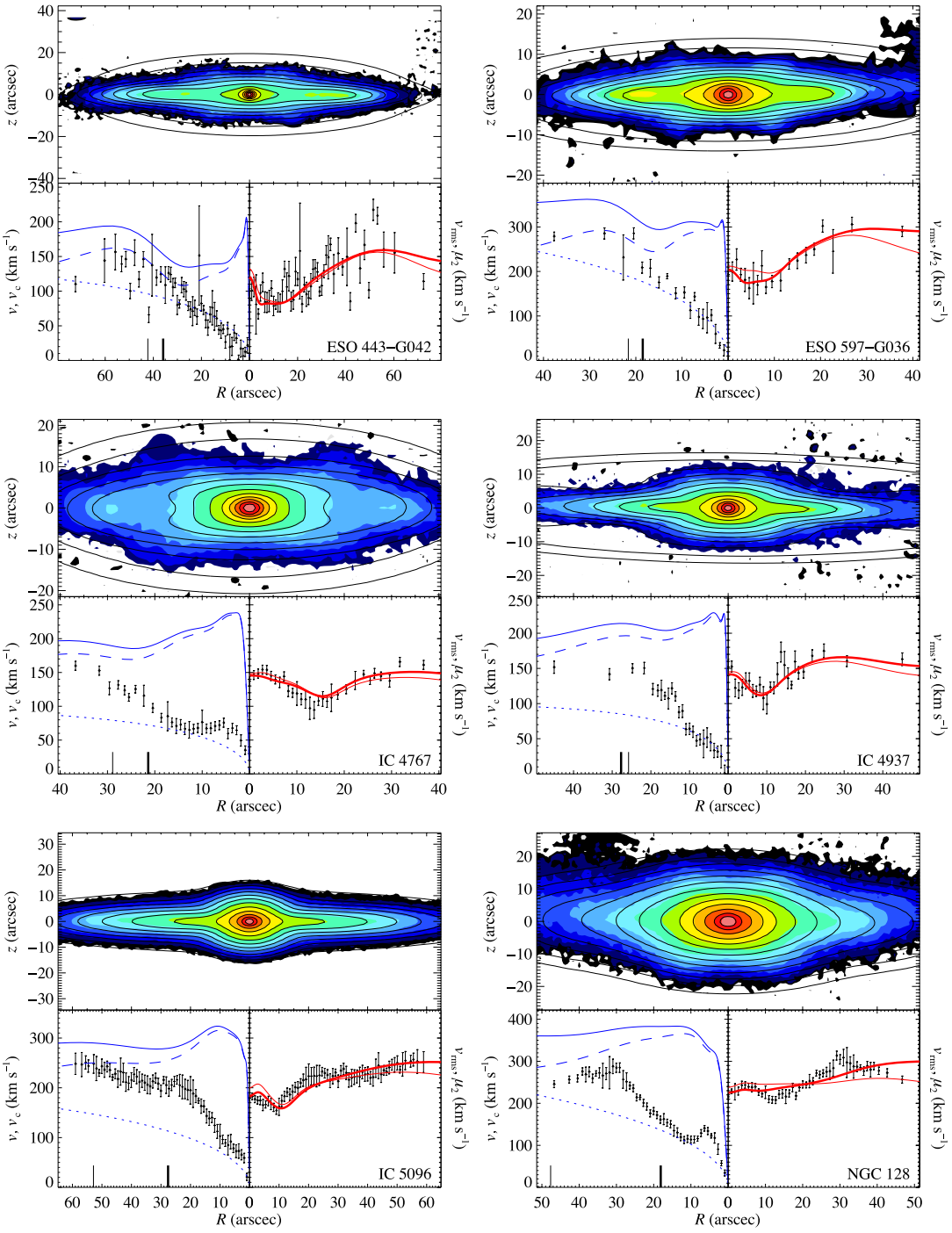

Figure 2.5: — continued

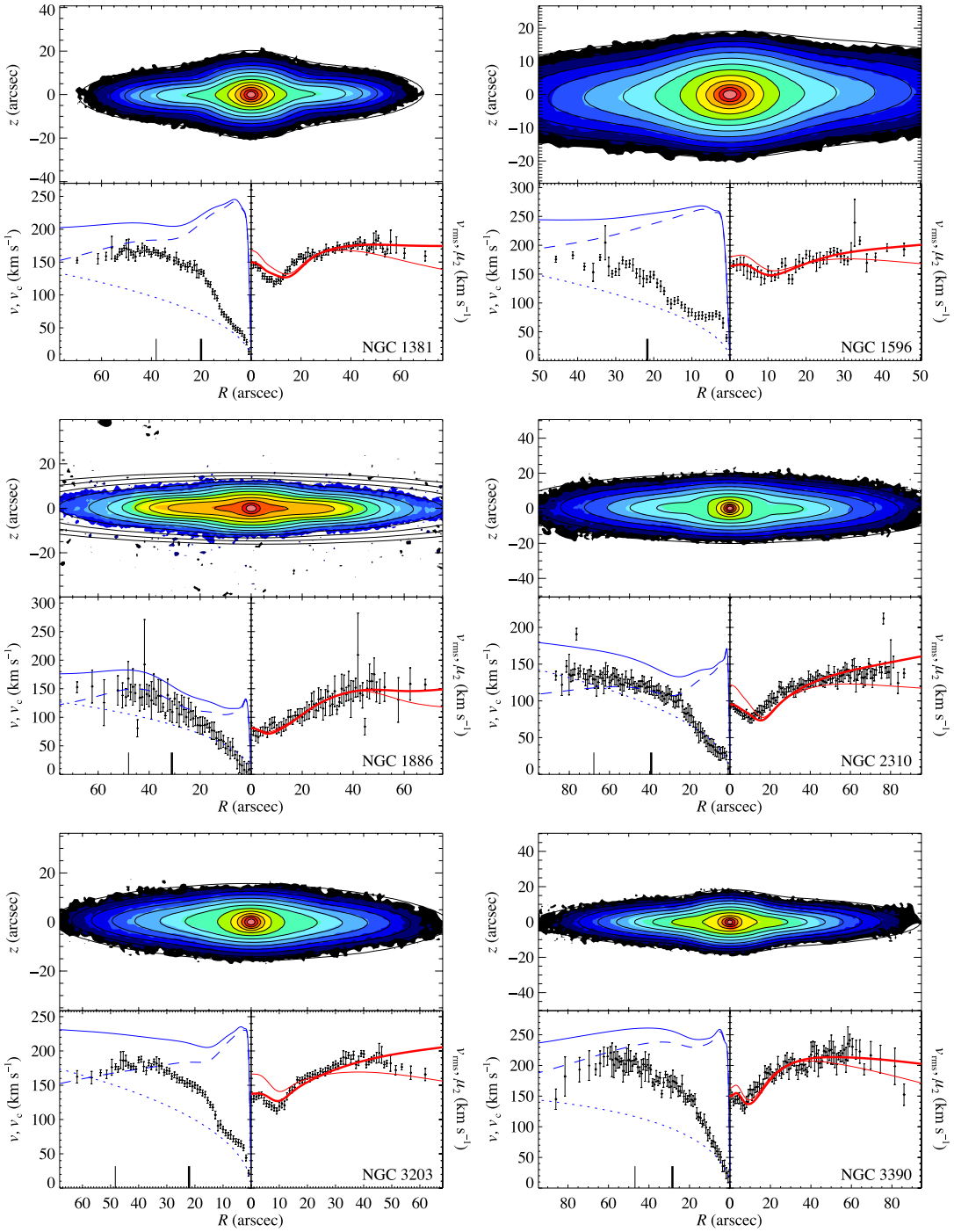

Figure 2.5: — continued

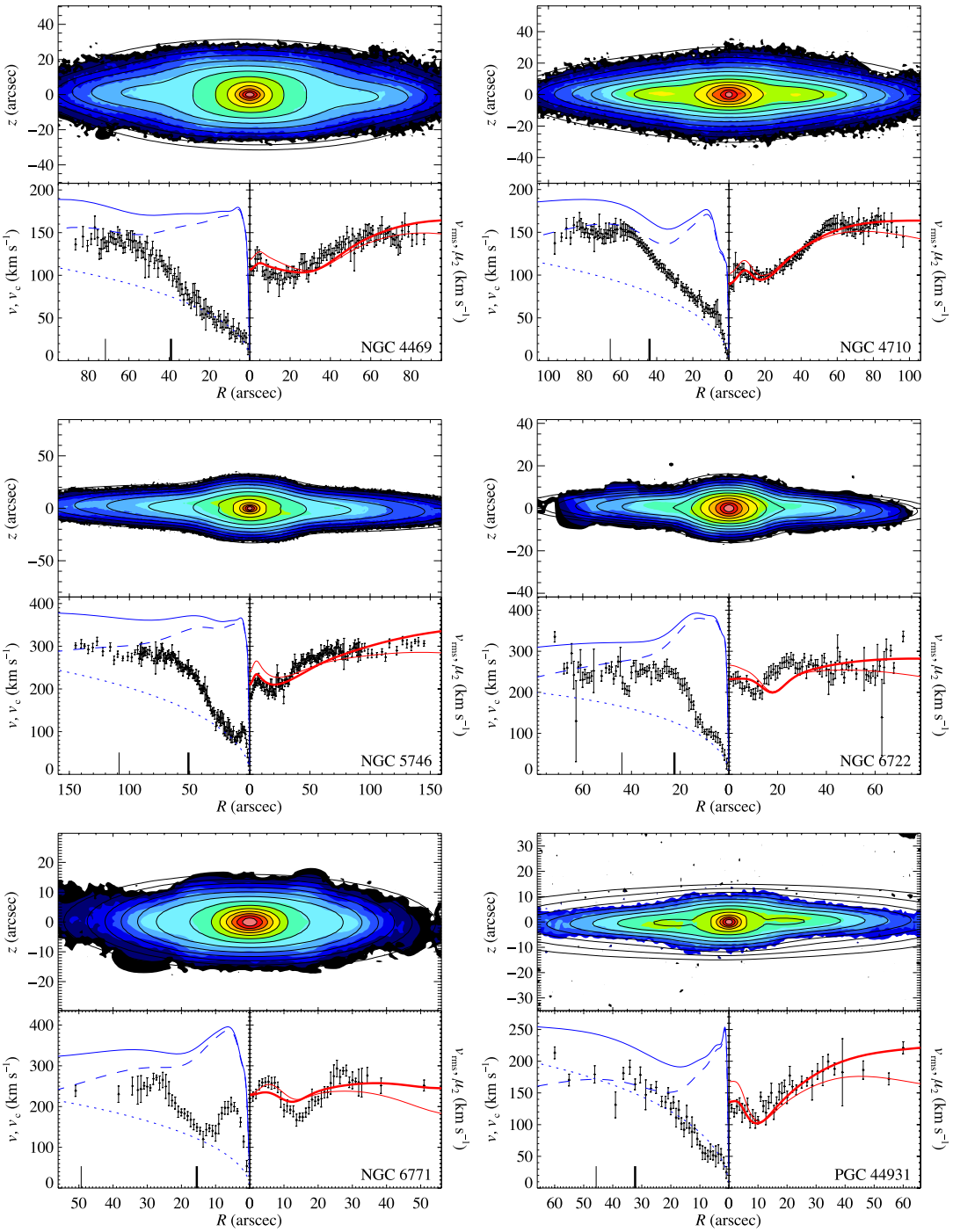

Figure 2.5: — continued

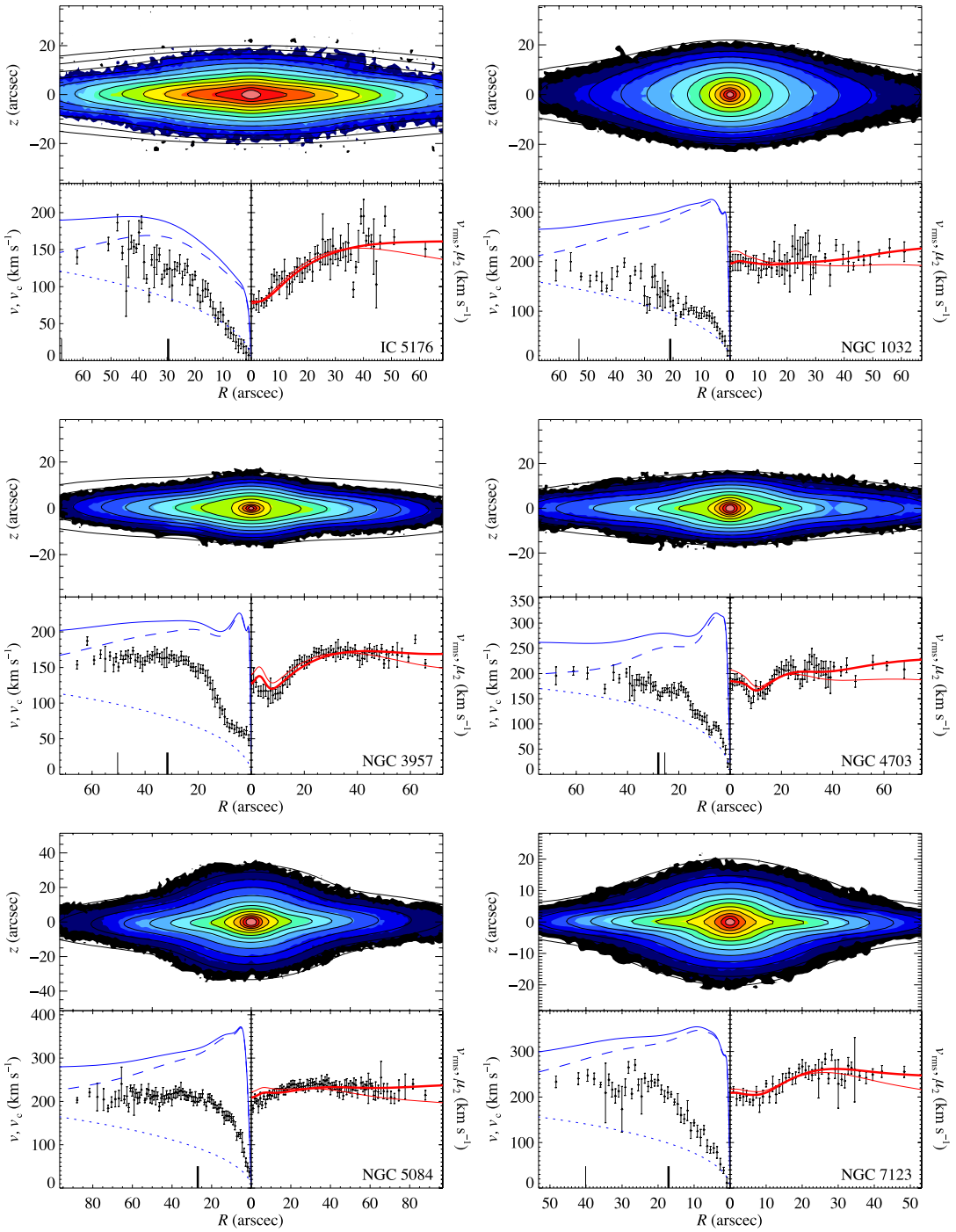

Figure 2.6: As Fig. 2.5 but for the control sample

2.4.2 *Best-fitting models*

The parameters of the best-fitting mass models are shown in Table 2.2. The complete results of the mass modelling and dynamical modelling procedures described in Section 2.2 are shown in Fig. 2.5 (B/PS bulges) and Fig. 2.6 (control sample). In each panel:

1. The top plot shows the image and the luminous component of the mass model. The filled contours are the observed light distribution while the solid lines are the isophotes of the best-fitting MGE model, projected and convolved with the PSF. Contours are separated by 0.5 mag arcsec^{-2}. The lowest contour is 7 mag arcsec^{-2} below the highest. The horizontal axes of these images are registered with those of the kinematic data below, which usually requires that the image be cropped. The full extent of the photometric data is presented in fig. 1 of Bureau et al. (2006).

2. The bottom left plot shows the observed line-of-sight velocity v (points with error bars) and the circular velocities of the total mass model (solid blue line), the luminous component (dashed blue line) and the dark halo (dotted blue line) of the best-fitting mass model (see below). We remind the reader that the ratio of the squares of the dark and luminous circular velocities at a particular radius gives the approximate ratio of dark to luminous matter enclosed within a sphere of that radius (this statement is strictly true for spherical models only).

3. The bottom right plot shows the observed root mean square velocity $v_{\rm rms}$ (points with error bars), the second velocity moment μ_2 of the best-fitting mass model with a dark halo (thick solid red line) and the second velocity moment of the best model without a dark halo (thin solid red line).

We mark the radial axis of the bottom left plot with $R_{25}/2$ and $R_{\rm eff}$, two distance scales used for spiral and elliptical galaxies, respectively. We place a mark at $R_{25}/2$ because R_{25} is always beyond the extent of the stellar kinematic data. Showing both scales aids comparison with previous studies of the influence of dark matter in both

classes of galaxies. This is especially interesting because our sample contains many S0s, which represent a transition between spirals and ellipticals.

We note that the effective radius of very flat objects is particularly sensitive to its definition. We define it here to be the semi-major axis of the ellipse containing half the integrated K_S-band light, which we determine directly from the photometry. We use the integrated light of the MGE model to determine the half-light radius rather than the more usual growth curve method. Using our MGE models, we tested that this definition yields a value similar to that which would obtained from an ideal observation with the galaxy oriented face-on. We found $R_{\rm eff}$(face-on) $= 0.9 R_{\rm eff}$ (edge-on) ± 0.1. For this definition of $R_{\rm eff}$ and for our sample of edge-on spirals and S0s, $R_{25} \approx 3.6\, R_{\rm eff}$ (see Fig. 2.7). This empirical finding will be used in this paper, and is probably true to within approximately 50 per cent for other edge-on objects, but it should obviously not be applied to less inclined spirals.

An alternative classic definition of $R_{\rm eff}$ is to measure the radius of the circle containing half the light, independent of the apparent ellipticity (Burstein et al., 1987; de Vaucouleurs et al., 1991; Jorgensen, Franx & Kjaergaard, 1996). We measured this value for our edge-on galaxies and found that it was typically smaller than the semi-major axis value by a factor 2.0 ± 0.2. It is therefore rather poorly related to the 'true' face-on value and we prefer to integrate within ellipses. It is important, however, to keep our definition of $R_{\rm eff}$ in mind when comparing our results to other studies.

Table 2.2: Mass modelling results

Galaxy	Best-fitting models with halo				Best-fitting models without halo		
	$(M/L)_{K_S}$	$\log(M_{\rm DM}/M_\odot)$	β_z	$\chi_{\rm red}$	$(M/L)_{K_S,\rm nohalo}$	$\beta_{z,\rm nohalo}$	$\chi_{\rm red,\,nohalo}$
			B/PS bulge bulges				
ESO 151-G004	$1.39^{+0.18}_{-0.16}$	$12.31^{+0.77}_{-1.44}$	$0.32^{+0.12}_{-0.20}$	1.16	$1.59^{+0.11}_{-0.11}$	$0.21^{+0.15}_{-0.21}$	1.38
ESO 185-G053	$1.03^{+0.10}_{-0.10}$	$12.22^{+0.81}_{-1.04}$	$0.34^{+0.09}_{-0.14}$	1.73	$1.15^{+0.08}_{-0.08}$	$0.21^{+0.11}_{-0.18}$	1.93
ESO 240-G011	$2.41^{+0.14}_{-0.14}$	$10.56^{+0.90}_{-...}$	$0.00^{+0.06}_{-0.00}$	1.76	$2.49^{+0.08}_{-0.08}$	$0.00^{+0.08}_{-0.00}$	1.76
ESO 311-G012	$0.82^{+0.10}_{-0.10}$	$13.39^{+0.86}_{-1.17}$	$0.32^{+0.11}_{-0.15}$	1.00	$0.99^{+0.07}_{-0.07}$	$0.24^{+0.12}_{-0.20}$	1.40
ESO 443-G042	$1.21^{+0.45}_{-0.57}$	$11.95^{+1.22}_{-2.21}$	$0.47^{+0.28}_{-0.47}$	2.05	$1.68^{+0.19}_{-0.18}$	$0.29^{+0.29}_{-0.29}$	2.10
ESO 597-G036	$1.31^{+0.41}_{-0.41}$	$13.30^{+0.86}_{-1.35}$	$0.37^{+0.26}_{-0.37}$	0.96	$1.87^{+0.23}_{-0.20}$	$0.00^{+0.40}_{-0.00}$	1.44
IC 4767	$1.36^{+0.18}_{-0.16}$	$11.45^{+0.72}_{-1.89}$	$0.24^{+0.14}_{-0.23}$	1.23	$1.51^{+0.13}_{-0.12}$	$0.17^{+0.17}_{-0.17}$	1.39
IC 4937	$1.07^{+0.25}_{-0.19}$	$11.45^{+0.90}_{-...}$	$0.18^{+0.21}_{-0.18}$	1.35	$1.21^{+0.13}_{-0.11}$	$0.08^{+0.28}_{-0.08}$	1.38
IC 5096	$1.06^{+0.10}_{-0.09}$	$12.62^{+0.50}_{-0.59}$	$0.00^{+0.06}_{-0.00}$	1.28	$1.29^{+0.05}_{-0.06}$	$0.00^{+0.05}_{-0.00}$	1.70
NGC 128	$1.04^{+0.07}_{-0.08}$	$13.61^{+0.45}_{-0.45}$	$0.23^{+0.06}_{-0.06}$	1.86	$1.28^{+0.06}_{-0.06}$	$0.17^{+0.08}_{-0.09}$	2.61
NGC 1381	$1.18^{+0.06}_{-0.08}$	$13.21^{+0.36}_{-0.40}$	$0.14^{+0.05}_{-0.11}$	1.89	$1.48^{+0.04}_{-0.04}$	$0.17^{+0.06}_{-0.08}$	2.85
NGC 1596	$1.26^{+0.16}_{-0.14}$	$14.59^{+0.66}_{-0.99}$	$0.14^{+0.11}_{-0.14}$	1.17	$1.58^{+0.11}_{-0.11}$	$0.12^{+0.11}_{-0.12}$	1.80
NGC 1886	$1.09^{+0.53}_{-0.47}$	$12.53^{+1.22}_{-...}$	$0.43^{+0.26}_{-0.43}$	1.04	$1.57^{+0.16}_{-0.15}$	$0.00^{+0.37}_{-0.00}$	1.12
NGC 2310	$0.88^{+0.09}_{-0.08}$	$13.26^{+0.18}_{-0.27}$	$0.00^{+0.18}_{-0.00}$	1.55	$1.49^{+0.07}_{-0.06}$	$0.00^{+0.03}_{-0.00}$	3.09
NGC 3203	$0.77^{+0.05}_{-0.05}$	$13.17^{+0.18}_{-0.23}$	$0.00^{+0.15}_{-0.00}$	1.92	$1.17^{+0.03}_{-0.03}$	$0.00^{+0.05}_{-0.00}$	3.94
NGC 3390	$0.87^{+0.07}_{-0.08}$	$12.18^{+0.45}_{-0.54}$	$0.00^{+0.09}_{-0.00}$	1.33	$1.06^{+0.04}_{-0.04}$	$0.00^{+0.05}_{-0.00}$	1.63
NGC 4469	$1.12^{+0.11}_{-0.11}$	$12.27^{+0.40}_{-0.59}$	$0.05^{+0.17}_{-0.05}$	1.44	$1.46^{+0.05}_{-0.06}$	$0.00^{+0.09}_{-0.00}$	1.81
NGC 4710	$0.71^{+0.06}_{-0.06}$	$12.31^{+0.31}_{-0.40}$	$0.00^{+0.06}_{-0.00}$	1.08	$0.95^{+0.03}_{-0.02}$	$0.00^{+0.02}_{-0.00}$	1.72
NGC 5746	$1.23^{+0.07}_{-0.05}$	$13.35^{+0.18}_{-0.22}$	$0.00^{+0.02}_{-0.00}$	2.13	$1.64^{+0.04}_{-0.03}$	$0.00^{+0.00}_{-0.00}$	3.08
NGC 6722	$1.14^{+0.10}_{-0.09}$	$12.72^{+0.27}_{-0.36}$	$0.14^{+0.09}_{-0.14}$	2.22	$1.47^{+0.06}_{-0.06}$	$0.20^{+0.08}_{-0.11}$	2.68
NGC 6771	$1.12^{+0.12}_{-0.12}$	$13.30^{+0.68}_{-0.81}$	$0.29^{+0.11}_{-0.18}$	2.05	$1.31^{+0.10}_{-0.10}$	$0.12^{+0.17}_{-0.12}$	2.34

continued ...

Table 2.2: Mass modelling results (continued)

Galaxy	Best-fitting models with halo				Best-fitting models without halo		
	$(M/L)_{K_S}$	$\log(M_{\rm DM}/M_\odot)$	β_z	$\chi_{\rm red}$	$(M/L)_{K_S,\rm nohalo}$	$\beta_{z,\rm nohalo}$	$\chi_{\rm red,\,nohalo}$
PGC 44931	$1.04^{+0.19}_{-0.16}$	$12.94^{+0.36}_{-0.41}$	$0.00^{+0.17}_{-0.00}$	1.75	$1.66^{+0.13}_{-0.12}$	$0.00^{+0.06}_{-0.00}$	2.79
Round bulge control sample							
IC 5176	$1.02^{+0.35}_{-0.29}$	$12.49^{+1.17}_{-...}$	$0.34^{+0.23}_{-0.34}$	1.38	$1.33^{+0.11}_{-0.10}$	$0.06^{+0.29}_{-0.06}$	1.44
NGC 1032	$1.10^{+0.18}_{-0.12}$	$12.85^{+0.63}_{-0.90}$	$0.00^{+0.21}_{-0.00}$	0.98	$1.34^{+0.16}_{-0.11}$	$0.08^{+0.18}_{-0.08}$	1.42
NGC 3957	$1.35^{+0.12}_{-0.12}$	$12.27^{+0.49}_{-0.63}$	$0.00^{+0.21}_{-0.00}$	1.22	$1.65^{+0.07}_{-0.06}$	$0.00^{+0.17}_{-0.00}$	1.63
NGC 4703	$0.83^{+0.10}_{-0.09}$	$12.40^{+0.36}_{-0.49}$	$0.09^{+0.23}_{-0.09}$	1.07	$1.06^{+0.08}_{-0.07}$	$0.12^{+0.21}_{-0.12}$	1.65
NGC 5084	$0.89^{+0.04}_{-0.05}$	$13.03^{+0.49}_{-0.59}$	$0.00^{+0.06}_{-0.00}$	1.18	$1.02^{+0.04}_{-0.03}$	$0.00^{+0.08}_{-0.00}$	1.68
NGC 7123	$0.84^{+0.07}_{-0.08}$	$12.62^{+0.81}_{-1.12}$	$0.09^{+0.15}_{-0.09}$	1.18	$0.95^{+0.05}_{-0.05}$	$0.06^{+0.14}_{-0.06}$	1.43

Notes. All values are computed assuming the distances in Table 2.1 and are presented in solar units at K_S-band, $(M/L)_{K_S,\odot}$ Errors are the formal fitting errors at the $3\,\sigma$ confidence level and neglect the uncertainties discussed in Section 2.5.5. If the lower error on halo mass $M_{\rm DM}$ is denoted with ellipsis, e.g. $\log M_{\rm DM} = 12.53^{+1.22}_{-...}$, then for this galaxy there is no lower bound on $M_{\rm DM}$ because $M_{\rm DM} = 0$ cannot be ruled out at the $3\,\sigma$ level. In such cases the quoted value for $M_{\rm DM}$ is highly unconstrained up to some upper limit, and should be used with caution. $\chi_{\rm red}$ and $\chi_{\rm red,\,nohalo}$ are the reduced χ for the models with and without dark haloes, i.e. $(\chi^2/{\rm DOF})^{1/2}$ where χ^2 is defined in equation (2.18) and DOF is the number of degrees of freedom.

2.5 DISCUSSION

The form of the observed $v_{\rm rms}$ as a function of radius is usually a double-humped curve (with the inner hump reaching a smaller speed), but sometimes a monotonically rising curve reaching a plateau toward the edge of the disk (rather like a typical observed rotation curve). For example, the observed second moment rises monotonically in NGC 1886 and IC 5176, is almost constant in NGC 1032 and NGC 5084, falls before rising again in NGC 1381 and NGC 2310, and rises then falls then rises again in NGC 3203 and NGC 6771. The position, height, depth and number of bumps is different for each galaxy. The first thing to note, therefore, is that the models are able to reproduce this whole range of behaviours. This is demonstrated by $\chi_{\rm red}$, the square root of the reduced χ^2 of the best-fitting models (see Table 2.2). The median $\chi_{\rm red}$ is 1.35 with an rms scatter of 0.40.

These low figures of merit are neither trivial given the wide range of kinematics observed, nor necessarily expected given the simplicity of the models. Although the MGE technique allows for accurate parametrization of the K_S-band photometry, the deprojected mass models are axisymmetric descriptions of objects that, in most cases, we have good reason to believe are in fact barred (see Bureau & Freeman, 1999; Chung & Bureau, 2004). Our one-parameter description of the dark halo is model dependent, and our total model contains only three free parameters. Despite this, we are able to accurately reproduce the wide range of observed second velocity moment profiles as far as outermost data point, which is typically at $R_{\rm max} \approx 2$–$3\,R_{\rm eff}$ or, equivalently, $R_{\rm max} \approx 0.5$–$1\,R_{25}$ (see Table 2.1). Because of the lack of freedom that we have to vary the *shape* of the predicted kinematics, it seems that a great deal of information about the kinematical structure of these early-type disk galaxies is contained in their photometry alone. This result is consistent with that of Cappellari (2008):

Given the extent to which our models reproduce the observed kinematics, we are justified to consider that they correspond in some way to the intrinsic properties of the galaxies. We defer our discussion of the possible systematics introduced by our assumptions to Section 2.5.5.3.

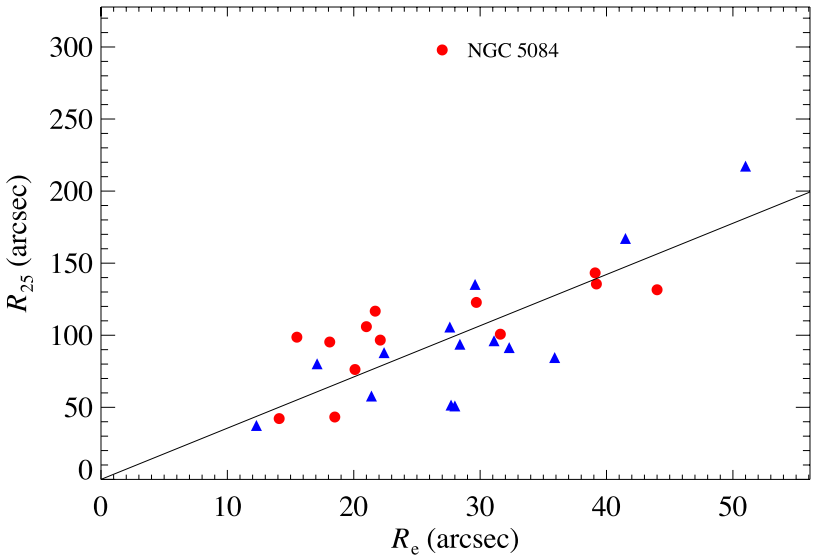

Figure 2.7: The B-band optical radius R_{25} shown as a function of the K_S-band effective radius $R_{\rm eff}$ (as defined in Section 2.4.2) for our sample. The line is a linear fit to the data with the intersect constrained to be 0 and the outlier NGC 5084 excluded. The best fit is $R_{25} = 3.6\,R_{\rm eff}$. Symbols are as in Fig. 2.2.

The following discussion of the model parameters is separated into two parts. In the first, we discuss the properties of the best-fitting mass models that include a dark halo. In the second, we discuss those without. We present the three parameters, $(M/L)_{K_S}$, $M_{\rm DM}$ and β_z, of the models with dark haloes and the two parameters, $(M/L)_{K_S}$ and β_z, of the models without in Table 2.2 and Fig. 2.8. We precede this discussion by noting than none of them appears to correlate with the absolute magnitude M_{K_S}, the stellar mass or the Hubble type.

2.5.1 *Models with dark haloes: mass-to-light ratios*

We find a median K_S-band mass-to-light ratio $(M/L)_{K_S} = 1.09$ with an rms scatter of 0.31. As we noted in the introduction, the mass-to-light ratios are themselves interesting because there are relatively few dynamical measurements of stellar K-band mass-to-light ratios and they are important for normalizing and constraining stellar population models in the near-infrared. We therefore compare our values to other

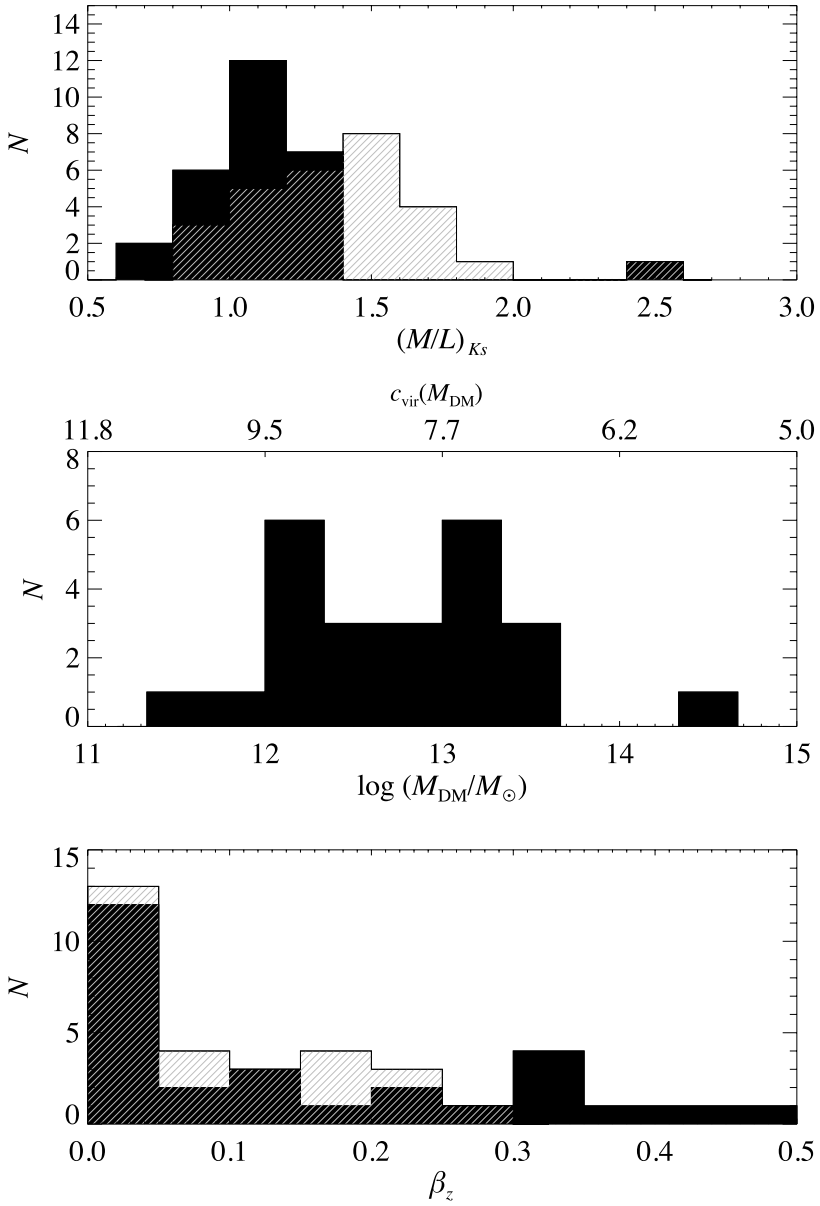

Figure 2.8: Distributions of the parameters of the best-fitting models with a dark halo (solid black) and without a dark halo (hatched white) in Table 2.2. We do not show halo masses where there is no lower mass limit. Corresponding values of concentration $c_{\rm vir}(M_{\rm DM})$ are shown on the upper horizontal axis of the halo mass histogram.

available dynamical and stellar population-based measures. Of course there have been many measurements of (M/L) ratio at wavebands other than K_S that can be transformed to K_S using a global colour. To minimize the uncertainties associated with such transformations, we restrict our discussion to direct determinations at H, K or, almost equivalently, K_S. $K - K_S \lesssim 0.03$ mag (the exact value depends on which K-band filter is used). For a given stellar mass, this is equivalent to a difference between $(M/L)_{K_S}$ and $(M/L)_K$ of less than 3 per cent. We neglect this difference in the discussion that follows.

2.5.1.1 *Comparison to previous dynamical measures of stellar* $(M/L)_K$

Devereux, Becklin & Scoville (1987) made among the earliest determinations of near-infrared mass-to-light ratios using nuclear dispersions and 1.65 μm (i.e. H-band) photometry. For 72 bright spiral, S0 and elliptical galaxies, they found a mean $(M/L)_H = 0.94$ (where we have updated the value they adopted for $M_{\odot,H}$ with a more recent determination). For a constant characteristic $H - K_S$ color of 0.28 mag (Jarrett et al., 2003), this implies $(M/L)_{K_S} \approx 0.7$. Kranz, Slyz & Rix (2003) determined maximal disk $(M/L)_K$ ratios by comparing the results of hydrodynamical simulations to the observed spiral patterns in spiral galaxies. For a sample of five high surface brightness late-type spiral galaxies, they find a mean $(M/L)_K \approx 0.6$. In the case of the small elliptical galaxy Cen A ($\sigma_e \approx 140\,\mathrm{km\,s^{-1}}$), there are two independent dynamical measurements of $(M/L)_K$ (Silge et al., 2005; Cappellari et al., 2009), both of which are ≈ 0.7. We therefore find that our direct dynamical measures of $(M/L)_{K_S}$, which we believe accurately account for dark matter, are somewhat larger than most previous dynamical estimates at around the 1–2 σ significance level. Our method depends on an assumed single-parameter NFW dark halo, rather than the two-parameter isothermal halo used by Kranz, Slyz & Rix (2003). It is however somewhat more direct and avoids the maximal disk assumption.

2.5.1.2 *Comparison to previous stellar population measures of* $(M/L)_K$

If our modelling assumptions are justified, then because mass is correctly shared between the luminous and dark components, the $(M/L)_{K_S}$ ratios that we measure should agree with those predicted by well-calibrated stellar population models. A forthcoming paper will present an extensive stellar population analysis of the galaxies in our sample using absorption line strengths and a more complete comparison to the predictions of models. For now though, we perform a preliminary check by comparing our results to the predictions of two models. In Fig. 2.9 we show the dynamically determined stellar mass-to-light ratios of our sample galaxies as a function their $B - K_S$ colour. We also show the predictions of two independent stellar population models.

We use the B-band magnitudes given in HYPERLEDA, which are corrected for both Galactic and internal extinction. We adopt the uncertainties in the uncorrected B-band magnitude, which neglect random and systematic errors in the extinction corrections and are therefore lower limits. The Galactic correction is derived from the dust maps of Schlegel, Finkbeiner & Davis (1998). The median Galactic correction at B is 0.2 mag and the uncertainties are probably rather smaller than this. ESO 311-G012 is close to the equatorial plane of the Galaxy (Galactic latitude $b = -8.0°$) so the Galactic correction for that galaxy is very large (1.7 mag) and is derived from a region of the Schlegel, Finkbeiner & Davis (1998) maps where extinction corrections are unreliable ($b \lesssim 5°$). The B-band internal extinction correction is based on the statistical method of Bottinelli et al. (1995), which parametrizes the correction as a function of axial ratio (and therefore inclination) and bulge-to-disk ratio (and therefore morphological type). In exactly edge-on spiral galaxies, the corrections used are both large (0.8–1.5 mag) and somewhat dubious. The K_S-band magnitudes include a small correction for Galactic extinction (the median correction is 0.02 mag) and neglect internal extinction. The effect on the parameters of the model of neglecting internal extinction in the K_S-band is discussed in Section 2.5.5.2, but as far as the $B - K_S$ colour is concerned this should introduce a systematic but small error (perhaps 0.1 mag in the spirals and

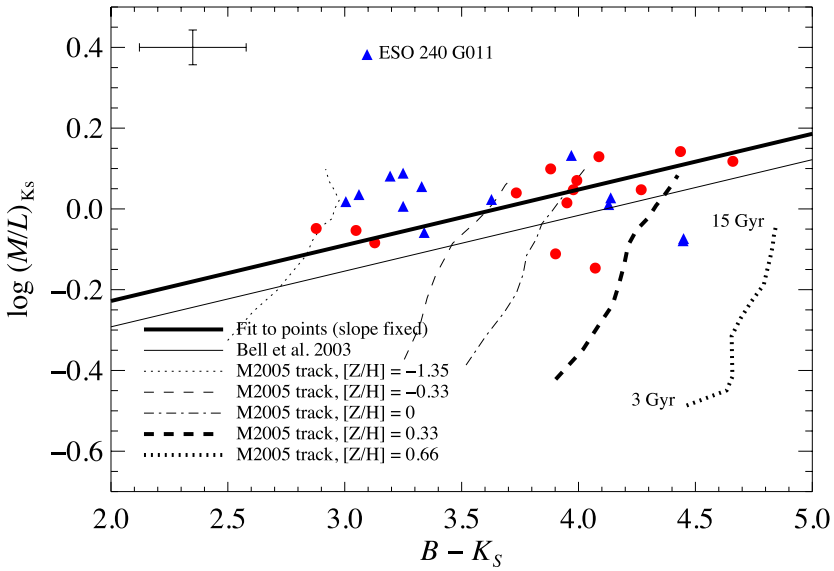

Figure 2.9: Stellar $(M/L)_{K_S}$ as a function of $B-K_S$ colour. The data points use the K_S-band mass-to-light ratios of the stellar components of the best-fitting mass-models including a dark halo, i.e. column (2) of Table 2.2 and B-band magnitudes, corrected for Galactic and internal extinction, are taken from HYPERLEDA. K_S-band magnitudes are derived from our MGE models which incorporate a correction for Galactic extinction. Internal extinction at K-band is neglected. A median error bar that does not include the uncertainties introduced by the extinction corrections is shown in the upper left corner (see text). Symbols are as in Fig. 2.2. The thin straight line is the prediction of the spectrophotometric galaxy evolution models of Bell et al. (2003). The thick straight line is a fit to our data constrained to the slope of the dashed line. The evolutionary tracks for a range of metallicities are from the models of Maraston (2005) and run from 3 Gyr (low mass-to-light ratio) to 15 Gyr (high mass-to-light ratio). Metallicity increases from left to right for these tracks.

less in the S0s). We therefore conclude that the uncertainties in the $B-K$ colours are dominated by large uncertainties in the corrections to the B-band magnitude, especially the internal correction.

The first prediction we compare our results to is the colour–(M/L) relation of Bell et al. (2003). This relation is derived from spectrophotometric galaxy evolution models that use the PEGASE stellar population model (see Fioc & Rocca-Volmerange 1997 and Bell et al. 2003) with a Salpeter initial mass function (IMF) modified by globally scaling down the stellar mass by a factor of 0.7. Bell et al. (2003) do not present relations involving near-infrared colours, so we adopt a characteristic $R-K_S$

colour of 2.2 mag to derive the line shown in Fig. 2.9 from their $(B-R)$–$(M/L)_{K_S}$ relation, yielding $\log(M/L)_{K_S} = 0.138 - 0.568(B-K_S)$. Bell & de Jong (2001) do use near-infrared colours, but their relations are based on a small selection of ages and metallicities rather than the distribution observed in the local universe. This leads them to derive a rather flatter relation than the ones shown in Bell et al. (2003).

We show in Fig. 2.9 a further comparison to an independent set of stellar population models from Maraston (2005) that predict K-band mass-to-light ratios for stellar populations with ages less than 15 Gyr and metallicities $-1.33 < [Z/H] < 0.67$. The models include a semi-empirical treatment of the thermally pulsing asymptotic giant branch, to which the near-infrared luminosity is particularly sensitive. We show models assuming a Kroupa IMF. These tracks can be transformed to predictions for the scaled down Salpeter IMF of Bell et al. (2003) and the normal Salpeter by adding 0.09 dex and 0.24 dex respectively to the logarithm of the (M/L) ratio. In this case we show evolutionary tracks for a range of metallicities rather than a statistical characterisations of local galaxies.

As the figure demonstrates, the predictions of the Bell et al. (2003) galaxy evolution models are below our dynamical determinations in all but four cases. A power law fit to our models, constrained to the same slope as the Bell et al. (2003) line and from which the outlier ESO 240-G011 is excluded, implies a systematic offset of $\Delta \log(M/L)_{K_S} = 0.06$ dex. At least part of this small offset could be due to the introduction of a systematic error in the approximate transformation of the Bell et al. (2003) to $B-K_S$. Our measurements are systematically toward the upper end, if not outside, the range of values predicted by the Maraston (2005) models. If the stellar population models are correct, this implies systematically old stellar populations, $\gtrsim 10$ Gyr. These differences are intriguing and could suggest problems in the stellar evolution models or the IMFs adopted, but we note four reasons which lead us to argue that our findings are broadly consistent with their predictions. Firstly, there is a random scatter of 0.1–0.2 dex in the Bell et al. (2003) relation (larger at the blue end). Secondly, there may be systematic errors in the $(B-K_S)$ colours adopted for our sample of edge-on galaxies due to internal extinction. These are difficult to quantify. Thirdly, in the case of the Maraston (2005) tracks, the mass-to-light ratios are for single

stellar population models, while many galaxies, especially spirals, are likely to have composite stellar populations. Finally, our sample of 28 bright early-type disk galaxies is not necessarily representative of local galaxies. We will perform a more detailed comparison on the models and data in a future work (see Section 6.2.1).

We end this discussion of the $(M/L)_{K_S}$ ratios measured by noting the existence of a significant outlier galaxy, ESO 240-G011, which has $(M/L)_{K_S} = 2.41 \pm 0.14$. This is more than four standard deviations above the median $(M/L)_{K_S}$ of the sample. ESO 240-G011 has the latest Hubble type in the sample, and later galaxies are generally thought to be more dark matter-dominated. However, our modelling method aims to correctly account for dark matter so $(M/L)_{K_S}$ should be the mass-to-light ratio of the stellar component, not the total matter distribution. This particular galaxy therefore remains puzzling.

2.5.2 *Models with dark haloes: dark halo masses*

For those galaxies with constrained halo masses, we find a median $M_{\rm DM} = 10^{12.85}\,M_\odot$ with an rms scatter of 0.7 dex. Using the concentration–halo mass correlation of Macciò, Dutton & van den Bosch (2008), which our haloes are constrained to lie on, this corresponds to $c_{\rm vir} = 7.9$ with an rms scatter of 1.2. These results should be treated with caution, however, because most of the dark mass lies beyond radii at which our models are constrained by either photometry or kinematics. $M_{\rm DM}$ is therefore strongly dependent on the assumptions described in Section 2.2.2.

With this strong caveat in mind, we note, however, that the virial masses $M_{\rm vir} = 1.2\,M_{\rm DM}$ of the models are at least consistent with the predictions of semi-analytic and halo occupation distribution models with respect to their stellar mass. We present a comparison in Fig. 2.10. Croton et al. (2006) and Somerville et al. (2008) use semi-analytic models of galaxy formation that, among other things, attempt to predict the relationship between the stellar mass and dark halo mass of a galaxy by modelling relevant physical processes such as the growth of structure, cooling, star formation and feedback. Wang et al. (2006) and Moster et al. (2010) use a halo occupation distribution

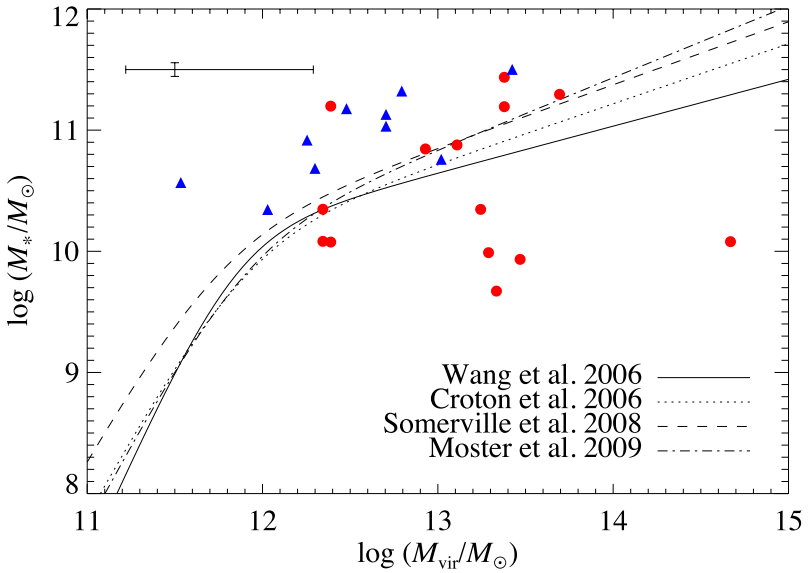

Figure 2.10: Comparison of the stellar and halo masses of our mass models (data points) to the independent predictions of Wang et al. (2006), Croton et al. (2006), Somerville et al. (2008) and Moster et al. (2010). Median error bars are shown in black in the upper left corner. Symbols are as in Fig. 2.2.

approach to populate a halo catalogue with stellar mass. The halo catalogue is taken from Springel et al. (2005). It is populated to reproduce the local observed stellar mass function and clustering function.

Our models do not agree with the predictions in a few cases, but there is no evidence of any systematic offset. The stellar and virial masses of our mass models do not seem to be correlated. This is not true of the predictions, especially below $M_{\rm vir} = 10^{12}\,M_\odot$, which we unfortunately do not probe. The comparison is therefore limited by both a lack of mass range in our sample, and the significant uncertainties in our halo mass determinations. We can only conclude that our galaxies have stellar mass to halo mass ratios consistent with the range predicted by the theoretical models for these halo masses. However, the assumptions and observational constraints used to make their predictions are quite independent from ours, so even this relatively weak statement is not trivial. Ignoring the predictions, we note that the spiral galaxies in our sample all have large $M_*/M_{\rm vir}$ ratios relative to the average S0.

The dark matter enclosed within a sphere of radius r is given by

$$M_{\rm DM}(r) = M_{\rm DM}\frac{A(r/r_{\rm s})}{A(c_{\rm vir})}. \tag{2.19}$$

From this and the ratios of the circular velocities of the dark and stellar components, we can calculate the dark-to-total mass fraction $X_{\rm DM}$ as a function of radius. We find a mean $X_{\rm DM}(R_{\rm eff})$ of 15 per cent (10 per cent rms scatter) and a mean $X_{\rm DM}(R_{25})$ of 49 per cent (15 per cent scatter). As we mentioned in the introduction, a maximal disk is strictly defined as one in which the stellar component contributes 75–95 per cent of the rotational velocity at $2.2\,R_{\rm disk}$, i.e. $X_{\rm DM}(2.2\,R_{\rm disk}) \leq 45$ per cent (Sackett, 1997) ($2.2\,R_{\rm disk}$ is the radius at which the rotation curve of a thin disk reaches its maximum). The disk scale length of edge-on, barred systems are uncertain (Bureau et al., 2006), but our estimates of $R_{\rm disk}$ suggest that $X_{\rm DM}(2.2\,R_{\rm disk})$ is 27 per cent (11 per cent scatter). The best fitting mass model is sub-maximal in only two cases [NGC 2310, $X_{\rm DM}(2.2\,R_{\rm disk}) = 46$ per cent and PGC 44931, $X_{\rm DM}(2.2\,R_{\rm disk}) = 50$ per cent].

We can also determine the radius at which dark and stellar matter contribute equally to the circular velocity and mass enclosed within a sphere. We do this in units of $R_{\rm eff}$ and R_{25} and find $R(X_{\rm DM} = 0.5)/R_{\rm eff} = 4.1$ (with rms scatter of 1.3) and $R(X_{\rm DM} = 0.5)/R_{25} = 1.0$ (with rms scatter of 0.5). These results should be treated with a little caution, however, because in several cases $R(X_{\rm DM} = 0.5) > R_{\rm max}$, the last kinematic data point. Beyond the kinematics, the models are obviously particularly model dependent.

As discussed in Section 2.5.5.1, $X_{\rm DM}$ and $R(X_{\rm DM} = 0.5)$ are almost unaffected by distance or photometric calibration errors. Finally, we note that there is no evidence of any significant difference between the dark matter content of the spirals and S0s in our sample, at least at the radii within which the models are constrained by the kinematic data.

2.5.3 *Models with dark haloes: anisotropies*

The best-fitting anisotropies for our models are in the range $0.0 \lesssim \beta_z \lesssim 0.5$. As we discussed in Section 2.2.3, however, the constraints on these measurements are weak because the galaxies in our sample are rotation-dominated and we do not have integral field data. Moreover, we assume a constant anisotropy throughout the galaxy,

which is of course a significant simplification, since many of our galaxies have a bulge, bar and disk. With these caveats in mind, the typical anisotropy we find is broadly consistent with the average of previous observations of ellipticals, that are expected to have similar dynamics to the bulges ($\beta_z \lesssim 0.4$, Cappellari et al. 2007; Thomas et al. 2009) and disks ($0.35 \lesssim \beta_z \lesssim 0.75$, Shapiro, Gerssen & van der Marel 2003).

2.5.4 *Neglecting dark matter*

As discussed in the introduction, previous studies have shown that it is usually possible to construct mass models of bright spiral galaxies that reproduce the general form of their rotation curves within R_{25} with no or only a sub-dominant contribution from dark matter. It is therefore not surprising that, in some cases, the improvement in fit quality when a dark halo added is not overwhelming.

How many galaxies can we fit without a dark halo? Many of the second velocity moments of the best mass models without a dark halo are, by eye at least, satisfactory fits to the observed kinematics (compare the thin red lines to the data points in the lower right plot of each panel in Figures 2.5 and 2.6). In the formal sense, in four cases (NGC 1886, IC 4937, ESO 240-G011, and IC 5176) the removal of the dark halo does not improve the fit at the $3\,\sigma$ level.

We therefore now discuss an Occam's Razor argument which states that, since we *can* fit some of these galaxies well without dark matter, dark matter is not a significant component by mass within the radii probed by our kinematic data (0.5–1 R_{25} or 2–3 $R_{\rm eff}$) in at least those cases. We reject this argument because the parameters of our best fitting mass models with dark matter are in line with independent expectations, whereas those for the haloless models are not. For example, the mass-to-light ratios we measure for mass models without haloes are inconsistent with stellar population results. We find the median $(M/L)_{K_S,\rm nohalo} = 1.25(M/L)_{K_S}$, where $(M/L)_{K_S,\rm nohalo}$ is the stellar mass to light ratio measured using a mass model without a dark halo. The $(M/L)_{K_S,\rm nohalo}$ we measure is therefore significantly higher than the predictions the stellar population models of Bell et al. (2003) and Maraston (2005). Either the

stellar population models and their assumptions are flawed, or the stellar mass models without dark matter have too much mass. The halo sizes (and concentrations) of the models with dark matter also match the expectations of galaxy formation. Of course, adding another free parameter to a model is always going to improve the quality of the fit, but if the true halo of a galaxy is not significant (or not present), the agreement between the halo masses that most improves the fits and the predictions and the expectations of ΛCDM would be a striking coincidence.

Indeed, the fact that the (M/L) ratio of a mass model including only stars systematically exceeds that of a mass model accounting for dark matter or a stellar population estimate can be used to estimate how 'wrong' the former is. The median $(M/L)_{K_S,\mathrm{nohalo}}$ must be *decreased* by 20 percent [$\Delta \log(M/L) \approx -0.10$] to match $(M/L)_{K_S}$, the dynamically determined stellar mass-to-light ratio with dark matter. This is similar to the finding of Cappellari et al. (2006), that the median I-band dynamical (M/L) ratio neglecting dark matter must be decreased by 30 per cent [$\Delta \log(M/L)_I \approx -0.15$] to match the stellar population (M/L) ratio.

2.5.5 *Uncertainties and assumptions*

2.5.5.1 *Random errors*

The errors presented in Table 2.2 are $3\,\sigma$ formal fitting errors. These neglect random errors due to distance uncertainties and photometric calibration. As shown in Table 2.1, we adopted surface brightness fluctuation distance estimates in two cases (NGC 1381 and NGC 1596) and the Virgo cluster distance in two others (NGC 4469 and NGC 4710). The uncertainties on these estimates is likely to be $\approx 1\,\mathrm{Mpc}$, limited either by the surface brightness fluctuation method or the physical size of the Virgo cluster. All other distance estimates are redshift-based estimates from NED assuming a Virgocentric flow model (Mould et al., 2000). The uncertainties on these distances are much larger, probably ≈ 20 per cent. Because of the calibration process described in Appendix 2.A, the error on the calibration of the K_S-band images we use is of order that of the

2MASS survey (Skrutskie et al., 2006), which is negligible compared to the distance uncertainties.

Random photometric and distance errors propagate linearly into the uncertainty in total dynamical mass of the model. In the presence of a dark halo these errors propagate into the stellar and dark parameters of the mass model in a complex and non-linear way. However, we find empirically that a given fractional error in photometric calibration or distance propagates into the same random error in $(M/L)_{K_S}$ and $M_{\rm DM}$ to within a factor of 2 or so. In fact, the formal fitting errors overwhelm these observational uncertainties. This can be seen from Fig. 2.4, where the $3\,\sigma$ confidence region allows us to constrain $M_{\rm DM}$ within $\approx$ 1–2 dex only, a much bigger uncertainty than the distance and photometry errors.

Despite the non-linear way in which photometric distance errors propagate into the stellar and dark masses of the mass models, we note that these errors almost cancel out in $X_{\rm DM}(R)$, the dark-to-total mass fraction at radius R. For example, plausible distance errors of 20 per cent result in changes in $X_{\rm DM}(R_{\rm eff})$, $X_{\rm DM}(2.2\,R_{\rm disk})$ and $X_{\rm DM}(R_{25})$ of less than 2 per cent.

2.5.5.2 *Systematic errors due to dust*

We now discuss two sources of systematic error, both of which are due to dust. Firstly, if the internal extinction at K_S-band in these galaxies is significant, then the current modelled mass-to-light are overestimates. If that absorption varies significantly across the projected galaxies, then this would also affect the halo masses determined. We believe that this effect leads to $\lesssim$ 10 per cent reduction in the total light detected at K_S-band, and probably much less. Absorption at K_S-band it typically smaller than at optical wavelengths by an order of magnitude. This is reflected in detailed examination of the R-band (Bureau & Freeman, 1999) and K_S-band (Bureau et al., 2006) images of the sample. Dust lanes that are prominent in the optical cannot usually be detected at K_S-band and half of the sample are S0s, which do not have optical dust lanes at all, so are likely to be totally unaffected by dust at near-infrared wavelengths.

The second potential systematic effect is due to the positioning of the slit used to measure the stellar kinematics. As described in Bureau & Freeman (1999) and Chung & Bureau (2004), in the dustiest, exactly edge-on systems the long-slit had to be moved a little away from the major axis. If the kinematics at this distance from the plane are significantly different from that along the major axis, then it would likely affect both the (M/L) ratio and halo mass determinations. The most likely result would be a systematic reduction of both parameters, since both rotational velocity and dispersion typically fall with height above the disk. In actual fact, however, the effect may be smaller than this in the B/PS sample. B/PS bulges are believed to rotate cylindrically, i.e. their kinematics do not vary with height (see Chapter 4 for a more detailed discussion). If this is true then this effect should be small within the B/PS bulges. More importantly, the sample was constructed to avoid placing the slit above the plane. The dustiest galaxies in the sample (e.g. NGC 5746) are in fact inclined at slightly less than 90°. It was therefore almost always possible for the centre of the galaxy to lie within the slit, without dust affecting observations much.

2.5.5.3 Systematic errors due to model assumptions

Finally we discuss the systematic errors introduced by our modelling technique, which assumes that the stellar mass-to-light ratio and anisotropy are constant across each galaxy, that the halo is of the form described in Section 2.2.2, and, most importantly that the galaxy is axisymmetric.

In the case of both $(M/L)_{K_S}$ and β_z, the best-fitting parameters may be thought of as global averages for each galaxy. We are, however, justified in assuming a constant value in both cases. The stellar population mass-to-light ratio at K_S-band varies relatively little between galaxies (Bell et al., 2003), and rather less within them. As discussed in Section 2.2.3 and Section 2.5.3, our results are largely insensitive to the anisotropy chosen because our galaxies are rotation-dominated. Choosing a more sophisticated, varying anisotropy would not change our conclusions.

It is one of the goals of this study to offer constraints on halo masses and dark

matter fractions by *assuming* a particular, theoretically motivated, single-parameter halo model. We are effectively asking how large haloes are, not what shape they have. If real haloes do not follow the NFW profile then our estimates of its virial mass are unlikely to be correct. We are encouraged, however, by the good correspondence between the stellar masses of the mass models including a halo and the predictions of stellar population models. This is strong circumstantial evidence that our method correctly apportions mass to the stellar and dark components, despite (or perhaps because of) the strong assumptions we make about the halo.

Conclusions drawn from these axisymmetric models may be flawed if the assumption of axisymmetry is significantly violated. In line with local disk galaxy demographics, a majority of the galaxies in our sample are thought to host bars (see Section 2.3). The possible consequences of the application of axisymmetric modelling to the present sample (or indeed any representative local sample) are therefore a concern. Indeed, there are hints of our modelling breaking down, presumably due to a bar, in the inner ≈ 10 arcsec of some galaxies, where the model second velocity moment overpredicts the observations (e.g. NGC 1381, ESO 240-G011 and NGC 3957). None of the models underpredicts the data in this region. This can easily be explained by the sample selection. The B/PS bulges dominating our sample are thought to be bars viewed side-on. As such, the orbits supporting the bars are elongated perpendicular to the line-of-sight, resulting in observed velocities smaller than the circular velocities of the equivalent axisymmetric mass distribution. End-on bars, which lead to the opposite effect, are systematically excluded from our sample as they appear round. This slight but systematic failure of our models in the central regions is therefore consistent with previous studies of this sample (Bureau & Freeman, 1999; Chung & Bureau, 2004; Bureau et al., 2006) and others (e.g. Kuijken & Merrifield, 1995; Merrifield & Kuijken, 1999) supporting a close relationship between B/PS bulges and bars.

This, however, does not mean that our axisymmetric mass models are not appropriate. Firstly, although a bar distorts the surface brightness of a galaxy, the potential and the shapes of the orbits themselves are significantly less distorted (see, e.g., figure 2 (a) of Bureau & Athanassoula, 1999, which demonstrates for a particular mass model

that the radial peak in the axial ratio of the x_1 orbits supporting the bar is quite narrow). It is these orbital shapes that the observed stellar kinematics depend upon. This probably explains why the region in which the over-prediction occurs is much smaller than the B/PS bulge. The effect of the bar, at least as far as our method is concerned, is restricted to only the inner few arcseconds.

Secondly, there is no systematic difference between the fit quality of haloless models in the inner regions of the galaxies with B/PS bulges and the control sample of six galaxies with spheroidal bulges. Unfortunately, we are limited by the rather size of the control sample. Demonstrating a statistically significant correlation between μ_2 being too large in the central few arcseconds and more reliable bar diagnostics (e.g. Bureau & Freeman, 1999; Chung & Bureau, 2004) is therefore unlikely.

Nevertheless, it seems that the pressing question is not so much why the stellar kinematics of so many galaxies deviate slightly but systematically in the central regions, but rather why Jeans modelling of axisymmetric mass distributions reproduces the kinematics of barred galaxies so well. The high quality of the kinematic fits perhaps suggests that the μ_2 profiles primarily trace the *enclosed masses* as a function of galactocentric radius and are fairly (but not entirely) insensitive to the details of the dynamics. Because of this, axisymmetric mass models that reproduce the 'bulge-plateau-disk' surface brightness profile often observed in this sample (see Fig. 2.1 and Bureau et al., 2006) can also reproduce the second velocity moment of intrinsically non-axisymmetric galaxies with the same radial profile. Irrespective of the importance of pressure support in our sample galaxies, μ_2 therefore appears to be analogous to the circular velocity in purely rotationally-supported systems.

We further note that there is no physically motivated evolutionary scenario which would systematically lead to axisymmetric galaxies with such a radial mass distribution, but such surface brightness plateaus develop naturally in barred disk galaxies due to the angular momentum and mass exchanges mediated by the bar (see, e.g., Bureau & Athanassoula, 2005). In effect, observations of μ_2 circularize the intrinsic mass distribution so μ_2 is simply too coarse a measurement to properly constrain the internal dynamics of galaxies. To do so requires knowledge of the full shape of the line-of-sight velocity distribution. This approach was used by Chung & Bureau (2004)

for this sample.

In summary, we argue that the overall overwhelming quality of the fits for galaxies with and without B/PS bulges provides confidence in the reliability of the derived masses and mass-to-light ratios, despite the likely non-axisymmetry of the inner regions of many of the galaxies. Our results, however, are not inconsistent with observations and simulations that demonstrate that these galaxies are barred. The application of the JAM technique to model galaxies of known non-axisymmetric morphologies is of course the best way to confirm definitively the validity of this argument.

2.6 CONCLUSIONS

We presented mass models for a large sample of spiral and S0 galaxies. These models allowed us to constrain the stellar and dark matter content of the sample galaxies. For each galaxy, the stellar mass distribution was derived from near-infrared photometry under the assumptions of axisymmetry and a constant stellar mass-to-light ratio. We added an NFW dark halo and assumed a correlation between concentration and virial mass. We solved the Jeans equations for the corresponding potential under the assumption of constant anisotropy in the meridional plane. By comparing the predicted second velocity moment to observed long-slit stellar kinematics, we determined the best-fitting parameters of the mass models. In some galaxies the observed second velocity moment rises monotonically, in others it plateaus at small radii, and in others it falls significantly before rising again. Despite this wide range of observed behaviours, our simple models, with only three free parameters (stellar mass-to-light ratio, dark halo mass and anisotropy), are able to reproduce the observed kinematics very well. The observed kinematics typically extend to 2–3 $R_{\rm eff}$ or, equivalently, 0.5–1 R_{25}, and $1 \lesssim \chi_{\rm red} \lesssim 2$ for all galaxies.

For our sample of 14 spirals and 14 S0s, we find a median $(M/L)_{K_S}$ of 1.09 $(M/L)_{K_S,\odot}$ with rms scatter 0.31. Our values are roughly consistent with the small number of previous independent determinations using different dynamical methods. The K_S-

band mass-to-light ratios that we measure are unique, however, because of the size of the sample and the way we have attempted to correctly apportion mass between the stellar and dark components of the galaxies, without resorting to either a maximal disk assumption or results from stellar population models. Because they do not depend on stellar population models, they can be used to attempt to constrain the normalization and IMF of such models in the near-infrared.

We also performed preliminary comparisons of our dynamical (M/L) ratios to the predictions of two stellar population models: the color–(M/L) relations of Bell et al. (2003), which use the PEGASE stellar population models, and evolutionary tracks in color–(M/L) space for a range of metallicities from Maraston (2005). The Bell et al. (2003) prediction is offset from our models by a small but systematic amount and some of our galaxies are just outside the range expected by the Maraston (2005) models. These differences could be due to systematic errors introduced in our comparison, but may also hint at problems with the stellar population models or the IMFs they assume. In a future work we will extend this comparison by determining absorption line strength indices for the present sample, allowing us to directly compare dynamical and stellar population estimates of (M/L) for individual galaxies.

Once accurately known, K_S-band mass-to-light ratios are particularly useful for constraining the stellar mass budget of the universe. Firstly, K_S (or K) is the waveband at which the effects of dust on observations of light from stars is minimized. Shorter wavelengths are subject to absorption and longer wavelengths have contributions from hot dust seen in emission. Secondly, K-band is dominated by light from the sub-solar mass main sequence stars that dominate the total mass budget (and trace the smooth potential) of galaxies. It therefore comes as no surprise that, as found dynamically in this work and using stellar population models (e.g. Bell et al., 2003), $(M/L)_{K_S}$ is a relatively constant quantity in the local universe compared to the (M/L) ratio at B-band. We both find that $(M/L)_{K_S}$ varies by $\lesssim 0.3$ dex (a factor of 2) across our samples. This is much less than the variations observed at shorter wavelengths. The K_S-band luminosity function can therefore be used as a reliable proxy (subject to the small variation in $(M/L)_{K_S}$) for the stellar mass density function (e.g. Bell et al., 2003; Arnouts et al., 2007; Devereux et al., 2009).

Our best-fitting mass models include NFW haloes with a median dark mass within the virial radius of $M_{\rm DM} = 10^{12.85}\,M_\odot$ with rms scatter of 0.7 dex. With our adopted concentration–halo mass correlation, this corresponds to a concentration $c_{\rm vir} = 7.9$ with rms scatter of 1.2. These parameters of the best-fitting dark haloes are defined in terms of their behaviour out to the virial radius, which is well beyond our kinematic constraints. They are therefore model dependent and should be treated with caution. The dark-to-total mass fraction within the galaxy is, however, a well-constrained quantity. We find that, on average, the haloes contribute around 15 per cent by mass within $R_{\rm eff}$ and 49 per cent within R_{25}. All but two galaxies are consistent with the maximal disk assumption defined in Sackett 1997. Models without dark matter are able to satisfactorily reproduce the observed kinematics in most cases, although there are problems at large radii in several galaxies. The improvement when a halo is added is statistically significant in all but four cases and the stellar mass-to-light ratios of mass models with dark haloes match the independent expectations of stellar population models better.

There is no systematic difference between the dark matter content of the S0, Sa and Sb galaxies in the sample. This hints at a homology between S0s and spirals. Emsellem et al. (2007) and Cappellari et al. (2007) show that elliptical and S0 galaxies exhibiting large-scale rotation (which they call fast-rotators) constitute a homogeneous class in terms of their shape, stellar kinematics and photometric properties. Assuming this direct link between S0s and fast-rotating ellipticals, our constraints on the dark matter content of Sa, Sb and S0 galaxies can in turn be applied to fast-rotating ellipticals, implying a continuum of properties from Sb spirals to fast-rotating ellipticals. Bertola et al. (1993) made a particularly interesting pioneering suggestion when, with limited data, they suggested that spirals and ellipticals share a common scale, $1.2\,R_{\rm eff}$, within which luminous and dark matter contribute an equal amount to the total mass. For our larger sample, which contains no elliptical galaxies, we find that this radius is, on average, $4.1\,R_{\rm eff}$ or $1.0\,R_{25}$.

The method we have used is generally applicable to axisymmetric (and spherically symmetric) galaxies and the code we have used is public. Although we have applied it to edge-on galaxies, it can equally be applied to any galaxy with a well-constrained

inclination. We assumed that the galaxies are axisymmetric but argued that even in galaxies that are probably barred the method gives sensible results. Application of the method to simulated barred galaxies is needed to demonstrate this definitively, however. Other limitations of our work include our inability to constrain anisotropy and the well-motivated but model-dependent way in which we eliminate one of the halo parameters. Kinematics constraints over an extended two-dimensional field, or additional constraints from strong and weak gravitational lensing could allow us to lift these degeneracies without making assumptions, which would provide even more robust observational tests of galaxy formation models and simulations.

APPENDIX 2.A PHOTOMETRIC RECALIBRATION WITH THE 2MASS EXTENDED SOURCE CATALOG

During the course of this work, we discovered that the photometric calibration zero points of Bureau et al. (2006) were incorrect, so we recalibrated them using K_S-band images of the same objects taken from the Two Micron All Sky Survey (2MASS) Extended Source Catalog (Skrutskie et al., 2006).

We did this by measuring the light in matching elliptical apertures for each pair of images, and shifting the CASPIR image by a constant zero point offset such that its radial profile coincided with that of the 2MASS image. This offset gives a new, corrected K_S-band surface brightness zero point for each CASPIR image.

Ensuring truly corresponding elliptical apertures enclosing identical locations on the sky is not trivial. The problem is that measurements of ellipticity and position angle based on two images of different depths will not necessarily yield identical results. Here the shallower 2MASS image does not reveal much of the faint discs, so important in determining the position angle and ellipticity. Corresponding apertures can trivially be ensured by using circular apertures. However, because circular apertures of increasing radii more quickly include noisy contributions from outside the galaxy (especially in edge on systems), they do not use as much of either galaxy image as possible, decreasing the reliability of the recalibration.

We therefore chose to impose the ellipticity measured for each CASPIR image on the corresponding 2MASS image and determined the position angle independently for both images by using an initial image truncated at the same approximate surface brightness. In truncating both images, we temporarily remove information from the deeper image so that it is missing as much of the disc as the shallower image.

Before use, we correct the 2MASS images for the effects foreground Galactic extinction using the dust maps of Schlegel, Finkbeiner & Davis (1998). This ensures that our recalibration incorporates this correction. The calibration also involves an incidental and very slight colour transformation from K_S to Kn. Much like the K_S filter used for 2MASS, the purpose of the Kn-band filter is to reject the thermal background admitted by a standard K-band filter at its long wavelength end (Skrutskie et al., 2006). We adopt a value for the absolute magnitude of the Sun at K_S-band of $M_{K_S,\odot} = 3.29$ (Blanton & Roweis, 2007). The result of this recalibration is presented in Table 2.3. The quantity Δ is the recalibration constant which should be added to the incorrectly calibrated Kn-band images presented by Bureau et al. (2006), which were too faint, typically by around 0.8 mag arcsec^{-2}.

Table 2.3: K_S-band calibration corrections applied to the surface brightness of the images presented by Bureau et al. (2006)

Galaxy	Δ (mag arcsec^{-2})	Galaxy	Δ (mag arcsec^{-2})
B/PS bulges		Control sample	
ESO 151-G004	-0.80	IC 5176	-0.82
ESO 185-G053	-0.70	NGC 1032	-0.87
ESO 240-G011	-0.82	NGC 3957	-0.73
ESO 311-G012	-0.83	NGC 4703	-0.78
ESO 443-G042	-0.75	NGC 5084	-0.97
ESO 597-G036	-0.64	NGC 7123	-0.92
IC 4767	-0.76		
IC 4937	-1.21		
IC 5096	-0.88		
NGC 128	-0.86		
NGC 1381	-0.75		
NGC 1596	-0.84		
NGC 1886	-0.80		
NGC 2310	-0.96		
NGC 3203	-0.78		
NGC 3390	-0.83		
NGC 4469	-0.82		
NGC 4710	-0.85		
NGC 5746	-0.85		
NGC 6722	-1.29		
NGC 6771	-0.82		
PGC 44931	-1.08		

3

THE TULLY-FISHER RELATIONS OF EARLY-TYPE SPIRAL AND S0 GALAXIES

The material in this chapter was originally published in 'The Tully-Fisher relations of early-type spiral and S0 galaxies', M. J. Williams, M. Bureau and M. Cappellari, 2010, MNRAS, 409, 1330. The definitive version is available at www.blackwell-synergy.com.

3.1 INTRODUCTION

Both early- and late-type galaxies follow scaling relations. The radii, velocity dispersions and luminosities of elliptical galaxies lie on a Fundamental Plane (Djorgovski & Davis, 1987; Dressler et al., 1987). The luminosities of disk galaxies scale with their sizes (Freeman, 1970), rotation speeds (Tully & Fisher, 1977) and colours (Tully, Mould & Aaronson, 1982). The existence, scatter and evolution of these scaling relations provides powerful constraints for models of galaxy formation and evolution.

In this work we concentrate on the Tully-Fisher relation (TFR), first discovered by Tully & Fisher (1977). In its original form, the TFR relates the global H I line widths of disk galaxies to their total luminosities. The line width of a rotationally-supported galaxy is a measure of the difference between the maximum rotation velocities of the approaching and receding sides. A galaxy's luminosity is related to the mass

of its luminous component (and the evolutionary state of the stellar populations). The observed correlation between global line widths and luminosities is therefore a manifestation of a more general connection between galaxy masses and rotational velocities. A correlation is of course expected for gravitationally bound systems in which the mass distribution is dominated by luminous matter.

Empirically, the correlation is tight enough to allow the TFR to be inverted and used to determine distances (e.g. Sakai et al., 2000; Tully & Pierce, 2000, hereafter TP00), but systematic variations of the residuals can arguably be used to infer the properties of dark haloes (Courteau & Rix, 1999). Efforts to simultaneously reproduce the zero-point of the TFR and the galaxy luminosity function with semi-analytical models of galaxy formation may reveal further information on the role of the halo, the importance of feedback and the evolution of the stellar populations (e.g. Baugh, 2006; Dutton et al., 2007). It is therefore clear that investigating variations of the local TFR with galaxy luminosity, size, type and other parameters should provide valuable insight into the growth of luminous structures in the Universe.

There are systematic variations in the slope, intercept and scatter of the TFR as a function of galaxy type. Roberts (1978) and Rubin et al. (1985) found that Sa spirals are fainter than Scs for a given rotational velocity at optical wavelengths. At least some of this difference has been attributed to variation in the shape of rotation curves related to the bulge-to-disk ratio (Verheijen, 2001; Noordermeer & Verheijen, 2007). The difference is much smaller in the near-infrared (Aaronson & Mould, 1983; Peletier & Willner, 1993). This has been taken as evidence that the discrepancy at optical wavelengths is at least partially due to the effects of recent star formation on the luminosity, which is reduced in the near-infrared. This effect has been measured for a large, bias-corrected sample by Masters, Springob & Huchra (2008). They find no evidence of any difference between the zero points of the Sb and Sc TFRs and a small effect for Sa galaxies, which they find have a variable offset compared to Sb – Sc spirals: ≈ 0.2 mag brighter at $v \approx 150\,\mathrm{km\,s^{-1}}$, no difference at $v \approx 180\,\mathrm{km\,s^{-1}}$ and ≈ 0.4 mag fainter at $v \approx 250\,\mathrm{km\,s^{-1}}$.

Particular attention has been paid to S0 galaxies, which are the earliest galaxies with rotationally-supported stellar disks. The fact that they are more common in the

centres of clusters, rarer on the outskirts, and rarest of all in the field, the opposite of the trend observed for spirals, suggests that environmental processes transform spirals into S0s (Spitzer & Baade, 1951; Dressler, 1980; Dressler et al., 1997). Processes such as ram-pressure stripping (Gunn & Gott, 1972), strangulation (Larson, Tinsley & Caldwell, 1980) and harassment (Moore et al., 1996) may have removed the gas from the disks of spiral galaxies and left them unable to form stars. S0s do however exist in the field, where such processes should be insignificant. Passive evolution or the effects of active galactic nuclei in spirals have been suggested as possible formation mechanisms outside dense environments (van den Bergh, 2009a). Problems remain with the disk fading picture, however: the bar fractions of spirals and S0s are discrepant (Aguerri, Méndez-Abreu & Corsini, 2009; Laurikainen et al., 2009), in a given environment S0s are at least as bright as spirals (Burstein et al., 2005), and the bulge-to-disk ratios of S0s are difficult to reconcile with those of their presumed progenitors (Christlein & Zabludoff, 2004). See Blanton & Moustakas (2009) for a modern review of this issue.

Unless they are violent, these processes should make only a slight change to the kinematics and dynamical masses of S0s, but a significant change to their luminosities. Assuming they do not have systematically different dark matter fractions, this change in stellar population should cause S0s to have fainter luminosities for a given rotational velocity and lie offset from the TFR of spirals. The size of any offset and the difference between the scatters of the S0 and spiral TFRs can therefore be used to constrain models of S0 formation and evolution (Bedregal, Aragón-Salamanca & Merrifield, 2006, hereafter BAM06). A well-constrained S0 TFR also raises the possibility of extending the Tully-Fisher distance determination technique to earlier galaxy types, and of probing variations of mass-to-light ratio with redshift.

Measuring the TFR of S0s is difficult because they do not usually have extended gaseous disks. Instead of using a gaseous emission line width as a measure of maximum rotation, several groups have used resolved rotation curves derived from stellar absorption lines. These raw observations must then be corrected for asymmetric drift (i.e. pressure support) before they can be presumed to trace the circular velocity (and therefore the potential of the galaxy). A number of groups have done just this and

found that S0s are indeed fainter than spirals for a given rotational velocity. Neistein et al. (1999) found that S0s lie on a TFR offset by 0.5 mag at I-band from the spiral TFR (with 0.7 mag intrinsic scatter). Hinz, Rix & Bernstein (2001) and Hinz, Rieke & Caldwell (2003) found an offset of 0.2 mag at I and H-band (with 0.5–1.0 mag intrinsic scatter). BAM06 combined these data with new observations of galaxies in the Fornax cluster and found that the combined sample of 60 S0s lies around 1.5 mag below the spiral TFR at B-band (0.9 mag scatter) and 1.2 mag below the spiral TFR at K_S-band (1.0 mag scatter). A promising alternative to stellar absorption line kinematics is sparse kinematic data from the emission lines of planetary nebulae. A pilot study of the nearby S0 galaxy NGC 1023 with the Planetary Nebula Spectrograph found that this particular S0 lies around 0.6 mag below a spiral TFR at K_S-band (Noordermeer et al., 2008).

An alternative approach to measuring and correcting the rotational velocities of the earliest type galaxies is to construct dynamical models that, in principle, directly probe the circular velocity of a system. At the expense of model-dependent assumptions, this approach removes the uncertainties associated with the asymmetric drift correction, which may be both significant and systematic. Mathieu, Merrifield & Kuijken (2002) did this for a sample of six edge-on S0s and found that they lie 1.8 mag below an I-band spiral TFR (with 0.3 mag intrinsic scatter). Modelling also allows the TFR to be extended to elliptical galaxies with little or no rotational support. As with S0s, previous dynamical modelling studies of ellipticals have found that they are fainter than spirals for a given rotational velocity: Franx (1993), 0.7 mag at R-band; Magorrian & Ballantyne (2001), 0.8 mag at I-band; Gerhard et al. (2001), 0.6 mag at R- and 1.0 mag at B-band; De Rijcke et al. (2007), 1.5 mag at B-, 1.2 mag at K_S-band.

However, all previous studies comparing the TFRs of S0s and ellipticals to those of spirals have used independently determined reference TFRs for spiral galaxies (taken from, e.g., Sakai et al. 2000; TP00). These reference TFRs are derived in the traditional way, using global line widths from H I observations. In Section 3.2 we discuss the technical and observational issues involved in characterizing the enclosed mass of a disk galaxy in an unbiased way. We argue that comparisons between TFRs derived from different measures of rotation are not *a priori* justified and are likely to introduce

artificial and uncertain offsets in practice.

The main astrophysical goal of the present work is thus to compare the TFRs of spiral and S0 galaxies in a way that is not vulnerable to these uncertain systematics, by using measures of luminosities and rotational velocities determined identically for both S0s and spirals. Readers who are more interested in the results of this comparison and its implication for the evolution of S0s, may wish to skip ahead to Section 3.3, where we present our sample. In Section 3.4 we describe the numerical method used to simultaneously determine the TFRs of spirals and S0s. We then present TFRs for the two samples in terms of near-infrared and optical luminosities, stellar mass and dynamical mass. In Section 3.5 we discuss our results in the context of models of S0 formation and evolution and previous analyses of S0 TFRs. We conclude briefly in Section 3.6.

3.2 MEASURES OF ROTATION

3.2.1 The problem

To construct a Tully-Fisher relation one needs a measure of rotation. This can be derived from, for example, the global H I line width, spatially-resolved H I, Hα or stellar rotation curves or velocity fields, sparse tracers (e.g. globular clusters and planetary nebulae), or the circular velocity of dynamical models at some fiducial location. In principle, all these measures are related to the rotation of the galaxy, but the relationship of these single numbers to the enclosed mass is complicated by the fact that observed rotation curves (and indeed modelled circular velocity curves) do not always flatten. Moreover, it not obvious that these observational measures directly and accurately comparable to each other. Both the nature of the observations and the corrections applied for different techniques could conceivably introduce systematics that vary with galaxy properties such as type, mass or size.

For example, the transformation of a global H I line width to a measure of rotation involves corrections for instrumental broadening and turbulent motion (e.g. Tully &

Fouqué, 1985; Verheijen, 2001). The extent to which these corrections are able to recover the intrinsic motion of the tracer or the true circular velocity of the galaxy potential has recently been questioned (Singhal, 2008). Meanwhile, stellar kinematics must be corrected for asymmetric drift, which typically involves making approximations which are difficult to justify prima facie (see Section 3.2.2). Finally, the construction of dynamical models often involves simplified modelling of the full distribution function (e.g. Mathieu, Merrifield & Kuijken, 2002) or assumptions about intrinsic morphology, anisotropy and the role of dark matter (e.g. Chapter 2, i.e. Williams, Bureau & Cappellari, 2009, hereafter WBC09).

These considerations place the direct comparisons of TFRs derived using different measures of rotation on shaky ground. Offsets which are ascribed to fading or brightening could in fact be due to systematic biases that differ between the measures of rotation used. For typical slopes of the TFR, a relatively small systematic difference in velocity of ~ 0.1 dex introduces an offset in the TFR that is indistinguishable from a ~ 1 mag difference in luminosity. This is of the order of the typical zero-point offsets claimed for S0 TFRs (Neistein et al., 1999; Hinz, Rix & Bernstein, 2001; Hinz, Rieke & Caldwell, 2003; Mathieu, Merrifield & Kuijken, 2002; Bedregal, Aragón-Salamanca & Merrifield, 2006), so it is crucial that we eliminate (or at least quantify) the systematics introduced by such comparisons. In the remainder of this section, we examine the differences between the results of three different measures of rotation when applied to the same 28 early-type disk galaxies, and discuss the implications for comparisons of the zero-point of the TFR.

3.2.2 *Four possible measures of rotation defined*

We aim to compare measures of rotation derived from global H I line widths (which we denote $v_{\mathrm{H\,I}}$), resolved gas rotation curves (v_{gas}), stellar kinematics (v_{drift}) and dynamical models (v_{model}) for the 28 galaxies in the present work. This sample, which consists of 14 spirals and 14 S0s, is described in Section 3.3.

For $v_{\mathrm{H\,I}}$, the rotational velocity derived from global H I line widths, we adopt the

quantity `vrot` from HYPERLEDA (Paturel et al., 2003). This is the inclination-corrected maximum gas rotation velocity, based on an average of independent H I line width determinations taken from the literature. Strictly speaking, HYPERLEDA also uses spatially-resolved Hα rotation curves to calculate `vrot`, but these observations were only present in HYPERLEDA for four of the galaxies in our sample, and there was no evidence that they systematically disagreed with the H I line width values at any more than the 0.01 dex level.

For $v_{\rm gas}$, we fit Gaussians to the position-velocity diagrams (PVDs) presented in Bureau & Freeman (1999). These are derived from [N II] emission lines. We only use the region of the PVD where the rotation curve is flat. This restriction means that it is not possible to measure $v_{\rm gas}$ for many of the galaxies in our sample, either because emission was not detected, or because it was not sufficiently extended.

We calculate the asymmetric drift-corrected stellar velocity, $v_{\rm drift}$, using the observed stellar kinematics presented in Chung & Bureau (2004). In order to more accurately measure the local circular velocity we attempt to correct these observations for the effects of line-of-sight integration and asymmetric drift using the same recipe as used in BAM06, which we describe briefly below. We make no attempt to improve this recipe, since one of our goals is to assess the biases in previous determinations of the TFR based on stellar kinematics. The raw observations and their corrected values are shown in Fig. 3.1.

The line-of-sight correction for an edge-on disk assumes that the local azimuthal velocity $v_\phi(R)$ at a galactocentric distance R (in the galaxy's cylindrical coordinate system (R, ϕ, z)) is related to $v_{\rm LOS}(x')$, the luminosity-weighted mean line-of-sight velocity at a projected distance from the galaxy centre x', by the equation

$$v_{\rm LOS}(x') = \frac{\int_0^\infty v_\phi(R)\rho(R)\cos\phi\,{\rm d}z'}{\int_0^\infty \rho(R)\,{\rm d}z'}. \tag{3.1}$$

Following the notation of, e.g., Binney & Tremaine (2008), (x', y', z') is the observer's coordinate system on the sky, in which the x' axis is aligned with the projected major axis of the galaxy and the z' axis is along the line of sight. $\rho(R)$ is the luminosity density. The integral is evaluated along that line-of-sight z'. By assuming that the local streaming velocity v_ϕ is independent of R, one can use the above relationship to

Figure 3.1: Observed, corrected and modelled kinematic data for all sample galaxies. The black points are the observed mean line-of-sight stellar velocities $v_{\rm LOS}$ and the grey points the line-of-sight velocity dispersions $\sigma_{\rm LOS}$, both from Chung & Bureau (2004). The open red squares are estimates of the circular velocity derived by correcting the observations for line-of-sight and asymmetric drift effects ($v_{\rm c,drift}$). There are missing points at small radii because the correction is unreliable where the local dispersion is large compared to the line-of-sight velocity. The solid blue line is the circular velocity of the galaxy dynamical model from WBC09 ($v_{\rm c,model}$). These models consist of contributions from a stellar component (dashed blue line) and a dark halo (dotted blue line). The vertical line is the radii beyond which the observed rotation curve is flat, which is important for our calculation of $v_{\rm drift}$ and $v_{\rm model}$, the single values used to characterize rotation. These are determined as described in the text. Their values for each galaxy are shown as filled red and blue squares respectively, at arbitrary large radii.

.

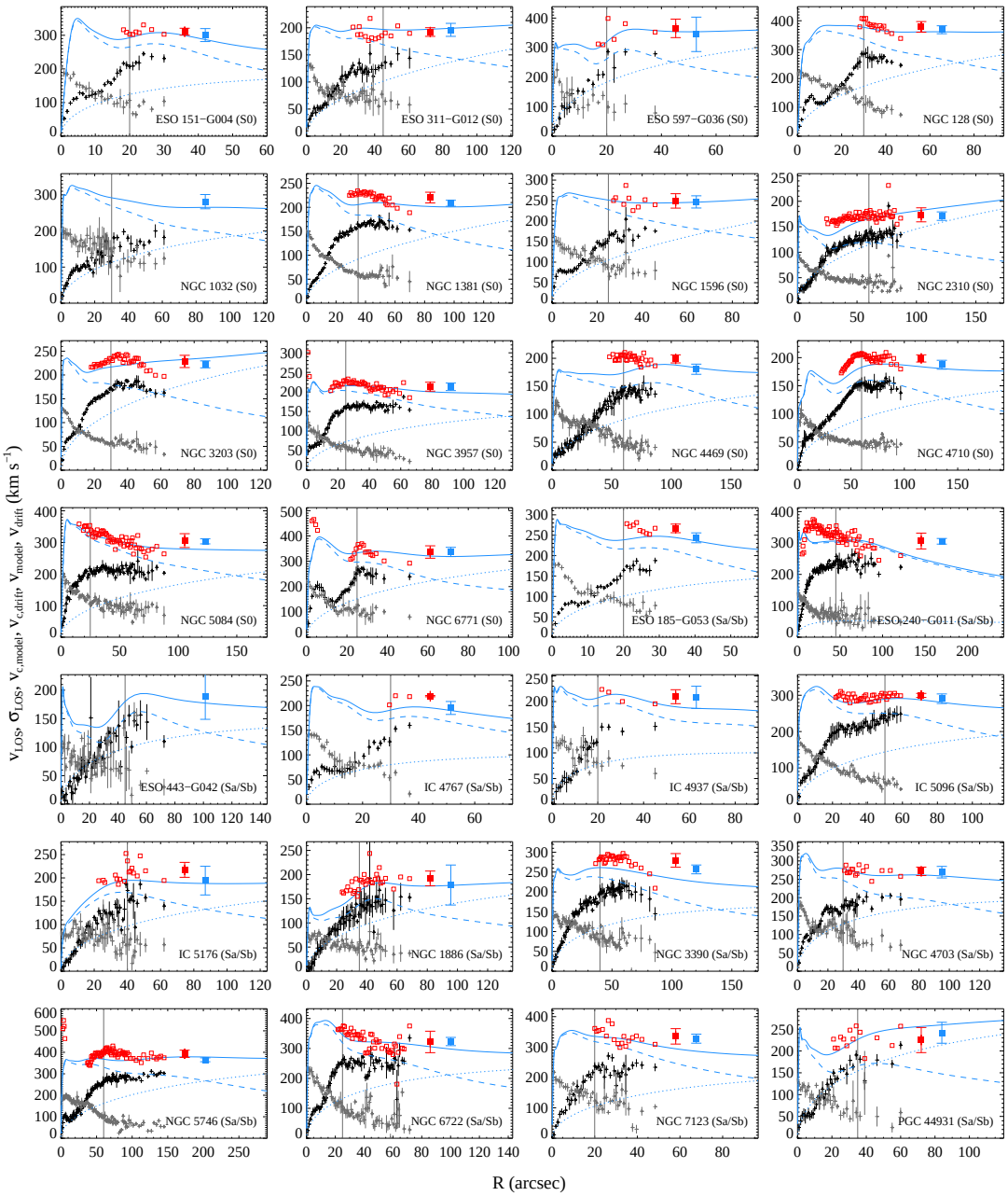
ESO 151−G004 (S0)
ESO 311−G012 (S0)
ESO 597−G036 (S0)
NGC 128 (S0)
NGC 1032 (S0)
NGC 1381 (S0)
NGC 1596 (S0)
NGC 2310 (S0)
NGC 3203 (S0)
NGC 3957 (S0)
NGC 4469 (S0)
NGC 4710 (S0)
NGC 5084 (S0)
NGC 6771 (S0)
ESO 185−G053 (Sa/Sb)
ESO 240−G011 (Sa/Sb)
ESO 443−G042 (Sa/Sb)
IC 4767 (Sa/Sb)
IC 4937 (Sa/Sb)
IC 5096 (Sa/Sb)
IC 5176 (Sa/Sb)
NGC 1886 (Sa/Sb)
NGC 3390 (Sa/Sb)
NGC 4703 (Sa/Sb)
NGC 5746 (Sa/Sb)
NGC 6722 (Sa/Sb)
NGC 7123 (Sa/Sb)
PGC 44931 (Sa/Sb)
v_{LOS}, σ_{LOS}, $v_{c,model}$, v_{cdrift}, v_{model}, v_{drift} (km s^{-1})
R (arcsec)

infer it. This assumption is valid only if R is at least the radius at which the intrinsic circular velocity curve flattens. To evaluate these integrals we assume $\rho(R)$ is an exponential disk of scale length $R_{\rm d}$, which we measure from the major-axis surface brightness profiles of our K_S-band images at radii outside the bulge (Bureau et al., 2006).

We then apply a correction for asymmetric drift to $v_\phi(R)$ to derive $v_{\rm c,drift}(R)$, an estimate of the true local circular velocity:

$$v^2_{\rm c,drift}(R) = v^2_\phi(R) + \sigma^2_\phi(R)\left(2\frac{R}{R_{\rm d}} - 1\right), \tag{3.2}$$

where $\sigma_\phi(R)$ is the azimuthal stellar velocity dispersion. This equation is derived from the Jeans equations (Jeans 1922; Binney & Tremaine 2008) by assuming a thin disk in a steady state and the epicyclic approximation ($\sigma^2_\phi/\sigma^2_R = 0.5$ for constant v_ϕ). To estimate $\sigma_\phi(R)$, we assume that it is equal to an exponential fit to the observed stellar line-of-sight velocity dispersion $\sigma_{\rm LOS}(x')$. This assumption is of course flawed, since the observed dispersion includes a contribution from the changing component of the azimuthal velocity along the line-of-sight. This effect will bias the asymmetric drift correction to be too high. However, the error is small in practice, and, crucially for the present work, it is not a strong function of galaxy type in the range S0–Sb. Under the assumptions described above, for disks with typical levels of pressure support ($v_\phi/\sigma_\phi \sim 5$ at the relevant radii $\approx 2-4\,R_{\rm d}$), numerical integration shows that the error introduced by wrongly assuming $\sigma_\phi(R) = \sigma_{\rm LOS}(x')$ causes $v_{\rm c,drift}$ to overestimate the true circular velocity by $\approx 0.04 \pm 0.01$ dex. This error is almost independent of v_ϕ/σ_ϕ in the range $2 \leq v_\phi/\sigma_\phi \leq 20$, a quantity which is in any case independent of morphological type for our sample.

Finally, the local circular velocity of the mass model, $v_{\rm c,model}$, is derived from the dynamical models presented in WBC09. In that work, we modelled the mass distribution of each galaxy by assuming it is composed of an axisymmetric stellar component with a constant mass-to-light ratio and a spherical NFW dark halo (Navarro, Frenk & White, 1997). The axisymmetric stellar component is based on an analytic fit to the observed near-infrared photometry of the composite bulge and disk. The absence of a triaxial bar component in our models does not significantly affect either the global

properties of the models or the local kinematics at the large radii relevant to the TFR (see section 5.5.3 of WBC09 for a more extensive discussion of this issue). We assumed a particular relationship between halo mass and concentration (Macciò, Dutton & van den Bosch, 2008). We determined the three parameters of the models (the stellar mass-to-light ratio, virial halo mass and orbital anisotropy) by comparing the observed stellar second velocity moment $v_{\rm rms}(x') = [v^2_{\rm LOS}(x') + \sigma^2_{\rm LOS}(x')]^{1/2}$ along the major axis to that predicted by solving the Jeans equations assuming a constant anisotropy (parametrized as $\beta_z = 1 - \sigma_z^2/\sigma_R^2$). The solution of the Jeans equations under these assumptions is described in Cappellari (2008). Note that while $v_{\rm c,drift}$ described above is weakly affected by our assumptions that $\sigma_\phi^2/\sigma_R^2 = 0.5$ and $\sigma_\phi(R) = \sigma_{\rm LOS}(x')$, $v_{\rm c,model}$ suffers from no such biases. Our solutions of the Jeans equation are constrained by a fit to the observed second velocity moment along the line-of-sight. The second moment is strictly independent of σ_ϕ^2/σ_R^2 so no assumption for this ratio is required, and the implementation rigorously accounts for line-of-sight integration.

To construct a TFR, the radial profiles of the asymmetric-drift corrected stellar kinematics, $v_{\rm c,drift}$ and of the model circular velocity, $v_{\rm c,model}$ must be characterized by a single number, $v_{\rm drift}$ and $v_{\rm model}$ respectively. We do this by determining the flat region of the observed rotation curve by eye. We then take $v_{\rm drift}$ to be the mean of the values of $v_{\rm c,drift}$ beyond this point. The continuous Jeans modelled circular velocity curve is evaluated at the same radii as the observed stellar kinematics. Its mean in the flat region of the observed rotation curve gives $v_{\rm model}$. Of course, it is possible to evaluate the circular velocity of the models at arbitrary radii, but by restricting ourselves to those radii for which we have stellar kinematic observations, we avoid using the mass models in regions where they are not constrained by the data. Fig. 3.1 shows these calculations for all sample galaxies.

3.2.3 *Comparison*

A comparison of the four measures of rotation is shown in Fig. 3.2. The upper panel demonstrates that $\langle \log(v_{\rm model}/v_{\rm drift}) \rangle = -0.015 \pm 0.003$ dex with an rms scatter of

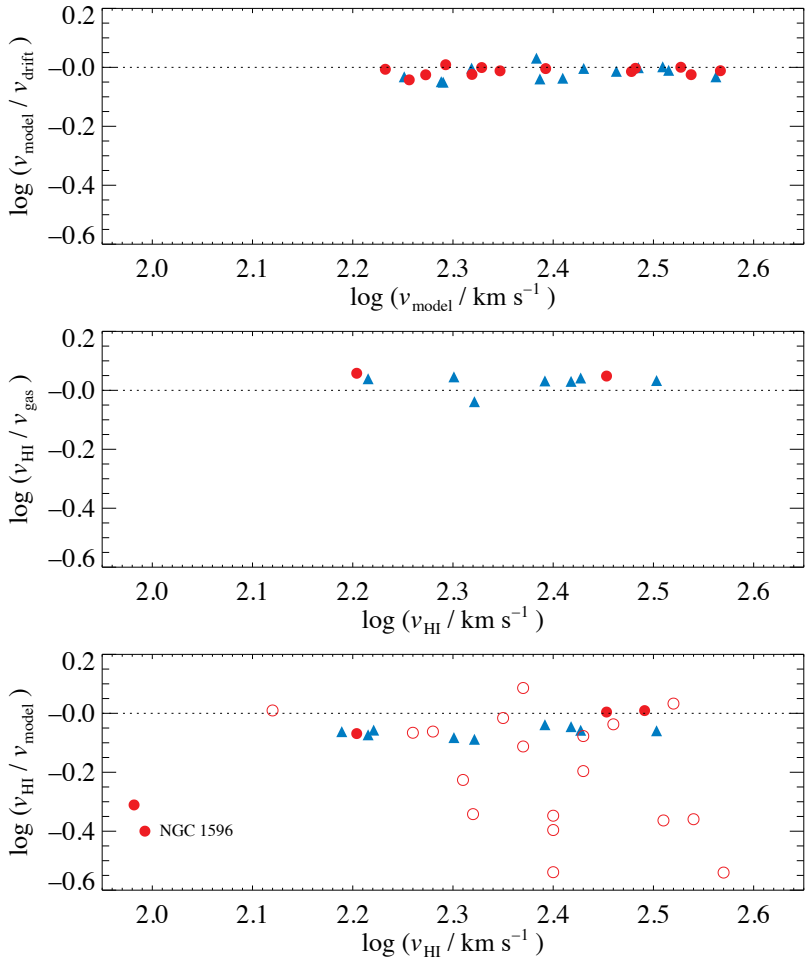

Figure 3.2: Comparisons of the circular velocities of the mass models ($v_{\rm model}$), observed stellar kinematics corrected for asymmetric drift ($v_{\rm drift}$) and rotational velocities derived from global H I line widths ($v_{\rm H\,I}$) and ionized gas position-velocity diagrams ($v_{\rm gas}$). The solid blue triangles are the Sa–Sb galaxies from our sample and the solid red circles the S0s. The open red circles are the S0s presented in BAM06. They do not estimate $v_{\rm model}$ so, in order to place these galaxies on the plot, we assume $v_{\rm drift} \approx v_{\rm model}$ for them.

0.019 dex for both spirals and S0s. This small difference, which is on average less than 4 per cent, is probably due to the additional approximations and assumptions introduced in the asymmetric drift correction compared to the Jeans models. We note in particular that it is consistent with the error due to assuming $\sigma_\phi(x') = \sigma_{\rm LOS}(x')$, as discussed in Section 3.2.2. The absolute offset between these measures is not significant in the context of the TFR and, crucially, there is no evidence of any systematic difference between S0s and spirals. The scatter is also extremely small. Since both $v_{\rm drift}$ and $v_{\rm model}$ are derived from the observed stellar kinematics, their close agreement is not of itself independent proof of the accuracy with which they trace the true circular velocity. The agreement of $v_{\rm drift}$ with the results of detailed and robust Jeans modelling does suggest, however, that the approximations inherent in eqns. (1–2) yield an approximately valid solution of the Jeans equations.

The middle panel demonstrates fairly good agreement between the two measures based on gas, $v_{\rm H\,I}$ and $v_{\rm gas}$. $\langle \log(v_{\rm H\,I}/v_{\rm gas}) \rangle = 0.032 \pm 0.009$ dex with a rms scatter of 0.029 dex. There is some evidence that $v_{\rm H\,I}$ systematically exceeds $v_{\rm gas}$ by 5 – 10 per cent. Statistics are poorer because gas is rare in S0s by definition, but there is no evidence of any systematic difference between $v_{\rm H\,I}/v_{\rm gas}$ in S0s and spirals.

However, the bottom panel of Fig. 3.2 shows that $v_{\rm model}$ (and therefore $v_{\rm drift}$) does not in general agree $v_{\rm H\,I}$ (and thus $v_{\rm gas}$): $\langle \log(v_{\rm H\,I}/v_{\rm model}) \rangle = -0.094 \pm 0.031$ dex with a rms scatter of 0.115 dex (or -0.18 ± 0.043 dex with a rms scatter of 0.243 dex if the BAM06 galaxies are included). Some of this difference and scatter is caused by pathological cases of $v_{\rm H\,I}$ derived from single dish measurements, i.e. spatially unresolved measurements of 21 cm signal from galaxies with a warped gas disk, polar rings or gas-rich nearby companions that fall within the telescope beam (e.g. this is almost certainly the case for the S0 galaxy NGC 1596, see Chung et al. 2006).

But even when possible pathological cases are avoided, for example by ignoring S0 galaxies, which are more likely to be problematic, there remains a clear systematic offset: $\langle \log(v_{\rm H\,I}/v_{\rm model}) \rangle = -0.063 \pm 0.005$ dex (15 per cent) with 0.02 dex rms scatter for the spirals in our sample. For these galaxies, the rotational velocity derived from the global H I line width is significantly and systematically smaller than that derived from stellar kinematics or dynamical modelling. Because $v_{\rm H\,I}$ is derived from spatially

unresolved data, this could be explained by the global H I line width probing the local gas velocity out to different radii than our typical stellar kinematic data (Noordermeer et al., 2007).

We find a similar systematic difference between $v_{\rm model}$ (or $v_{\rm drift}$) and $v_{\rm gas}$: $\left\langle \log(v_{\rm gas}/v_{\rm model}) \right\rangle = -0.086 \pm 0.008$. $v_{\rm gas}$ is derived from a spatially resolved PVD taken from the same long-slit optical spectrum with which we derive the stellar kinematics. We can therefore verify directly that it does not suffer from either pathological problems related to gas-rich companions, warps or polar rings, or doubt about the radii probed compared to our stellar kinematics. We show this in Fig. 3.3 for the five sample galaxies with optical emission that extends to the disk. It is clear that the stars and gas are associated with the same galaxy and are observed at similar radii. Therefore, unless light-emitting gas is absent from the tangent point along the line-of-sight in these edge-on galaxies (a possibility we cannot rule out), the emission line gas kinematics and absorption line stellar kinematics should imply the same local circular velocity and the same single characteristic measure of rotation, ($v_{\rm gas}$, $v_{\rm drift}$ or $v_{\rm model}$).

But in these five galaxies galaxies, the stars and gas rotate with essentially the same velocity as a function of position in the outer, flat parts of the observed rotation curve. The stars have non-negligible dispersion so we know they do not trace the local circular velocity by an amount that can be calculated using the Jeans equations. Given this observation, it is not surprising that $v_{\rm gas}$ is significantly less than $v_{\rm model}$.

In summary, while agreement between $v_{\rm gas}$ and $v_{\rm H\,I}$ is fairly good, and from this we conclude that $v_{\rm model}$ and $v_{\rm drift}$ (based on stars seen in absorption) do not imply the same circular velocity as $v_{\rm H\,I}$ and $v_{\rm gas}$ (based on gas seen in emission). This is not a new result. In early-type disk galaxies, the observed stellar kinematics and the well-understood Jeans equations often imply a local circular velocity greater than the observed rotational velocity of gas (e.g. Kent, 1988; Kormendy & Westpfahl, 1989; Bertola et al., 1995; Cinzano et al., 1999; Corsini et al., 1999; Cretton, Rix & de Zeeuw, 2000; Vega Beltrán et al., 2001; Pizzella et al., 2004; Krajnović et al., 2005; Weijmans et al., 2008; Young, Bureau & Cappellari, 2008; Puglielli, Widrow & Courteau, 2010). This puzzle is made more acute by the small velocity dispersions observed in the

emission line PVDs. We will return to the gas dispersion in a future work.

A definitive resolution of this issue is outside the scope of the present work and, fortunately, it is unnecessary for our goals. For the purposes of comparing TFRs (or for determining relative distances; see e.g. Courtois et al. 2009), it does not matter which measure is 'right', as long as we use the same measure for the two samples and the measure chosen does not introduce a systematic bias between samples. We see no evidence of this in our data, for any of the four measures explored.

Our conclusions in this section have three consequences for previous works that measure the TFR of S0 galaxies using stellar kinematics corrected for asymmetric drift (e.g. Neistein et al., 1999; Hinz, Rix & Bernstein, 2001; Hinz, Rieke & Caldwell, 2003, BAM06): (i) the asymmetric drift correction they use yields similar results to detailed Jeans modelling; (ii) the drift correction does not seem to introduce a systematic bias between spirals and S0s and, if applied to samples of both spirals and S0s, can indeed be used to compare the TFRs of the two classes; (iii) however, a TFR derived from asymmetric drift-corrected stellar kinematics can*not* be directly compared to TFRs derived from global H I line widths or resolved emission line PVDs, as these previous authors did. As we argue above, such comparisons are not a priori justified and, in the case of both our sample and the larger sample of BAM06, they appear to introduce systematic errors that, on a Tully-Fisher plot, are of the same order (and in the same direction) as the TFR offsets that are usually interpreted as luminosity evolution. The conclusions of previous works regarding the offset of the S0 TFR should therefore be treated with caution. In addition, given the large scatter we observe in $\log(v_{\rm H\,I}/v_{\rm model})$ and $\log(v_{\rm H\,I}/v_{\rm drift})$, it is far from clear that any simple additive or multiplicative correction could eliminate the bias.

For our sample, we are able to side-step this issue completely by using a single measure of rotation for both spirals and S0s. In this way we compare the TFRs of S0, Sa and Sb galaxies in a manner which is not subject to the possible systematics discussed above. We adopt $v_{\rm model}$ as our fiducial measure of rotation for *both* spirals *and* S0s. The figures and discussion that follow use only this measure.

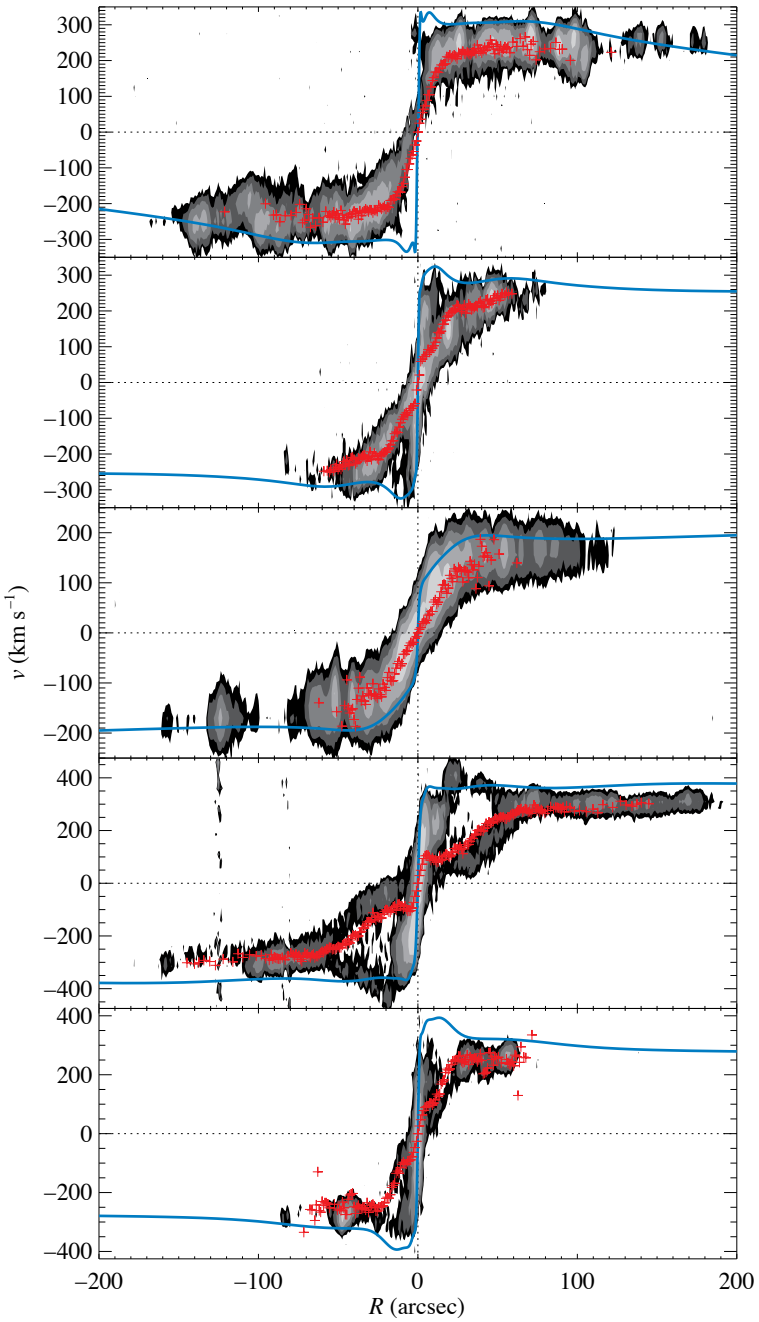

Figure 3.3: Comparisons of [N II] λ6584 position–velocity diagrams, stellar kinematics, and the circular velocity implied by Jeans modelling for the five galaxies in the sample with optical emission that extends to the disk. From top to bottom: ESO 240-G011, IC 5096, IC 5176, NGC 5746 and NGC 6722. The filled contours are the continuum-subtracted optical spectra originally presented in Bureau & Freeman (1999). The observed mean stellar velocities (Chung & Bureau, 2004) and the circular velocity profiles inferred from detailed Jeans modelling of the light distribution and stellar kinematics (WBC09) are overplotted as red crosses and blue lines respectively.

3.3 SAMPLE AND DATA

To make the reliable comparison we described in the previous section, we use the sample of 14 early-type spirals (Sa and Sb) and 14 S0s presented in Table 3.1. Dynamical models of these galaxies were constructed in WBC09. All of the galaxies are oriented close to edge-on (within $\approx 5^{\circ}$). Many of the galaxies have boxy bulges, which are believed to be bars viewed side-on (e.g. Kuijken & Merrifield, 1995; Merrifield & Kuijken, 1999; Bureau & Freeman, 1999; Chung & Bureau, 2004), and it was to probe these bulges that the sample was constructed and observed. The bars should not, however, affect the results we present here because we use measures of rotational velocity well outside the boxy bulge region. The fraction of galaxies with boxy bulges in the sample ($\approx$ 75 per cent) is not in any case significantly different to the fraction of barred galaxies in the local universe ($\approx$ 65 per cent; see, e.g. Eskridge et al., 2000; Whyte et al., 2002; Marinova & Jogee, 2007).

The sample was selected without regard for environment, and so includes galaxies in a wide range of environments. Two S0s are members of the Virgo cluster, an S0 and a spiral are members of the Hydra cluster, and an S0 is a member of the Fornax cluster. Cross-referencing our sample with the 2MASS Redshift Survey (2MRS) Group Catalog (Crook et al., 2007) demonstrates that the remainder of the sample is made up of members of intermediate-size groups and relatively isolated galaxies.

All the galaxies are relatively bright and fast-rotating, and the spirals and S0s cover the same range of luminosities. This means that we are not vulnerable to variation in the slope of the TFR at the low or high mass end, as has been observed (e.g. Peletier & Willner, 1993; Noordermeer & Verheijen, 2007). We further note that the sample contains some very bright S0s, such as ESO 151-G004 and NGC 6771, that have large boxy bulges. If these bulges are in fact bars, and therefore the products of secular evolution, then these particular bright S0s are unlikely to be the elliptical-like products of major mergers, as has previously been suggested (Poggianti et al., 2001; Mehlert et al., 2003; Bedregal et al., 2008; Barway et al., 2009).

Table 3.1: Tully-Fisher relation sample

Galaxy	M_{K_s} (mag)	M_B (mag)	$\log(M_\star/M_\odot)$	$\log(M_{\rm dyn}/M_\odot)$	$R_{\rm d}$ (arcsec)	$v_{\rm model}$ (km s^{-1})	$v_{\rm drift}$ (km s^{-1})	$v_{\rm H\,I}$ (km s^{-1})	$v_{\rm gas}$ (km s^{-1})	2MRS LDC group size	Cluster
(1)	(2)	(3)	(4)	(5)	(6)	(7)	(8)	(9)	(10)	(11)	(12)
					S0						
ESO 151-G004	−24.85	−20.41	11.40	11.46	8.2	301	311	...	...	[a]	
ESO 311-G012	−23.06	−19.92	10.45	10.53	28.3	196	192	96	...	...	
ESO 597-G036	−25.36	−20.70	11.58	11.73	14.4	345	365	...	...	3	
NGC 128	−25.35	−21.40	11.47	11.56	16.7	369	379	...	...	...	
NGC 1032	−24.47	−20.71	11.13	11.22	33.0	281	...	284	254	...	
NGC 1381	−22.76	−18.77	10.49	10.59	12.3	208	220	...	...	43	Fornax
NGC 1596	−22.86	−18.98	10.56	10.66	20.5	247	249	98	...	30	
NGC 2310	−22.48	−19.43	10.25	10.48	25.2	171	173	...	...	...	
NGC 3203	−23.89	−19.99	10.76	10.94	16.3	222	228	...	...	210	Hydra
NGC 3957	−23.29	−19.20	10.76	10.85	19.1	213	213	...	178	13	
NGC 4469	−23.01	−19.02	10.56	10.68	16.5	180	199	...	...	300	Virgo
NGC 4710	−23.47	−19.40	10.56	10.68	23.6	187	199	160	140	300	Virgo
NGC 5084	−24.73	−21.85	11.16	11.22	34.7	303	306	310	...	15	
NGC 6771	−25.08	−20.81	11.40	11.46	16.2	337	337	...	284	97	
					Sa–Sb						
ESO 185-G053	−24.22	−20.09	11.01	11.06	5.0	244	267	...	...	42	
ESO 240-G011	−24.79	−21.56	11.56	11.57	35.7	305	306	268	243	3	
ESO 443-G042	−23.49	−20.21	10.76	10.90	11.4	190	...	166	...	38	
IC 4767	−23.69	−19.72	10.93	10.97	8.2	195	219	...	...	97	
IC 4937	−24.67	−20.46	11.18	11.24	18.7	208	210	...	...	3	
IC 5096	−24.93	−21.21	11.27	11.36	14.5	290	300	262	244	5	
IC 5176	−23.31	−19.95	10.60	10.72	20.9	194	217	164	150	...	
NGC 1886	−22.90	−19.73	10.47	10.63	14.5	178	192	155	...	...	
NGC 3390	−24.90	−21.49	11.19	11.27	20.4	257	279	210	229	210	Hydra
NGC 4703	−25.43	−20.92	11.38	11.49	29.2	269	272	246	229	80	
NGC 5746	−25.64	−22.30	11.63	11.75	69.1	365	393	319	295	45	

continued ...

Table 3.1: — continued

Galaxy	M_{K_S} (mag)	M_B (mag)	$\log(M_\star/M_\odot)$	$\log(M_{\rm dyn}/M_\odot)$	$R_{\rm d}$ (arcsec)	$v_{\rm model}$ (km s^{-1})	$v_{\rm drift}$ (km s^{-1})	$v_{\rm H\,I}$ (km s^{-1})	$v_{\rm gas}$ (km s^{-1})	2MRS LDC group size	Cluster
(1)	(2)	(3)	(4)	(5)	(6)	(7)	(8)	(9)	(10)	(11)	(12)
NGC 6722	−25.38	−21.97	11.49	11.60	12.5	323	322	...	263	97	
NGC 7123	−25.29	−20.81	11.35	11.40	19.2	327	335	...	...	...	
PGC 44931	−24.46	−21.33	11.07	11.27	21.1	242	225	200	180	80	

Notes. Sample divided into S0s and spirals based on classifications of Jarvis (1986), de Souza & Dos Anjos (1987), Shaw (1987) and Karachentsev, Karachentseva & Parnovskij (1993). (1) Galaxy name. (2)–(3) Total K_S-band and B-band absolute magnitude. (4)–(5) Total stellar and dynamical mass. (6) Disk scale length measured using K_S-band images presented in Bureau et al. (2006). (7) Circular velocity derived from the best-fit mass model presented in WBC09. (8) Rotational velocity derived from the observed stellar kinematics presented in Chung & Bureau (2004), corrected for line-of-sight effects and asymmetric drift. Missing values are cases where the drift correction was too large to be considered reliable. (9) Rotational velocity derived from the global H I line width, i.e. the quantity `vrot` from HYPERLEDA where available. (10) Ionized gas rotational velocity measured by a Gaussian fit to [N II] position-velocity diagrams presented in Bureau & Freeman (1999). (11) Number of companion group members in the Low Density Contrast 2MRS Group Catalog (Crook et al., 2007). Ellipses indicate that a galaxy was not found in the catalog, implying that it had 2 or fewer nearby companions. ([a]) ESO 151-G004 is not present in the 2MASS Extended Source Catalog (Jarrett et al., 2000) and so is not included in the 2MRS database. (12) Cluster membership. For full details of how the quantities in Columns (2)–(10) were determined, see Section 3.2.2 and Section 3.3.

In Fig. 3.4 we present the spiral and S0 TFRs as functions of K_S-band luminosity, B-band luminosity, stellar mass and dynamical mass, all discussed below. Throughout this work we assume an absolute solar magnitude $M_{Ks,\odot} = 3.29\,\mathrm{mag}$ (Blanton & Roweis, 2007).

Firstly, all the vertical axes in Fig. 3.4 require a distance estimate for each galaxy. As described in WBC09, we use surface brightness fluctuation (SBF) estimates where available (NGC 1381 from Jensen et al. 2003 and NGC 1596 from Tonry et al. 2001) and the Virgo cluster distance where appropriate (NGC 4469 and NGC 4710, Mei et al. 2007). For all other galaxies we adopt the redshift distance presented in the NASA/IPAC Extragalactic Database, corrected for a Virgocentric flow model (Mould et al., 2000). We assume a *Wilkinson Microwave Anisotropy Probe* five-year (WMAP5) cosmology ($H_0 = 70\,\mathrm{km\,s^{-1}\,Mpc^{-1}}$, Komatsu et al. 2009). Of course, we avoid distance estimates derived from TFRs.

The total apparent magnitude at K_S-band is measured using the analytically derived total light in the multi-Gaussian expansions (Emsellem, Monnet & Bacon, 1994; Cappellari, 2002) of our near-infrared images, as described and tabulated in WBC09. The total apparent magnitude at B-band is taken from HYPERLEDA (Paturel et al., 2003). We apply corrections for Galactic (A_G) and internal (A_i) extinction in both bands using the Galactic dust maps of Schlegel, Finkbeiner & Davis (1998) and the internal extinction correction presented in Bottinelli et al. (1995), as tabulated in HYPERLEDA (Paturel et al., 2003), both of which we transform to the appropriate bands using the extinction law of Cardelli, Clayton & Mathis (1989), implying that $A_\mathrm{G}(K_S)/A_G(B) = A_\mathrm{i}(K_S)/A_\mathrm{i}(B) = 0.084$. The internal extinction correction is a function of both bulge-to-disk ratio and morphological type. This correction is $\lesssim 0.1\,\mathrm{mag}$ at K_S-band for our spirals and smaller still for the S0s.

With the exception of the Virgo galaxies and the two galaxies with SBF distances, we adopt characteristic distance errors corresponding to a $200\,\mathrm{km\,s^{-1}}$ uncertainty in the flow model (e.g. Tonry et al., 2000), and 0.05 mag uncertainties in the apparent magnitudes. These uncertainties completely overwhelm any error in the Galactic or internal extinction at K_S-band. At B-band, we adopt uncertainties of 0.16 mag in Galactic extinction (Schlegel, Finkbeiner & Davis, 1998) and 0.1 mag in the internal

extinction. We emphasize, however, that internal extinction corrections in edge-on spiral galaxies are both large and uncertain. The *B*-band TFR is problematic with even favourably inclined spirals, but with our edge-on sample the internal extinction correction and its uncertainties may introduce significant systematic errors. The *B*-band data are therefore included in this work merely to aid comparison with previous work, and we do not make use of these results in our interpretation.

The stellar mass, $M_\star$, is derived from the total absolute K_S-band luminosity and the constant stellar mass-to-light ratio, $(M/L)_{K_S}$, of each galaxy determined in WBC09. As described in Section 3.2.2, this uses dynamical methods that make assumptions about the dark halo and stellar dynamics, but are not vulnerable to zero-point or colour-dependent uncertainties due to the initial mass function or stellar evolution.

The dynamical mass, $M_{\rm dyn}$, is estimated using the total absolute K_S-band luminosity and the *dynamical* mass-to-light ratio at K_S-band for each galaxy, also determined in WBC09 in which it is referred to as $(M/L)_{K_S,\rm nohalo}$. Unless there is no dark matter (or its distribution closely follows that of the luminous matter), the dynamical (M/L) ratio is likely to be a quantity that varies significantly within a galaxy, increasing toward the edge of the optical disk where dark matter normally begins to dominate. The value we use is, however, effectively an average for each galaxy within the radii constrained by the stellar kinematic data, typically 2-3 $R_{\rm eff}$ (where $R_{\rm eff}$is the projected K_S-band half-light radius), but dominated by the central regions. Because of this, $M_{\rm dyn}$ is a somewhat ill-defined quantity.

An alternative approach would be to adopt the mass within the three-dimensional half-light volume, $M_{1/2}$. We show how this can be evaluated from observations or models of the circular velocity in disk galaxies in Appendix 3.A. We also show there that, in practice, $2M_{1/2} = M_{\rm dyn}$ to within 13 per cent. Neither choice is optimal but in the context of the present work, we can think of no reason why one choice or the other would introduce systematic biases that vary between spirals and S0s. The choice is therefore somewhat arbitrary and has no affect on the discussion of the relationship between spirals and S0s that follows where we use $M_{\rm dyn}$. This choice follows precedent (it is the definition used by, e.g., Magorrian et al. 1998, Häring & Rix 2004 and Cappellari et al. 2006) and avoids the possible concern that the argument

Figure 3.4: Tully-Fisher relations for our samples of S0 and spiral galaxies. From top to bottom, as a function of v_{model}: total absolute K_S-band luminosity, total absolute B-band luminosity, total stellar mass and total dynamical mass. Spiral galaxies are shown as blue triangles and S0 galaxies as red circles. A median error bar is shown in the top left corner of each plot. The best fit relations found by inverse regression are shown as solid lines (blue for spirals, red for S0s). Their parameters are given in Table 3.2. The dashed, dotted and dot-dashed lines are a selection of TFRs found by previous authors for different morphological types. See text for a full discussion of these relations.

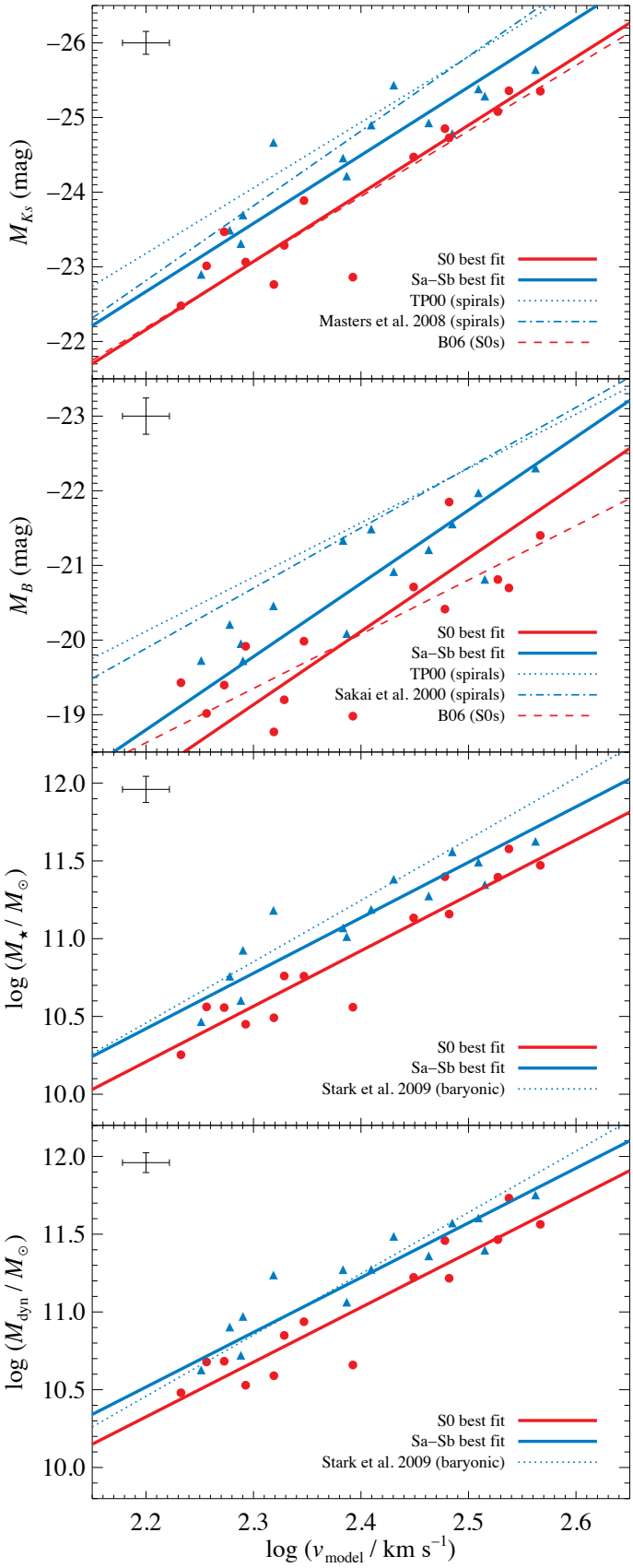
M_{K_S} (mag)
S0 best fit
Sa–Sb best fit
TP00 (spirals)
Masters et al. 2008 (spirals)
B06 (S0s)
M_B (mag)
Sakai et al. 2000 (spirals)
log ($M_\star$ / $M_\odot$)
Stark et al. 2009 (baryonic)
log (M_{dyn} / $M_\odot$)
log (v_{model} / km s^{-1})

we present in Section 3.5.2 is circular, but we emphasize that $M_{1/2}$ gives the same results and is a better defined quantity.

For reference, we show in Fig. 3.4 the spiral TFRs determined using global H I line widths at K-band by TP00, at K_S-band by Masters, Springob & Huchra (2008) and at B-band by TP00 and Sakai et al. (2000). We do this assuming that the global H I line width, once corrected for inclination, broadening and turbulent motion, is exactly twice the rotational velocity. The zero points of the TP00 and Sakai et al. (2000) TFRs were determined using known Cepheid distances to 4 galaxies in the case of TP00 at K-band (1 Sab, 2 Sb and 1 Sc; see the companion paper by Rothberg et al. 2000), 24 galaxies for TP00 at B-band (3 Sab, 14 Sb – Sc and 7 Scd – Sd) and 21 galaxies for Sakai et al. (2000) (3 Sa – Sab, 16 Sb – Sc and 2 Scd). We position the Masters, Springob & Huchra (2008) K_S-band TFR on our plots using our adopted value of H_0. The difference between the two K-band and two B-band relations gives an idea of the uncertainty in the absolute location of the late-type spiral TFR (the difference between the K-band filter used by TP00 and the 2MASS K_S-band filter is not significant in this context). These comparison spiral TFRs are unconstrained by observations above $\log(v/\mathrm{km\ s^{-1}}) \approx 2.45$, while a third of our sample is above this value.

Unlike BAM06, we do not shift the zero-points of the TP00 TFRs by -0.207 mag. BAM06 did this to make the value of H_0 implied by TP00's data ($77 \pm 8\,\mathrm{km\,s^{-1}\,Mpc^{-1}}$) consistent with their adopted value ($70\,\mathrm{km\,s^{-1}\,Mpc^{-1}}$). However, we believe that this correction was in error, since the absolute locations of the TP00 TFRs were set by independent Cepheid distances, which imply rather than assume a particular value of H_0.

We also show an extrapolation to high mass systems of the baryonic TFR presented in Stark, McGaugh & Swaters (2009), which was calibrated using gas-dominated dwarf galaxies (hence minimizing uncertainties associated with the stellar mass-to-light ratio). Neither of our mass estimates $M_\star$ or $M_{\rm dyn}$ are designed to reproduce the baryonic mass $M_{\rm bar}$ used by Stark, McGaugh & Swaters (2009). In practice, however, one expects $M_\star \approx M_{\rm bar}$ to within a few per cent for gas-poor S0s and to within perhaps ten per cent for giant Sa–Sb spirals, while $M_{\rm dyn} \approx M_{\rm bar}$ to within a factor of 2 for both S0s and spirals (dark matter is no more than 50 per cent of the mass within the

optical radius of disk galaxies, e.g. van Albada & Sancisi 1986; Persic, Salucci & Stel 1996; Palunas & Williams 2000; Cappellari et al. 2006; Kassin, de Jong & Weiner 2006, WBC09). The comparison of our stellar and dynamical mass TFRs to the baryonic TFR is therefore meaningful, and we note that the Stark, McGaugh & Swaters (2009) TFR is broadly consistent with our spirals. The good agreement gives us confidence in our mass models.

It is crucial to emphasize that at no point in our analysis do we do anything that might systematically affect the S0s in the sample differently to the spirals. One slight but unavoidable observational bias may be introduced by the presence of dust along the major axes. If the slit is placed exactly on the major axis, then absorption by dust may make it impossible to recover the full line-of-sight velocity distributions (LOSVDs). Depending on the optical thickness, this may truncate the low velocity wing or, in very dusty disks, the high velocity peak of the LOSVDs. When Gaussians are fitted to these distribution (Chung & Bureau, 2004), this could therefore increase or, perhaps more likely, decrease the derived line-of-sight velocities. This effect would propagate into the rotation curves from which $v_{\rm model}$ and $v_{\rm drift}$ are derived, and also into the mass-to-light ratios inferred in WBC09, from which $M_\star$ and $M_{\rm dyn}$ are derived. However, in cases where the dust absorption was strong, the slit was simply shifted from the major axis by ≈ 2 arcsec to ensure the full LOSVD was sampled, and the objects with strong dust lanes were selected to be very slightly away from perfectly edge-on (Bureau & Freeman, 1999).

If the rotational velocity is a strong function of z, the height above the equatorial plane in the cylindrical coordinate system of the galaxy (R, ϕ, z), this intentional shift could itself bias the velocities and inferred masses in dustier galaxies (i.e. spirals). In Chapter 4 we present pseudo-integral-field data (i.e. a sparse velocity fields constructed from multiple long-slit positions) for six of the galaxies in the present sample. In these data we see no evidence that $\mathrm{d}\,v/\mathrm{d}\,|z| \neq 0$ in the disks of five of the galaxies. At most, there is a gradient of $-30\,\mathrm{km\,s^{-1}\,kpc^{-1}}$ in the disk of NGC 7123. This is broadly consistent with observations of planetary nebulae in the edge-on spiral NGC 891 (Merrifield et al., 2010) and of extraplanar gas (e.g. NGC 891, Heald et al. 2007, Oosterloo, Fraternali & Sancisi 2007; NGC 4302 and NGC 5775, Heald et al. 2007;

the Milky Way, Levine, Heiles & Blitz 2008), which find a typical falloff in rotation $\mathrm{d}v/\mathrm{d}|z| \approx -20\,\mathrm{km\,s^{-1}\,kpc^{-1}}$. In the worst case scenario, in which all our spirals (and none of the S0s) suffered from absorption strong enough to require shifting the slit, the spiral velocities would typically be biased by $\lesssim -0.02\,\mathrm{dex}$. We estimate that the overall effect on our sample of spirals, most of which did not require this slit shift, may be to bias their velocities by up to $\approx -0.01\,\mathrm{dex}$. In practice, the slit was 1.8 arcsec wide and rather difficult to align precisely for both spirals and S0s. This imprecision, which introduces velocity scatter in both samples, likely overwhelms any systematic velocity falloff in the spirals due to intentionally shifting the slit.

3.4 FITTING PROCEDURE

For each measure of luminosity or mass as a function of $x = \log(v_{\mathrm{model}}/\mathrm{km\ s^{-1}})$, we simultaneously fit a straight line of the form $y = a(x - 2.4) + b$ to the spiral galaxies and $y = a(x - 2.4) + b + \delta$ to the S0s. The two straight lines are therefore constrained to have the same slope, a, but they have zero-points which differ by δ. In separate fits to the two samples, we find that their slopes are consistent within the uncertainties. Constraining them to be equal therefore significantly simplifies the interpretation of our results in terms of zero-point evolution. The $x = 2.4$ reference value is defined to minimize the covariance between errors in a and b (e.g. Tremaine et al., 2002). Its choice does not affect the results of this work, in which were are mainly interested in the zero point offset δ.

To find the optimal combination of a, b and δ for a given scatter, we define and minimize the figure of merit

$$\begin{aligned}\chi^2 \equiv & \sum_{i=0}^{N_{\mathrm{Sa\,Sb}}} \frac{1}{\sigma_i^2}\{y_i - [a(x_i - 2.4) + b]\}^2 \\ & + \sum_{i=0}^{N_{\mathrm{S0}}} \frac{1}{\sigma_i^2}\{y_i - [a(x_i - 2.4) + b + \delta]\}^2,\end{aligned} \tag{3.3}$$

where $N_{\mathrm{Sa\,Sb}}$ is the number of spirals, N_{S0} the number of S0s and

$$\sigma_i^2 \equiv \sigma_{y,i}^2 + a^2\sigma_{x,i}^2 + \sigma_{\mathrm{int}}^2. \tag{3.4}$$

The extra scatter $\sigma_{\rm int}$ is iteratively adjusted to ensure that

$$\chi^2_{\rm red} \equiv \frac{\chi^2}{(N_{\rm Sa,Sb} + N_{\rm S0} - 3)} \approx 1. \tag{3.5}$$

If the observational errors for each galaxy $\sigma_{x,i}$ and $\sigma_{y,i}$ are well-estimated then $\sigma_{\rm int}$ is the intrinsic, astrophysical scatter in the TFR.

We also define a total rms scatter $\sigma_{\rm tot}$, essentially a weighted mean of the scatter of the data about the fits (and therefore in the same units as the y-axis):

$$\begin{aligned}\sigma^2_{\rm tot} \equiv & \left(\sum_{i=0}^{N_{\rm Sa\,Sb}} \frac{1}{\sigma_i^2}\{y_i - [a(x_i - 2.4) + b]\}^2 \right. \\ & \left. + \sum_{i=0}^{N_{\rm S0}} \frac{1}{\sigma_i^2}\{y_i - [a(x_i - 2.4) + b + \delta]\}^2 \right) \Bigg/ \sum_{i=0}^{N_{\rm gal}} \frac{1}{\sigma_i^2}\end{aligned} \tag{3.6}$$

$$= \frac{\chi^2}{\sum_{i=0}^{N_{\rm gal}} 1/\sigma_i^2}, \tag{3.7}$$

where $N_{\rm gal}$ is the total number of both spiral and S0 galaxies. Comparing $\sigma_{\rm tot}$ with $\sigma_{\rm int}$ gives an idea of what fraction of the scatter is intrinsic and what fraction is due to measurement errors. We minimize equation (3.3) using the MPFIT package (Markwardt, 2008).

Following previous analyses of the Tully-Fisher relation, we also fit the 'inverse' relation, i.e. we regress the observed rotational velocities rather than the luminosities or masses onto the model (see, e.g., TP00, Verheijen 2001, Pizagno et al. 2007 and references therein). We rewrite the spiral and S0 straight lines as $x = Ay + B + 2.4$ and $x = Ay + B + 2.4 + \Delta$ and minimize

$$\begin{aligned}\chi^2_{\rm inv} \equiv & \sum_{i=0}^{N_{\rm Sa\,Sb}} \frac{1}{\varsigma_i^2}[x_i - (Ay_i + B + 2.4)]^2 \\ & + \sum_{i=0}^{N_{\rm S0}} \frac{1}{\varsigma_i^2}[x_i - (Ay_i + B + \Delta + 2.4)]^2,\end{aligned} \tag{3.8}$$

where

$$\varsigma_i^2 = \sigma_{x,i}^2 + A^2\sigma_{y,i}^2 + \varsigma_{\rm int}^2 \tag{3.9}$$

and

$$\varsigma^2_{\rm tot} = \frac{\chi^2_{\rm inv}}{\sum_{i=0}^{N_{\rm gal}} 1/\varsigma_i^2}. \tag{3.10}$$

To compare these values to those determined using the forward relation, we use the fact that a best-fitting inverse relation has an equivalent forward slope $1/A$, zero-point $-B/A$, offset $-\Delta/A$ and y-axis intrinsic and total scatters $A\varsigma_{\rm int}$ and $A\varsigma_{\rm tot}$. Our implementation of the fitting procedure described above is publicly available[1].

Forward and inverse fitting is only symmetric if there is no intrinsic scatter ($\sigma_{\rm int} = \varsigma_{\rm int} = 0$) (Tremaine et al., 2002). This is not generally the case and the slopes can be very different. In analyses of the TFR with observed data, it has been shown that there is a significant bias in the slope of the forward line of best fit (Willick, 1994), which is why the inverse relationship is usually preferred. The figures in this paper use this inverse fitting approach, but to aid comparison with future work, we present both forward and inverse fits in Table 3.2. The slopes of the forward and inverse fits to our data are indeed discrepant, often to the extent that they do not lie within each other's error bars (especially at B-band). We are fortunate, however, that the choice of whether to use the forward or inverse relationship does not affect our conclusions, which depend entirely on the zero-point offset of the S0 TFR and the total scatter.

3.5 DISCUSSION

3.5.1 *The TFR zero-point offset at K_S-band and B-band*

While the TFR zero point and offset are formally sensitive to the choice between forward or inverse regression, in practice they are almost unchanged by this choice. In the discussion that follows, we adopt the means of the forward and inverse values and their errors.

We detect a statistically significant difference between the zero-points of the TFRs of spiral and S0 galaxies (see Table 3.2). At a given $v_{\rm model}$, local S0s are 0.53 ± 0.15 mag fainter at K_S-band and 0.68 ± 0.22 mag fainter at B-band than local spirals. The systematic uncertainty is due to the slit positioning issue described at the end of Section 3.3. We emphasize again that the B-band offset we measure is dubious

[1] `http://purl.org/mike/mpfitexy`

Table 3.2: Parameters of the best fitting TFRs

y	a	b	δ	$\sigma_{\rm int}$	$\sigma_{\rm tot}$
		Forward regression			
M_{K_S}	-8.15 ± 0.76	-24.53 ± 0.11	0.55 ± 0.15	0.27	0.37
M_B	-7.67 ± 1.02	-20.82 ± 0.14	0.73 ± 0.20	0.39	0.50
$\log(M_\star/M_\odot)$	3.45 ± 0.26	11.14 ± 0.04	-0.22 ± 0.05	0.06	0.13
$\log(M_{\rm dyn}/M_\odot)$	3.34 ± 0.27	11.23 ± 0.04	-0.20 ± 0.05	0.07	0.13
		Inverse regression			
M_{K_S}	-9.13 ± 0.87	-24.49 ± 0.12	0.51 ± 0.16	0.28	0.39
M_B	-9.81 ± 1.26	-20.76 ± 0.16	0.64 ± 0.23	0.44	0.56
$\log(M_\star/M_\odot)$	3.57 ± 0.27	11.13 ± 0.04	-0.21 ± 0.05	0.06	0.13
$\log(M_{\rm dyn}/M_\odot)$	3.52 ± 0.28	11.22 ± 0.04	-0.19 ± 0.05	0.08	0.13

Notes. $x = \log(v_{\rm model}/{\rm km\,s^{-1}})$, $y = a(x-2.4)+b$ for spirals and $y = a(x-2.4)+b+\delta$ for S0s. $\sigma_{\rm int}$ is the intrinsic scatter required to yield $\chi_{\rm red} = 1.00 \pm 0.01$ and $\sigma_{\rm tot}$ is the total scatter (see equation 3.6). a is in units of y/x, all other quantities are in units of y, i.e. magnitudes or dex of solar masses.

because of the very uncertain (and very large) internal extinction corrections at optical wavelengths in edge-on spirals. The K_S-band value is, however, robust.

We estimate that the intentional misalignment of the slit in the dustiest galaxies may introduce a bias of up to ≈ -0.01 dex in the observed velocities of spirals (see the end of Section 3.3). In principle, this may bias our measurement of the K_S-band offset to be too large by ≈ 0.07 mag. This is less than uncertainty in the intercept of the spiral TFR (±0.10 mag) or the offset of S0 TFR (±0.15 mag), so we do not discuss it further.

We restate that our fiducial TFRs use $v_{\rm model}$ as the measure of rotation. We emphasize, however, that the *offsets* we measure between the spiral and S0 TFRs are completely insensitive to this choice. Using $v_{\rm drift}$, there is an offset at K_S-band of 0.45 ± 0.18 mag. Using $v_{\rm gas}$, there is an offset of 0.48 ± 0.24 mag. Unless all three of these measures of rotation are flawed then our principal result, the measurement of the offset of the S0 TFR, is reliable. (We neglect $v_{\rm H\,I}$ because it is based on spatially unresolved data and sometimes unphysically discrepant from the other measures of rotation. See Section 3.2.3.)

Since high redshift spirals are thought to be the progenitors of local S0s, we

would really like to compare our local S0 TFR to the high redshift spiral TFR. As we emphasize in Section 3.2, however, the comparison of TFRs derived using different measures of rotation is uncertain at best, so the zero-points of high-redshift TFRs cannot be compared to our local results in a meaningful way. In addition to the uncertainties in comparing the velocities of different tracers in the local universe, the move to high-z raises the possibility that the intrinsic *shapes* of rotation curves have changed, which we cannot rule out. Provided, however, that these differences have been correctly accounted for by other authors, the relative shifts between the local and high-z TFRs should be fairly insensitive to the measure of rotation used. We therefore make that unavoidable assumption in order to proceed.

Conselice et al. (2005), Flores et al. (2006) and Kassin et al. (2007) find no evidence for evolution in either the slope or zero-point of the K-band spiral TFR from the local universe to $z \approx 1$. However, Puech et al. (2008) detect a dimming of 0.66 mag at K_S-band from $z = 0$ to $z \approx 0.6$. We first discuss the possibility that the spiral TFR has not evolved with redshift. If this is correct, our results imply that local S0s are 0.53 ± 0.15 mag fainter at K_S-band for a given rotational velocity than their presumed spiral progenitors.

To get a feeling for how long such a fading would take, we follow BAM06 by using the Bruzual & Charlot (2003) stellar population synthesis code to assign an approximate timescale to such a fading under various star formation scenarios. We assume solar metallicity and a Chabrier initial mass function (Chabrier, 2003) and use an updated prescription for the thermally-pulsing asymptotic giant branch (Marigo & Girardi 2007; Charlot 2009, private communication). Following a constant star formation episode lasting 5 Gyr, the synthetic stellar population takes $0.9^{+0.4}_{-0.5}$ Gyr to fade by 0.53 ± 0.15 mag at K_S-band and $0.2^{+0.2}_{-0.1}$ Gyr to fade by 0.67 ± 0.21 mag at B-band. If we add an instantaneous 'last gasp' burst of star formation comprising 10% of the mass of the galaxy at the end of the 5 Gyr episode (Bedregal et al., 2008), the timescales increase to $1.4^{+0.4}_{-0.2}$ Gyr at K_S-band and $0.5^{+0.2}_{-0.1}$ Gyr at B-band.

For plausible star formation histories, the timescales implied by the offsets at the two wavelengths are inconsistent. This is perhaps not surprising given the uncertainty in the dust corrections at B-band. However, the K_S-band offset is far less susceptible

to this possible systematic error, and this measurement implies an uncomfortably short timescale since the truncation of star formation of $\lesssim 1.4\,\mathrm{Gyr}$, corresponding to a redshift $z \approx 0.1$. As noted by BAM06, it would be a surprising coincidence if we were living in an era so soon after the S0s in our sample transformed from spirals. Observationally, this possibility appears to be ruled out by high-redshift observations: while Dressler et al. (1997) show that the S0 fraction has risen at the expense of spirals since $z \approx 0.5$ (5 Gyr ago), Fasano et al. (2000) find that the present relative fraction of S0s and spirals was largely already in place in clusters at $z \approx 0.2$ (2.5 Gyr ago) and there was no shortage of S0s in groups at $z \approx 0.4$ (4 Gyr ago, Wilman et al. 2009). In the absence of strong environmental processes, we naively expect the transformation of field spirals to S0s to be gradual, and therefore that present day field S0s would need to have begun their transformation even earlier. We therefore conclude that a simple scenario of passive fading of spirals into S0s is inconsistent with the TFRs of our sample and the evolution of the S0/spiral fraction with redshift. This interpretation of the offset of the S0 TFR is consistent with that of Neistein et al. (1999). With limited data they measured a very similar S0 TFR offset to us, but with much larger uncertainties, and with respect to a line width-based TFR (a comparison we argue is flawed in Section 3.2).

We now discuss the possibility that the zero-point of the TFR was fainter at earlier times. If the *K*-band spiral TFR has evolved with redshift and was, for example, 0.66 mag fainter at $z \approx 0.6$ than the local relation (as found by Puech et al. 2008), then present-day S0s are approximately as luminous at a given rotational velocity as spirals were 6 Gyr ago, i.e. there is no evidence for any evolution in the velocity–luminosity plane between local S0s and their presumed high redshift progenitors. A simple star formation truncation scenario is then even harder to reconcile with our results.

The above analysis is based on the assumption that an S0 of a given rotational velocity used to have the luminosity of a high-redshift spiral of the same rotational velocity. From this assumption we have gone on to consider in isolation the evolution of a single broadband colour. The parameter space of possible star formation histories is, however, highly degenerate and this is far from the ideal way to constrain star formation histories. It is nevertheless clear from our sample that something other than

simple fading beginning at the redshifts at which S0s are first observed (and without subsequent star formation), is transforming spirals to S0s. The evidence for recent (and even ongoing) star formation in local S0s from UV (Kaviraj et al., 2007; Jeong et al., 2009) and mid-infrared (Temi, Brighenti & Mathews, 2009a,b; Shapiro et al., 2010) observations is in fact strong.

3.5.2 *Stellar and dynamical mass*

We also detect a significant difference between the zero points of the S0 and spiral stellar mass TFRs. The S0s have around 0.2 dex less stellar mass for a given rotational velocity than the spirals. Because of the relative gas richness of spirals, the offset in the baryonic relation (i.e. stellar mass + gas mass, e.g. McGaugh et al., 2000) is likely larger and certainly no smaller. Assuming that $v_{\rm model}$ traces the enclosed dynamical mass equally well for S0s and spirals, this might naively suggest that S0s have less stellar mass per dynamical mass within 2–3 $R_{\rm eff}$ (the extent of our kinematic data), and therefore contain fractionally more dark matter than spirals. This is generally consistent with the idea that S0s are older systems that are found in denser environments at the bottom of deeper potential wells. If this is indeed the case, using dynamical rather than stellar mass should eliminate the offset. The dynamical mass TFR is essentially a plot of a one measure of dynamical mass (from a mass model) against another (the observed rotational velocity), and since gravity applies equally to spirals and S0s there should be no difference.

Having said that, the difference between the spiral and S0 zero points persists almost unchanged in the dynamical mass TFR (see Table 3.2). Our dynamical modelling approach does necessarily make approximations and assumptions, but it is unlikely that the models could be systematically biased by morphological type. Our stellar and dynamical mass spiral TFRs are also consistent with the reliably calibrated baryonic TFR of Stark, McGaugh & Swaters (2009). This raises the possibility that S0s are systematically smaller or more concentrated than spirals. Recall that $M_{\rm dyn} \propto v^2 R$, where R is some characteristic radius. If R is systematically smaller in S0s at a given

rotational velocity, or if the dynamical mass is more concentrated such that more mass is enclosed within a given characteristic radius, then that could explain the offset in the dynamical mass TFR. In other words, spirals and S0s do not form a homologous family. In this scenario, the offset of the S0 dynamical mass TFR should not be thought of as a -0.18 dex offset in mass (as presented in Table 3.2), but, because of the slope of the TFR, a $+0.05$ dex offset in velocity. This could be due either to S0s being approximately 80% of the size of spirals of the same rotational velocity, or their dynamical mass being distributed more compactly such that the characteristic radius probed by measures like $v_{\rm model}$ and $v_{\rm drift}$ contains approximately 25% more dynamical mass. Again, since S0s are thought to be older, more evolved systems with bulge-to-disk ratios that are larger on average than those of spirals, this is perhaps consistent with naive expectations, but is it true for our sample? In the spirit of Courteau & Rix (1999) and Courteau et al. (2007), the possibility that the luminous component of the dynamical mass is smaller or more concentrated in S0s at a given velocity can be tested directly by measuring the size of our galaxies.

We define $R_{\rm d}$ as described in Section 3.2.2 (where it is used as a parameter of the asymmetric drift correction) and $R_{\rm eff}$ as the semi-major axis of the ellipse containing half the light at K_S-band (see section 4.2 of WBC09 for a discussion of alternative definitions). In an edge-on galaxy with a boxy bulge, such as those in our sample, the radial surface brightness profile often contains a plateau or even a secondary maximum (Bureau et al., 2006). This means the disk scale length is not well defined. Measurement of $R_{\rm eff}$ depends sensitively on the ellipticity of the aperture used (WBC09). Moreover, our data probe a relatively small range in $v_{\rm model}$. Together, these difficulties mean that the constraints we can place on the parameters of the size–velocity relation are very weak. We recover a correlation $R_{\rm d} \propto R_{\rm eff} \propto v_{\rm model}^{\gamma}$, where $\gamma \approx 1.5 \pm 0.5$. Significantly, we also detect some evidence of a systematic difference between the zero points of the size–velocity relations of S0s and spirals. Using the simultaneous line fitting approach described in Section 3.4, we find that S0s are on average 0.15 ± 0.10 dex smaller than spirals at a given $v_{\rm model}$. This result is of weak statistical significance, but is consistent with our interpretation. We see no significant difference between the mean compactness of the light distribution, C_{82}, of

the S0s and spirals. $C_{82} \equiv R_{80}/R_{\rm eff}$, where R_{80} is the semi-major axis of the ellipse containing 80% of the light.

The large sample of Courteau et al. (2007) does not include S0s, but extends from Sa to Sc and is made up of galaxies that are more favourably inclined for measurements of size. Recalling that K_S-band luminosity is a good proxy for stellar mass (e.g. Bell & de Jong, 2001), which is a reasonable proxy for dynamical mass in the optical parts of disk galaxies (e.g. van Albada & Sancisi, 1986; Englmaier & Gerhard, 1999; Palunas & Williams, 2000; Weiner, Sellwood & Williams, 2001), Courteau et al. (2007) find a morphological trend in the sense required to explain our result: earlier-type spirals are smaller for a given K_S-band luminosity than later-types (see their table 3 and figure 11). At a characteristic K_S-band luminosity of $10^{11} L_{\odot}$, they find that Sas are around 80% the size of Sbs, which are in turn around 80% the size of Scs. If this trend extends to S0s, then its sense and magnitude are consistent with the offset we see in our dynamical mass TFR.

There is also the possibility that the dark halos (rather than the baryonic mass distribution) of S0s are smaller or more concentrated than those of spirals. Unfortunately we are unable to quantify this with our kinematic data, which are not radially extended enough to break the well known degeneracy between halo mass and concentration (van Albada et al., 1985). However, the inability of the dynamical models presented in WBC09 to quantify the amount of halo contraction has no effect on the results presented here. This is because, even if one assumes different dark halo shapes, the parameters of the best fitting models always conspire to produce an almost unchanging $v_{\rm c}$ profile in the region constrained by the data. This is ultimately the reason why the degeneracy exists in the first place. A quantitative illustration of the robustness of the circular velocity profiles recovered from dynamical models to the degeneracy in the halo concentration is given in, e.g., fig. 9 of Thomas et al. (2009).

The interpretation of the systematic offset of the S0 TFR to higher velocities due to a more concentrated mass distribution or smaller size than spirals is consistent with the discussion of the shapes of very extended gas rotation curves in Noordermeer et al. (2007) and Noordermeer & Verheijen (2007). Their kinematic data extend well beyond the optical disks of the galaxies, and allow them to study the asymptotic

behaviour of the rotation curves. They find that the earlier galaxies in their sample of S0–Sab galaxies have rotation curves that reach a maximum that is greater than their asymptotic velocity and occurs at smaller radii. They argue that this behaviour can be understood in terms of the larger bulge-to-disk ratios of the earlier-type galaxies in their sample. The scatter of their earlier-type galaxies away from the TFR of the late type galaxies is reduced by using the asymptotic velocity, which again suggests the Tully-Fisher relation is a manifestation of a close connection between galaxy luminosity (or mass) and halo mass.

If the size/concentration argument discussed above is indeed the explanation for the difference between the zero points of the S0 and spiral TFRs as a function of dynamical mass, then the offsets we observe as a function of luminosity (and discuss extensively in Section 3.5.1 in the context of fading relative to the high-redshift spiral TFR) are in fact due to differences in the distributions of dynamical mass in spirals and S0s. The offset between spirals and S0s in the Tully-Fisher (luminosity–velocity) relation may therefore not be a property of their stellar populations as argued in BAM06, but rather the result of more fundamental offset between spirals and S0s in the mass–size (or luminosity–size) projections of the luminosity–size–velocity plane occupied by disk galaxies. Models of S0 formation in which S0s are end points of spiral evolution should consider this possibility.

3.5.3 *Scatter of the TFRs*

The B-band luminosities we use, which are drawn from HYPERLEDA, are less accurate than our K_S-band magnitudes, which are based on a relatively recent, homogeneous set of observations. The extinction corrections at B-band are also particularly large and uncertain for edge-on galaxies like ours. These uncertainties are probably not reflected properly in our error estimates, and this may contribute to the fact that the scatter of the TFR at B-band (0.53 mag, of which 0.42 mag is intrinsic rather than observational) is larger than that at K_S-band (0.38 mag, of which 0.28 mag is intrinsic).

These scatters are broadly consistent with dedicated studies of the spiral TFR

scatter (e.g. Pizagno et al., 2007), which is perhaps somewhat surprising given the expected poor quality of our distance estimates and the importance and uncertainty of internal extinction in edge-on spirals. It should be borne in mind, however, that such studies fit a single line to a range of morphological types, while we separately fit two lines to two sub-samples, which reduces the measured total and intrinsic scatters. If a single line is fitted to the composite sample of spirals and S0s then the scatter increases to 0.50 mag, of which 0.41 mag is intrinsic.

Because our sample is drawn from a wide range of environments, the S0s may have been transformed from spirals via multiple channels (or one channel which began at different times in different galaxies). If so, then the extent to which S0s have left the spiral TFR should vary, and their scatter about the TFR should be larger than that of spirals. Our fitting method implicitly assumes that spirals and S0s have the same intrinsic scatter. However, our analysis also shows that there is no evidence of any difference between the intrinsic or total scatter of spiral galaxies about their line of best fit and that of S0s about theirs. The absence of increased scatter in the S0 TFR is problematic for all explanations of the offset (passive fading, environmental stripping, minor mergers and the possible non-homology described in Section 3.5.2).

There is no significant difference between the total scatters of the stellar mass TFRs (0.13 dex, i.e. 35 per cent) and the scatter at K_S-band (0.32 mag, i.e 34 per cent in luminosity). This is probably due to the relative constancy of mass-to-light ratios in the near-infrared, from which the masses are derived. The difficulty of assigning errors to the total masses of the dynamical models makes drawing strong conclusions from the intrinsic scatter of the stellar mass or dynamical mass TFRs difficult.

3.5.4 Classification of edge-on disk galaxies

The ability to reproducibly and correctly distinguish between spiral and S0 galaxies is crucial for this work. Although spirals arms are not visible in edge-on disk galaxies, the classification of edge-on galaxies as spirals or S0s is clearly specified by the presence of extended dust (see, e.g., Hubble, 1936; Sandage, 1961; de Vaucouleurs

et al., 1991). It is clear, therefore, that the classification of edge-on galaxies is objective and reproducible.

Although the classification of edge-on disk galaxies is reproducible, would a galaxy be classified as the same type if viewed face-on? To answer this concern, we note that if the effects of dust are visible in a face-on spiral then, due to line-of-sight projection, they would be even clearer if the same galaxy were viewed edge-on. For the simple distinction between spiral and S0 galaxies (rather than more detailed division into the Sa–Sd classes based on bulge size and the tightness of spiral arms), edge-on orientation is thus arguably the optimal viewing angle. This is also true of the distinction between S0s and ellipticals, where a face-on orientation makes it extremely difficult to detect the featureless stellar disk of an S0. Having said that, it is clear that if an edge-on galaxy has just enough dust to be classified as a spiral, it would probably (but perhaps wrongly) be classified as an S0 if viewed face-on. This will occur only for limiting cases, however, and it is clear that the majority of edge-on classifications are correct.

Having established that a meaningful morphological classification of edge-on disk galaxies is possible, we now ask whether this simple spiral–S0 division based on the presence of dust is dynamically significant. To test this, we randomly divided the complete sample of 28 galaxies into two sub-samples of 14 galaxies each and then measured the offset δ between the zero points of the TFRs of the two random sub-samples. We repeated this procedure 50,000 times to build up an idea of how the offset between randomly selected sub-samples is distributed, and how exceptional the adopted morphological classification is. This idea is a simplification of the non-parametric test presented in the context of comparing local and high-redshift TFRs by Koen & Lombard (2009). Our results are presented in Fig. 3.5. It is clear that the offsets observed between our S0s and spirals cannot to be due to chance. In all cases ($y = M_{K_S}$, M_B, $M_\star$ or $M_{\rm dyn}$, and for both forward and inverse regressions), the observed offset is at least three standard deviations away from the mean of the offsets between randomly selected sub-samples. This result clearly demonstrates that a purely morphological classification of edge-on early-type disk galaxies, based only on the presence of dust, divides them into two truly kinematically distinct classes.

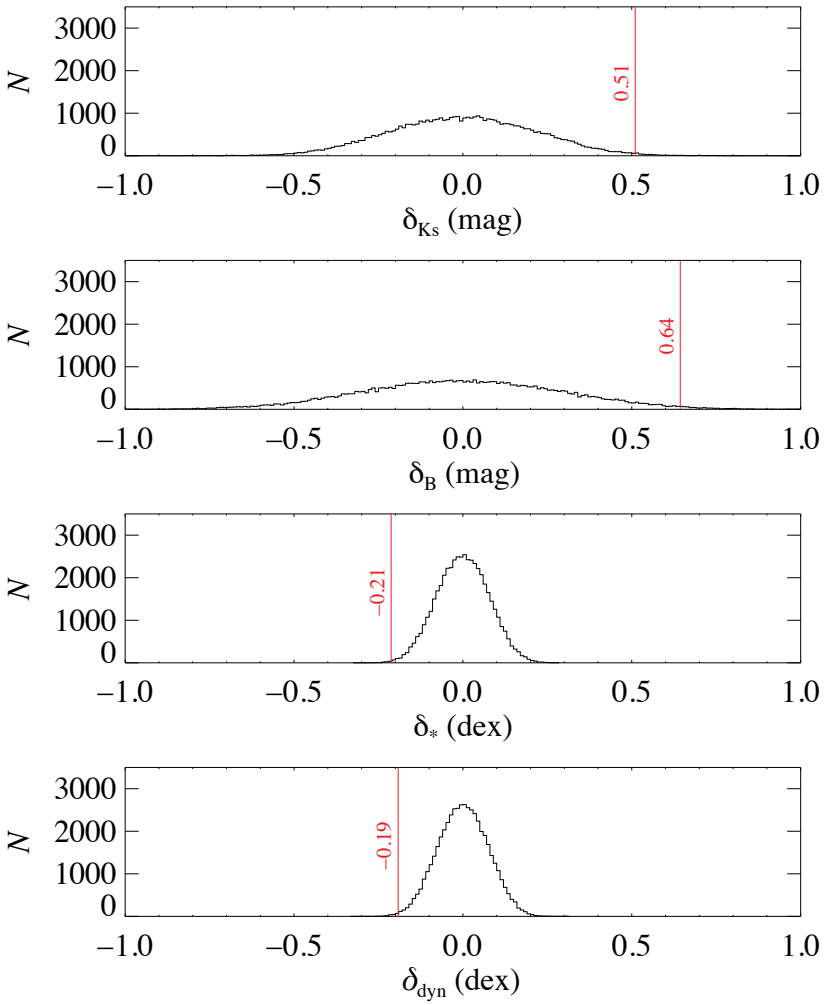

Figure 3.5: Distribution of the TFR zero-point offset δ between two sub-samples drawn randomly (with no regard to classification) from our full sample of 28 galaxies. The inverse regression fitting procedure was repeated 50,000 times to construct the histograms. From top to bottom, we show the offsets for the K_S-band, B-band, stellar mass and dynamical mass TFRs as a function of $v_{\rm model}$. The vertical lines show the value of the zero-point offset measured for the spiral and S0 sub-samples used here.

3.5.5 *Comparison to previous work*

The absolute location of our S0 TFR is almost identical to that measured in BAM06 at both K_S and B-band. They used $v_{\rm drift}$ rather than $v_{\rm model}$, so this is a reflection of the consistency of these two measures of rotation. If BAM06 could have used our spiral TFR as a reference zero point, they would have measured the same offset as us. However, they used the TFRs of TP00. As a result, our offsets are in the same sense (S0s are fainter than spirals) but significantly smaller in size than those measured in BAM06 (1.0 ± 0.4 mag at K_S, 1.6 ± 0.4 mag at B-band, where we have removed their correction of the TP00 zero point). Because the zero-point offsets we measure are smaller than those in BAM06, the timescale for a simple synthetic stellar population with a plausible star formation history to fade is shorter too. There are at least two reasons for the larger offsets measured in BAM06, which could combine to account for the entirety of the difference, making our results consistent.

The first is the possible intrinsic difference between the zero point of the spiral TFR we compare our S0s to in the present work, and the spiral TFR used in BAM06. Our spiral TFR is constructed using Sa and Sb galaxies, while that of TP00, which is used by BAM06, is calibrated using later types (mostly Sbc and later). As shown by Masters, Springob & Huchra (2008), in the velocity domain of the present work ($\langle v \rangle \approx 250\,{\rm km\,s^{-1}}$), Sa spirals are ≈ 0.4 mag fainter than Sb and Sc spirals of the same rotational velocity. On the other hand, Courteau et al. (2007) estimate that Sas are just 0.1 mag fainter than Sbs. Indeed, with our much smaller statistics, we see no evidence of a zero point variation between the Sa and Sb galaxies in our sample.

The second possible effect is the systematic bias introduced by comparing an S0 TFR derived from stellar kinematics to a spiral TFR derived from global H I line widths. Comparing the methods shows that Sa–Sb galaxies are measured to be rotating ≈ 0.08 dex slower in H I than in their stellar kinematics (see Fig. 3.2). At a typical K_S-band TFR slope of ≈ 8, this corresponds to a magnitude shift of ≈ 0.6 mag. However, as we emphasized in Section 3.2, applying a constant shift to correct for the difference between stellar and H I rotation measures is dubious because of the large

scatter in this difference (admittedly less so for spirals).

It is easy to see how morphological differences between galaxies in the reference spiral samples could combine with the systematic bias introduced by the use of different measures of rotation to account for the discrepancy between the fiducial offset presented here (0.53 ± 0.15 mag) and that in BAM06 (1.0 ± 0.4 mag).

Another possible source of bias in the offset measured in BAM06 is the fact that the TP00 spiral TFR is constrained by observations of a sample of relatively low mass spirals with $v \approx 150\,\mathrm{km\,s^{-1}}$, while BAM06's S0s have a mean $v \approx 250\,\mathrm{km\,s^{-1}}$. If the slope of the TFR changes with mass, as has been suggested (e.g. Peletier & Willner, 1993; Noordermeer & Verheijen, 2007), then the fact that the S0s and spirals in our sample lie in the same velocity domain is a crucial advantage.

In any case, because the rotation measure bias is unphysical and unrelated to the formation and evolution of S0s, we argue that the method we have employed here should be preferred if the goal is to determine how much fainter local S0s are than local spirals.

Finally, we note that BAM06 found a much larger scatter in their S0 TFR than we do here, ≈ 0.9 mag at K_S-band. This may be explained by the relatively homogeneous nature of our data compared to the multiple sources from which BAM06 drew theirs, and perhaps to the larger velocity and luminosity ranges their data probe.

3.6 CONCLUSIONS

We have demonstrated that the comparison of Tully-Fisher relations derived from H I line widths, ionized gas PVDs, stellar kinematics corrected for asymmetric drift or the circular velocity profiles of dynamical models is influenced by systematic and uncertain biases introduced by the different measures of rotation used. We therefore argue that to constrain the relative locations of the spiral and S0 TFRs, the same tracer and methods must be used for both samples. In practice, because of the paucity of extended, undisturbed H I and ionised gas in S0s, this means one must use stellar kinematics or dynamical models.

In this work we used the circular velocity profiles of mass models to construct TFRs for 14 Sa–Sb spirals and 14 S0s, eliminating the biases introduced by mixing measures of rotation. The circular velocity curves are those of models derived by solving the Jeans equations for mass models comprising an axisymmetric stellar component and a spherical NFW halo (WBC09). The parameters of the models are constrained by observed long-slit major-axis stellar kinematics (Chung & Bureau, 2004). We characterized the circular velocity profile for each galaxy by single numbers, $v_{\rm model}$, by taking the average in the flat part of the observed rotation curve.

By simultaneously fitting two offset relations with a common slope to this spirals and S0s, we find that S0s are systematically 0.53 ± 0.15 mag fainter at K_S-band than local Sa–Sb spirals of the same rotational velocity. This measurement is almost identical if we use estimates of the rotational velocity derived from ionized gas PVDs or stellar kinematics corrected for asymmetric drift.

If the high-redshift spiral TFR has the same zero point as the local spiral TFR, this is inconsistent with the observed evolution of the spiral/S0 fraction with redshift and a simple scenario in which star formation in the spiral progenitors of S0s was truncated at some time in the past. More complex star formation histories or even ongoing star formation in S0s may be the explanation. An alternative interpretation is revealed by the stellar mass and dynamical mass TFRs. The TFR offset persists as a function of both stellar and dynamical mass, and we show that this may be evidence of a small (10–20%) but systematic contraction of spirals as they transform to S0s. This is consistent with the trend with morphological type of the size–luminosity relation in the local universe (Courteau et al., 2007). If, on the other hand, the zero point of the TFR has dimmed from the present day to high redshift by ≈ 0.5 mag, then the putative transformation from spirals to S0s involves essentially no movement in the velocity–luminosity plane.

It seems clear that S0s are not primeval objects, but are an end point of spiral evolution. The processes responsible for this evolution can perhaps be accelerated by the environment. The variation of the zero point of the TFR with galaxy type and other parameters is just one approach among a number available that will allow us to constrain S0 formation and evolution. It is uniquely powerful because it

encodes information about the amount and distribution of dynamical mass of a galaxy. Modelling work complementary to the observations presented here is underway (Trujillo-Gomez et al., 2010; Tonini et al., 2010). One should be sure that the inevitable compromises introduced by high redshift observations do not introduce biases similar to those ones discussed in Section 3.2. We should also not forget the crucial role that spectroscopy has to play, especially in constraining the star formation history.

APPENDIX 3.A DEFINITIONS OF DYNAMICAL MASS IN DISC GALAXIES

In Section 3.3 we discussed two ways to define or characterize the dynamical mass of a galaxy. The first is to multiply the K_S-band luminosity L by the dynamical mass-to-light ratio $(M/L)_{K_S,\mathrm{nohalo}}$ (taken from WBC09 for our galaxies). As we noted, this method is relatively straightforward, and we adopt it as our fiducial method in the main body of this paper (denoting it M_{dyn}). This quantity does not have a precise physical meaning, but here we show it is equal, to a good approximation, to $2\,M_{1/2}$, where $M_{1/2}$ is the dynamical mass contained within the three-dimensional half-light volume.

We estimate $M_{1/2}$ by inverting the expression for the circular velocity of the mass model at the $r_{1/2}$. For a spherical system (i.e. flattening $q \equiv c/a = 1$) this gives

$$M_{1/2} = r_{1/2} v_{\mathrm{c}}^2(r_{1/2})/G, \tag{3.11}$$

where $v_{\mathrm{c}}(r_{1/2})$ is the circular velocity at $r_{1/2}$. Note that $r_{1/2}$ is *not* the projected half-light (effective) radius, R_{eff}. For a wide range of radial profiles, $r_{1/2} \approx 1.33\,R_{\mathrm{eff}}$ (Hernquist, 1990; Ciotti, 1991; Wolf et al., 2010).

Disc galaxies are not spherically symmetric, so a more useful definition in these cases is the dynamical mass within an oblate spheroid of semi-major axis $r_{1/2}$, which we denote $M_{1/2,q}$. For a given circular velocity, $M_{1/2} > M_{1/2,q}$. This is because the mass that must be spherically distributed to maintain a given circular velocity is larger than that necessary to achieve the same circular velocity in the midplane of a flattened system. The ratio $M_{1/2}/M_{1/2,q}$ is simultaneously a function of the radial profile of the

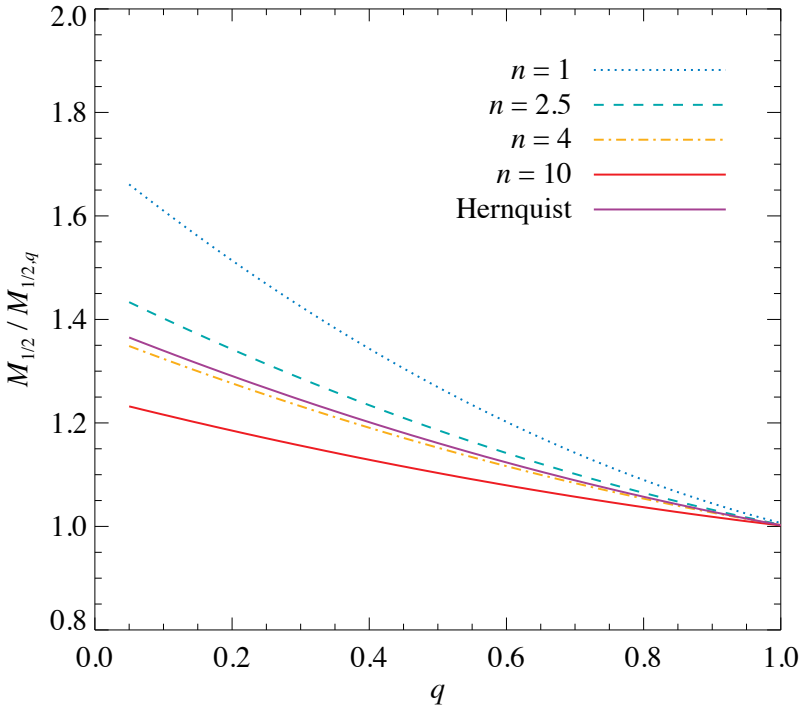

Figure 3.6: $M_{1/2}/M_{1/2,\,q}$ for a selection of potentials as a function of the flattening of the potential q. The behaviour of the Hernquist (1990) profile is shown in solid purple. The other lines are Sérsic profiles of order $n = 1$ (exponential), 2.5 (typical classical bulge–pseudobulge transition), 4 (de Vaucouleurs) and 10. The de Vaucouleurs and Hernquist lines are well described by the fitting formula $M_{1/2}/M_{1/2,\,q} = 1.38 - 0.52q + 0.14q^2$.

mass distribution and q. For a full analytic discussion see, for example, the comparison between the circular velocities of oblate spheroids as a function of q and mass profile in section 2.5.2 of Binney & Tremaine (2008). For our purposes, an approximate estimate of $M_{1/2}/M_{1/2,\,q}$ is sufficient. Using a range of analytic potentials, we examine the behaviour of the ratio $M_{1/2}/M_{1/2,\,q}$ as a function of q in Fig. 3.6. The circular velocity of each flattened model is conveniently calculated numerically by flattening a multi-Gaussian fit to the mass distribution and using standard integrals to determine the circular velocity of the arbitrarily flattened distribution (Cappellari, 2002). Disc galaxies typically have $q \approx 0.2$ and potentials of the form $\exp\left(-R/R_{\rm eff}\right)^{1/n}$, where $1 \leq n \leq 4$. In such galaxies, $1.3 \lesssim M_{1/2}/M_{1/2,\,q} \lesssim 1.5$, and so from equation (3.11)

$$M_{1/2,\,q} \approx r_{1/2} v_{\rm c}^2(r_{1/2})/1.4G. \tag{3.12}$$

Furthermore, $r_{1/2} \approx 1.33 R_{\rm eff}$, where in non-spherical systems the observable $R_{\rm eff}$ is

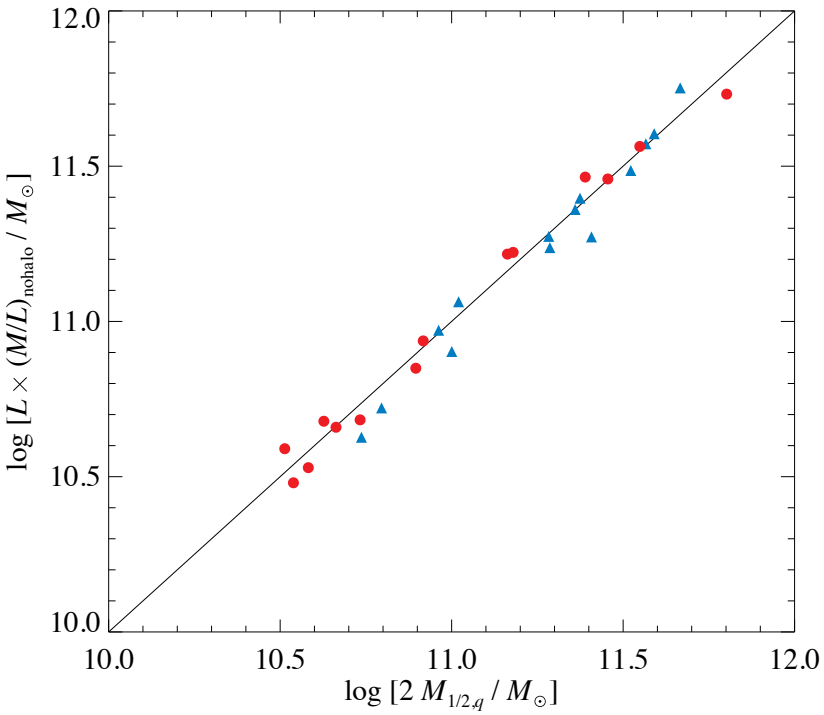

Figure 3.7: A comparison of the two estimates of the dynamical mass for the 28 disk galaxies in the present sample. The horizontal axis is $2M_{1/2,q}$ as defined in equation (3.13), incorporating an approximate correction for flattening. The vertical axis is the K_S-band luminosity L multiplied by the dynamical mass-to-light ratio $(M/L)_{K_S,\mathrm{nohalo}}$ as presented in WBC09. The symbols are as in Fig. 3.2. The solid line is the line $y = x$. The two estimates agree on average to better than 2 per cent with 13 per cent rms scatter and no evidence of a systematic difference between spirals and S0s.

defined as the semi-major axis of the projected half-light ellipse. For disc galaxies we can therefore write

$$M_{1/2,q} \approx R_{\mathrm{eff}} v_c^2 (1.33\, R_{\mathrm{eff}})/G. \tag{3.13}$$

The circular velocity at $1.33\, R_{\mathrm{eff}}$ can easily be estimated to an accuracy consistent with the derivation of this formula from dynamical modelling, stellar kinematics corrected for asymmetric drift or resolved gas kinematic observations. For typical values of q and the analytic potentials explored here, this expression is accurate to about 15 per cent. Of course in real disc galaxies, the flattening q is a function of radius, the potential is not described by a single Sérsic or Hernquist profile and even R_{eff} is not simple to measure, so equation (3.13) is probably a little less reliable in practice.

Nevertheless, when doubled, $M_{1/2,\,q}$ closely matches fiducial estimates of the dynamical mass of our sample galaxies, i.e. the product of their luminosities L and dynamical mass-to-light ratios $(M/L)_{\rm nohalo}$, inferred in this case from stellar kinematic data extending to 2–3 $R_{\rm eff}$ and K_S-band photometry in WBC09. We show this comparison in Fig. 3.7. We use $v_{\rm model}$, the circular velocity of the WBC09 mass models in the flat region of the observed rotation curve, as $v_{\rm c}$ in equation (3.13), but in cases where a reliable asymmetric drift correction is possible at 1.33 $R_{\rm eff}$, $v_{\rm drift}$ gives almost identical results. The excellent agreement between $2M_{1/2,\,q}$ and $L \times (M/L)_{\rm nohalo}$ may be a coincidence. The two measures would be systematically offset (and perhaps more scattered) if our kinematic data extended significantly further in radius (and the dynamical mass-to-light ratios we measured were therefore larger). Crucially, however, Fig. 3.7 demonstrates that, for the purposes of the present work comparing the TFRs of spirals and S0s, the choice of definition of dynamical mass does not affect spirals and S0s differently.

4

THE VERTICAL STRUCTURE OF BOXY BULGES: STELLAR KINEMATICS AND POPULATIONS OF 5 GALAXIES

The material in this chapter was originally pubished in 'The stellar kinematics and populations of boxy bulges', M. J. Williams, M. Zamojski, M. Bureau, M. Merrifield, P. T. de Zeeuw and K. Kuijken, 2011, MNRAS, 414, 2163. The definitive version is available at www.blackwell-synergy.com.

4.1 INTRODUCTION

The central regions of disk galaxies host bulges whose nature (or absence) must be explained by any model of galaxy formation and evolution. A bulge is a physical protrusion of stars above and below the plane of the disk and/or an excess of light above the inwards extrapolation of the radial exponential profile of the disc. There are three principal observational classes of bulges: classical bulges, pseudobulges, and boxy or peanut-shaped bulges.

Classical bulges have dynamical and photometric properties and stellar populations that are similar to elliptical galaxies of the same mass (Kormendy & Illingworth, 1982; Davies et al., 1983; Emsellem et al., 2004; Kormendy & Kennicutt, 2004; Falcón-Barroso et al., 2006; Thomas & Davies, 2006; MacArthur, González & Courteau, 2009) and are thought to be the end products of the same formation processes: either

monolithic collapse (e.g. Eggen, Lynden-Bell & Sandage, 1962; Larson, 1974; Carlberg, 1984; Pipino & Matteucci, 2004)) or multiple hierarchical mergers (e.g. White & Rees, 1978; Cole et al., 1994; Thomas, Greggio & Bender, 1999).

Pseudobulges have embedded spiral structure, disc-like near-exponential light profiles, flattened axial ratios, and rotation-dominated dynamics (see Kormendy & Kennicutt, 2004, and references therein). They are thought to be secularly rearranged disk material that was driven inwards by bars, ovals and possibly spiral arms. The observational constraints on the stellar populations of pseudobulges are less strong because studies have focussed on bigger and brighter classical bulges, decomposing their extended star formation history is more complicated than in classical bulges and ellipticals, and dust is a significant problem for the late-type discs in which pseudobulges are more usually found. Nevertheless, the available population data are not strongly inconsistent with the secular model (Peletier et al. 1999; Gadotti & dos Anjos 2001, but see the pilot sample of MacArthur, González & Courteau 2009).

An important third class of bulge, and the focus of this paper, is the boxy and peanut-shaped bulges, which are present in about half of edge-on disk galaxies. Their demographics (Lütticke, Dettmar & Pohlen, 2000), major-axis stellar and gas kinematics (Kuijken & Merrifield, 1995; Merrifield & Kuijken, 1999; Bureau & Freeman, 1999; Chung & Bureau, 2004; Méndez-Abreu et al., 2008) and light profiles (Bureau et al., 2006) are consistent with simulations of the formation and buckling of galactic bars (Combes et al., 1990; Raha et al., 1991; Athanassoula & Bureau, 1999; Bureau & Athanassoula, 2005) and point to them being bars viewed in projection. Peanut-shaped bulges are thought to be bars whose orientation is exactly perpendicular to the line-of-sight, while boxy bulges are seen in galaxies whose bar is at an intermediate angle. Bars oriented exactly parallel to the line-of-sight do not appear boxy or peanut-shaped. In that sense, boxy and peanut-shaped bulges are not the axisymmetric features normally thought of as 'bulges'. Since the dominant model is that they are bars, which are not the end products of collapse or merger, but rather redistributed disk material, boxy bulges are also sometimes referred to as pseudobulges. However, for the purposes of clarity in the present paper, we avoid this, since boxy bulges are truly thick.

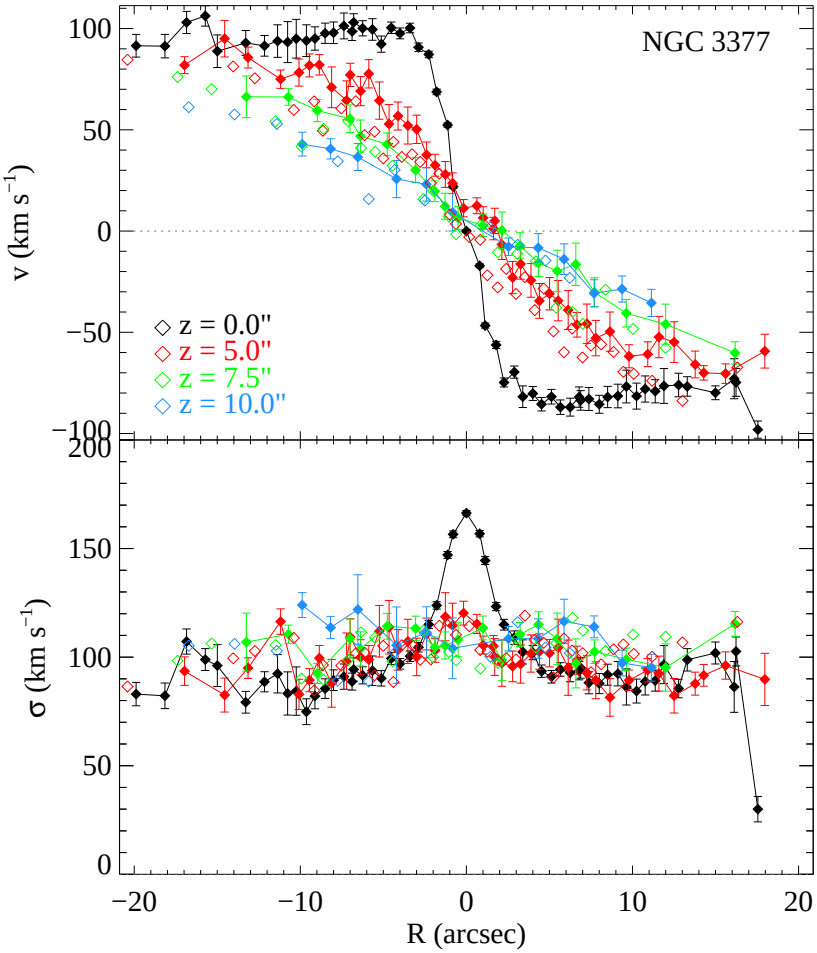

Figure 4.1: Stellar line-of-sight rotation curves and velocity dispersion profiles for two non-cylindrically rotating edge-on galaxies from the SAURON sample (the fast rotator elliptical NGC 3377 and the classical bulge of the S0 NGC 4570), constructed by extracting pseudoslits from the integral-field kinematics presented in Emsellem et al. (2004). The stellar kinematics along the major axis are shown in black, and those from pseudoslits offset from, but parallel to, the major axis are shown in order of increasing distance from the major axis in red, green and blue. The offset distance z is shown. Data from one side of the major axis are shown as filled diamonds (joined by lines), and data from the other side as open diamonds (with error bars omitted for clarity). The vertical dotted lines at $R = 14''$ for NGC 4570 indicate the effective radius $R_{\rm eff}$, i.e. the approximate extent of the bulge (beyond which the figure is shaded grey). The effective radius of NGC 3377 is $38''$, i.e. beyond the radial range shown. Note that, within each bulge at a given R, v falls systematically with height above the major axis, i.e. the rotation pattern is not cylindrical.

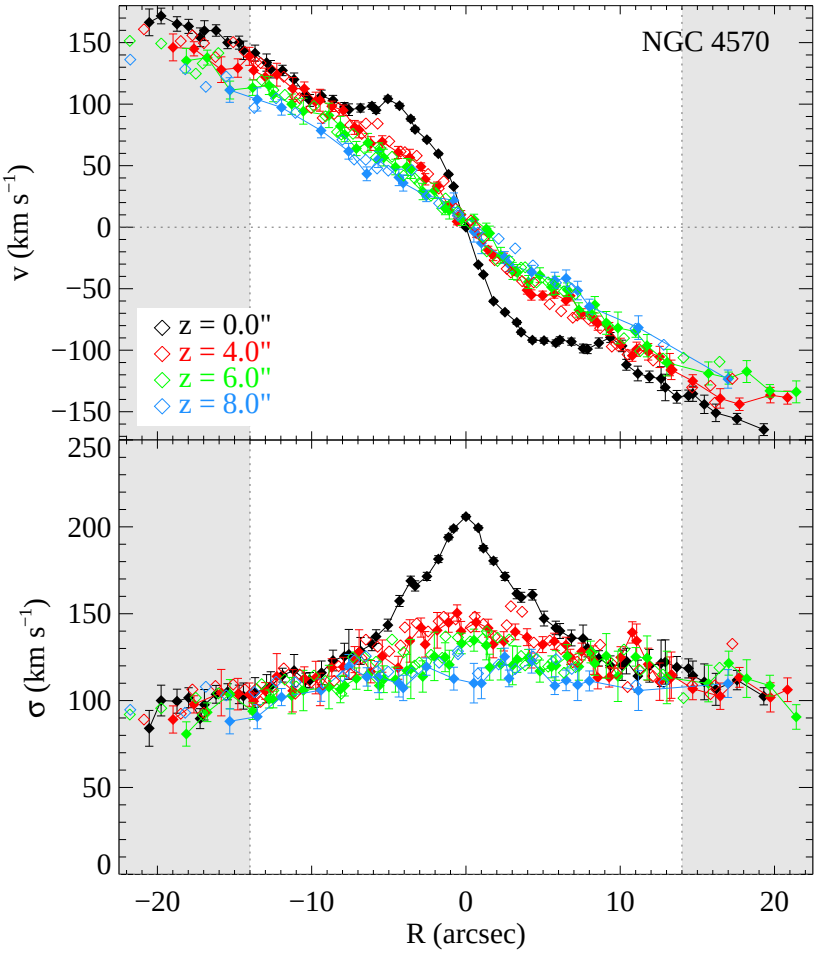

Figure 4.1: — continued

In the absence of transformational mergers, bars, which are found in two-thirds of disk galaxies (Eskridge et al., 2000; Whyte et al., 2002; Marinova & Jogee, 2007), are expected to play a crucial and perhaps dominant role in disk galaxy evolution (e.g. Sellwood & Wilkinson, 1993; Kormendy & Kennicutt, 2004; Hopkins et al., 2010). Boxy and peanut-shaped bulges therefore provide a unique perspective on a feature that is crucial for understanding galaxy evolution. By observing them above the plane of the disc, one can determine the intrinsic properties of bars in a way that is almost free of thin disk light pollution. Moreover, the observed dynamics of bars as a function of height above the plane is a crucial additional constraint on models of the nature of bulges, including ruling out the presence of a dynamically hot classical bulge/merger remnant. For example, Shen et al. (2010) modelled the line-of-sight mean velocity and

velocity dispersion of M giant stars in the Milky Way bulge observed by the BRAVA survey (Howard et al., 2009). They placed an extremely low upper limit on the mass of any hot spheroid component, $\lesssim$7%; i.e. the Milky Way appears to be a pure disc galaxy (but see Babusiaux et al. 2010). Giant pure disk galaxies present an acute challenge for cosmological simulations of galaxy formation (e.g. van den Bosch, 2001; Carollo et al., 2007; Dutton, 2009; Kormendy et al., 2010).

Perhaps the most discriminatory prediction of dynamical models of bars viewed in projection is that, within the bulge, the rotational velocity does not change with height (Combes et al., 1990; Athanassoula & Misiriotis, 2002). That is to say, lines of constant velocity are parallel to each other and perpendicular to the major axis, such that $\partial v / \partial |z| \sim 0$, where v is the line-of-sight velocity and z is along the minor axis of the (edge-on) galaxy. This unusual behaviour was first identified in the boxy bulge of NGC 4565 by Kormendy & Illingworth (1982), who named it 'cylindrical rotation'. Cylindrical rotation has since been noted in the following eight galaxies, all of which have bulges that are, more or less, boxy: NGC 128 (Jarvis, 1990), NGC 3069 (Shaw, Wilkinson & Carter, 1993), NGC 1055 (Shaw, 1993), NGC 4442 (Bettoni & Galletta, 1994), NGC 7332 (Fisher, Illingworth & Franx, 1994; Falcón-Barroso et al., 2004), NGC 4220 and NGC 4425 (Falcón-Barroso et al., 2006), and the Milky Way (Howard et al., 2009). Cylindrical rotation is not expected for classical bulges, where velocity falls systematically with height, even within the bulge (see Fig. 4.1 for two illustrative examples from the SAURON sample; de Zeeuw et al. 2002; Emsellem et al. 2004).

In our search of the literature, we found no report of the absence of cylindrical rotation in a boxy bulge, or the presence of cylindrical rotation in a non-boxy bulge. One of the goals of the present targeted study of boxy bulges is to determine whether this is confirmation bias, or whether cylindrical rotation is truly ubiquitous in boxy bulges and therefore a requisite property of all realistic models of bars.

Our second goal is to examine the stellar populations of boxy bulges. The null hypothesis might be that, since bars are secularly rearranged disk material (rather than material accreted or formed during rapid mergers), the metallicities of boxy bulges should be similar to those of their host discs. If, however, the metallicities of

boxy bulges differ from those of their discs, or if they have metallicity gradients, this is not necessarily a problem for the bar buckling scenario. As pointed out by Freeman (2008), the stars that have been scattered furthest from the disk are the oldest stars, and therefore formed from the least metal-enriched fuel. The buckling process may therefore establish a negative minor-axis metallicity gradient. Indeed, such behaviour is observed in the Milky Way (Zoccali et al., 2008) and in NGC 4565, the archetypal boxy, cylindrically-rotating bulge (Proctor, Sansom & Reid, 2000). The strength of the metallicity gradient established in this way must be a function of both the rate of enrichment in the disk and the timescale over which the bar buckles and heats the disc. The process must also establish a corresponding positive age gradient. We know of no chemodynamical simulations of this process and, in particular, no prediction of the extent to which minor-axis gradients in boxy bulges are expected to differ from those in classical bulges.

Moreover, we know of no prediction regarding the relative abundance of α-elements in boxy bulges. The naive expectation, however, is that the [α/Fe] ratio of a boxy bulge should match that of its host disc. It is difficult to understand how secularly rearranged disk material could be segregated such that a boxy bulge of disk origin is α-enhanced with respect to its disc. Enhanced [α/Fe] ratios indicate that material was α-enriched by core collapse (type II) supernovae before type Ia supernovae Fe-enrichment, which implies a formation timescale $\lesssim 1$ Gyr. Bulges that are α-enhanced with respect to their disk would therefore indicate that their stars formed on much shorter timescales than the disk stars (and not just at earlier times). If observed in a galaxy, this would suggest that its bulge is at least partially comprised of material formed in a merger or rapid collapse, or material of external origin. We discuss some of the issues that complicate this naive expectation in Section 4.5

In this paper we present a focussed spectroscopic analysis of the boxy bulges of five edge-on disk galaxies. In Section 4.2 we describe the sample, the data and their reduction. We present the derived stellar kinematics in Section 4.3 and the stellar populations in Section 4.4. We summarise our results and suggest future work in Section 4.5.

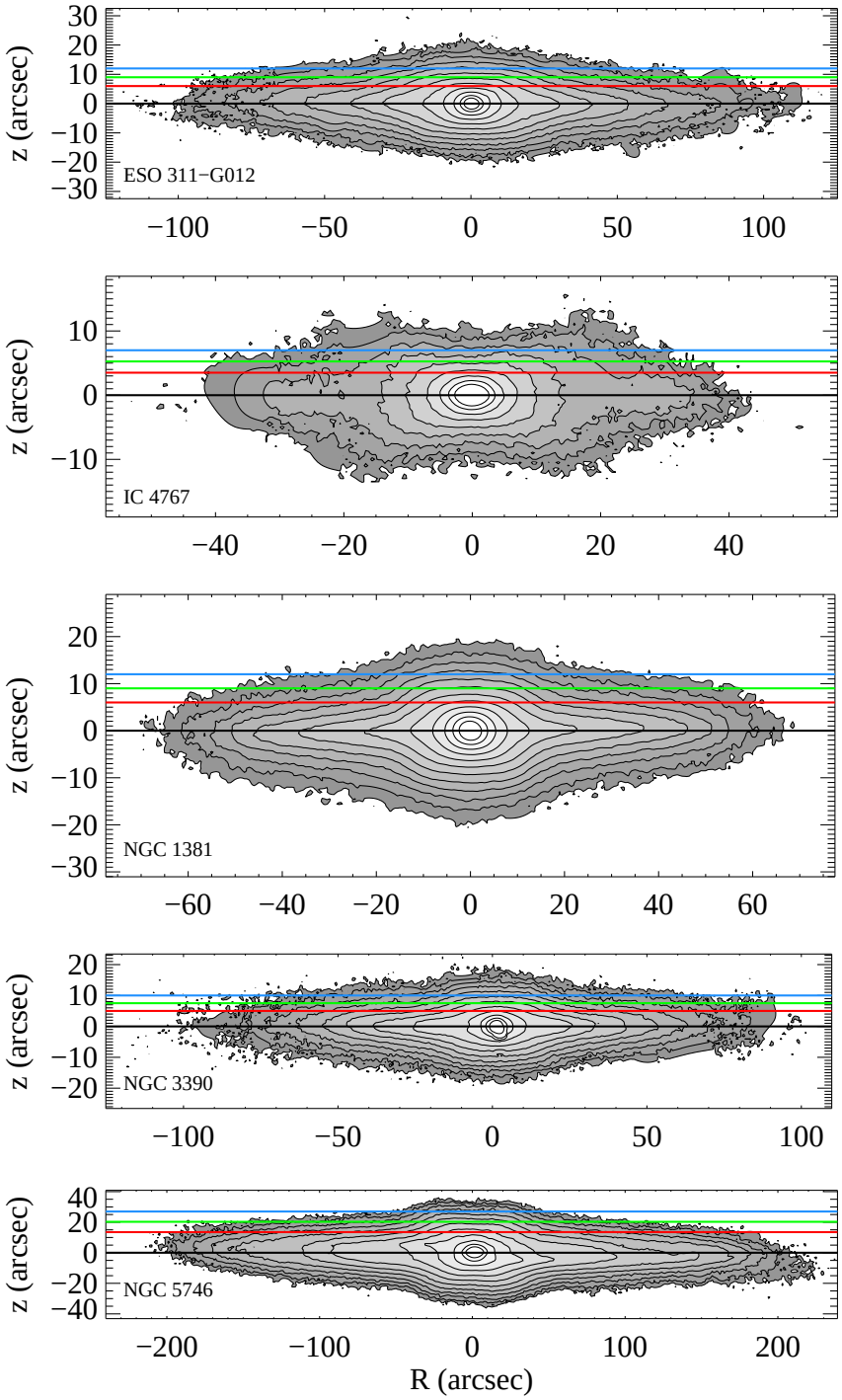

Figure 4.2: *K*-band images of the sample galaxies with the slits overlaid. Contours are separated by 0.5 mag. Images taken from Bureau et al. (2006).

Table 4.1: NTT/EMMI sample properties and slit positions.

Galaxy	RC3 classification	Bulge type	R_{box} (arcsec)	Offset slit positions (arcsec)		
ESO 311-G012	S0/a?	Boxy	15	6.0	9.0	12
IC 4767	S0+^	Peanut	18	3.5	5.25	7
NGC 1381	SA0	Boxy	10	6.0	9.0	12
NGC 3390	Sb	Boxy	10	5.0	7.5	10
NGC 5746	SAB(rs)b?	Peanut	20	13.5	20.25	27

Notes. R_{box} is the radius of the maximum scale height of the galaxy, as measured from the vertical photometric parametrizations presented in Bureau, Aronica & Athanassoula (in preparation). It coincides with the approximate edge of the boxy bulge, and is therefore correlated with the projected length of the bar. The offset slit positions are the distance each slit was offset from the major axis of the galaxy.

4.2 OBSERVATIONS AND DATA REDUCTION

Our sample for this chapter consists of five galaxies drawn from the complete Bureau & Freeman (1999) sample, whose bulges were classified as boxy or peanut-shaped by Lütticke, Dettmar & Pohlen (2000) using Digitized Sky Survey images. All of the galaxies are edge-on or nearly edge-on. NGC 5746 is the furthest from edge-on in the sample. It is inclined at 85°.5 measured by fitting an ellipse to the prominent ring visible in near-infrared *Spitzer* archive Infrared Array Camera images (PI: Giovanni Fazio).

We observed the sample using the New Technology Telescope's ESO Multi-Mode Instrument (NTT/EMMI) in long-slit spectroscopy mode. The observations were made in 2000 January, May and October (programmes 64.N-0545, 65.N-0126 and 66.B-0073). We positioned the slit along the major axis and then parallel to it at three offset positions. In this way we built up spatial coverage similar to that of a sparse, wide-field integral-field spectrograph. We present the sample properties and slit positions in Table 4.1. We show the slits superimposed on images of the sample in Fig. 4.2.

We also observed three other galaxy bulges, two of which are not boxy, during the runs (NGC 1055, NGC 1247 and NGC 7123) but we dropped them from the present analysis because the data is poor or incomplete, and the work since the data was

taken has superseded any contribution these observations could have made to our understanding of the dynamics and populations of classical bulges (e.g. Proctor & Sansom, 2002; Emsellem et al., 2004; Thomas & Davies, 2006; Falcón-Barroso et al., 2006).

We reduced the data using standard techniques in IRAF (Image Reduction and Analysis Facility), yielding flat-fielded, wavelength-calibrated sky-subtracted two-dimensional spectra at four slit positions for each galaxy. Exposure times ranged from 30 minutes for the major axis slits to up to 3 hours for the slits furthest from the disc. The reduced two-dimensional spectra were linearly binned in wavelength and cover the range 4830–5470 Å. The spectral resolution of the instrument is 1.0 Å full-width half-maximum (equivalent to $\sigma_{\rm inst} \approx 25\,{\rm km\,s^{-1}}$ at 5150 Å). The spatial axis has a pixel scale of 0.9 arcsec/pixel. We determined the central bin (i.e. the spectra for which the cylindrical radius $R = 0$) using a Sérsic fit to the profile of each spectrum. This measurement is correct at the sub-arcsec level for the major axis slit, but is uncertain by $\lesssim 5$ arcsec away from the midplane, where the profile is noisy and weakly peaked. The central bin for each slit may therefore be a point that does not lie exactly on the minor axis. This uncertainty may introduce a small, systematic relative offset between the kinematic profiles derived for each slit.

Spectrophotometric flux standards were not observed during the observing runs, so that we are unable to precisely flux calibrate our data. However, as described in Section 4.4, this does not significantly affect our ability to measure line strengths.

4.3 STELLAR KINEMATICS

4.3.1 *Methods*

In order to determine the stellar kinematics, we first binned the data spatially to enhance the signal-to-noise ratio (S/N). To measure the line-of-sight mean velocity, we typically binned to a S/N of about 10 per Å but lowered this to 5 per Å for a few of the most offset slits. The outermost bin in each slit often does not reach the

desired S/N level, but was analysed (and included in these figures) for completeness. To measure the velocity dispersion we rebinned the data to twice the S/N, sacrificing spatial resolution.

We extracted absorption line stellar kinematics from the binned spectra using penalized pixel fitting (PPXF; Cappellari & Emsellem 2004). All galaxies except NGC 1381 show clear signs of Hβ or [O III] emission in their major-axis spectrum, but the data in each bin are of insufficient S/N to constrain the emission line properties and subtract the emission in a physically motivated way using, e.g., GANDALF (Sarzi et al., 2006). To derive the absorption line stellar kinematics, the appropriate spectral regions are therefore simply masked.[1] We also masked a series of bad columns on the CCD at a rest wavelength of $\approx$5050 Å.

We used a subset of 88 stars from the MILES library of 985 observed stellar spectra as templates (Sánchez-Blázquez et al., 2006b). The MILES spectra have a spectral resolution of 2.3 Å while our spectra have a resolution of 1.0 Å so we first degraded our spectra to the MILES resolution. In principle, the penalized pixel fitting algorithm can robustly recover dispersions down to around half of this degraded spectral resolution, i.e. $\approx$28 km s^{-1}. Using the Fourier Correlation Quotient method (Bender, 1990) and a template library with a spectral resolution of $\approx$32 km s^{-1}, Chung & Bureau (2004) measured dispersions > 50 km s^{-1} along the major axis of all five galaxies in the present sample. Since the true dispersions of these galaxies is of order the resolution of the MILES library, working at the MILES resolution should not affect our results for the line-of-sight velocity dispersion. To verify this, we repeated the kinematic extraction for NGC 1381 working at the resolution of our observations. To do these we used degraded template spectra from the ELODIE library of 1388 stars (whose spectra have a resolution of 12 km s^{-1}, i.e. higher than that of our observations, Prugniel & Soubiran 2001). Within the uncertainties, the v and σ radial profiles we recovered agree with those recovered using the MILES library, with no sign of any systematic disagreement.

Our data are of insufficient S/N to constrain h_3 (skewness) and h_4 (kurtosis) using

[1] Note that we do treat emission properly when determining the absorption line strengths in Section 4.4, where we bin to much higher S/N.

a Gauss-Hermite parametrization of the line-of-sight velocity distribution (LOSVD). We therefore enforce a pure Gaussian LOSVD. Our conclusions regarding cylindrical rotation, which depend only on v, are not affected by this decision.

We estimated the uncertainties on the derived kinematics by running PPXF on 100 random realisations of each spectrum. The realisations were constructed by adding wavelength-independent Gaussian noise assuming Poisson statistics. To these uncertainties we added uncertainties due to wavelength calibration, which we estimate to be $\lesssim 0.2$ Å, i.e. $\lesssim 10\,\mathrm{km\,s^{-1}}$. These wavelength calibration uncertainties generally dominate the uncertainties in v, but are less important for σ, where the spectral noise dominates.

4.3.2 *Results*

The line-of-sight mean stellar velocity v and velocity dispersion σ calculated as described above are presented in Fig. 4.3. The kinematics of the major axis slit are shown in black and those of the offset slits are shown in order of increasing distance from the major axis in red, green and blue. In each plot, we indicate the approximate extent of the bulge with dotted vertical lines.

The boxy bulge of NGC 3390 is a clear example of cylindrical rotation. Within the uncertainties, it shows no systematic variation of rotational velocity as a function of height at all.

The behaviour of the boxy bulge of ESO 311-G012 is close to cylindrical. The major-axis rotation is somewhat discrepant from that of the offset slits; the rotation curve along the plane of the disk is 'double-humped', while those of the offset slits are not. This does not mean that the boxy bulge is not rotating cylindrically. The strong double-hump feature is seen in simulations of barred galaxies (Bureau & Athanassoula, 2005) and is likely the dynamical signature of bar-driven inward transport of material (e.g. Kormendy & Kennicutt, 2004), which leads to the formation of a flattened round excess of light, i.e. a pseudobulge. The distinguishing feature of cylindrical rotation is therefore that v does not vary systematically with height away from the major axis,

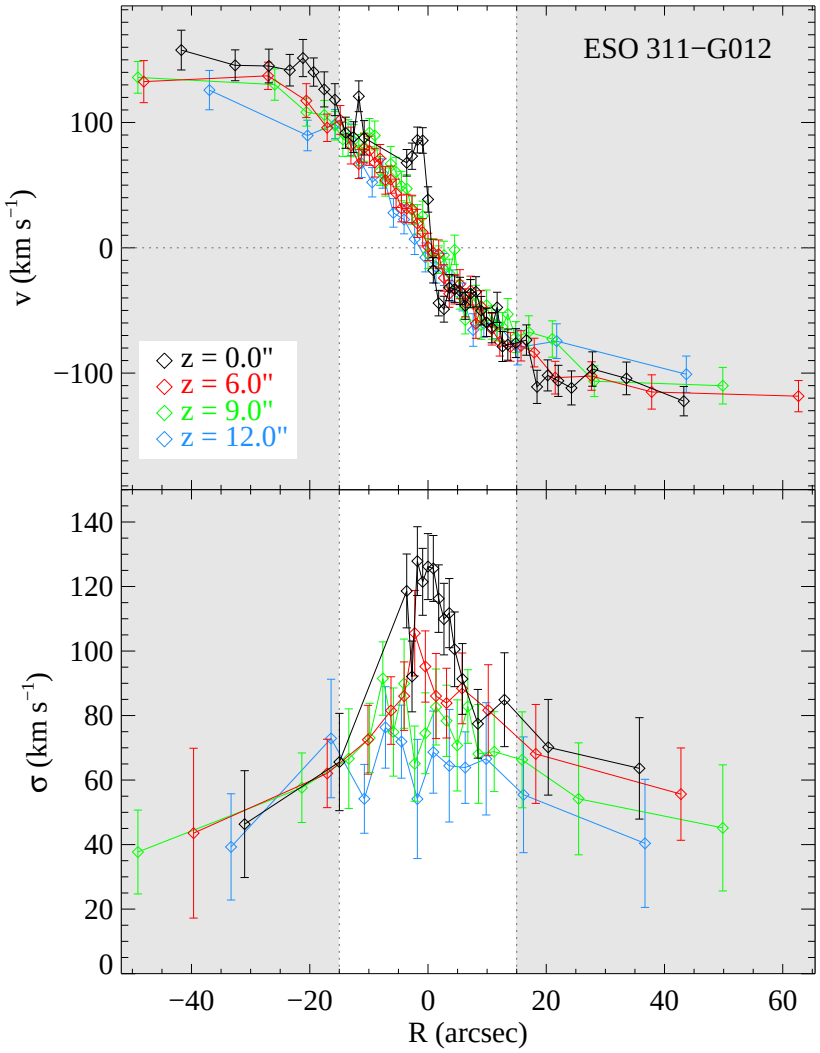

Figure 4.3: Stellar line-of-sight mean velocity (top) and velocity dispersion (bottom) for the five sample galaxies. The stellar kinematics of the major axis are shown in black, and those of the offset slits are shown in order of increasing distance from the major axis in red, green and blue. See Table 4.1 and Fig. 4.2 for the slit positions. The vertical dotted lines indicate $R_{\rm box}$, the approximate extent of the boxy bulge (see Table 4.1). The shaded regions at large radii therefore correspond roughly to the galaxy disc. The same systemic velocity has been subtracted from all points, determined from a PPXF fit to the total major axis spectrum.

.

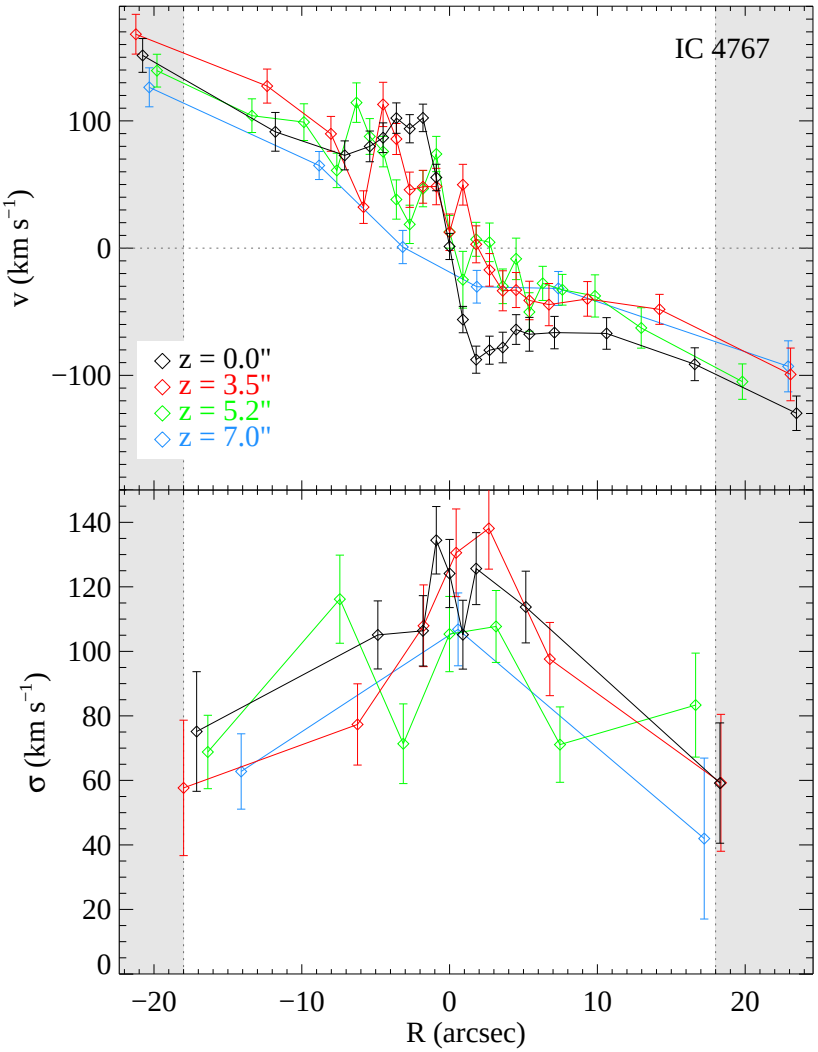

Figure 4.3: — continued

which is true of ESO 311-G012. Taken together, we interpret the presence of a double hump in the rotation curve along the major axis and cylindrical rotation in the offset slits as consistent with simulations of the formation and dynamics of bars (Combes et al., 1990; Athanassoula & Misiriotis, 2002; Bureau & Athanassoula, 2005).

The classification of the type of rotation in the boxy bulge of NGC 1381 is marginal. The velocity along the major axis is extremely discrepant from that along the offset slits. The slits at 6″ and 9″ are corotating, but the slit at 12″ is of extremely low S/N, and is binned to a correspondingly coarse spatial resolution. This galaxy lacks the clear systematic drop of v with increasing z seen in the examples in Fig. 4.1, but it is not a clean case of cylindrical rotation either.

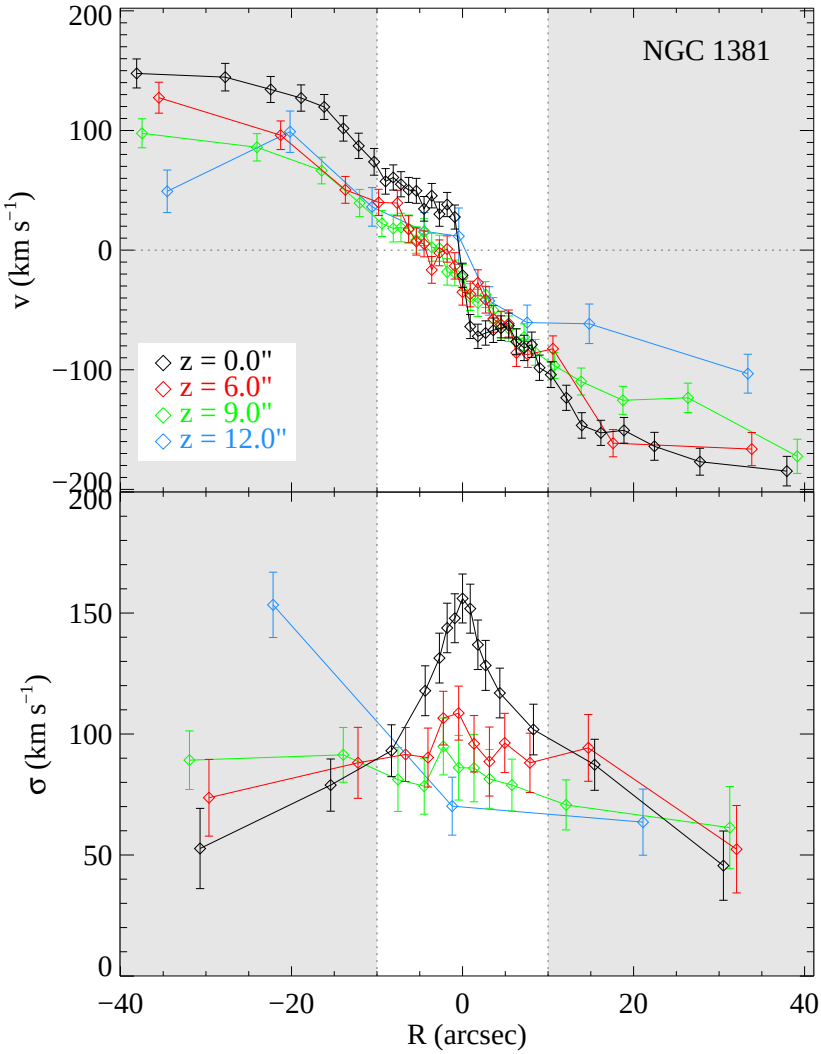

Figure 4.3: — continued

The same is true of the peanut-shaped bulge of NGC 5746, but the picture is further complicated here by the rather irregular rotation curves within the bulge. This may be due to the prominent and dust 'lane' in NGC 5746, which, because this galaxy is a few degrees away from edge-on obscures a fraction of the galaxy. Strong absorption may cause the local mean line-of-sight velocity to differ significantly from the azimuthal velocity at the tangent point along the line-of-sight, and the extent of this difference may vary in a complicated way with distance along the minor axis.

The peanut-shaped bulge of IC 4767 is not cylindrically rotating. At negative R, even accounting for the uncertainties and the irregularity of the rotation curve, v falls systematically with z. At positive R, the signature of non-cylindrical rotation is less

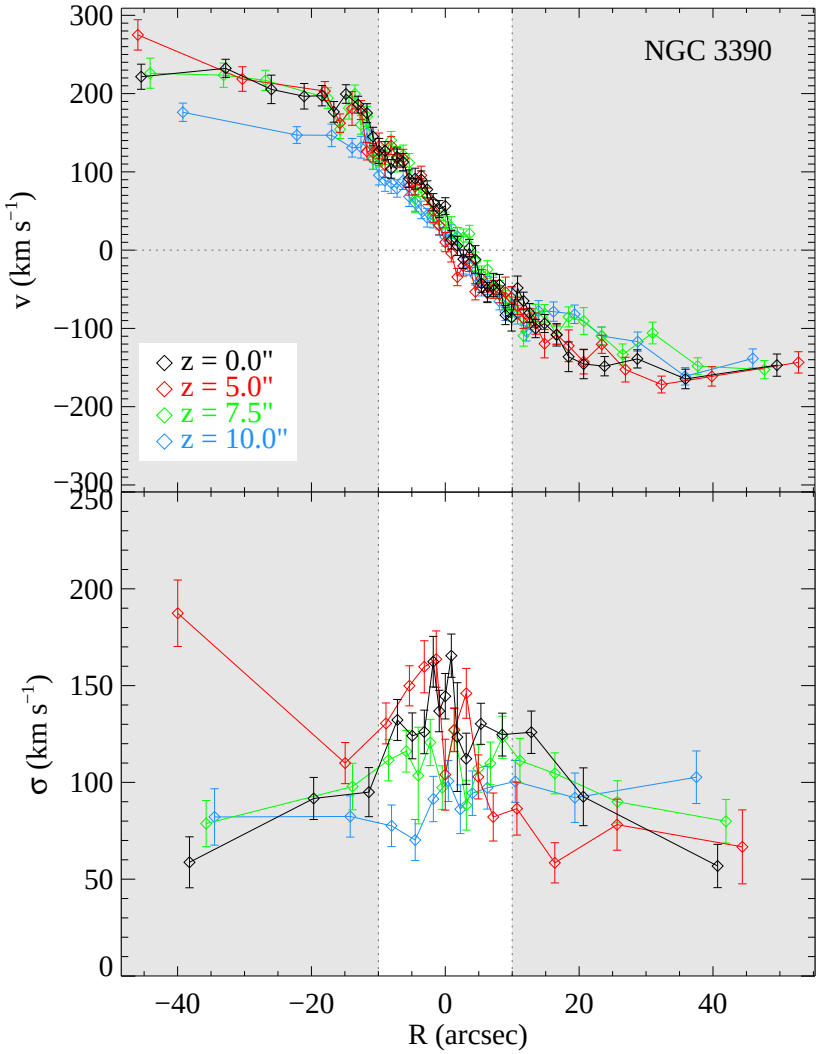

Figure 4.3: — continued

clear.

Cylindrical rotation is therefore not a ubiquitous feature of boxy and peanut-shaped bulges. There is some evidence that it is less strong or even absent in peanut-shaped bulges compared to boxy bulges. It is worth considering whether this might have a dynamical origin. In simulations, bars in edge-on galaxies appear peanut-shaped when viewed with the bar perpendicular to the line-of-sight, and boxy when the bar is at an intermediate angle (e.g. Combes et al., 1990). End-on bars appear neither boxy or peanut-shaped. The velocity fields of these simulated galaxies vary with the orientation of the bar in the sense that the closer the bar is to end-on (i.e. the less strongly peanut-shaped it appears), the more closely packed

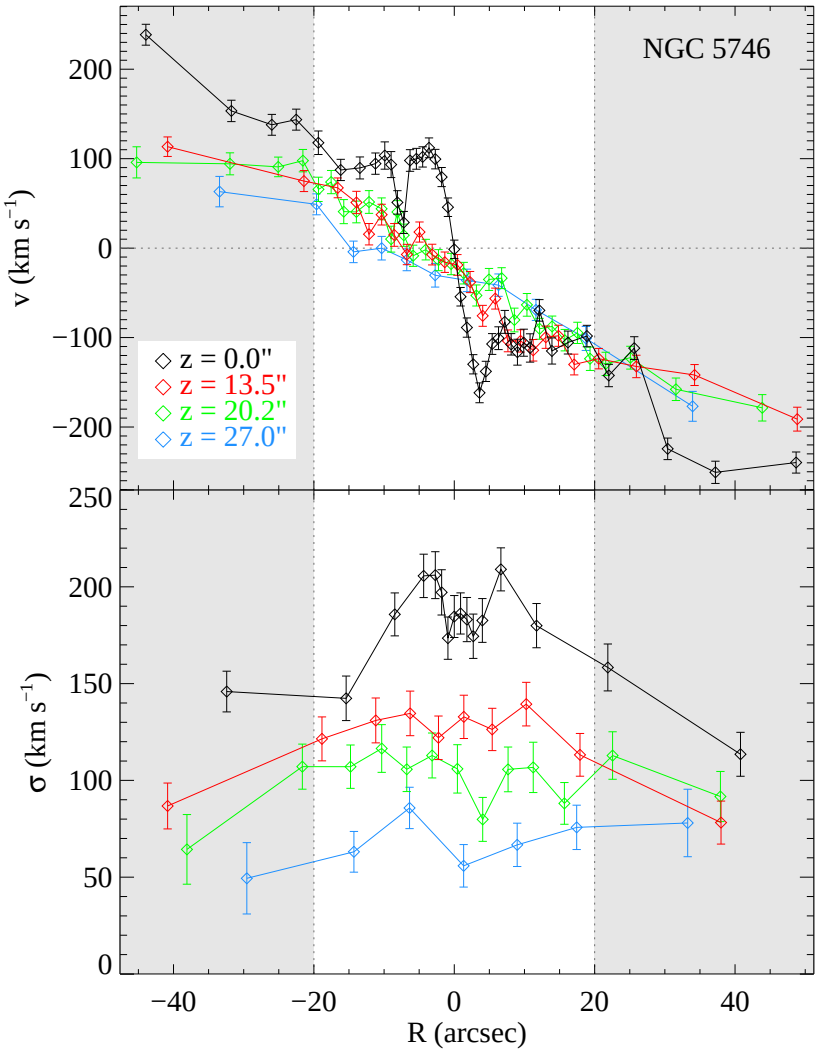

Figure 4.3: — continued

are the lines of constant velocity (e.g. figure 6 of Combes et al. 1990 and figure 12 of Athanassoula & Misiriotis 2002). These is, however, no clear sign of a systemic strengthening or weakening of cylindrical rotation as the viewing angle varies in these published studies.

On a different note, in ESO 311-G012, NGC 1381, NGC 3390 and NGC 5746 (i.e. all the galaxies with boxy or peanut-shaped bulges except IC 4767), there is a general downwards trend in velocity dispersion with increasing height above the disc. This is most clear in ESO 311-G012 and NGC 5746. This behaviour is also seen in classical bulges (Fig. 4.1), but the details of the variation of the velocity dispersion with height were crucial constraints in the Milky Way models of Howard et al. (2009)

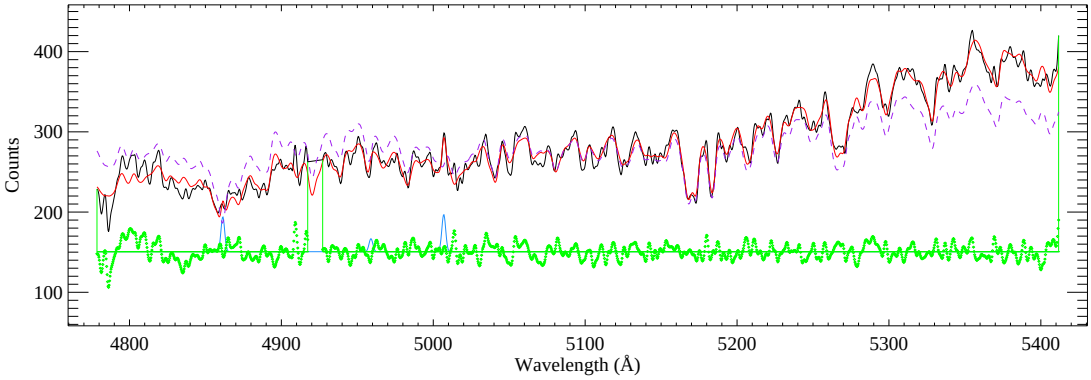

Figure 4.4: Example GANDALF fit for one of the two disk spectra of NGC 3390. We show the observed spectrum (degraded to the MILES resolution) in black and the GANDALF best fit in red. The green points are the difference between the best fit and the observed spectrum, shifted by an arbitrary positive offset so they appear on the scale. The best fit is comprised of the Hβ and [O III] emission lines (shown in blue) and a combination of MILES template stars that are convolved by a LOSVD (purple dashed line) and multiplied by a 6th order polynomial to account for the relative continuum differences between our setup and the MILES library. The anomalous feature at $\approx$4920 Å is due to a problem with the CCD, and is masked for all analyses.

and Shen et al. (2010). The authors placed an upper limit on the possible contribution of any dynamically hot spheroid component by comparing photometric and kinematic observations to dynamical models. Their analysis implies that the Milky Way has, at most, an extremely low-mass classical bulge, i.e. it is a pure disc galaxy (but see Babusiaux et al., 2010). Without a comparison to dynamical models custom-made for each galaxy, which is beyond the scope of the present work, it is not possible here to draw such a strong conclusion on the basis of our velocity and dispersion profiles.

4.4 LICK INDICES AND STELLAR POPULATIONS

4.4.1 Methods

The spatial variations of stellar population properties offer additional constraints on the nature and evolution of bulges. We therefore measured the strengths of the absorption lines present in our data (Hβ, Fe5015, Mg b, Fe5270, Fe5335 and Fe5406)

in the Lick/IDS system (Burstein et al., 1984; Worthey, 1994; Trager et al., 1998) and compared these to single stellar population (SSP) models, yielding SSP-equivalent luminosity-weighted ages, metallicities [Z/H] and α-element enhancement [α/Fe].

To make these measurements, we require high S/N to reliably subtract nebular emission and thus accurately measure the absorption line properties. We therefore bin the major-axis slit into three large bins: a single bin for the bulge and two disk bins (one from each side of the galaxy). We collapsed each of the three offset slits into single bins dominated by bulge light (rejecting the very small amount of thick disc light at larger galactocentric radii). This yields one bulge-dominated measurement from the centre of the bulge, two disc-dominated measurements along the major axis and three minor-axis bulge measurements at increasing galactic height. With data at four positions along the z-axis, it is not really possible to quantify vertical gradients (although as we discuss in the introduction, these are of interest). However, we can test our naive picture that a boxy bulge should have [α/Fe] similar to that of its host disc.

Of the absorption lines in our data, only Hβ provides a strong constraint on stellar age that is weakly dependent on metallicity (Worthey, 1994), but this absorption feature is unfortunately often filled in by emission. To compare the population properties of galaxy discs and bulges, we therefore restrict our analysis to those galaxies whose major-axis disk spectra are either free of emission or of sufficient S/N to allow reliable subtraction of the Hβ emission using GANDALF (Sarzi et al., 2006). This is only true for NGC 1381, which has no emission, and NGC 3390. The analysis that follows is therefore restricted to those two galaxies only.

We show an example GANDALF fit in Fig. 4.4. The best fitting GANDALF solution is comprised of the Hβ and [O III] emission lines and a combination of flux-calibrated MILES template stars that are convolved by a LOSVD and multiplied by a 6th order polynomial to account for the relative continuum differences between our setup and the MILES library. To produce an emission-cleaned spectrum that can be used to measure absorption line properties and compared to models, we subtract the GANDALF emission lines from the observed spectrum and divide it by the 6th order polynomial, achieving a rough relative flux calibration. In practice, the polynomial

is extremely slowly varying and close to first order over the bandpasses of the Lick indices, so this affects the measured line strengths at a level significantly below the uncertainties due to the noise.

It is then possible to measure the strengths of the lines in the Lick/IDS system, which we do using the method of Kuntschner (2000). But before these measurements are made, the spectra must be broadened by a wavelength-dependent Gaussian to account for the difference between the spectral resolution of our setup and that of the Lick/IDS system. The resulting indices are further corrected for (1) the broadening effects of the galaxies' velocity dispersions (which generally reduce the strength of absorption features) and (2) the small systematic offsets caused by, e.g., the remaining differences between the continuum shapes our spectra and the Lick/IDS spectra. We apply the offsets from the MILES system given in the appendix of Paudel et al. (2010). This offset of course only affects the absolute value of the indices, not their spatial gradients.

We use the line strengths to measure stellar population properties using the models of Thomas, Maraston & Bender (2003). These models incorporate non-solar [α/Fe]. The best fitting SSP-equivalent model for each spectrum is found by exploring an interpolated grid of model Lick indices in age, [Z/H]and [α/Fe](see, e.g., Proctor, Sansom & Reid, 2000; Kuntschner et al., 2010). We exclude Fe5015 from this analysis. It is still sometimes contaminated by [O III] emission, it is close to the bad pixels on the CCD, and it covers an extremely wide bandpass so is subject to relatively large continuum systematics and Lick offsets. This line provides very little additional constraints on the optimal SSP over those offered by the other three Fe lines.

4.4.2 Results

We show the derived Lick indices and corresponding SSP-equivalent luminosity-weighted age, [Z/H] and [α/Fe] as a function of height above the galactic plane in Fig. 4.5. There are two additional points on the major axis ($z = 0$), which are the measurements from the two disk bins.

In both galaxies, there is no sign of a systematic trend in the age-sensitive Hβ line as a function of z, or in the derived age.

In NGC 1381 there are broadly decreasing trends with increasing height in the metallicity-sensitive Fe and Mg lines. These are qualitatively similar to the minor-axis trends seen in the SAURON classical bulges shown in Fig. 4.1 (see Kuntschner et al. 2006 for the corresponding line strength maps). The SSP-equivalent stellar population properties derived from these line strengths suggest that the bulge is comprised of an old stellar population, $\gtrsim 10$ Gyr with no systematic trend in age as a function of z, but there is a clear decreasing trend in [Z/H]. We also note that [α/Fe] in the bulge at large z is greater than that in the disk bins (and indeed the central bin of the major axis). The simplest interpretation of these results is that NGC 1381 is comprised of a disk and a bulge whose stars formed rapidly. This explains the general trend in [α/Fe] as a function of height, as disk light (with its lower [α/Fe]) contributes less and less to the integrated spectrum. In summary, the bulge of NGC 1381 is chemically similar to that of classical bulges and elliptical galaxies.

Given this classical bulge behaviour, how do we explain the boxy appearance of the bulge? We speculate that this is a composite bulge: its chemical properties are explained by the presence of a classical bulge, but its appearance suggests the simultaneous presence of a bar (which appears boxy in projection). This is consistent with the stellar rotation, neither cylindrical nor strongly non-cylindrical. The double-hump of the rotation curve even hints at the presence of a small discy pseudobulge. This galaxy thus seems to have all three kinds of bulges.

The situation in NGC 3390 is much simpler. Within the (not insignificant) uncertainties, its bulge has no minor-axis metallicity gradient, and the [α/Fe] measurements in the bulge bins at large z are entirely consistent with those of the disc. That is to say, this galaxy's bulge is made of material similar to that in its disc, and the process that has scattered it to large z has not established a systematic metallicity gradient. This is consistent with the kinematics of this bulge, which is cylindrically rotating to great precision in all the slits (including the major axis). The simplest interpretation of NGC 3390 is therefore that it is a pure disk galaxy.

4.5 DISCUSSION

We analysed the kinematics and stellar populations of the boxy or peanut-shaped bulges of a sample of five edge-on disk galaxies. One boxy bulge (NGC 3990) rotates perfectly cylindrically, while another (ESO 311-G012) is very close to cylindrical. It is not possible to determine the nature of the rotation in the boxy bulge of NGC 1381 or the peanut-shaped bulge of NGC 5746. The peanut-shaped bulge of IC 4767 is in normal rotation, the velocity falling systematically with height. Cylindrical rotation is therefore not ubiquitous in bulges that appear boxy or peanut-shaped. We tentatively note that cylindrical rotation may be less strong or even absent in peanut-shaped bulges, compared to boxy bulges. Our sample is small and this work is exploratory, but the ubiquity of strongly cylindrical rotation in simulations of bar formation is in apparent contradiction with these observations.

Low S/N and the presence of emission are less of a problem when determining absorption line stellar kinematics than when measuring absorption line strengths of SSP-equivalent population properties. We were therefore only able to measure minor-axis trends in Lick indices and luminosity-weighted SSP-equivalent age, [Z/H] and [α/Fe] in two of the five galaxies. Of these, NGC 3390 exhibits behaviour consistent with being a pure disc: there is no significant difference in [Z/H] and [α/Fe] between the disk and the boxy bulge at large galactic heights, suggesting that the boxy bulge formed from redistributed disk material. NGC 1381, however, shows a clear negative metallicity gradient as a function of z, while [α/Fe] in the bulge at large z is significantly enhanced compared to that in the disc. This behaviour is consistent with a simple disk + classical bulge model (e.g. Norris, Sharples & Kuntschner, 2006, for the edge-on S0 NGC 3115). Combined with the marginal cylindrical rotation and the boxy shape of the bulge, this suggests that the centre of NGC 1381 hosts a composite bulge comprised of a classical bulge, a discy pseudobulge and a thick bar.

The naive expectation that we described in our introduction, that a boxy bulge should have the same [α/Fe] as its host disk if it formed through the bar buckling scenario and is part of a pure disk galaxy, is one part of our argument that NGC 3390

Figure 4.5: Lick indices and luminosity-weighted SSP-equivalent ages, metallicities and [α/Fe] ratios as a function of the perpendicular distance to the major axis for NGC 1381 and NGC 3390. Measurements are made at the center of the galaxy (black circle at z = 0), two disk bins along the major axis (blue diamonds) and three points at increasing distance along the minor axis (black circles at $z \neq 0$). The disk bins correspond to spectra at $z = 0$, but we added a spatial offset of $\pm 1''$ for clarity in these plots. The $z = 12''$ bulge spectrum in NGC 1381 has some line strengths that are consistent with an equivalent width of zero, and the uncertainties in [α/Fe] for this bin extend over the full model grid. The position is shown merely for completeness. The Fe5406 feature is redshifted beyond the observed wavelength range for NGC 3390 and could therefore not be measured.

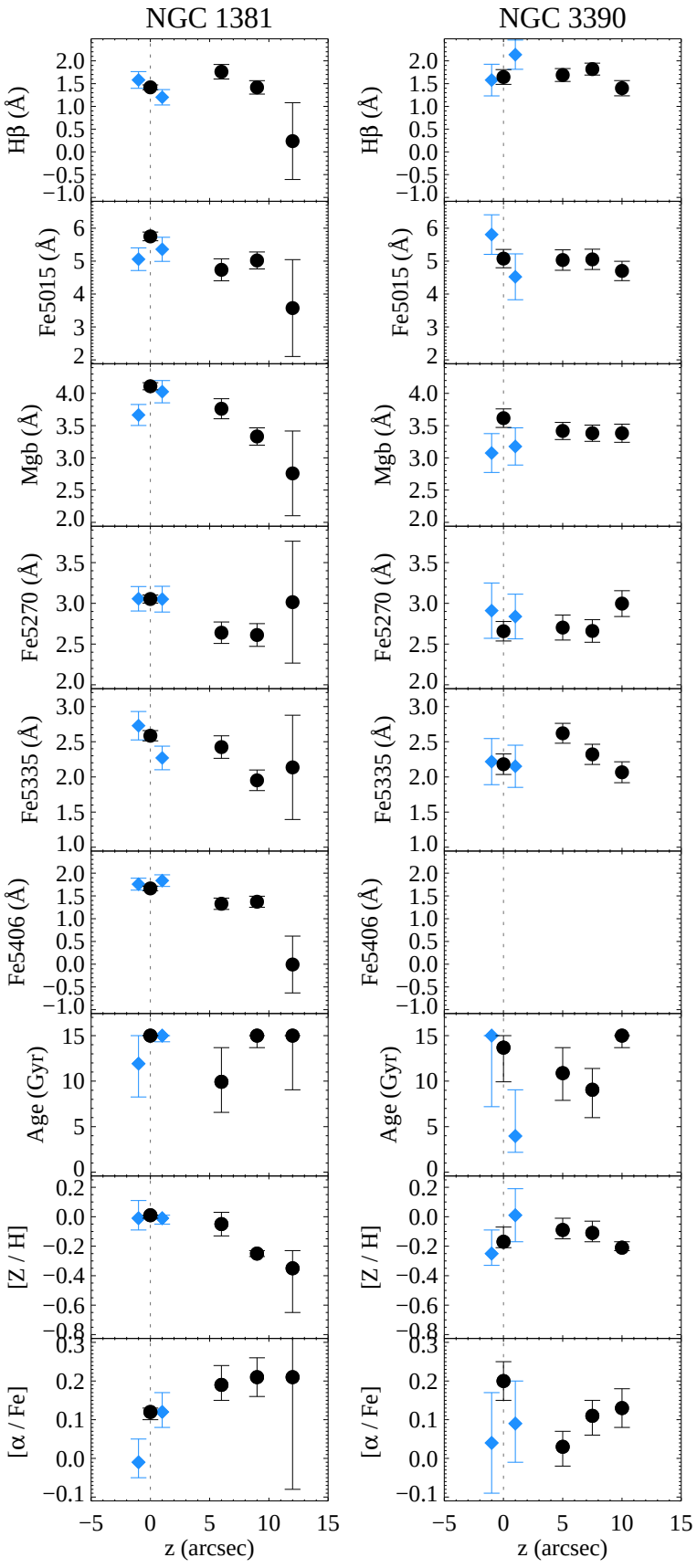
NGC 1381
NGC 3390
Hβ (Å)
Fe5015 (Å)
Mgb (Å)
Fe5270 (Å)
Fe5335 (Å)
Fe5406 (Å)
Age (Gyr)
[Z / H]
[α / Fe]
z (arcsec)

may be a pure disk galaxy. This picture is complicated by at least two issues. (1) The disk could have formed rapidly and then buckled promptly, forming an α-enhanced bar, and (2) In a system made up of stars in which [α/Fe] is anticorellated with [Z/H] (e.g. as seen in young stars in the Galaxy, Edvardsson et al. 1993), a negative spatial metallicity gradient would necessarily coincide with a positive spatial [α/Fe] gradient.

Regarding point (1), we note that the 'wild disc' scenario (in which early star formation in the progenitors of disk galaxies takes place on short timescales in massive clumps, e.g. Noguchi 1999; Elmegreen, Elmegreen & Hirst 2004; Bournaud, Elmegreen & Elmegreen 2007) probably cannot explain how a bar could be α-enhanced with respect to its host disc. In simulations, these clumps rapidly migrate inward through dynamical friction and combine to form an axisymmetric feature that would probably look like an α-enhanced classical bulge (both in terms of populations and dynamics). Chemodynamical simulations of bar formation are clearly necessary.

Such studies should also address the more general questions raised by this work. (1) Is the double hump we see in the rotation curve along the major axis of two of the boxy and peanut-shaped bulges definitely associated with a flattened discy pseudobulge? How far does its influence extend above the plane? (2) How does the viewing angle of the bar affect the observed kinematics? For example, do we expect weaker cylindrical rotation in peanut-shaped bulges? (3) Do the minor-axis metallicity and age gradients of simulated bars differ systematically from those of classical bulges? (4) Can simulated bars form in a way that explains the presence of a positive minor-axis [α/Fe] gradient, as seen in NGC 1381, without the additional presence of a classical bulge?

The α-enhanced bulge of NGC 1381 suggests that not all boxy bulges are found in pure disk galaxies (although some, including the Milky Way, may be). Since the prevalence of giant pure disk galaxies is an acute problem for simulations of galaxy formation in a cosmological context, it is clear that a combined analysis of stellar dynamics and populations of the central regions of galaxies in an extremely powerful tool.

The sample we have studied in the present work is unusual because it is dominated by boxy and peanut-shaped bulges. Such galaxies are unique laboratories

to investigate the nature of the bars which drive secular evolution. Moreover, they raise the possibility that a demographically significant fraction of giant disk galaxies, making up about half the population that happen to be oriented edge-on, are pure disk galaxies. We have shown that a property as simple as the degree of cylindrical rotation varies significantly amongst boxy/peanut-shaped bulges, as do the properties of their stellar populations. Since simulations indicate that cylindrical rotation is a fairly universal feature of such bulges created from buckling bars, even this modest sample is sufficient to demonstrate that the formation of these systems cannot be entirely explained by this single mechanism. Clearly, if we want to further our understanding of the formation of boxy and peanut-shaped bulges, we need data in larger quantities, to look for correlations with other galaxy properties such as their environment. Higher-quality two-dimensional data from integral-field units would also be beneficial, allowing the population properties to be determined with greater precision and the dynamics to be modelled in detail and without the uncertainties associated with slit alignment and aperture effects.

5

THE RADIAL STRUCTURE OF BOXY BULGES: STELLAR KINEMATICS, GAS KINEMATICS AND STELLAR POPULATIONS OF 28 GALAXIES

5.1 INTRODUCTION

In Section 4.1 we described the three observational classes of bulges (classical bulges, pseudobulges and boxy/peanut-shaped bulges). In that introduction we also discussed in a qualitative sense their stellar populations in comparison to elliptical galaxies and to each other. This chapter is devoted to those populations, so we begin by discussing them in more detail.

The properties (age, metallicity, abundance ratios) of spatially unresolved populations of stars are most directly probed through their integrated absorption line spectra. The usual approach is to measure the equivalent widths of individual absorption features in the spectrum (e.g. Faber et al., 1985; Worthey, 1994). Although observationally more time-consuming to determine than other probes of the chemical properties of galaxies, e.g. broadband colours or the emission spectra of H II regions, absorption line strengths have advantages that are particularly relevant for the sample of edge-on disk galaxies studied in the present work: (1) because each line covers a narrow range in wavelength they are almost unaffected by dust along the line-of-sight (MacArthur,

2005), and (2) they can be studied in galaxies of all types, including those with little gas, which eliminates the systematic uncertainties associated with comparisons across the Hubble sequence.

5.1.1 *Central and global scaling relations in ellipticals and bulges*

Among the many correlations between the line strengths and photometric and structural properties of elliptical galaxies (see Renzini 2006 for a review), perhaps the strongest and best-studied is that between the strength of the Mg b feature (either in the centre of the galaxy or averaged over some aperture) and the central velocity dispersion or mass (e.g. Terlevich et al., 1981; Bender, Burstein & Faber, 1993; Burstein et al., 1988; Kuntschner, 2000; Thomas et al., 2005; Kuntschner et al., 2006). Stellar population models demonstrate that Mg b absorption line strength is a strong function of metallicity [Z/H], and a weaker function of the enhancement of α-elements [α/Fe] and of stellar age. The existence of the Mg b–σ relation is therefore the observable consequence of presumably more fundamental relations between the mass of ellipticals and their global or central stellar populations. Indeed detailed analysis of multiple absorption features and comparison to population models reveals such scaling relations: for increasing velocity dispersion or mass, elliptical galaxies are older, more metal rich and are more [α/Fe] enhanced (e.g. Thomas et al., 2005; Kuntschner et al., 2010).

As we mentioned in Section 4.1, analogous observations and analysis of the bulges of disk galaxies are more challenging than in ellipticals: the bulges are fainter and embedded in disks, and they may have complicated or ongoing star formation histories, nebular emission, and significant dust absorption. Nevertheless, the consensus is that very similar central and global scaling relations are observed in the bulges of early-type (S0-Sbc) disk galaxies; at a given velocity dispersion, their line strengths and the implied stellar populations are, on average, the same as those of ellipticals (Proctor & Sansom, 2002; Thomas & Davies, 2006; Falcón-Barroso et al., 2006; Bedregal et al., 2008; MacArthur, González & Courteau, 2009). In combination with dynamical and structural similarities, this is taken as evidence that the (classical) bulges of these

galaxies formed in a similar way to ellipticals. The good agreement between bulges and ellipticals breaks down to a degree in the bulges of late-type spirals. For example, Ganda et al. (2007) observed that the bulges of a sample of 18 Sb–Sd galaxies lie below the Mg b–σ and above the Hβ–σ relation of ellipticals/classical bulges. These differences may be evidence that they formed or are currently affected by different processes to ellipticals/classical bulges, the most likely being the secular and internal rearrangement of disk material (Kormendy & Kennicutt, 2004).

5.1.2 *Gradients in ellipticals and bulges*

The determination of radial trends in absorption line strengths or stellar populations is naturally more challenging than central or global properties, but they act as a powerful discriminant between competing models of galaxy formation. Monolithic collapse models (e.g. Eggen, Lynden-Bell & Sandage, 1962; Larson, 1974; Carlberg, 1984; Pipino & Matteucci, 2004) predict steep negative metallicity gradients of Δ[Z/H] between -0.35 and -1.0.[1] Hierarchical models predict that these gradients become shallower as radial trends are diluted by mergers, although the star formation that takes place in gas-rich mergers complicate this basic picture (Kobayashi, 2004; Hopkins et al., 2009a,b).

The observational constraints on radial stellar population gradients in ellipticals (e.g. Davies, Sadler & Peletier, 1993; Kuntschner et al., 2006; Spolaor et al., 2009; Kuntschner et al., 2010) may be summarized as follows (1) For most galaxies, $\Delta \log(\mathrm{age/Gyr}) \approx 0$. This is not true in galaxies with central star formation (which is more common in lower velocity dispersion/lower mass systems), where the depressed central ages lead to positive age gradients. (2) $\Delta[\mathrm{Z/H}] \approx -0.2 \pm 0.1$. Below a central velocity dispersion of $\approx 150\,\mathrm{km\,s^{-1}}$ (equivalent to a dynamical mass $\approx 3 \times 10^{10}\mathrm{M}_{\odot}$), there is evidence of a correlation between the steepness of this gradient and velocity dispersion, in the sense that more massive systems have steeper gradients (Spolaor et al., 2009). Above these characteristic values, the correlation between gradient

[1] We follow convention by characterizing radial gradients with linear fits in $\log R$, and using the notation $\Delta \mathrm{X} \equiv \partial \mathrm{X}/\partial \log R$, where X is [Z/H], [$\alpha$/Fe] or log(age/Gyr).

and dispersion or mass becomes much weaker, but the metallicity gradients remain negative. (3) $\Delta[\alpha/\mathrm{Fe}]$ is very close to zero at all dispersions and masses.

The radial trends in the bulges of spiral galaxies are known with considerably less certainty. The major studies are Moorthy & Holtzman (2006, long-slit observations of the bulges of 38 galaxies ranging from S0 to Sbc), Falcón-Barroso et al. (2006) and Peletier et al. (2007, SAURON IFU observations of the bulges of 24 Sa galaxies), Ganda et al. (2007, SAURON IFU observations of the bulges of 18 Sb–Sd galaxies), Jablonka, Gorgas & Goudfrooij (2007, *minor* axis long-slit observations of the bulges of 30 edge-on S0 to Sc galaxies), Morelli et al. (2008, long-slit observations of the bulges 18 S0–Sbc galaxies) and MacArthur, González & Courteau (2009, long-slit observations of the bulges of 8 Sa–Sd galaxies). Among the areas of agreement of these studies is the finding that most bulges have negative metallicity gradients. Compared to ellipticals, however, there is rather more scatter in these gradients and more diversity in the structure of the radial profiles.

5.1.3 Radial trends in bars

This observation brings us on to the subject of bars (and, by implication, boxy/peanut-shaped bulges), since the presence and strength of bars in disk galaxies may be the driver of the diversity in radial stellar population abundance trends in disk galaxies. Simulations of chemodynamical evolution of barred disk galaxies find that they drive inflow of gas within corotation and outflow beyond corotation (e.g. Friedli, Benz & Kennicutt, 1994; Friedli, 1998). This radial transport naturally flattens pre-existing gradients (see Fig. 5.1).

Consistent with this prediction, relatively flat abundance profiles in the gaseous H II regions of barred spirals were discovered some time ago (e.g. Vila-Costas & Edmunds, 1992; Zaritsky, Kennicutt & Huchra, 1994; Dutil & Roy, 1999). Moreover, the transition from the steep gradient presumed to be maintained by vigorous star formation enrichment in the region within corotation, to the shallower gradient caused by radial transport in the absence of star formation in the region beyond, has also

Figure 5.1: Radial abundance profiles in simulations of barred galaxies (figure taken from Friedli 1998, ommited here for copyright reasons). *Left:* Time evolution of the stellar radial abundance profile in a galaxy model forming a strong bar. CR indicates the location of the corotation radius at 2000 Myr. *Right:* Comparison of radial gradients between systems having no bar, a weak bar, and a strong bar (at T = 2000 Myr).

been observed (Zaritsky, Kennicutt & Huchra, 1994; Martin & Roy, 1995; Roy & Walsh, 1997).

Until very recently, equivalent observations of abundance gradients in the stellar populations of barred galaxies were missing. They are a crucial addition to our knowledge because the bars that reside in two-thirds of disk galaxies likely play a significant role in transforming the stellar populations of their hosts, and the simulations suggest that the behaviour of the abundance trends in the stellar phase are different in detail to those in the gas phase (for which we do have observational constraints). Stellar populations also allow us to probe the history of star formation as a function of radius, which is of interest in the light of simulations that predict local minima in stellar age at the resonances at the end ends of bars (Wozniak, 2007).

Perez et al. have made the first systematic attempt to study radial stellar population trends in barred galaxies (Pérez, Sánchez-Blázquez & Zurita, 2007, 2009). They used optical spectra taken from long slits oriented along the bar major axis of of a sample of 20 face-on and moderately-inclined galaxies. Crucially, they restrict their analysis to a region beyond the central bulge but within the bar (determined by ellipse fitting).

Among these 20 galaxies, they identify three classes of radial abundance trends along along bars (1) bars with negative metallicity gradients, low central velocity dispersions and relatively young (< 2 Gyr) mean stellar populations (2) bars with no metallicity gradients and negative age gradients (i.e. a young population at the end of the bar), and (3) bars with positive metallicity gradients, large central velocity dispersions and older mean population. We note that the second of these classes is consistent with the simulations of Friedli, Benz & Kennicutt (1994) and Wozniak (2007) described above, i.e. shallow metallicity gradients and a young population at the end of the bar.

The goal of the present chapter is to study central values and radial trends in the stellar populations of bulges and bars by determining absorption line strengths and Single Stellar Population (SSP) equivalent age, [Z/H] and [α/Fe]. We use the Bureau & Freeman (1999) sample of edge-on disk galaxies. The majority (22/28) of the galaxies in this sample host bulges that are boxy or peanut-shaped, i.e. bars viewed in projection. In Section 5.2 we describe the sample, observations and data reduction. In Section 5.3 we describe the methods used to determine the stellar and gas kinematics, and to clean the spectra of nebular emission. In Section 5.4 we describe the measurement of Lick/IDS absorption line indices and their comparison to SSP models. Finally, in Section 5.5 we discuss the central and global stellar populations, and in Section 5.6 we discuss the radial trends and gradients.

5.2 OBSERVATIONS AND DATA REDUCTION

The sample of 28 galaxies is described in Section 1.4. Spectroscopic observations of the sample were made between December 1995 and April 1997 by Martin Bureau on a series of ten runs on the Double Beam Spectrograph (DBS) on the 2.3 m telescope at Siding Springs. In the instrumental setup used, the DBS takes two spectra, each covering a range of ≈ 1000Å. The blue arm was centred on the continuum absorption features around the Mg b triplet (rest wavelength of 5167, 5172 and 5183 Å). The red arm was centred on the Hα emission line when detected (6563 Å) or moved to the Calcium triplet (8498, 8542 and 8662 Å). The red spectra therefore suffer from emission

Table 5.1: DBS sample data. See Tables 2.1 and 3.1 for additional properties

Galaxy	R_{box} (arcsec)	S/N (per Å)	Hβ	Fe5015	Mg b	Fe5270	Fe5335	Fe5406
			B/PS bulge sample					
ESO 151-G004	10	20.2	X	X	X	X	X	X
ESO 185-G053	14	27.0	X	X	X	–	X	X
ESO 240-G011	6	33.7	X	X	X	–	X	X
ESO 311-G012	15	33.7	X	X	X	–	–	X
ESO 443-G042	13	20.2	X	X	X	–	X	X
ESO 597-G036	10	20.2	X	X	X	X	X	–
IC 4767	18	20.2	X	X	X	–	X	X
IC 4937	9	20.2	X	X	X	–	X	X
IC 5096	8	27.0	X	X	X	–	X	X
NGC 128	15	33.7	X	X	X	–	X	X
NGC 1381	10	40.5	X	X	X	–	–	X
NGC 1596	14	40.5	X	X	X	–	–	X
NGC 1886	7	27.0	X	X	X	–	–	X
NGC 2310	16	40.5	X	X	X	–	–	X
NGC 3203	17	27.0	X	X	X	–	X	X
NGC 3390	11	27.0	X	X	X	–	X	X
NGC 4469	25	27.0	X	X	X	X	–	X
NGC 4710	21	40.5	X	X	X	X	X	X
NGC 5746	21	40.5	X	X	X	–	–	X
NGC 6722	9	27.0	X	X	X	–	X	X
NGC 6771	15	27.0	X	X	X	–	X	X
PGC 44931	16	20.2	X	X	X	–	X	X
			Round bulge control sample					
IC 5176	–	27.0	X	X	X	–	–	X
NGC 1032	–	33.7	X	X	X	–	X	X
NGC 3957	9	27.0	X	X	X	–	–	X
NGC 4703	11	33.7	X	X	X	–	X	X
NGC 5084	–	67.5	X	X	X	–	–	X
NGC 7123	8	32.4	X	X	X	–	X	X

Notes. R_{box} is the radius of the maximum scale height of the galaxy, as measured from the vertical photometric parametrizations presented in Bureau, Aronica & Athanassoula (in preparation). It coincides with the approximate edge of the boxy bulge, and is therefore correlated with the projected length of the bar (see Section 5.5.1). S/N is the minimum signal-to-noise to which each galaxy spectra was binned. 'X' denotes an absorption feature whose Lick index was used to constrain the SSP fit, while '–' denotes a feature that was not used (see Section 5.4)

or strong atmospheric absorption and cover a wavelength range where SSP models are poorly constrained. The blue arm spectra are the sole focus of this chapter.

We reduced the data from the blue arm using the same standard IRAF techniques we applied in Chapter 4, yielding a flat-fielded, wavelength-calibrated sky-subtracted long-slit spectrum along the major axis of each galaxy. Cumulative exposure times ranged from 200 to 400 minutes per object. The reduced two-dimensional spectra were linearly binned in wavelength and cover the range 4755–5710 Å. The spectral resolution

of the instrument is 1.2 Å full-width half-maximum (equivalent to $\sigma_{\rm inst} \approx 30\,{\rm km\,s^{-1}}$ at 5150 Å). The spatial axis has a pixel scale of 0.91 arcsec/pixel.

5.2.1 *A note on flux calibration*

To measure Lick indices reliably, spectra should be flux calibrated so that any variation in the flux response of the instrument on the scale of the relevant absorption features is, at most, first order as a function of wavelength. We were unable to directly flux calibrate the NTT/EMMI spectra we used in Chapter 4 because spectrophotometric flux standards were not observed during each run. This was not of great concern with the those data because the response function of that instrument is stable across the relevant wavelength range, with no sign of higher order variation on the scale of the Lick indices, except at the very edges of the spectra.

This is not the case with the DBS spectra in the present chapter. Among other difficulties, the blue arm of the DBS spectrograph has a prominent 'kink' in its response function at a wavelength of ≈ 5000 Å (which is often within the redshifted Hβ Lick index range). The DBS data was collected in 10 runs over a period of 16 months, but spectrophotometric standards were only observed during the final run. However, the spectra of a handful of K stars were observed alongside the galaxies on every run. These stars were originally observed with the intention of using them as templates to convolve with trial LOSVDs to determine the stellar kinematics, which is indeed how they were used in Chung & Bureau (2004). However, we took advantage of them in the present work to perform a 'secondary' flux calibration. Using the observations of spectrophotometric standards taken on the final run and standard IRAF techniques (the `standard`, `sensfunc` and `calibrate` tasks), we flux calibrated the velocity standards. We then used these flux-calibrated velocity standard spectra as secondary flux standards, with which we flux calibrated the galaxy spectra observed in earlier runs.

This somewhat convoluted procedure was necessary because we had no reason, *a priori*, to believe that the DBS spectrograph had a stable flux response over the 18

months that separated the first and last run. In practice, however, the response function of the instrument was found to be extremely stable from run to run so this secondary standard procedure turned out to be more complex than was necessary. Had we applied the response function from the final run to all the other runs directly, we would have recovered Lick indices that agreed at a level well within the observational uncertainties with the those we measured using the more sophisticated calibration procedure we actually used. This process therefore does not affect the results that follow.

5.3 STELLAR AND GAS KINEMATICS

Our goal in the present work is to measure the strengths of the absorption lines present in our data and to compare these to single stellar population (SSP) models. It is not to study the stellar or gas kinematics per se, but these are prerequisites and by-products of the measurement of absorption line properties.

To reliably measure the stellar kinematics, emission line properties and absorption line strengths, we binned the outer regions of each spectra spatially. Our target S/N per Å was 30, but this was not possible in all cases (see Table 5.1). The relatively low S/N of some of the spectra are reflected in the uncertainties on the derived quantities that follow (especially the line strengths) and the lack of spatial resolution of the binned spectra.

Stellar kinematics were extracted using identical techniques to those used in Chapter 4, i.e. using penalized pixel fitting (PPXF; Cappellari & Emsellem 2004). The reader is referred to Section 4.3 where we describe the principles and technical details of this procedure. As in Chapter 4, we used a subset of 88 stars from the MILES library of 985 observed stellar spectra as templates (Sánchez-Blázquez et al., 2006b). Unlike the NTT/EMMI data, however, the DBS data are of sufficient noise to constrain the skewness (h_3) and kurtosis (h_4) of the Gauss-Hermite parametrization of the LOSVD.

The next step is to clean any Hβ, [O III] and [N I] emission, which are the three nebular emission features present in our wavelength range. The Hβ emission line

occurs in the central passband of the Hβ absorption Lick index, while [O III] and [N I] occur in the continuum passbands of Fe5015 and Mg b respectively. The emission lines are cleaned by measuring their positions, widths and amplitudes using GANDALF (Sarzi et al., 2006). GANDALF takes as input a library of template spectra, the (known) stellar kinematics, and the approximate kinematics and rest wavelength of the emission lines, and returns the best fitting kinematics of each emission line and a spectrum cleaned of emission. The LOSVDs of the emission lines are assumed to be pure Gaussians.

We follow the SAURON project in using physically motivated and well-understood SSP spectra as continuum templates for GANDALF, rather than the real stars favoured for PPXF (Emsellem et al. 2004 and Cappellari et al. 2007 for PPXF; Sarzi et al. 2006, 2010 for GANDALF). In particular, we use the same subset of Vazdekis et al. (2010) SSP templates augmented by semi-empirical templates derived from emission-free regions of SAURON galaxies used in Sarzi et al. (2010). A detailed investigation of template selection and its consequences for the inferred emission line properties is outside the scope of the present work. We note, however, that this choice has an effect on the subsequently measured absorption line widths that is much smaller than the associated uncertainties on those properties due to the photon statistics of the continuum.

Because our data are of relatively low S/N, it is difficult to independently constrain the kinematics of each emission line. The Hβ line, which sits at the bottom of the strong Hβ absorption feature, is particularly problematic. When the kinematics of this emission line are fitted independently in low S/N bins, we recover velocity dispersions that are unphysically discrepant from those of the [O III] emission line and the stellar kinematics (often larger by $\gtrsim 100\,\mathrm{km\,s^{-1}}$). We therefore impose the kinematics of the [O III] emission line on the Hβ and [N I] lines. This simplification is justified for our limited goals (cleaning emission) because (1) in the high S/N galaxies in our sample, where the kinematics of the Hβ emission line can be reliably constrained, there is no evidence that they differ systematically from those of the [O III] line, and (2) there is also no evidence that the Hβ and [O III] emission line kinematics differ by an amount greater than their uncertainties in similar analyses of

either the SAURON early-type sample (Sarzi et al., 2006) or the SAURON spiral bulge sample (Falcón-Barroso et al., 2006).

We only remove emission from the spectrum if a line is detected. We deem an emission line 'detected' if its amplitude A exceeds the rms of the residuals of the fit N by some constant multiple (see Fig. 4.4). If the A/N threshold is set too low then poorly constrained or spurious emission features are detected and erroneously cleaned (false positives). If A/N is set too high then emission is not cleaned (false negatives). Extensive simulations led the SAURON project to set these thresholds at 3, 4 and 4 for Hβ, [O III] and [N I] respectively (Sarzi et al., 2006). We adjust these thresholds downwards to 2, 3 and 3 for the following reasons.

False negatives can result in systematic errors $\sim \mathrm{EW}_{\mathrm{max}}$ in the measured strengths of nearby absorption features, where $\mathrm{EW}_{\mathrm{max}}$ is the maximum equivalent width of an undetected emission line. $\mathrm{EW}_{\mathrm{max}}$ is given by eqn. 1 of Sarzi et al. (2006):

$$\mathrm{EW}_{\mathrm{max}} = \frac{A/N \times \sqrt{2\pi}\sigma}{S/N}, \tag{5.1}$$

where σ is the typical width in Å of an emission line (including the effects of instrumental broadening). This relation shows that for a given A/N threshold, stronger emission features can go undetected as S/N falls. For example, if $\sigma \approx 100\,\mathrm{km\,s^{-1}}$ (i.e. $\sigma \approx 1.7$ Å at [O III] λ5007) and S/N per Å ≈ 30, which is typical of the DBS sample, this yields $\mathrm{EW}_{\mathrm{max}} \approx 0.14\,A/N$ Å. False negatives in [O III] and [N I] are a relatively insignificant problem for the Fe5015 and Mg b absorption features; the emission is in the continuum passband for these features, and the features themselves are strong (in the Lick/IDS system they typically have equivalent widths > 3 Å). However, false negatives are a problem for Hβ; they fill in the absorption line itself, the Hβ Lick index is often as small as 1.5 Å, and the SSP-equivalent age is an extremely sensitive function of Hβ in this range, varying by 10 Gyr for just a few tenths of an Å change in Hβ. To ameliorate all these problems in our low S/N data, we reduce the SAURON A/N thresholds. We emphasize, however, that reasonable choices of this threshold do not qualitatively affect the results we present in this chapter.

The results of our measurements of the stellar and gas kinematics are presented in Section 5.A. As we mentioned at the beginning of this section, our goal in the

present work is not to investigate the stellar or gas kinematics. Both have been extensively discussed elsewhere (Bureau & Freeman, 1999; Chung & Bureau, 2004). Nevertheless, we briefly mention a few notable features. We see striking examples of counter-rotating gas in NGC 128, NGC 1596 and NGC 3203 (previously reported in Bureau et al. 2006). The stellar kinematics we recover with PPXF agree very well with those measured on the same spectra using the Fourier Correlation Quotient method in Chung & Bureau (2004). The exception is h_4. On average, we recover h_4 kurtosis parameters that are more likely to be positive than was found in Chung & Bureau (2004). We attribute this to our larger template library of 88 stars, which minimises mismatch (Chung & Bureau 2004 used only three template stars). Finally, we note the that the mean line-of-sight velocity of the gas appears to be significantly greater than that of the stars in the B/PS bulges of NGC 4469, NGC 5746 and PGC 44931, and in the round bulge of NGC 1032. This may be due to the concentration of gas on the x_2 orbits associated with bars, and is discussed extensively in Bureau & Freeman (1999).

5.4 MEASURING LICK INDICES AND SSP-EQUIVALENT PROPERTIES

Using the stellar kinematics and emission-cleaned spectra determined as described above, we measure the strengths of the absorption lines present in our data (Hβ, Fe5015, Mg b, Fe5270, Fe5335 and Fe5406) in the Lick/IDS system (Burstein et al., 1984; Worthey, 1994; Trager et al., 1998). We compare these Lick index measurements to a grid of SSP models, yielding SSP-equivalent luminosity-weighted ages, metallicities [Z/H] and α-element enhancement [α/Fe]. This procedure is described in detail in Section 4.4.1, but differed for the DBS data in two ways. (1) The spectra were flux calibrated at the reduction stage (see Section 5.2.1) so we did not multiply them by a corrective polynomial before measuring the Lick indices. (2) We use a different subset of the Lick indices to constrain the fit to the SSP-equivalent model. Unlike with the NTT/EMMI data we always use Fe5015 to constrain the SSP model since S/N was sufficient to subtract [O III] with confidence and the flux calibration is reliable. The Fe5270 or Fe5335 feature (depending on the galaxy redshift) were excluded because of

a prominent bad column on the CCD of the blue arm of the DBS. Fe5406 is excluded in the most distant galaxy because that line is redshifted into the strong [O I] sky line at 5577 Å. We tabulate the lines used for each galaxy in Table 5.1.

We show the complete results in Appendix 5.A. As in Chapter 4, the SSP models used for comparison are those of Thomas, Maraston & Bender (2003, TMB03 hereafter). The full fitting procedure is multidimensional, but for each galaxy we show a projection of the grid that is useful for visualization. The horizontal axis of this projection is [MgFe]′, a composite index given by

$$[\mathrm{MgFe}]' \equiv [\mathrm{Mg}\, b(0.72 \times \mathrm{Fe5270} + 0.28 \times \mathrm{Fe5335})]^{1/2}. \tag{5.2}$$

TMB03 showed that [MgFe]′ minimizes dependence on [α/Fe] and serves as the best tracer of [Z/H]. The vertical axis of the projection we show is simply Hβ, the best tracer of mean stellar age in our dataset (large Hβ corresponds to young SSP-equivalent age).

5.5 CENTRAL LINE STRENGTHS AND SSP PROPERTIES

Before addressing the radial trends in our data, we consider the line strengths and SSP-equivalent populations within a central aperture. To aid comparison with previous studies, we convert Lick indices to units of magnitudes using the definition

$$I^* \equiv -2.5 \log_{10} (1 - I/\Delta I) \tag{5.3}$$

where I is the index value and ΔI is the width of the index bandpass, both of which are measured in Å.

5.5.1 *Notes on aperture definitions*

The smallest meaningful aperture is set by seeing limit of the observations and the width of the slit, i.e. $3'' \times 1.8''$. We refer to the average quantities within this aperture as 'central', and denote them $\langle X \rangle_0$, where X is the Lick index or SSP-equivalent

quantity, e.g. $\langle \mathrm{Mg}\, b \rangle_0$ or $\langle [\mathrm{Z/H}] \rangle_0$. We also investigate quantities averaged over the range $0 < |R| < R_{\mathrm{eff}}$, which we denote, e.g. $\langle [\mathrm{Z/H}] \rangle_{\mathrm{eff}}$.

The final aperture we investigate is the boxy bulge, i.e. the bar. Estimating the size of a bar is not a trivial problem even in face-on galaxies (Erwin, 2005). In edge-on galaxies like our sample it is particularly problematic, since the relatively well-understood objective methods preferred in face-on galaxies (e.g. ellipse-fitting, Fourier analysis) are not appropriate. It is outside the scope of the present work to investigate this issue in detail. We therefore merely characterize (rather than measure) the size of the boxy/peanut-shaped region of the bulge by defining a quantity R_{box}, the radius of the local maximum in scale height that occurs near the edge of the box/peanut (Bureau, Aronica & Athanassoula, in preparation). This definition has the virtue of being objective and, in principle at least, correlated with the projected size of the bar. This quantity is undefined for the non-boxy bulges in the control sample, but for the boxy bulges we define the aperture $0 < |R| < R_{\mathrm{box}}$ and denote quantities averaged within this aperture, e.g. $\langle [\mathrm{Z/H}] \rangle_{\mathrm{box}}$.

There is little, if any, correlation between R_{eff} and R_{box} (see Fig. 5.2). This is presumably due to the fact that, while R_{eff} is related to the gross size of the galaxy, R_{box} is a function of the size of the galaxy, the size of the bar (which is correlated with the size of the galaxy, but with scatter, Erwin 2005), and the angle of the bar with respect to the line of the sight. Beyond our knowledge that the bar is probably not oriented very close to end-on (in which case it would not be strongly boxy), this viewing angle is unknown and certainly introduces further scatter.

We determine all aperture quantities by taking the luminosity-weighted mean average of the relevant quantity in the bins whose luminosity-weighted centre lies within the appropriate aperture. Formally, to measure the average line strength or SSP-equivalent populations within an aperture, one should make these measurements on a single binned spectrum constructed from the original 2D spectrum. However, this creates difficulties with the stellar and gas kinematics procedures described above because, in a rotationally supported galaxy, the larger the bin, the less Gaussian the LOSVD. Strongly non-Gaussian (or even double-horned) LOSVDs make determining the stellar kinematics or cleaning the emission extremely difficult, and both are

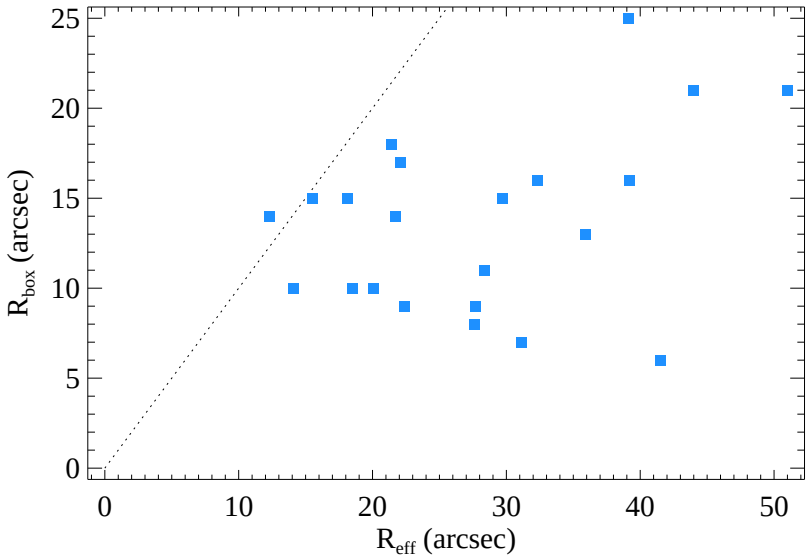

Figure 5.2: $R_{\rm eff}$ and $R_{\rm box}$ for the boxy/peanut-shaped bulges in our sample. The dashed line is the line $R_{\rm eff} = R_{\rm box}$.

prerequisites for measuring the strength of absorption lines. Kinematic measurements are best done in small bins, where the Gaussian (or Gauss-Hermite) approximation is valid. Luckily, in practice the difference between the true aperture line strengths or SSP-equivalent properties and those found by averaging smaller bins within the aperture is negligible with respect to the other errors on the line strengths or SSP-equivalent properties (see Appendix A of Bureau et al., 2011).

5.5.2 *Results*

We show our results in Fig. 5.3 (Lick indices) and Fig. 5.4 (SSP-equivalent populations). In both cases we show a representative comparison scaling relation for ellipticals and S0s. We find that there is no evidence that the central populations of our early-type disk galaxies differ from those of ellipticals at a given velocity dispersion.

Almost all of these galaxies are barred, and therefore good candidates for observing the effects of secular evolution. At least in terms of their central values, however, the stellar populations of these barred early-type disk galaxies are no different to those of elliptical galaxies (or indeed the six unbarred disk galaxies in our own sample). If,

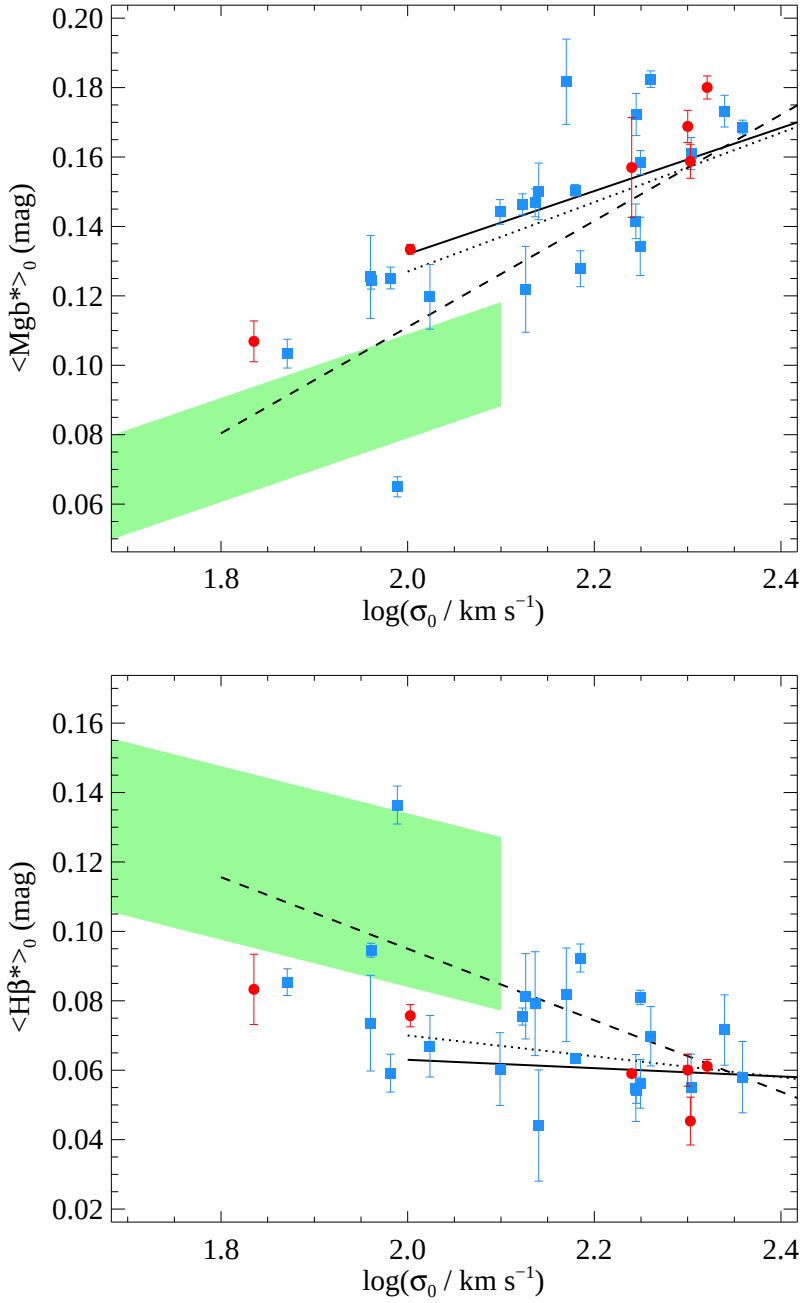

Figure 5.3: Central Hβ and Mg b Lick indices as a function of central velocity dispersion. Boxy/peanut-shaped bulges are shown as blue squares, and round bulges are red circles. The lines are comparison relations for elliptical and S0 galaxies taken from the literature. The solid and dotted lines are the Sánchez-Blázquez et al. (2006a) ellipticals in high and low density environments respectively. The dashed lines are the relations for the SAURON sample (Kuntschner et al., 2006). The shaded green regions are the regions populated by the bulges of late-type (Sb–Sd) spirals in the sample of Ganda et al. (2007). The comparisons are shown over the approximate range in velocity dispersion in which they are constrained by data.

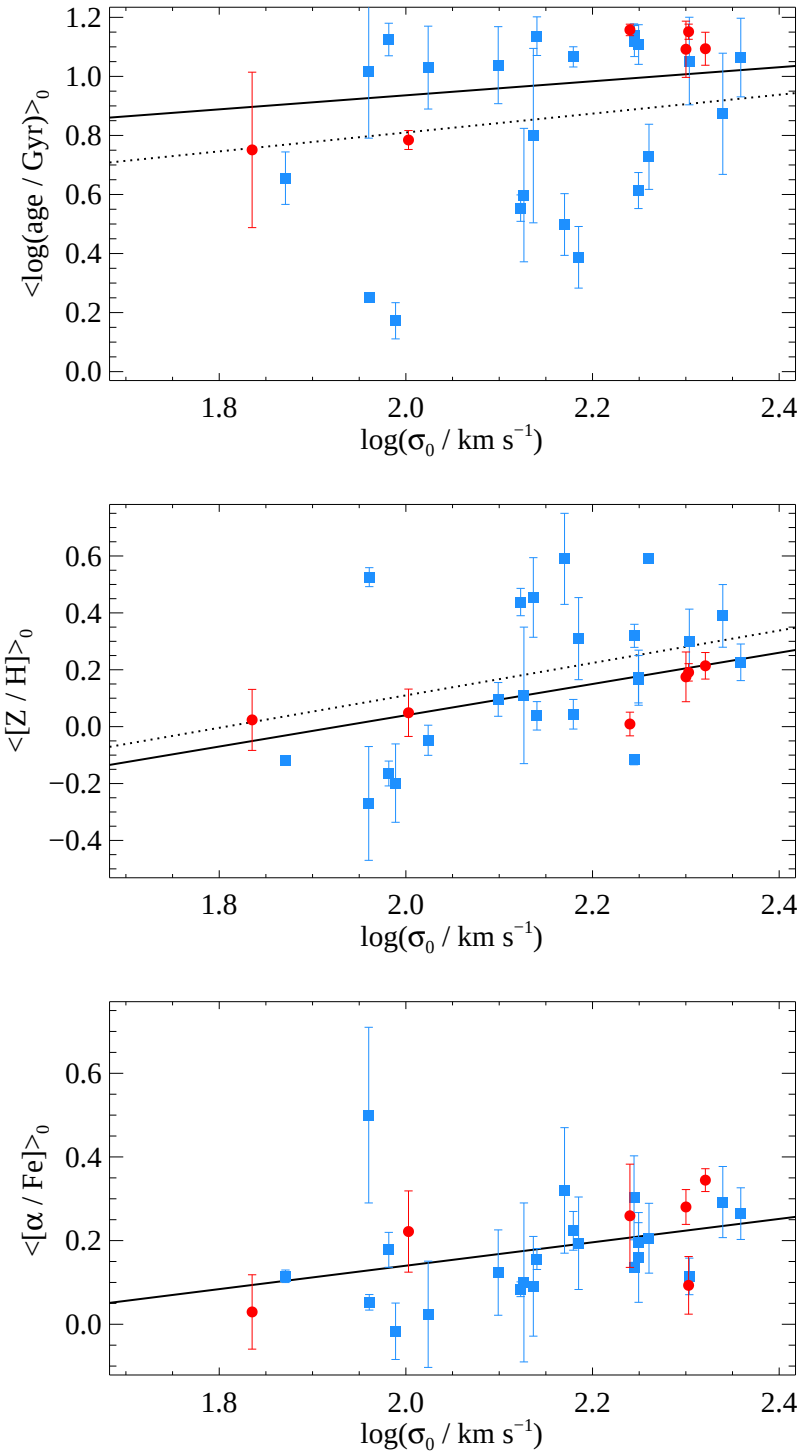

Figure 5.4: Central luminosity-weighted SSP-equivalent populations as a function of central velocity dispersion. Symbols as in Fig. 5.3. The lines are comparison relations for elliptical galaxies taken from Thomas et al. (2005), which, like our models, use the TMB03 SSP models. Solid lines are for high-density environments, dashed lines for low-density environments (the high- and low-density $[\alpha/\mathrm{Fe}]$–σ relations are identical).

when present, secular evolution transforms the central populations of galaxies, then these results suggest that secular evolution is not important in galaxy types earlier than Sb, *even if they are barred*. We note that this result is consistent with the findings of Thomas & Davies (2006) who studied the central stellar populations of spiral bulges across a broad range in Hubble types, but did not consider the role of bars in detail. It does not necessarily contradict the apparent observation of secular evolution's effects on stellar populations in later-type (Sb–Sd) bulges by Ganda et al. (2007).

There is at least as much observed scatter in the [Z/H]–$\log\sigma$ as in the [α/Fe]–$\log\sigma$ relation, despite the fact that the observational uncertainties on [α/Fe] are on average considerably larger. This suggests that there is more *intrinsic* scatter in the [Z/H]–$\log\sigma$ relation. Similar behaviour is observed in the ellipticals and S0s studied in Kuntschner et al. (2010). This possibility deserves further attention from both observations and simulations.

5.6 RADIAL GRADIENTS

We fit gradients to the radial profiles of [Z/H] and [α/Fe] using the outlier-resistant ROBUST_LINEFIT IDL procedure. We manually exclude points within the seeing limit (whose $\log R$ is poorly constrained), and the outermost points (which are always below the target S/N of the binned spectrum). These fits can be seen in Appendix 5.A. We do not attempt to fit the age profiles because the data is of insufficient quality. See below, however, for a qualitative discussion of age gradients.

We plot Δ[Z/H] and Δ[α/Fe] as a function of central velocity dispersion in Fig. 5.5. For comparison, we show the [Z/H] and [α/Fe] gradients from a catalogue of early-type galaxies assembled by Spolaor et al. (2010). The original sources of these data are Proctor (2003, 11 early-type galaxies in the Leo cloud and Virgo cluster), Brough et al. (2007, 3 brightest group/cluster galaxies), Reda et al. (2007, 12 isolated early-type galxies), Sánchez-Blázquez et al. (2007, 11 early-type galaxies covering a range of mass and environment), Spolaor et al. (2008, the S0 NGC 1400 and the elliptical NGC 1407), and Spolaor et al. (2010, 14 low mass early-types in Virgo and Fornax). All are based

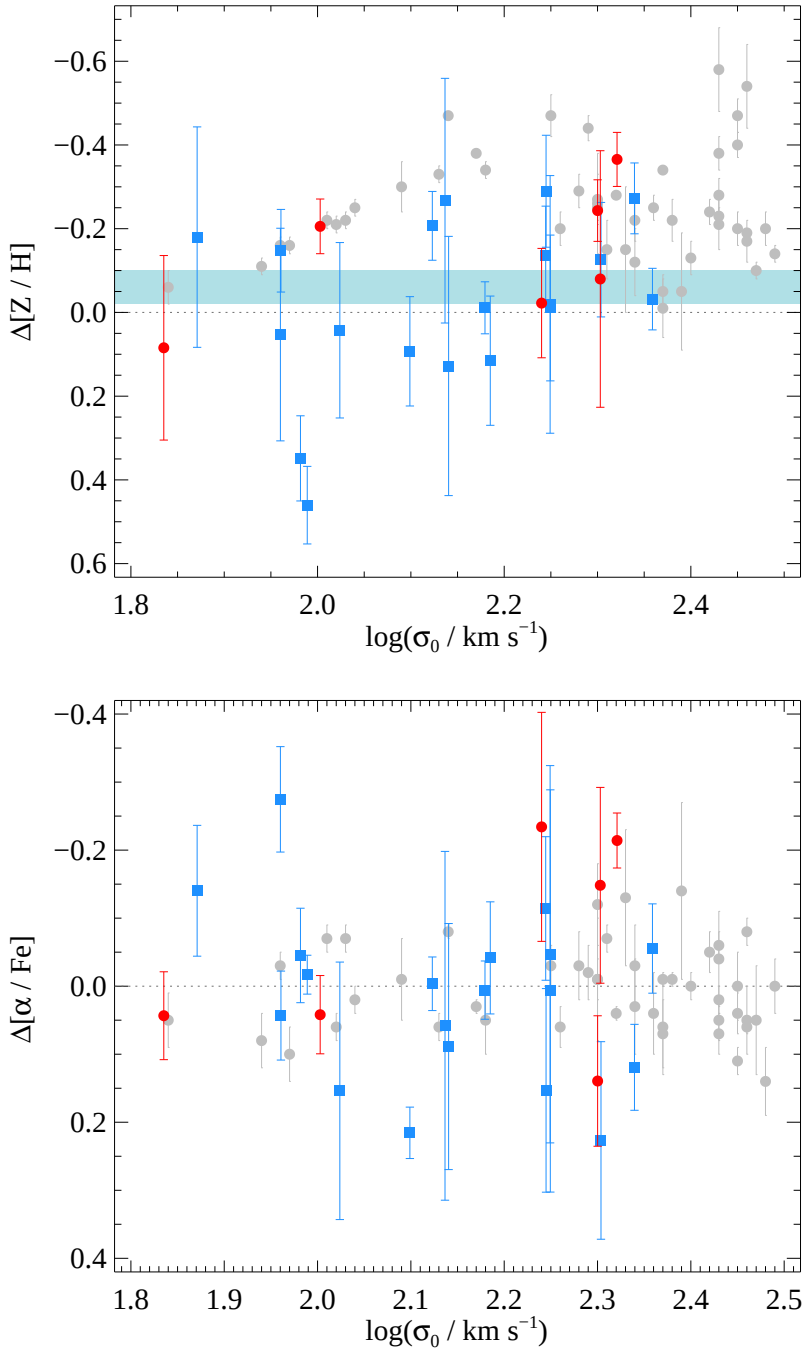

Figure 5.5: Radial [Z/H] and [α/Fe] gradients as a function of central velocity dispersion. Symbols as in Fig. 5.3. The thick blue line is the mean Δ[Z/H] for the B/PS bulges. Its thickness is the uncertainty on this mean. The grey circles are comparison data for the S0s and ellipticals catalogued by Spolaor et al. (2010). The original sources of these data are given in Section 5.6.

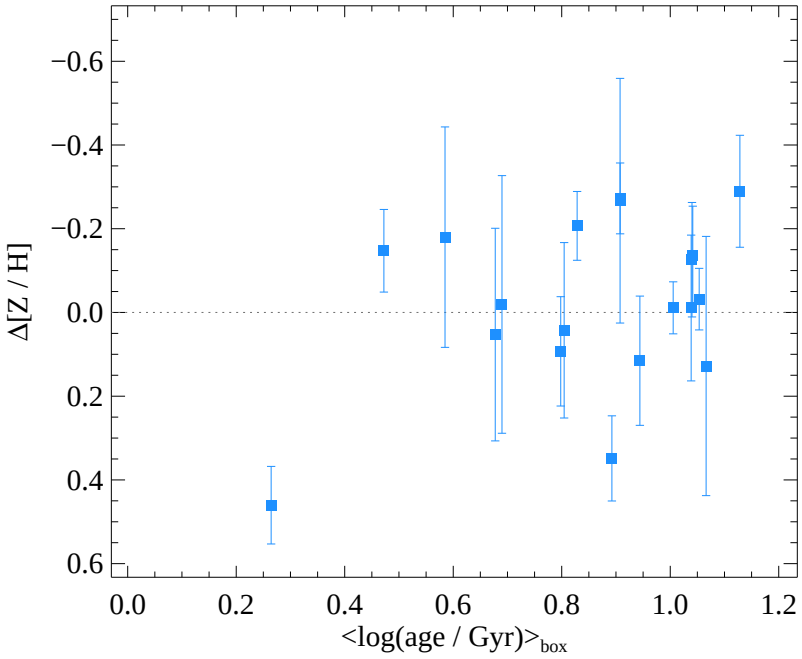

Figure 5.6: Radial [Z/H] gradient as a function of mean SSP-equivalent stellar age within the boxy bulge

on long-slit observations, and all sources except Proctor (2003) use the TMB03 SSP models. We note in any case that, while the choice of SSP models may affect the absolute stellar population parameters derived, the radial gradients are unlikely to be strongly affected (Kuntschner et al., 2010).

The uncertainties on our data are large by modern standards, but we can safely conclude the following. (1) There is no evidence that Δ[Z/H] or $\Delta[\alpha/\mathrm{Fe}]$ of our boxy bulges are correlated with velocity dispersion. This is in opposition to low mass early-type bulges, which show a clear trend in the sense that higher mass bulges have steeper (negative) gradients (Spolaor et al., 2009). (2) It is clear that the boxy bulges of our sample of barred galaxies have shallower metallicity gradients than those of ellipticals, both on average and at a given velocity dispersion. The mean value of Δ[Z/H] for the boxy and peanut-shaped bulges is -0.06 ± 0.04 and there are several cases of positive metallicity gradients. (3) There is no evidence for non-zero abundance ratio gradients, in agreement with the results for early-types.

Results (1) and (2) are qualitatively consistent with the simulations of Friedli, Benz & Kennicutt (1994), who find that outflows and inflows in barred galaxies make

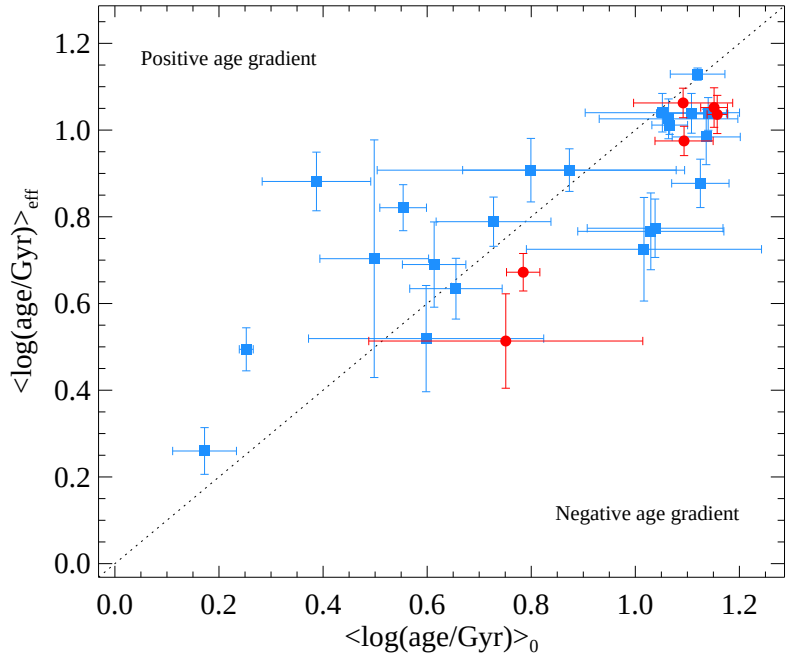

Figure 5.7: Mean SSP-equivalent stellar age within the effective radius as a function of central SSP-equivalent stellar age

pre-existing radial gradients less steep.

If the SSP-equivalent age of the stellar populations in a bar is correlated with the age of the bar structure itself, and the bar makes gradients more shallow with time (as predicted by Friedli, Benz & Kennicutt 1994), one might expect a correlation between between metallicity gradient and $\langle \text{age} \rangle$. We see no evidence of this (Fig. 5.6).

As mentioned above, it would stretch credibility to fit lines to many of the age profiles observed in our sample. Nevertheless, we examine these radial trends in a qualitative way by comparing $\langle \log(\text{age/Gyr}) \rangle_{\text{eff}}$ to $\langle \log(\text{age/Gyr}) \rangle_0$ in Fig. 5.7. One should allow for the fact that many of the central ages are close to the limit of the SSP model grid, and for the age of these galaxies, the only way is down as radius increases. This effect is probably responsible for the cluster of galaxies showing negative gradients with age $> 10\,\text{Gyr}$. With that in mind, there is no evidence of age gradients in our sample as an ensemble. Examining the age profiles, we see little evidence of the local minima in stellar age at the ends of the boxy bulge/bar predicted by Wozniak (2007). However, we note that our observations are of edge-on galaxies, and therefore pass through a line-of-sight that might make such effects difficult to

observe.

5.6.1 *Notes on individual galaxies*

NGC 2310 shows signs of a steep-shallow transition in its radial [Z/H] profile and has a young stellar population throughout, but particularly at the centre. This is consistent with observations of steep-shallow transitions in the abundance profiles of H II regions in barred spirals (Zaritsky, Kennicutt & Huchra, 1994; Martin & Roy, 1995; Roy & Walsh, 1997), and is a prediction of the models of Friedli, Benz & Kennicutt (1994), where steep radial gradients are maintained in the central regions for the first few Gyr due to vigorous star formation, while the bar smears out gradients at larger radii.

NGC 4710 shows a very clear positive metallicity gradient, visible by eye in both the metal-sensitive lines and the derived [Z/H]. This galaxy, along with NGC 4469 (which shows a weaker positive metallicity gradient), is a member of the Virgo cluster. These galaxies are therefore perhaps the most likely in the sample to have undergone recent interactions, and the positive metallicity gradients may be due to accreted metal-poor material at the galaxy centre.

5.7 DISCUSSION

In this chapter we analysed global and radial trends in the stellar populations in the bulges of a sample of 28 edge-on S0–Sb disk galaxies, 22 of which are boxy/peanut-shaped, i.e. barred. Our principal findings are (1) At a given velocity dispersion, the central stellar populations of galaxies with boxy/peanut-shaped bulges are indistinguishable from those of of elliptical galaxies. If secular evolution has effects on stellar populations that are different to those of monolithic collapse or mergers then this suggests that secular evolution is not important in the central regions of these galaxies, despite the fact that they are barred. (2) The radial metallicity gradients of boxy/peanut-shaped bulges are uncorrelated with velocity dispersion and are, on

average, shallower than those of unbarred early-type galaxies. This is qualitatively consistent with chemodynamical models of bar formation, in which radial inflow and outflow smears out pre-existing gradients.

It is clear that the role of bars in transforming the stellar populations of disk galaxies is a significant lacuna in our understanding of galaxy evolution. This work suggests several possible avenues for further study. Simulations should attempt to go beyond the qualitative statement that bars make pre-existing abundance gradients shallower, perhaps by drawing their initial conditions of abundance profiles from samples such as Spolaor et al. (2009), in which Δ[Z/H] is correlated with velocity dispersion. Simulations can also make predictions of the minor axis gradients of barred galaxies as a function of radius (e.g. Friedli, 1998). Integral field observations of the boxy/peanut-shaped bulges of edge-on galaxies are the ideal observational tests of such results. Observations of face-on galaxies are complementary to this, and are of course a much better way of looking for anticipated azimuthal variation in stellar populations such as local minima in age at the bar ends (Wozniak, 2007).

Bedregal et al. (2008) raise the possibility that the remarkably tight Mg b–σ relation is even tighter if σ is replaced with a measure of total dynamical mass that accounts for rotational support (which may be significant even in early-type galaxies, Emsellem et al. 2007). Scott et al. (2009) demonstrate that Mg b is correlated with the escape velocity at both a global and local level. A more detailed analysis of our sample of disk galaxies should consider these possibilities.

APPENDIX 5.A KINEMATICS, LICK INDICES AND SSP-EQUIVALENT POPULATIONS OF THE FULL SAMPLE

The stellar and gas kinematics, Lick indices and SSP-equivalent stellar populations of the full sample are shown in the figures on the following pages.

Figure 5.8: In the figures that follow, the top two panels are observed properties of the spectra (kinematics and Lick indices) while the bottom two panels show derived quantities (SSP-equivalent age, [Z/H] and [α/Fe]).

Top left: Stellar (absorption line) and gas (emission line) kinematics. We show stellar kinematics in black (with corresponding uncertainties) and gas line-of-sight velocity and dispersion in red/blue diamonds. If the blue half of the diamond is filled then the Hβ emission line reached the Hβ A/N threshold for detection (and therefore cleaning). If the red half is filled then the [O III] line reached the [O III] A/N threshold. $R_{\rm box}$ is indicated by the vertical dotted lines at $R \neq 0$.

Top right: Lick indices as a function of $\log(R/\mathrm{arcsec})$. Measurements taken from the positive R side of the galaxy are shown as filled diamonds, while measurements from the negative R side are shown as open diamonds. The solid blue circle is the value in the central bin ($R = 0$), and the open blue circles are measurements from bins at radii smaller than the seeing limit (indicated by the dashed line at $\log(R/\mathrm{arcsec}) \approx 0.2$). These blue symbols are shown at arbitrary $\log R$. The vertical dashed line at larger radius [typically at $\log(R/\mathrm{arcsec}) \sim 1$] is $R_{\rm box}$.

Bottom left: The composite index [MgFe]$'$ and the Lick index Hβ plotted over the TMB03 SSP grid for [α/Fe] $= 0.0$ (solar). Symbols as in the top right panel.

Bottom right: SSP-equivalent age, [Z/H], and [α/Fe] as a function of $\log(R/\mathrm{arcsec})$. Symbols as in the top right panel. The log-linear fit to [Z/H] and [α/Fe] is shown as a solid line. The maximum and minimum values allowed by the models are shown as horizontal dashed lines. Points shown in blue (i.e. measurements at radii inside the seeing limit) or as crosses (i.e. the outermost points) are excluded from this fit.

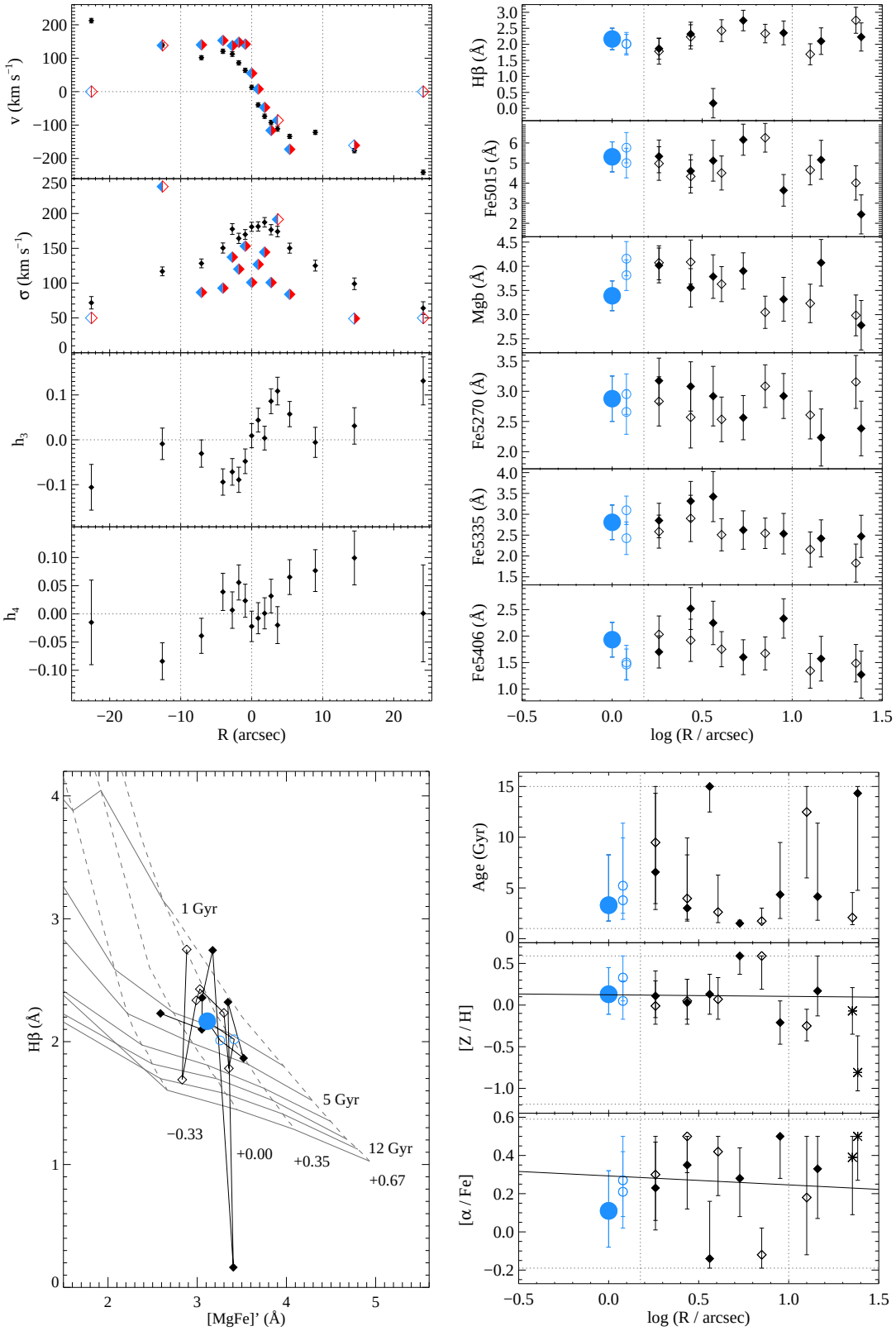

Figure 5.8: ESO 151-G004 (B/PS bulge)

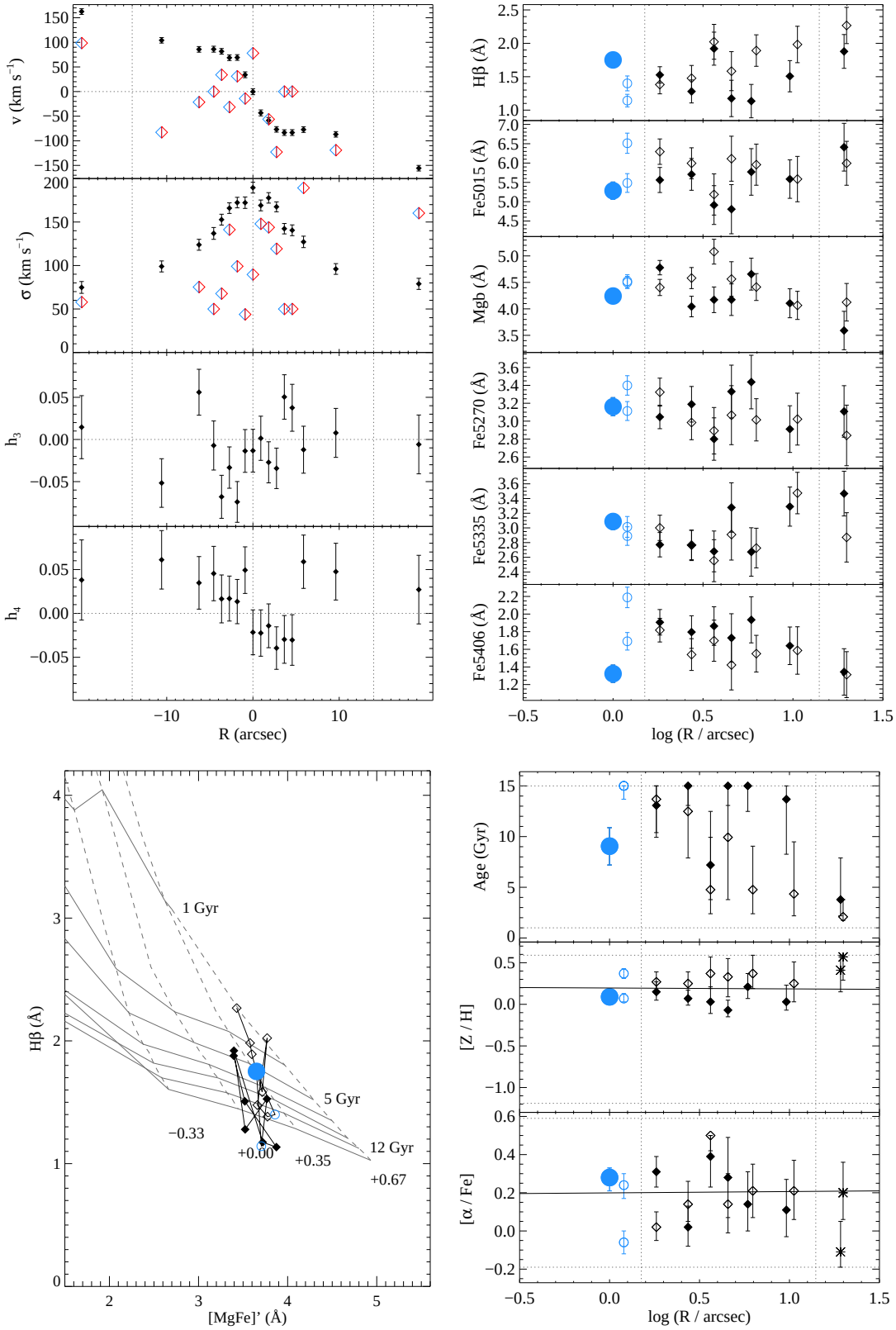

Figure 5.8: ESO 185-G053 (B/PS bulge)

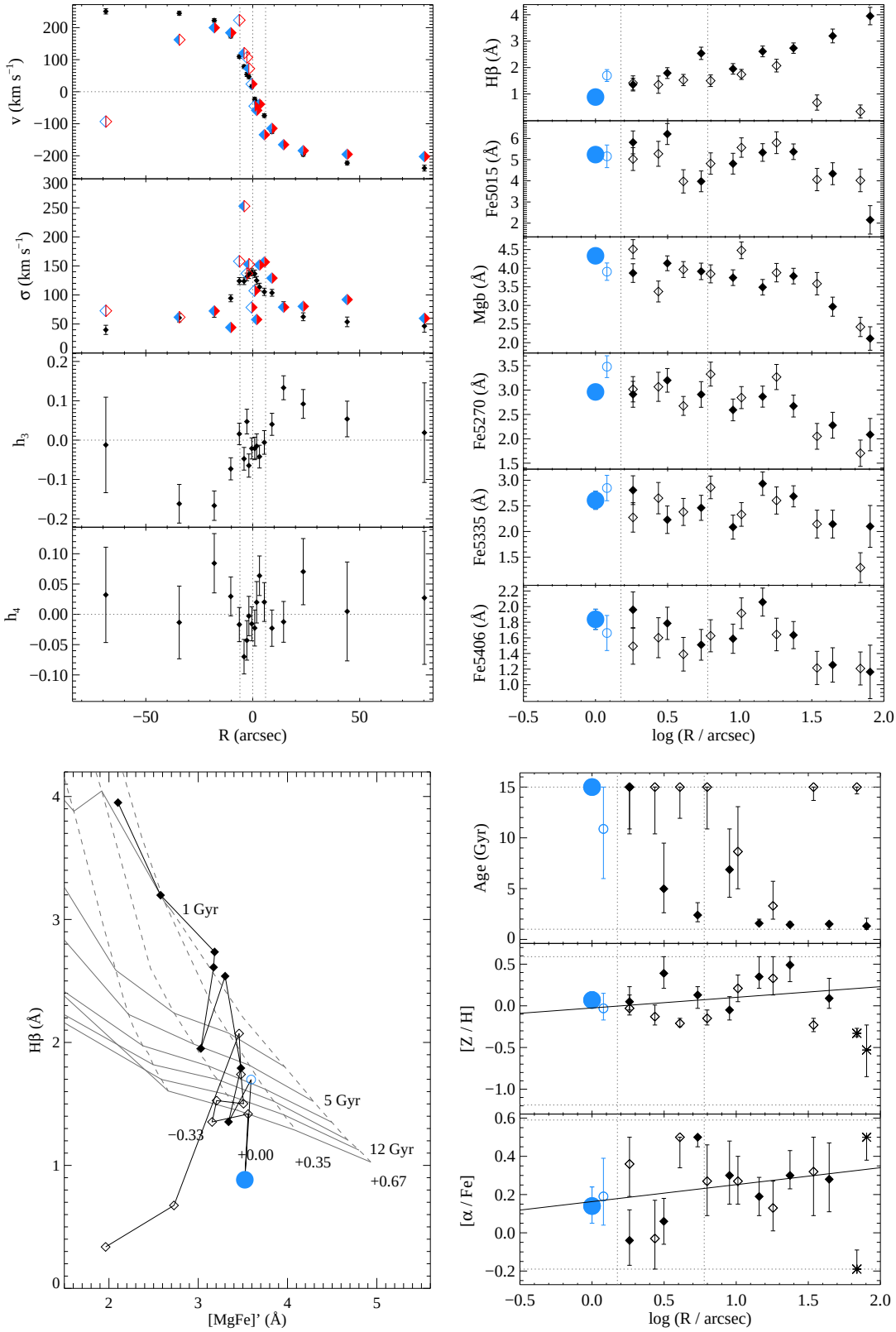

Figure 5.8: ESO 240-G011 (B/PS bulge)

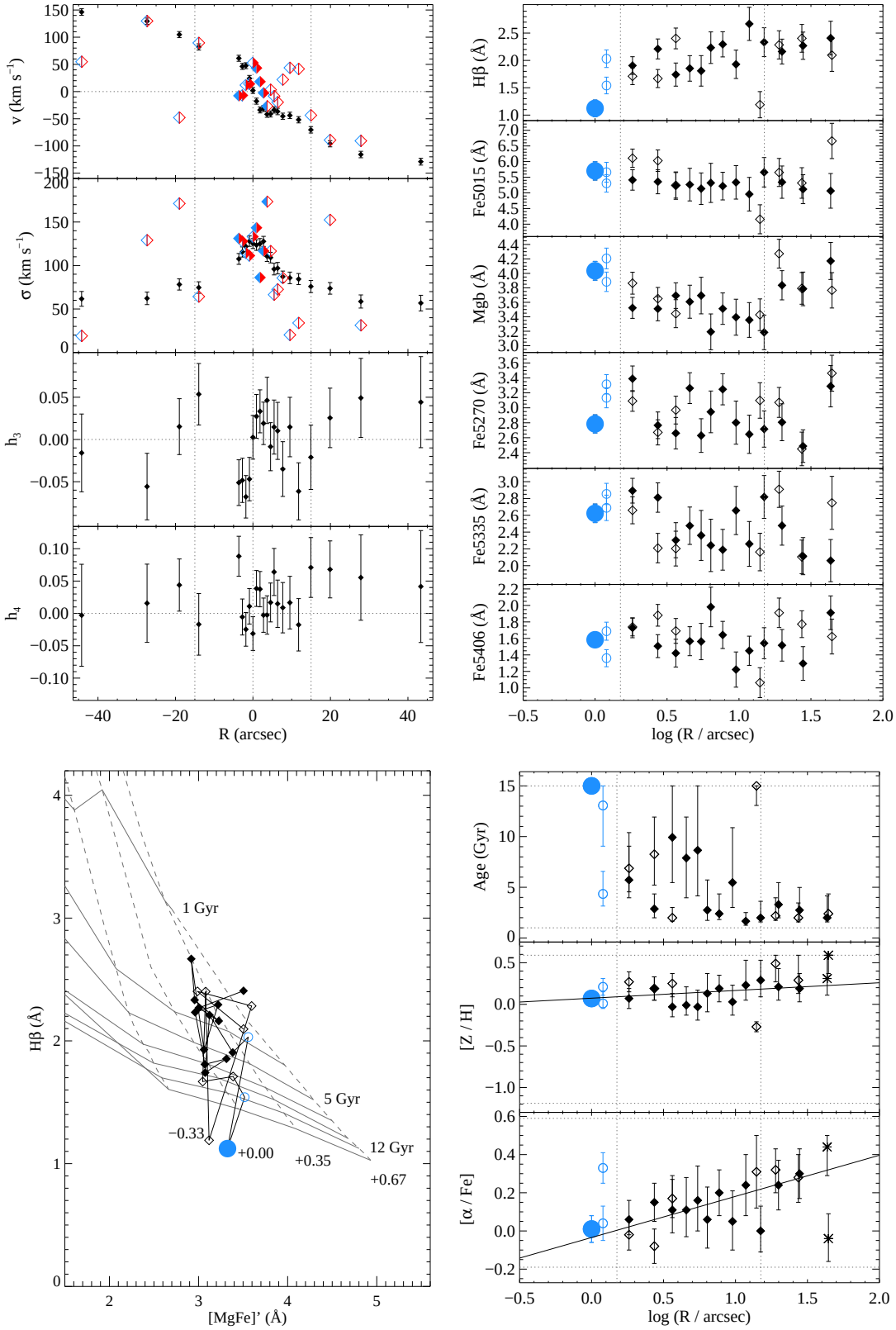

Figure 5.8: ESO 311-G012 (B/PS bulge)

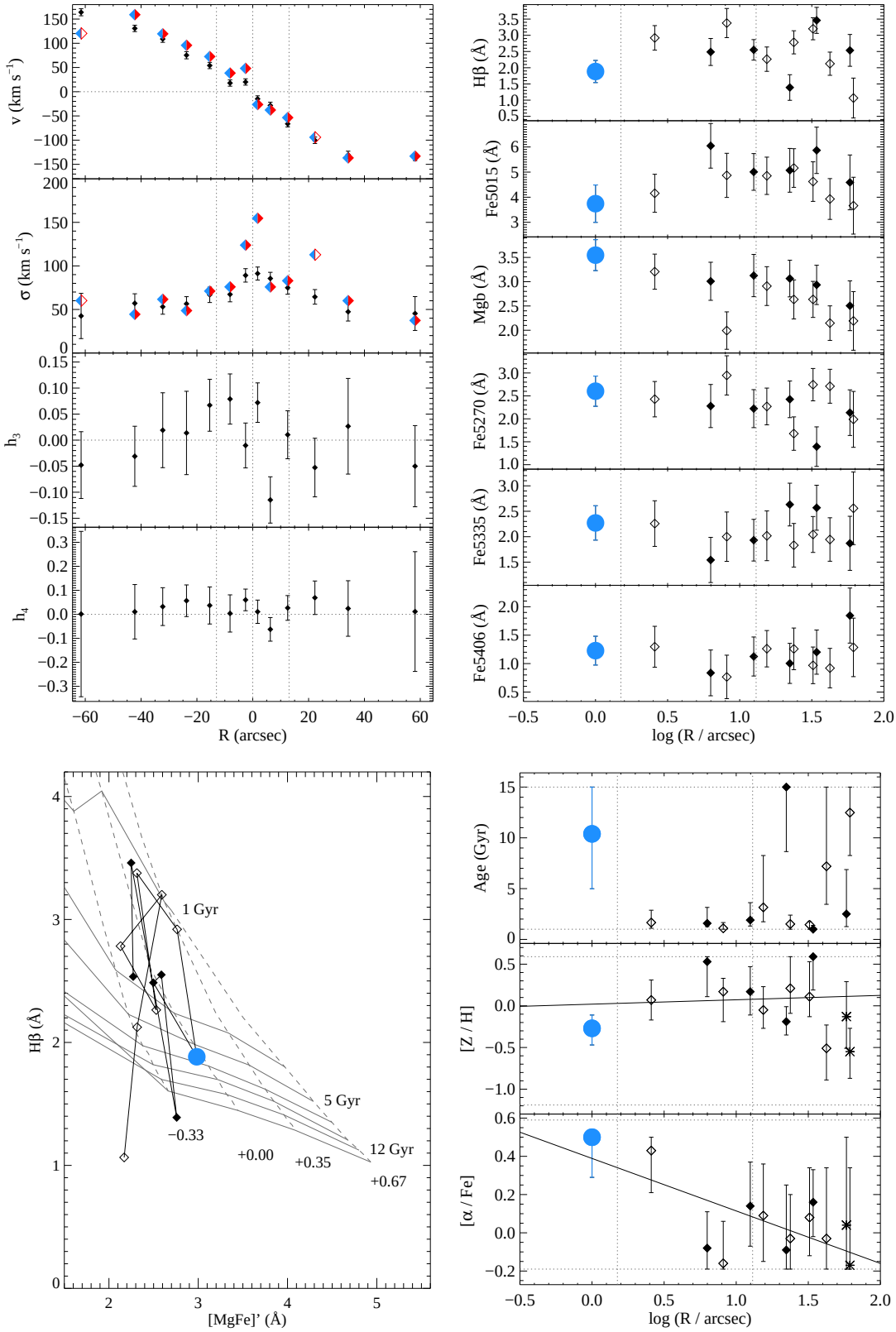

Figure 5.8: ESO 443-G042 (B/PS bulge)

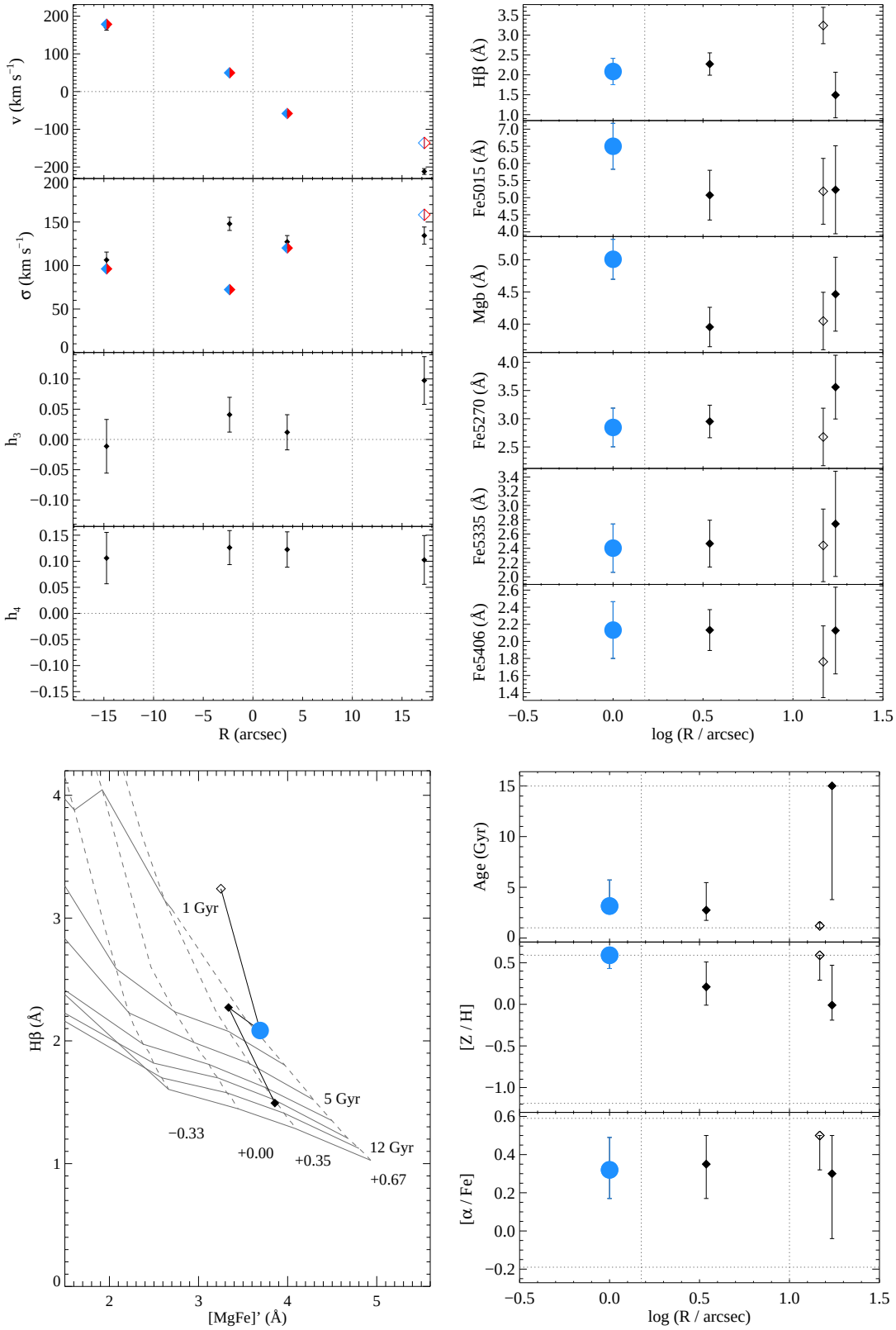

Figure 5.8: ESO 597-G036 (B/PS bulge)

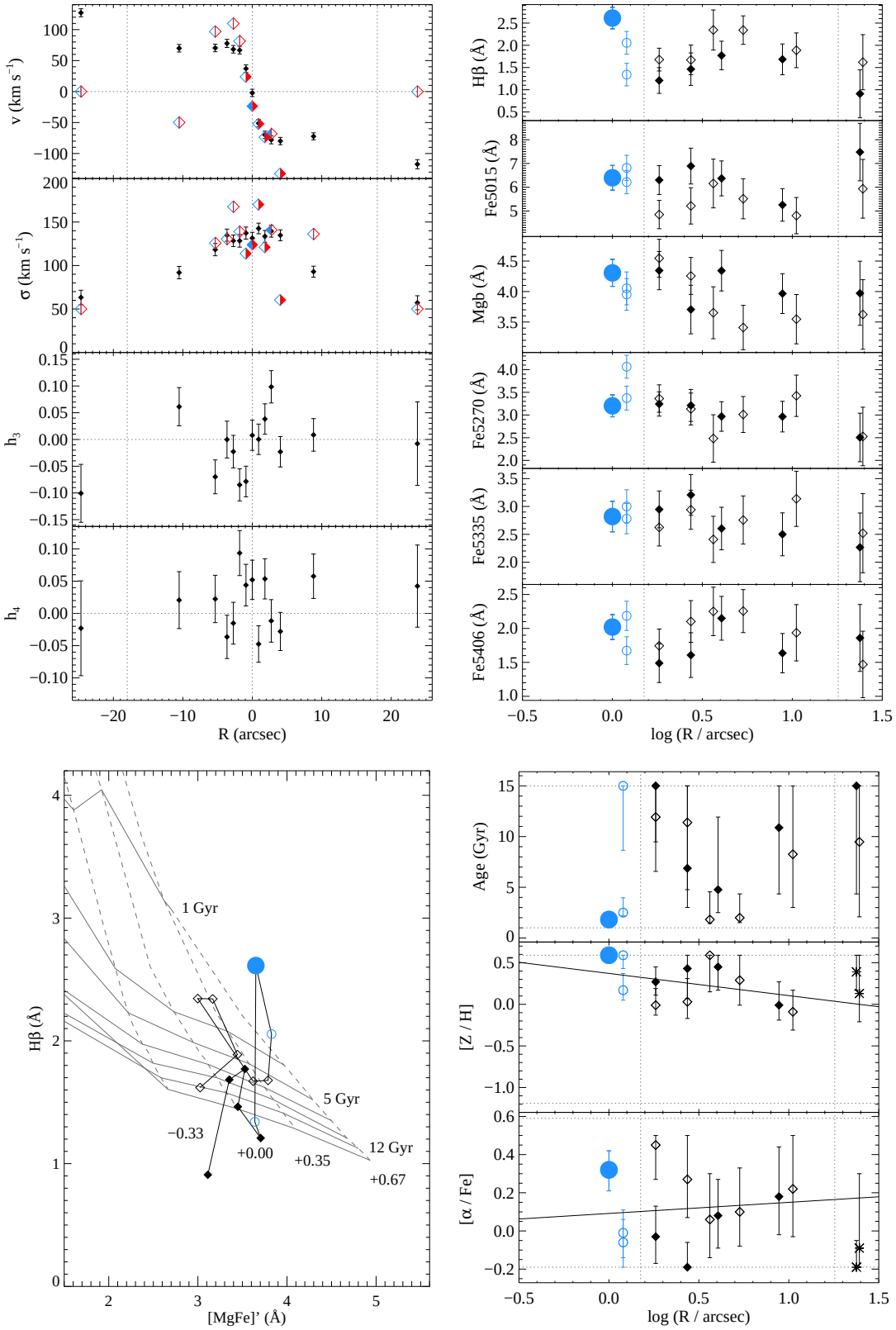

Figure 5.8: IC 4767 (B/PS bulge)

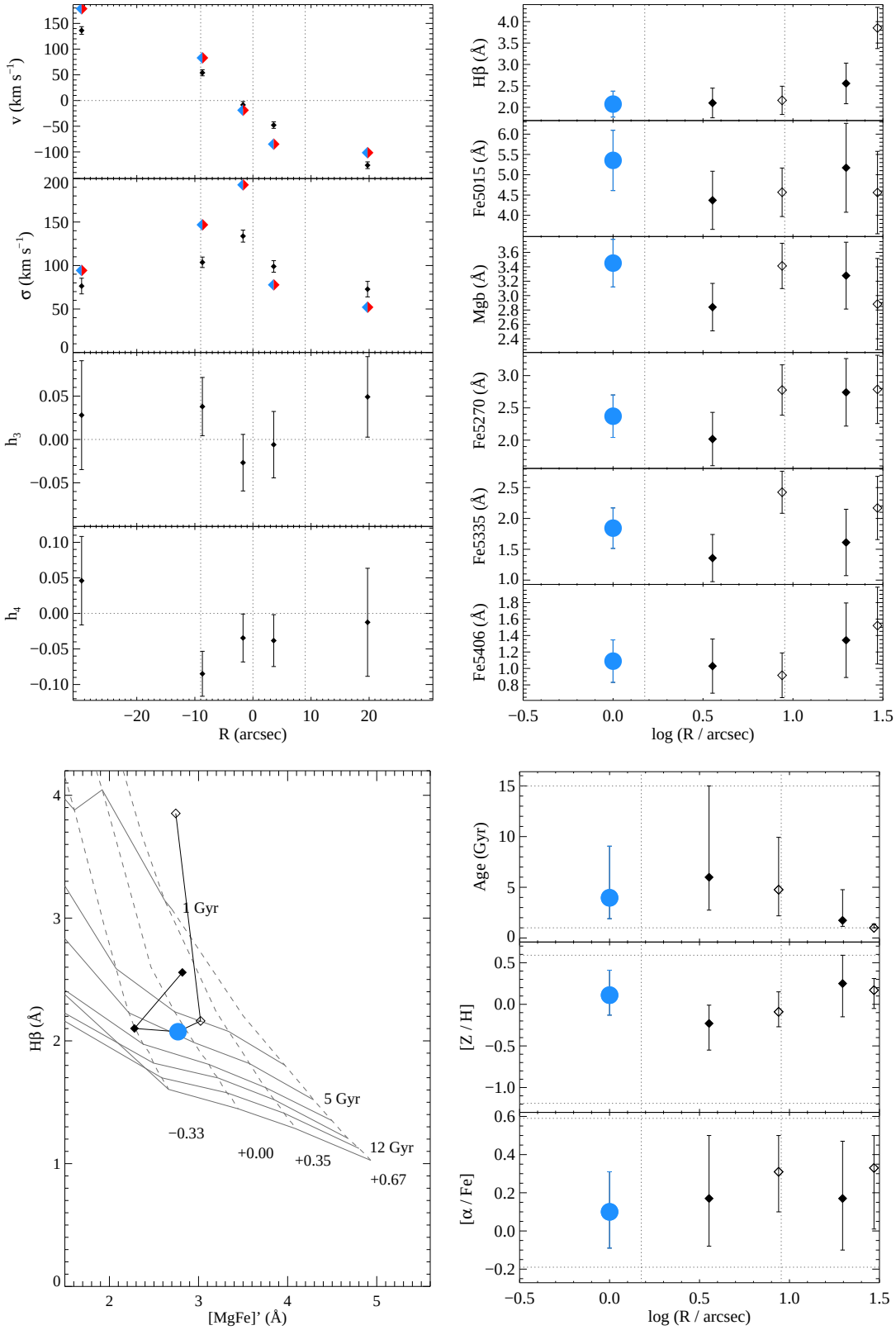

Figure 5.8: IC 4937 (B/PS bulge)

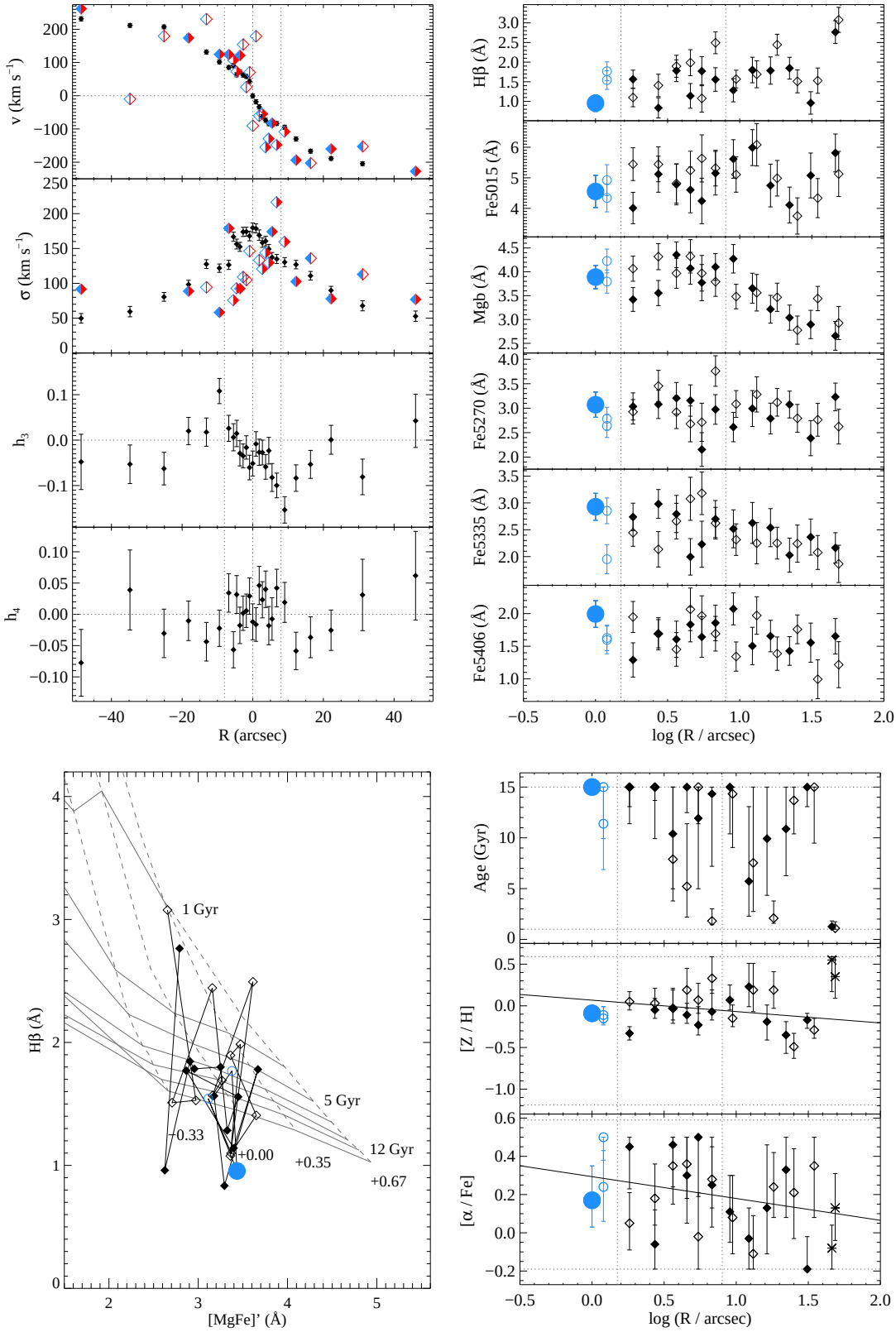

Figure 5.8: IC 5096 (B/PS bulge)

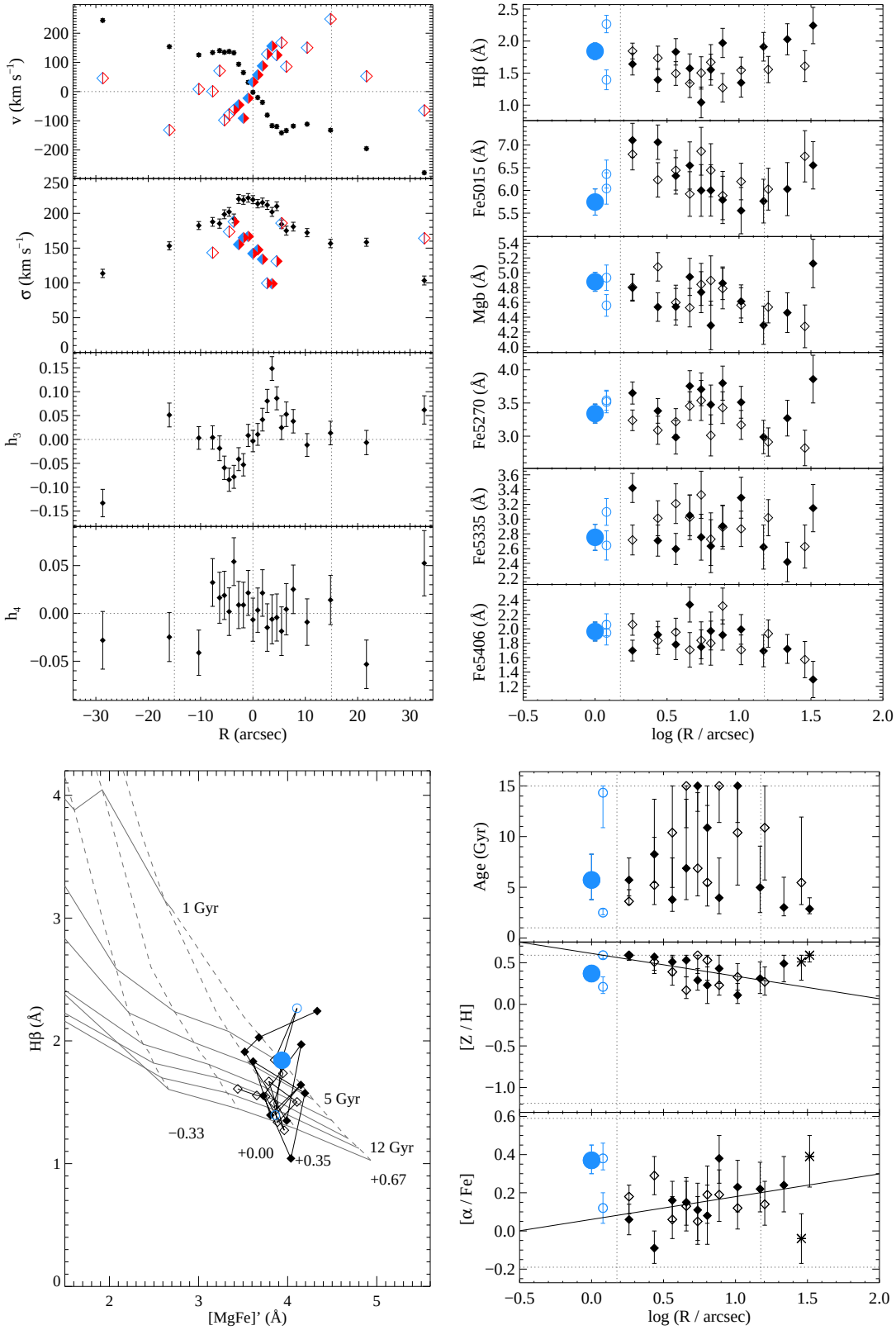

Figure 5.8: NGC 128 (B/PS bulge)

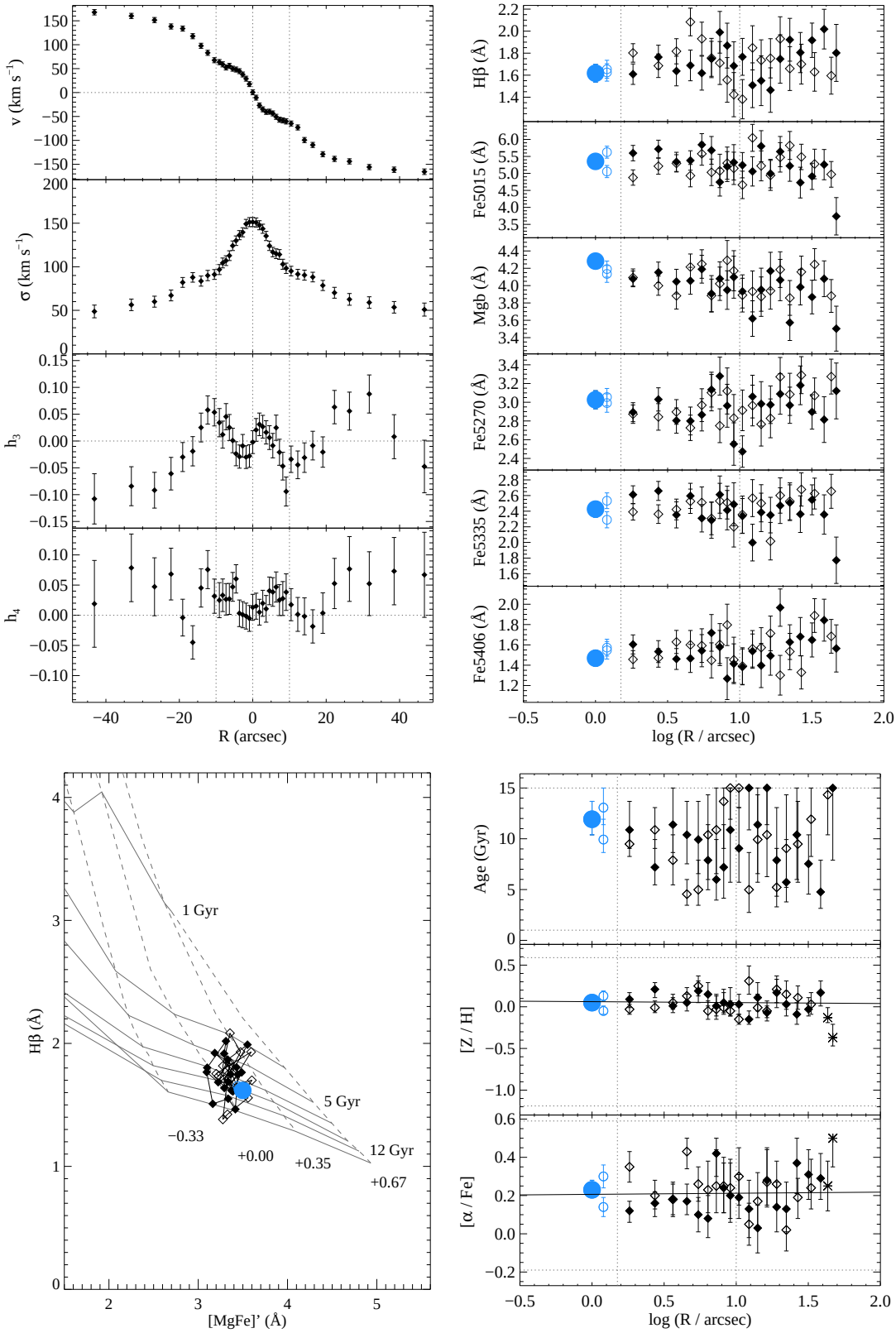

Figure 5.8: NGC 1381 (B/PS bulge)

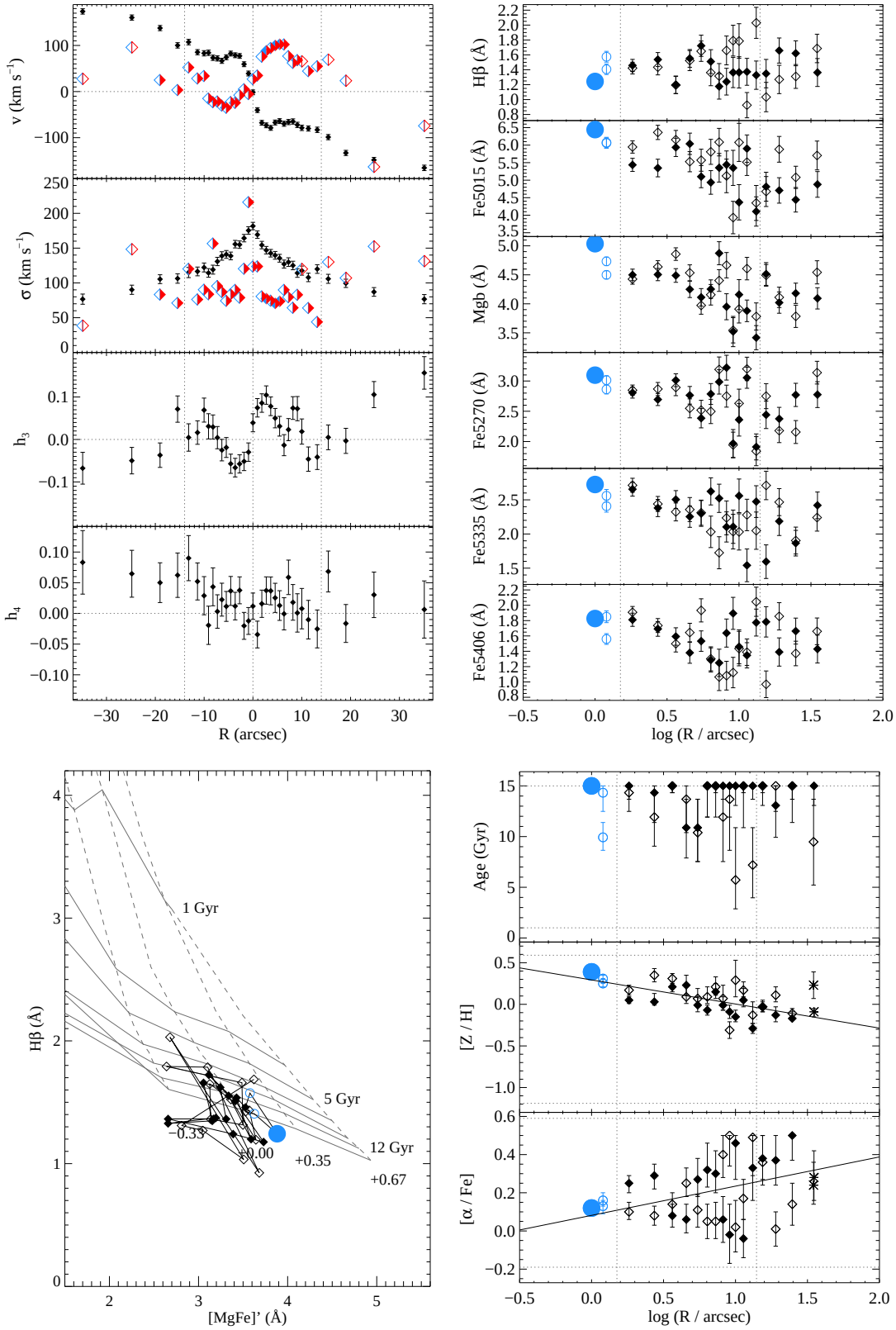

Figure 5.8: NGC 1596 (B/PS bulge)

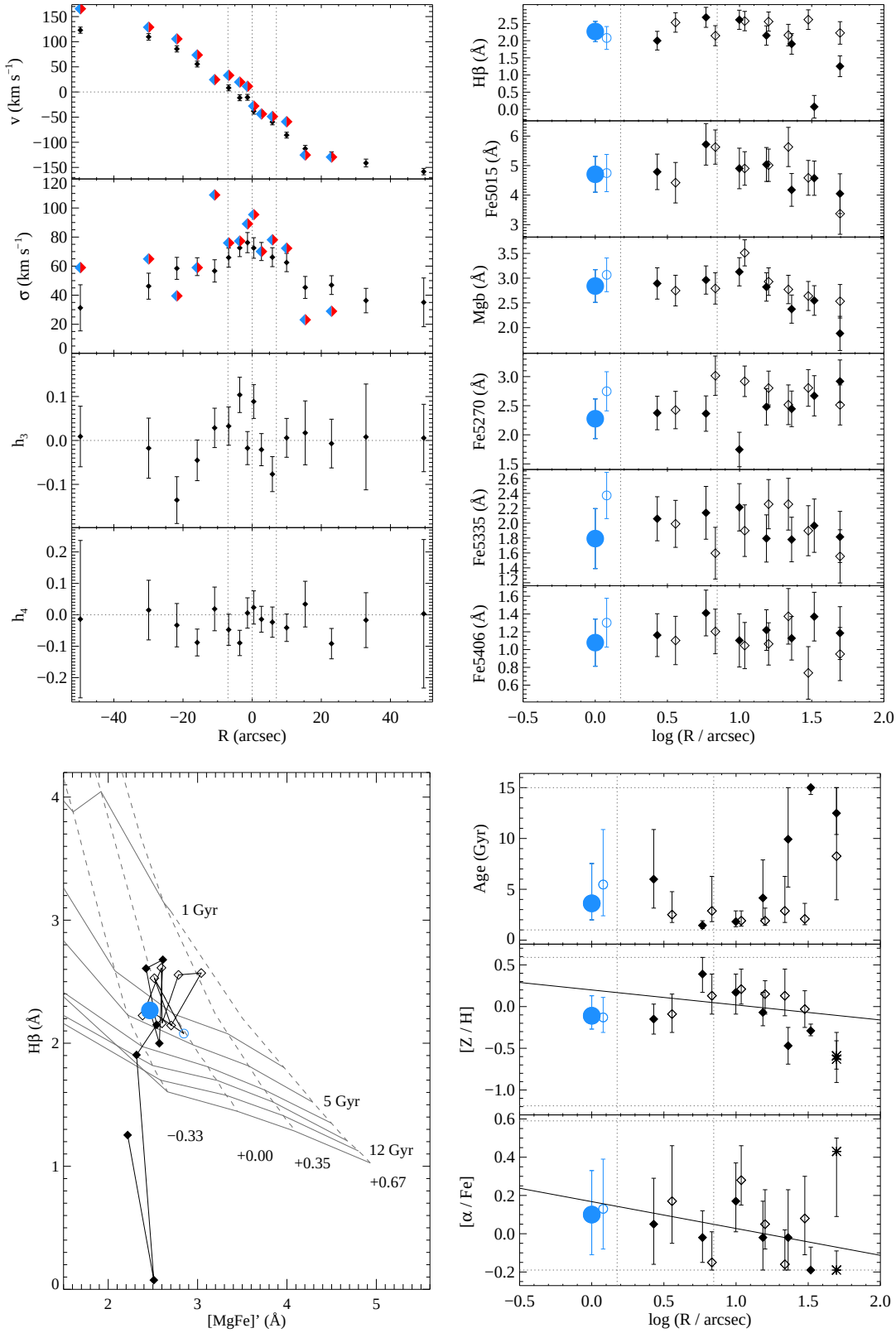

Figure 5.8: NGC 1886 (B/PS bulge)

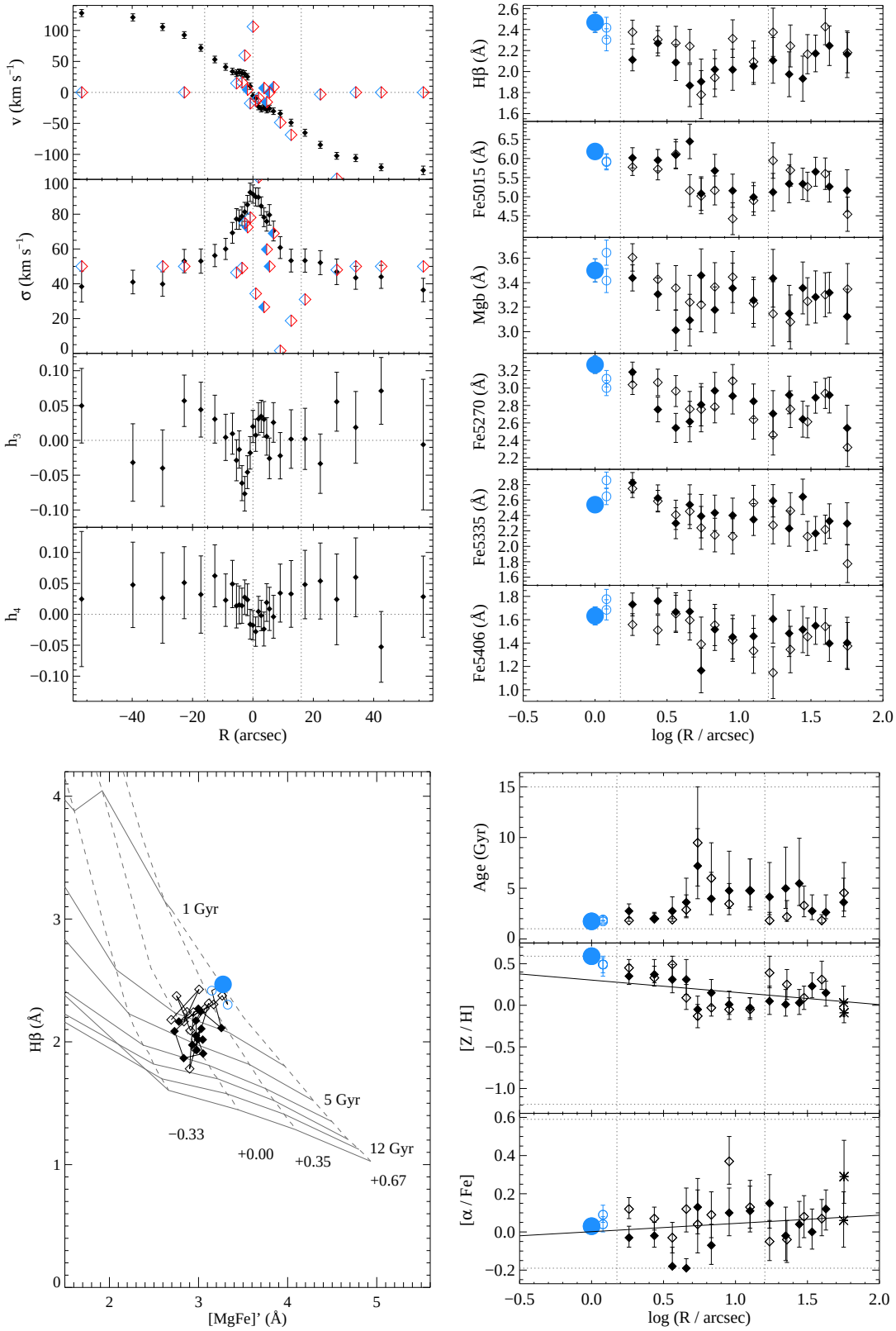

Figure 5.8: NGC 2310 (B/PS bulge)

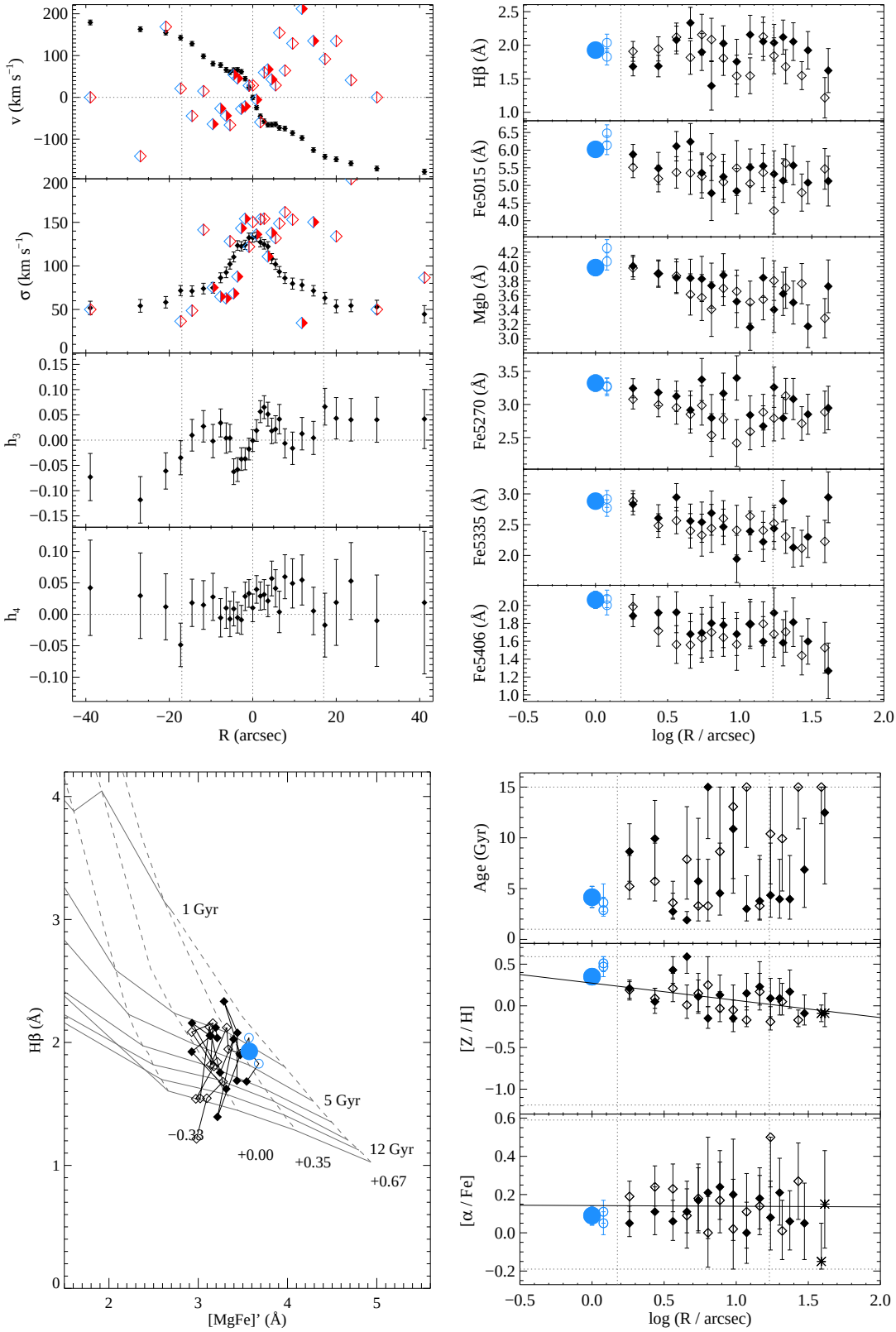

Figure 5.8: NGC 3203 (B/PS bulge)

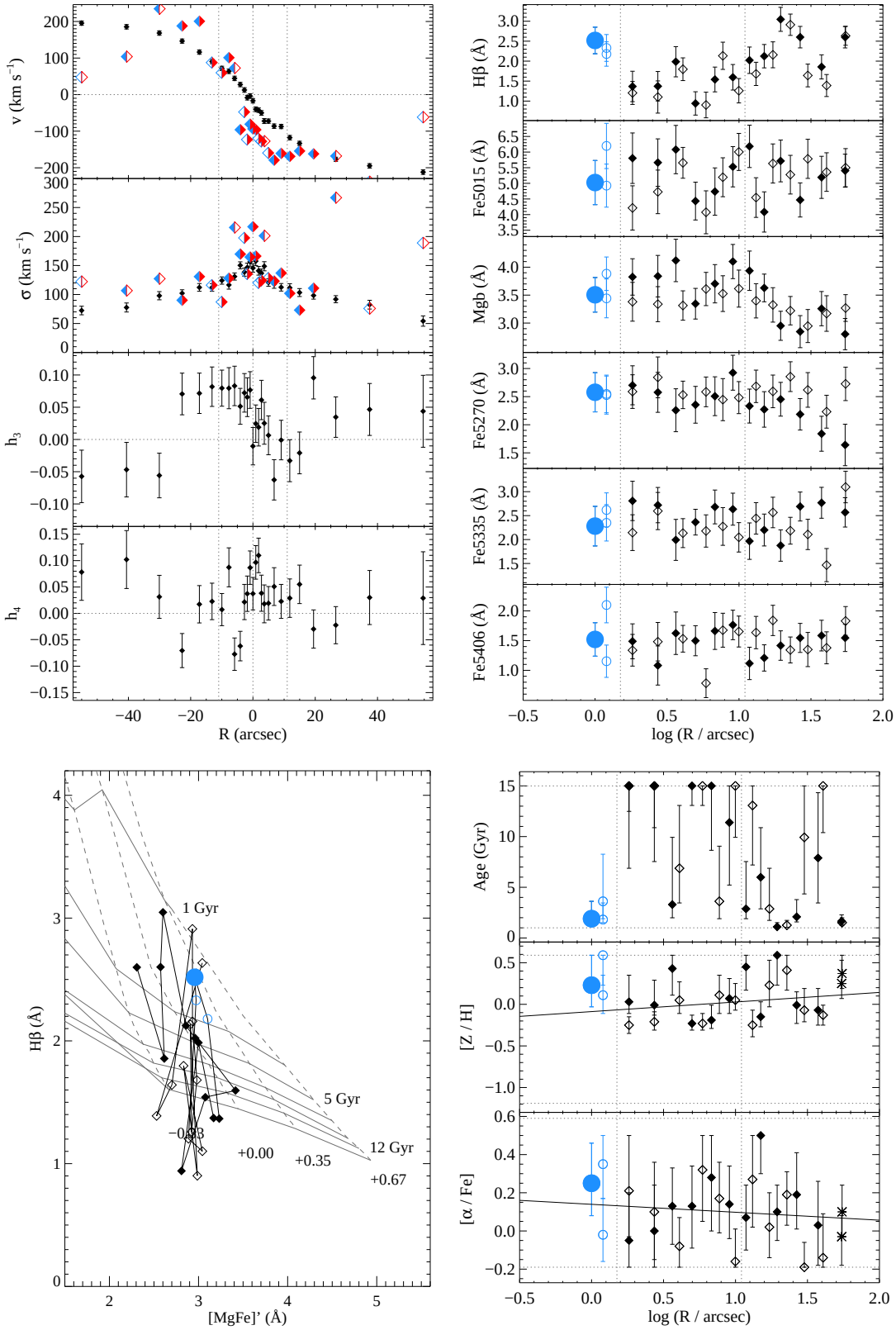

Figure 5.8: NGC 3390 (B/PS bulge)

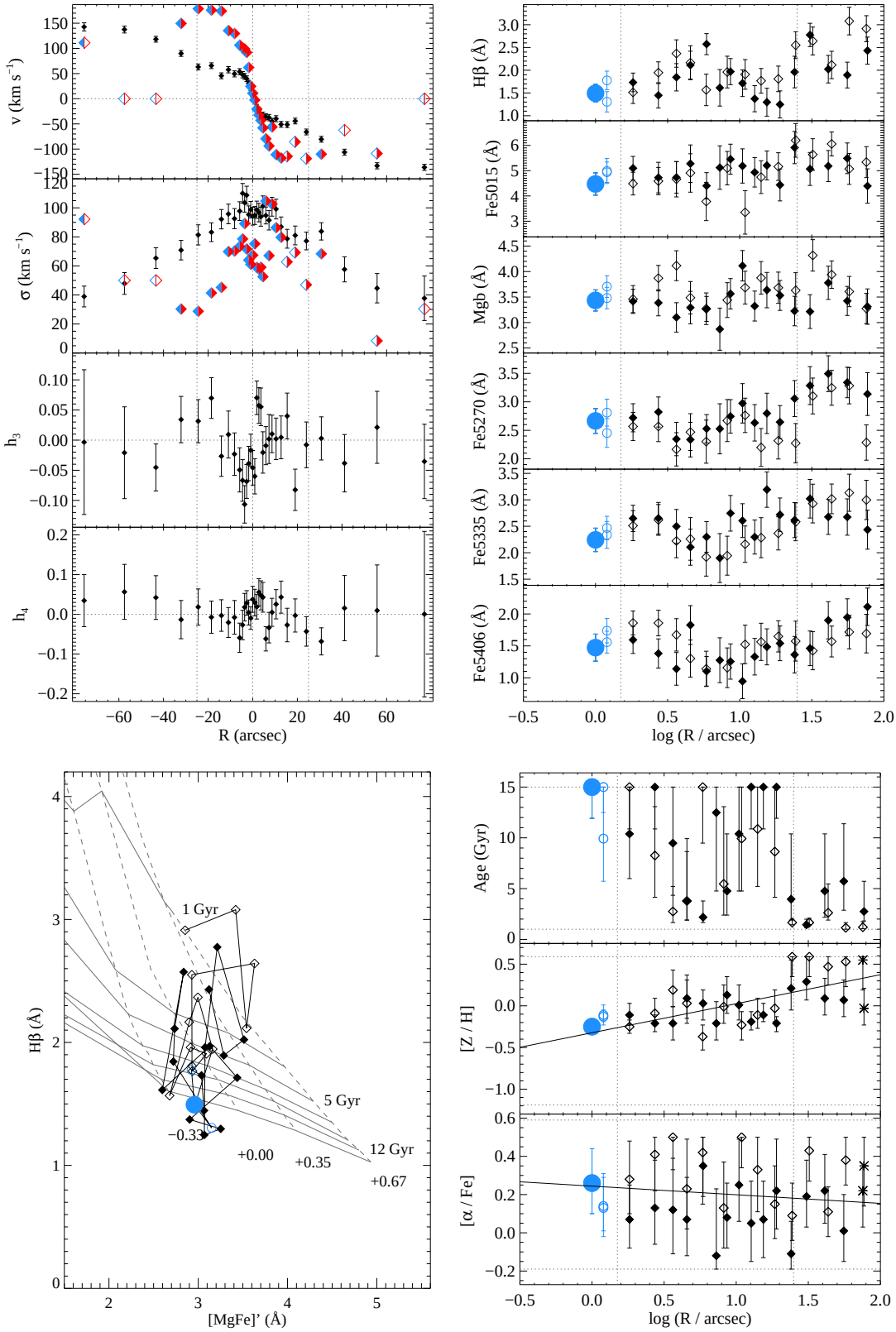

Figure 5.8: NGC 4469 (B/PS bulge)

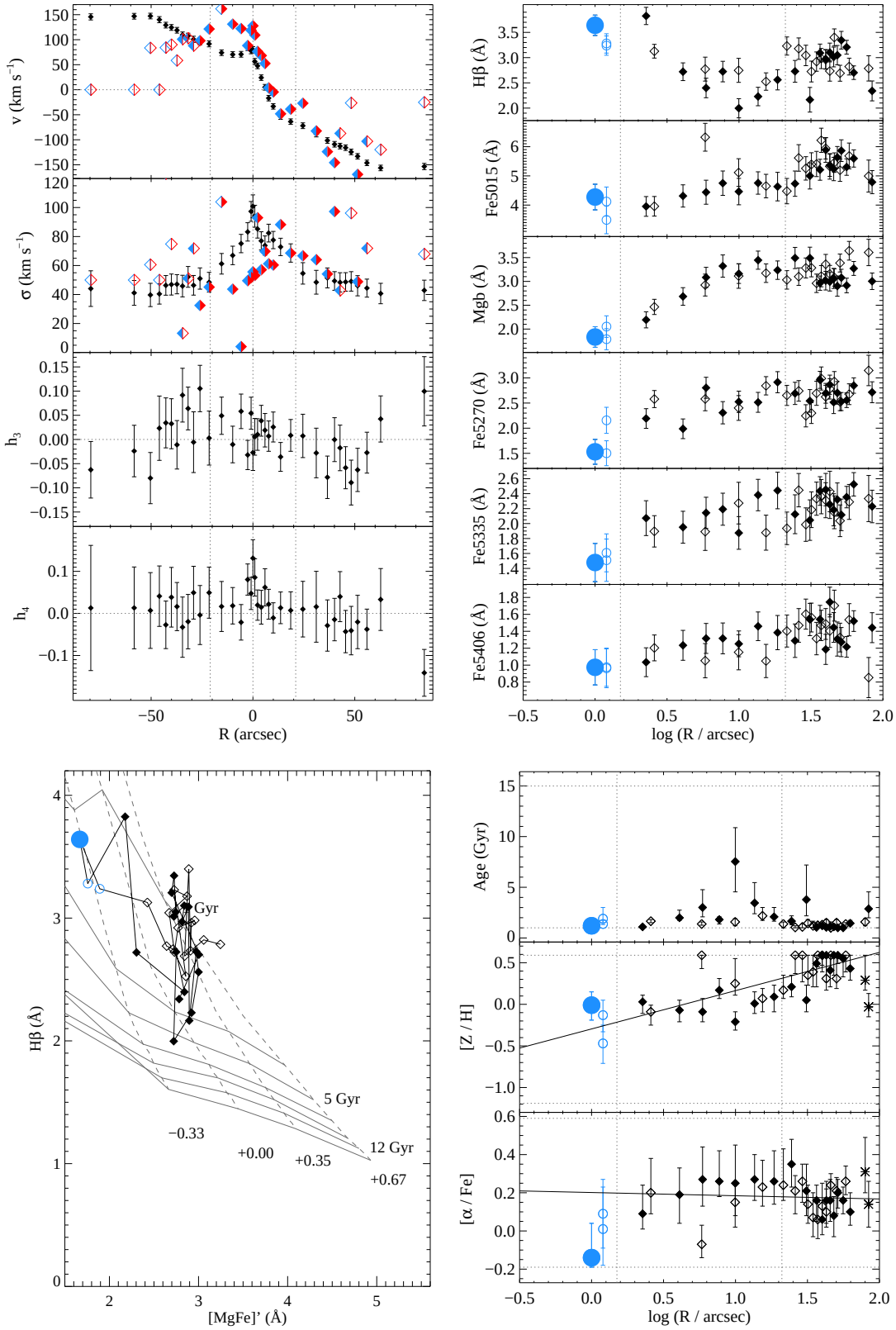

Figure 5.8: NGC 4710 (B/PS bulge)

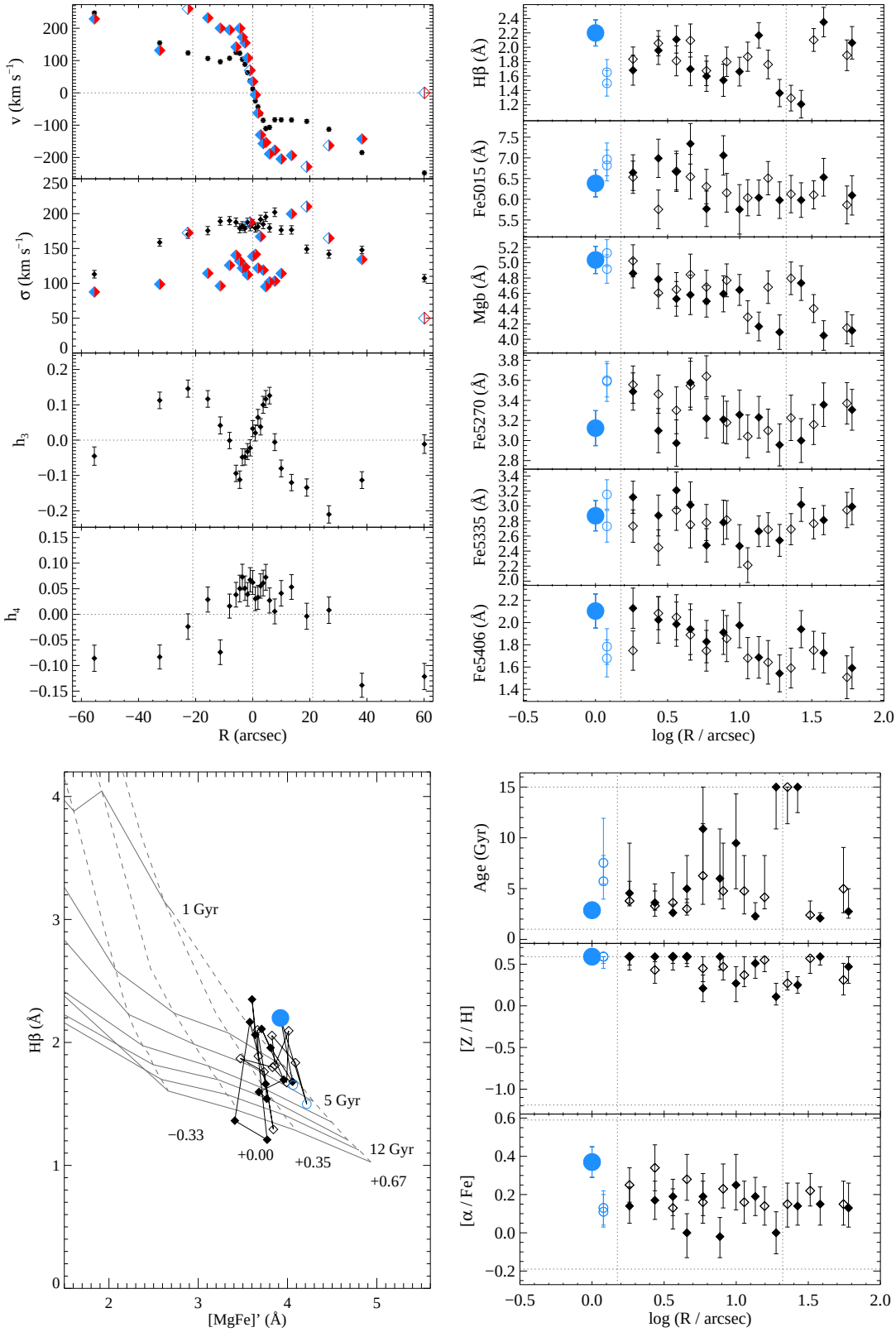

Figure 5.8: NGC 5746 (B/PS bulge)

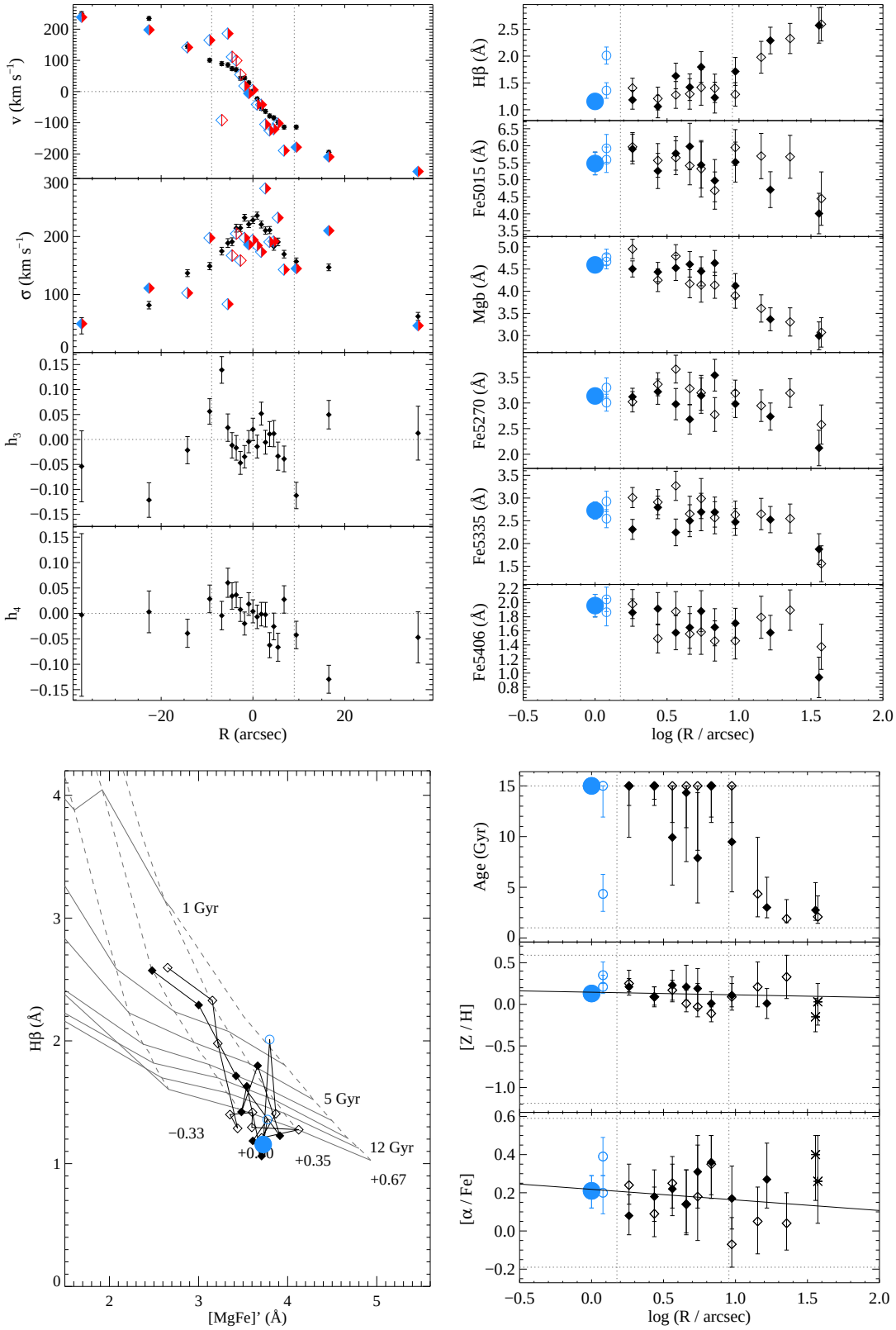

Figure 5.8: NGC 6722 (B/PS bulge)

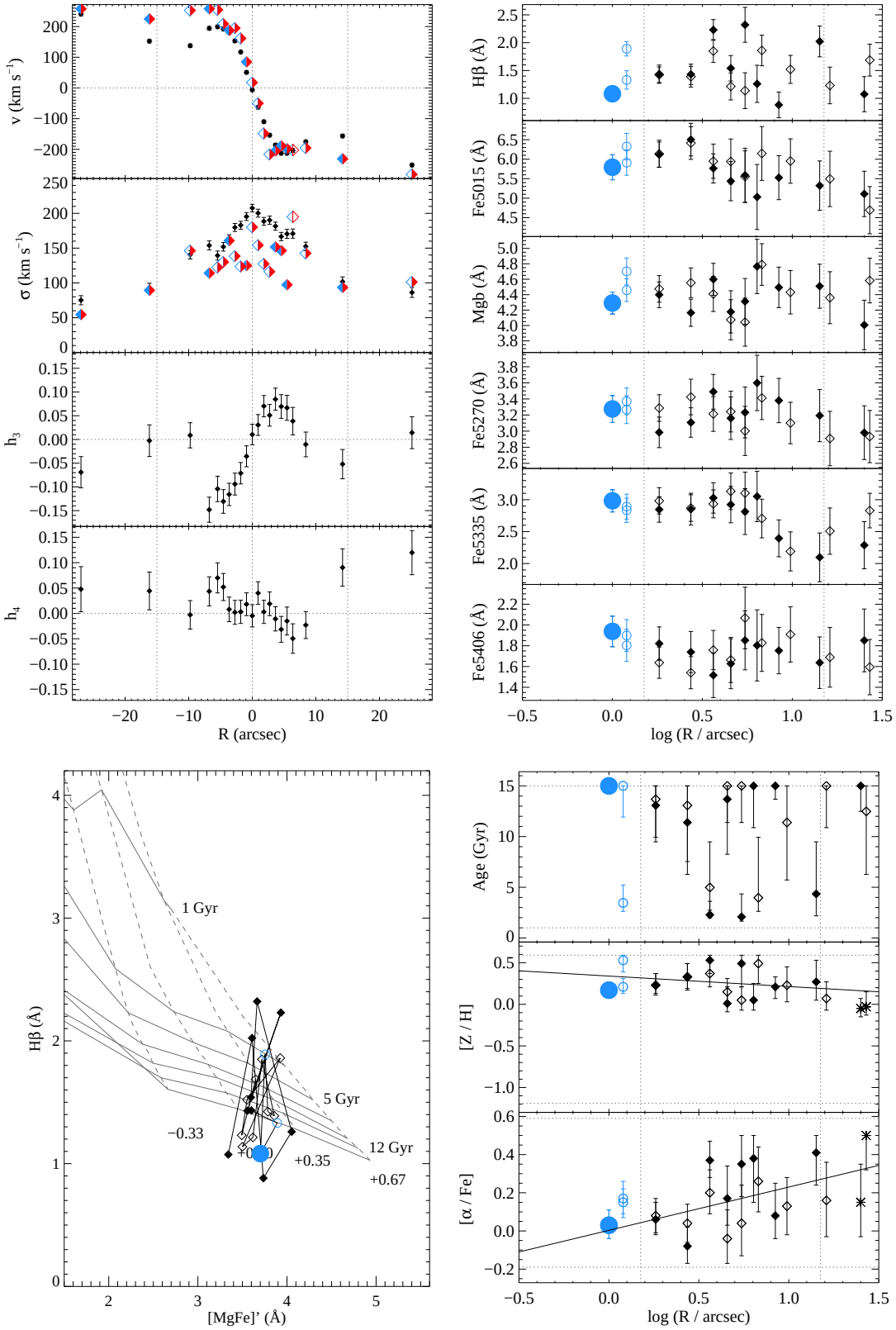

Figure 5.8: NGC 6771 (B/PS bulge)

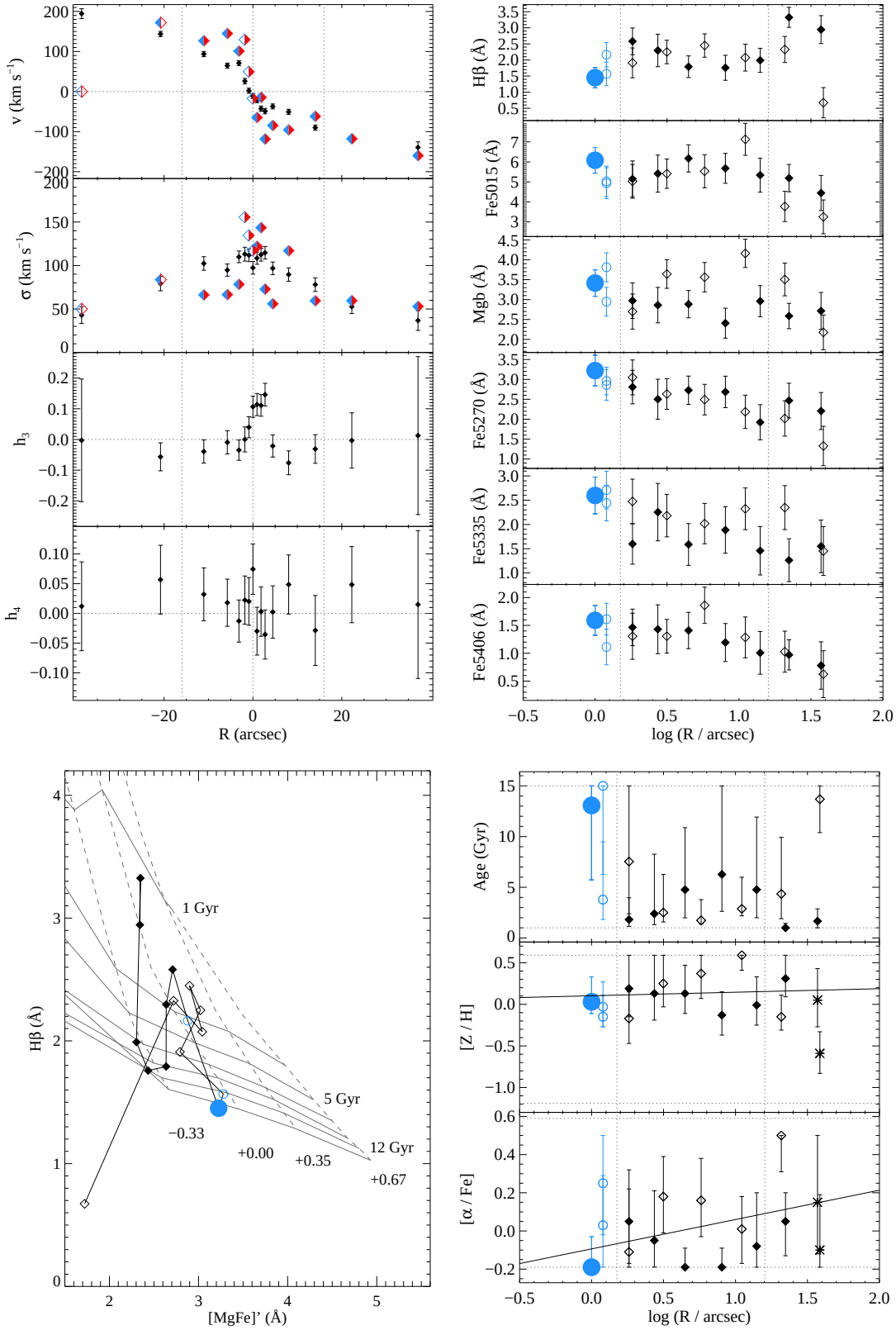

Figure 5.8: PGC 44931 (B/PS bulge)

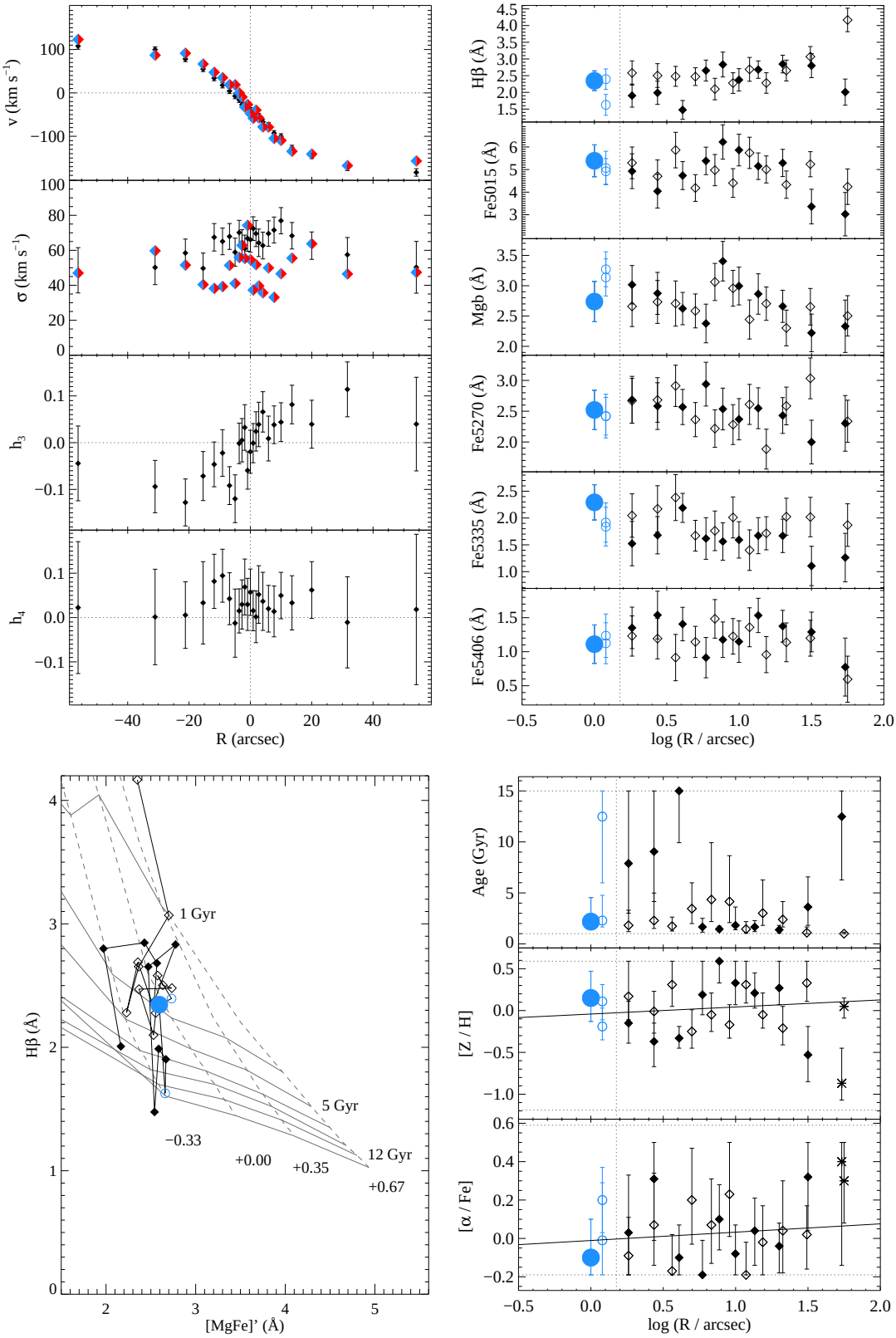

Figure 5.8: IC 5176 (round bulge)

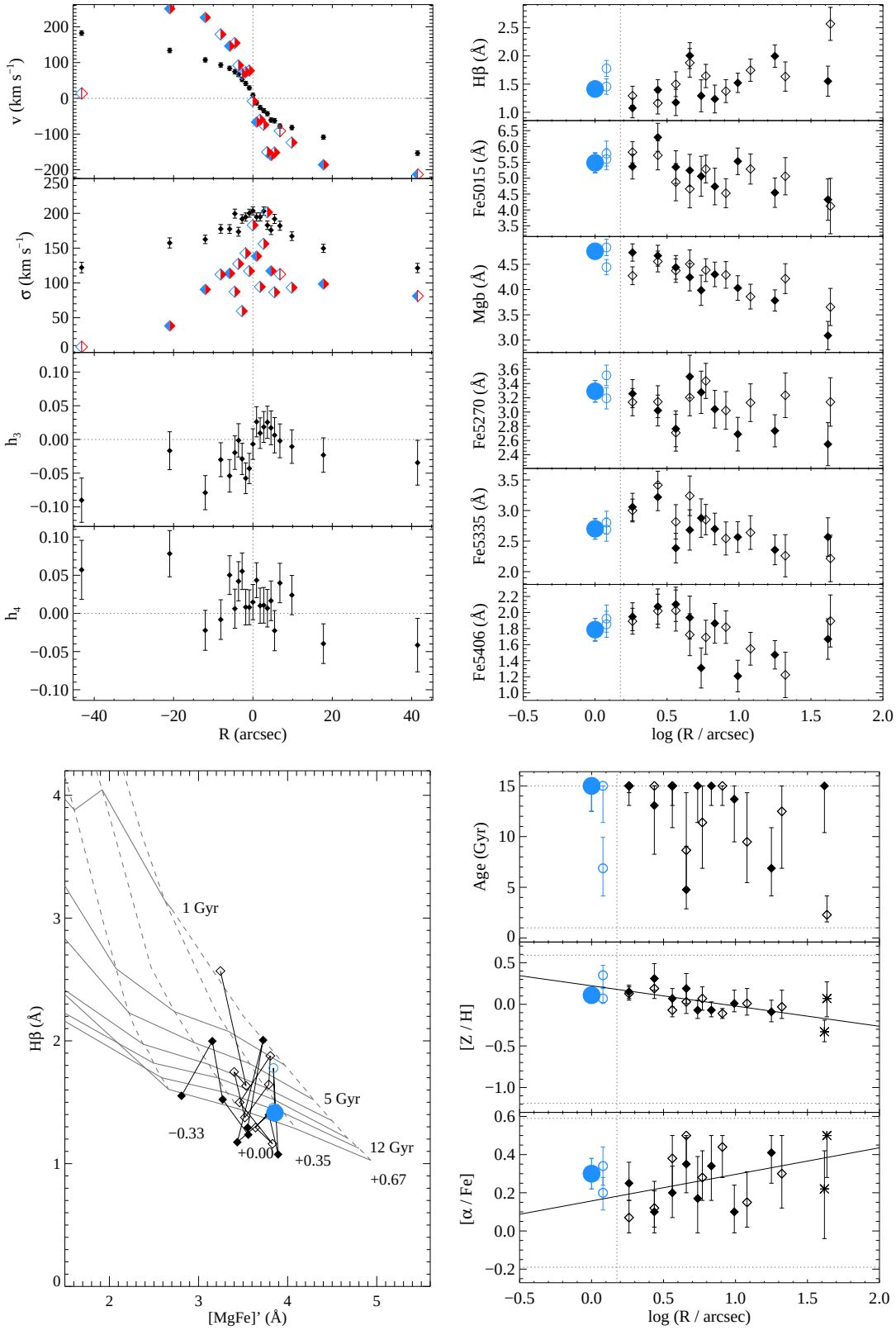

Figure 5.8: NGC 1032 (round bulge)

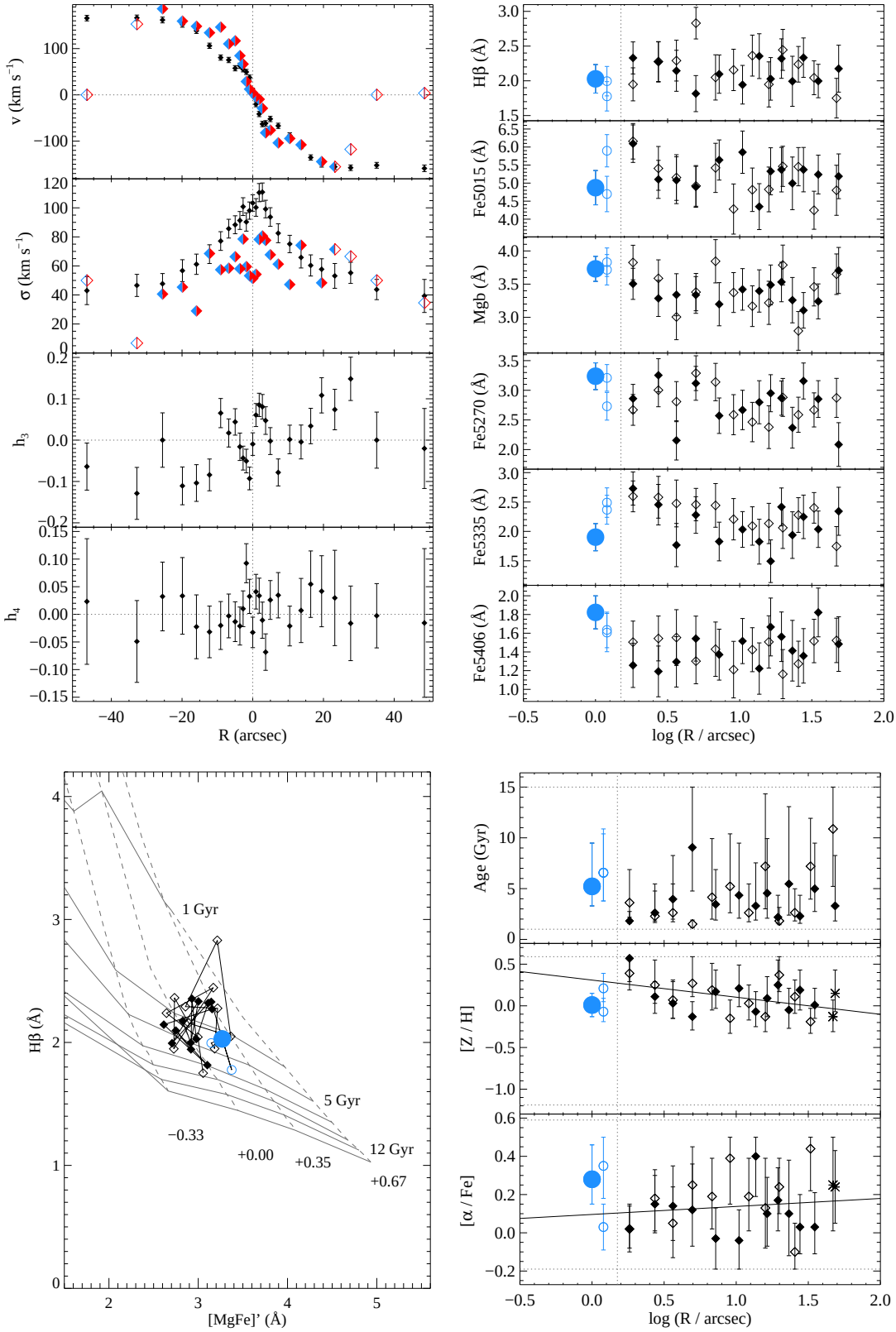

Figure 5.8: NGC 3957 (round bulge)

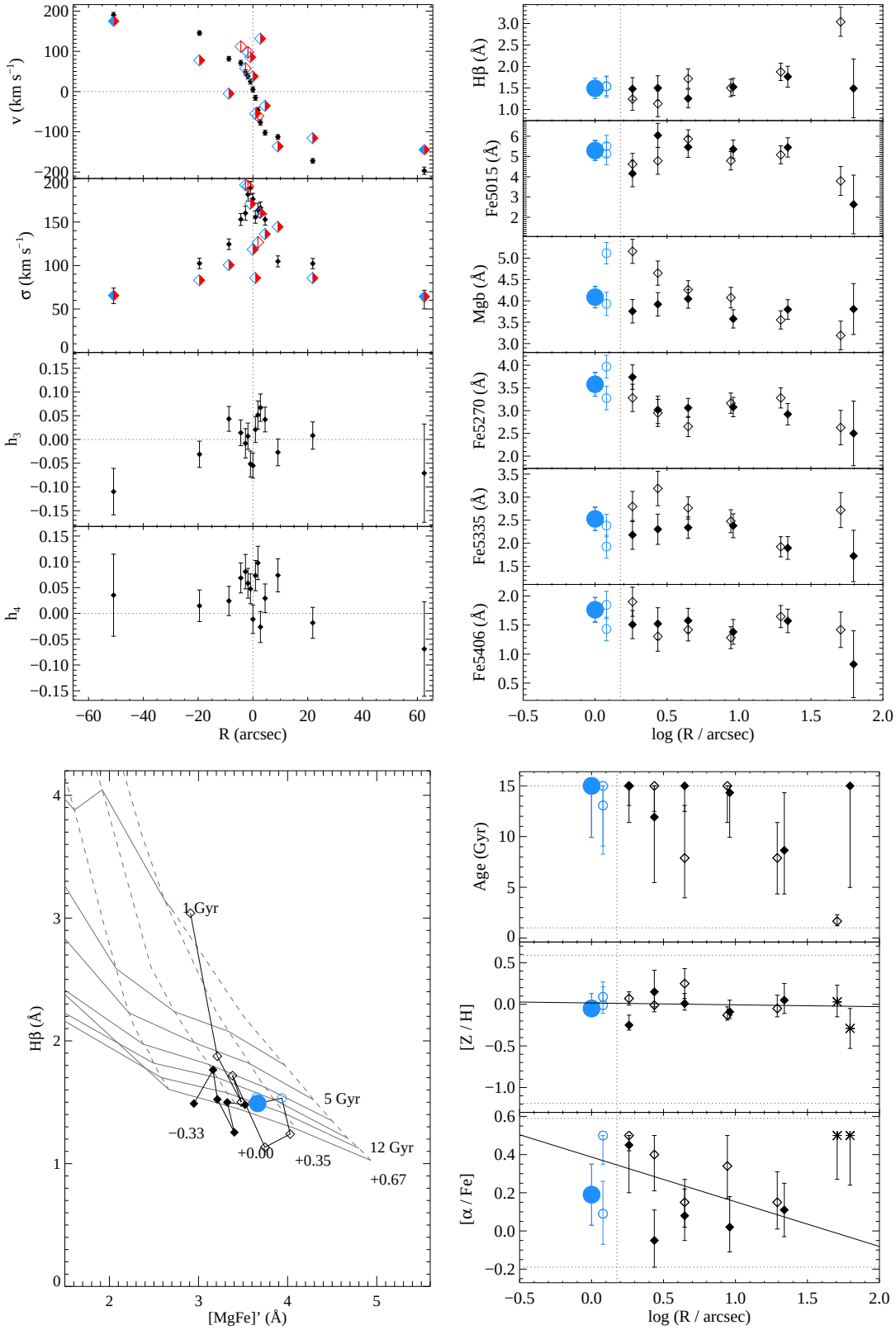

Figure 5.8: NGC 4703 (round bulge)

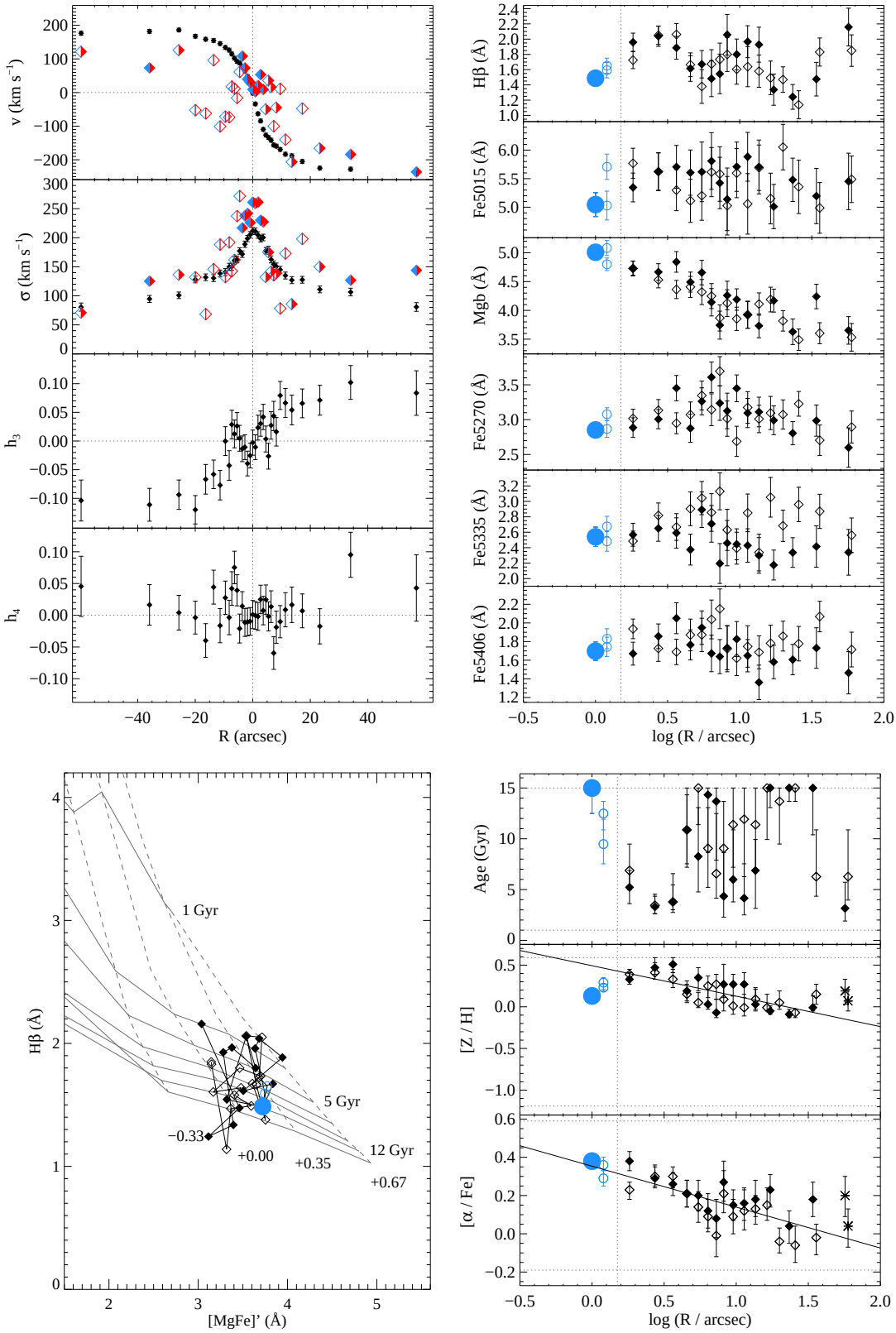

Figure 5.8: NGC 5084 (round bulge)

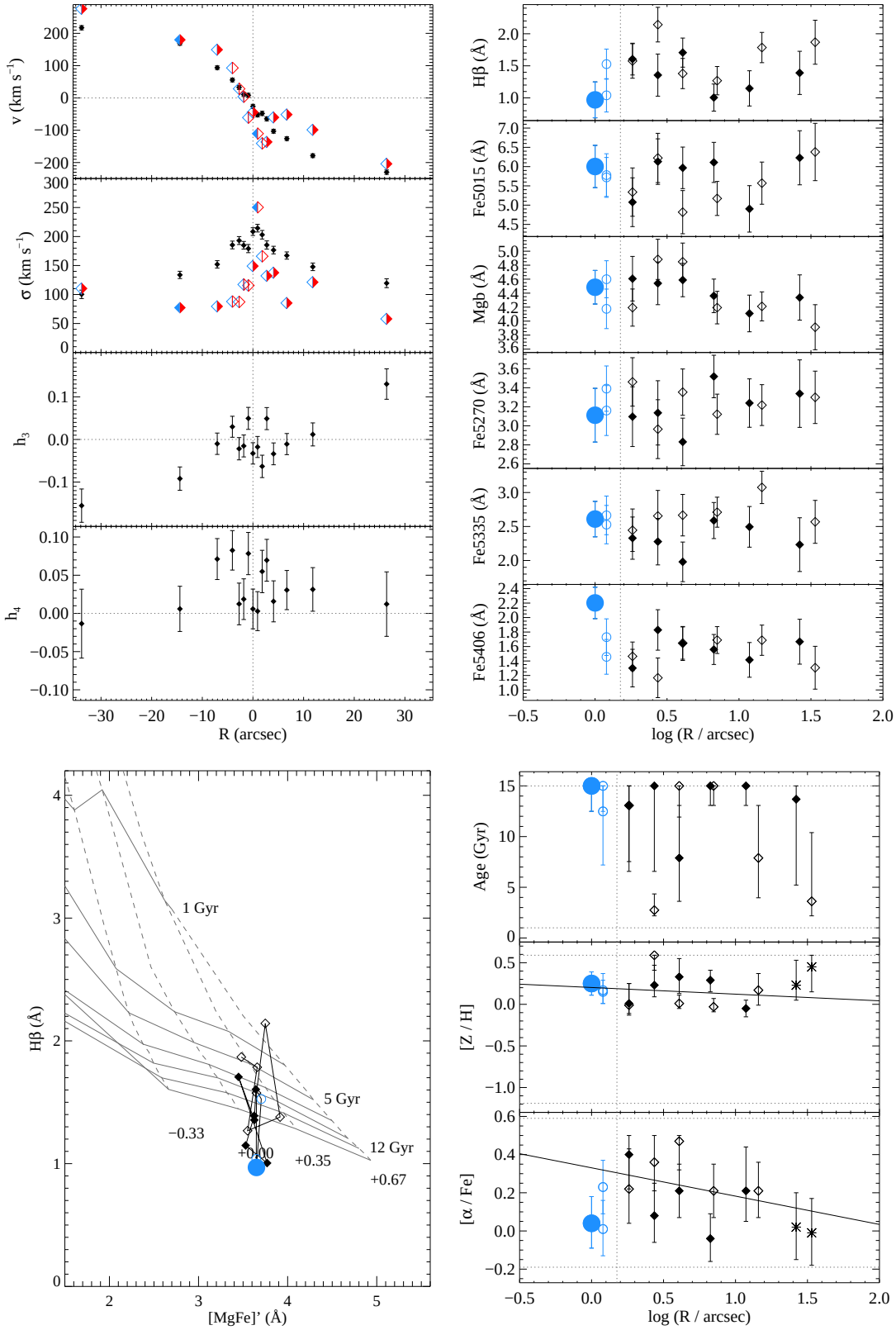

Figure 5.8: NGC 7123 (round bulge)

6

CONCLUSION

6.1 SUMMARY OF MAIN RESULTS

In this thesis I investigated the dynamics and stellar populations of a sample of 28 early-type disk galaxies. All the galaxies in the sample are oriented close to edge-on. Half are S0s and half are spirals. The majority (22) host a bulge that is boxy or peanut-shaped.

6.1.1 Mass models

In Chapter 2, I presented mass models of the sample. For each galaxy I derived the stellar mass distribution from near-infrared photometry under the assumptions of axisymmetry and a constant K_S-band stellar mass-to-light ratio, $(M/L)_{K_S}$. To this I added a dark halo assumed to follow a spherically symmetric Navarro, Frenk & White (1997) profile and a correlation between concentration and dark mass within the virial radius, $M_{\rm DM}$. I solved the Jeans equations for the corresponding potential under the assumption of constant anisotropy in the meridional plane, β_z.

By comparing the predicted second velocity moment to observed long-slit stellar kinematics, I determined the three best-fitting parameters of the model: $(M/L)_{K_S}$,

$M_{\rm DM}$ and β_z. These simple axisymmetric Jeans models are able to accurately reproduce the wide range of observed stellar kinematics, which typically extend to $\approx$ 2–3 $R_{\rm eff}$ or, equivalently, $\approx$ 0.5–1 R_{25}. I find a median stellar mass-to-light ratio at K_S-band of 1.09 $(M/L)_{K_S,\odot}$ with an rms scatter of 0.31. I presented preliminary comparisons between the dynamically-determined stellar mass-to-light ratios and the predictions of stellar population models. The stellar population models predict slightly lower mass-to-light ratios than I measure. The mass models contain a median of 15 per cent dark matter by mass within an effective radius $R_{\rm eff}$ (defined here as the semi-major axis of the ellipse containing half the K_S-band light), and 49 per cent within the optical radius R_{25}. Dark and stellar matter contribute equally to the mass within a sphere of radius 4.1 $R_{\rm eff}$ or 1.0 R_{25}. There is no evidence of any significant difference in the dark matter content of the spirals and S0s in the sample. Although the sample contains barred galaxies, I argue a posteriori that the assumption of axisymmetry does not significantly affect my results. Models without dark matter are also able to satisfactorily reproduce the observed kinematics in most cases. The improvement when a halo is added is statistically significant, however, and the stellar mass-to-light ratios of mass models with dark haloes match the independent expectations of stellar population models better.

6.1.2 The Tully-Fisher relations of early-type spirals and S0s

In Chapter 3, I compared the Tully-Fisher (luminosity–velocity) relations of the spirals and S0 galaxies in the sample. I began by demonstrating that the comparison of Tully-Fisher relations (TFRs) derived from global H I line widths to TFRs derived from the circular velocity profiles of dynamical models (or stellar kinematic observations corrected for asymmetric drift) is vulnerable to systematic and uncertain biases introduced by the different measures of rotation used. I therefore argued that to constrain the relative locations of the TFRs of spiral and S0 galaxies, the same tracer and measure must be used for both samples.

I found that S0s lie on a TFR with the same slope as the spirals, but are on average

0.53 ± 0.15 mag fainter at K_S-band at a given rotational velocity. This is a significantly smaller offset than that measured in earlier studies of the S0 TFR, which I attributed to my elimination of the bias associated with using different rotation measures and our use of earlier type spirals as a reference. Since this measurement of the offset avoids systematic biases, it should be preferred to previous estimates.

A spiral stellar population in which star formation is truncated would take ≈ 1 Gyr to fade by 0.53 mag at K_S-band. If S0s are the products of a simple truncation of star formation in spirals, then this finding is difficult to reconcile with the observed evolution of the spiral/S0 fraction with redshift. Recent star formation could explain the observed lack of fading in S0s, but I showed that the offset of the S0 TFR persists as a function of both stellar and dynamical mass. The offset of the S0 TFR could therefore be explained by a systematic difference between the total mass distributions of S0s and spirals, in the sense that S0s are to be smaller or more concentrated than spirals.

6.1.3 The vertical structure of boxy bulges

In Chapter 4, I studied the vertical structure of the boxy and peanut-shaped bulges of a subset of five galaxies drawn from the main sample. Such bulges are seen in around half of edge-on disk galaxies are bars viewed in projection. This is consistent with simulations of bar formation and evolution, and observations of the demographics, photometry and major-axis gas and stellar kinematics of such bulges. If the properties of boxy bulges can be entirely explained by assuming that they are bars, this may imply that such galaxies are pure disk galaxies with no classical bulge (Shen et al., 2010). This raises the possibility that a demographically significant population (which make up half of edge-on giant disk galaxies) are pure disk galaxies. Cosmological simulations of galaxy formation in a hierarchical universe currently fail to form such galaxies, so they are of great interest. The orientation of these galaxies provides us with a unique perspective from which to observe the internal structure of bars and their role in driving secular evolution.

A handful of these bulges, including that of the Milky Way, have been observed to rotate cylindrically, i.e. with a velocity independent of height above the disk (e.g. Kormendy & Illingworth, 1982; Howard et al., 2009). In order to assess whether such behaviour is ubiquitous in boxy bulges, and whether the pure disk picture is consistent with their stellar populations, I analysed the kinematics and stellar populations of the boxy or peanut-shaped bulges of a sample of five edge-on galaxies. I used NTT/EMMI spectroscopic data from long slits placed along the major axis and at three offset but parallel positions to build up spatial coverage of each galaxy. In one case (NGC 3390), the boxy bulge rotates perfectly cylindrically within the spatial extent and uncertainties of the data. This observation is consistent with its stellar populations, which show no difference between the relative abundance of α-elements in the disk and the bulge. This galaxy is a probably pure disk galaxy. However, the other boxy bulges in the sample do not rotate cylindrically, and in one case (NGC 1381) the bulge is significantly α-enhanced with respect to its disk, suggesting a composite bulge comprised of a classical bulge and bar (and possible disky pseudobulge). Cylindrical rotation is therefore not ubiquitous in bulges that appear boxy or peanut-shaped, and not all such galaxies are pure disks. This small sample was sufficient to demonstrate that the formation of these systems cannot be entirely explained by the buckling of bars in pure disk systems, at least as insofar as it is currently understood.

6.1.4 The radial structure of boxy bulges

Finally, in Chapter 5, I analysed global and radial trends in the stellar populations of the bulges of a sample of 28 edge-on S0–Sb disk galaxies, 22 of which are boxy/peanut-shaped. My principal finding are as follows. (1) At a given velocity dispersion, the central stellar populations of galaxies with boxy/peanut-shaped bulges are indistinguishable from those of of elliptical galaxies. If secular evolution has effects on stellar populations that are different to those of monolithic collapse or mergers then this suggests that secular evolution is not important in the central regions of these galaxies,

despite the fact that they are probably barred. (2) The radial metallicity gradients of boxy/peanut-shaped bulges are uncorrelated with velocity dispersion and are, on average, shallower than those of unbarred early-type galaxies. This is qualitatively consistent with chemodynamical models of bar formation, in which radial inflow and outflow smears out pre-existing gradients.

6.2 ONGOING WORK

I now describe two ongoing projects which make use of the sample and results presented in this thesis.

6.2.1 Stellar mass and the IMF

As discussed in Section 2.5.1.2, the comparison of purely dynamical measurements of galaxy stellar masses to those derived using stellar population models is of great interest. It has the potential to constrain the structure of dark haloes, including their deformation by baryons, the late phases of stellar evolution which are responsible for much of the light at near-infrared wavelengths, and the initial mass function (IMF) from which stellar masses in a population a drawn. This subject has recently been the focus of much attention in both early-types (e.g. Cappellari et al., 2006; Schulz, Mandelbaum & Padmanabhan, 2009; Treu et al., 2010; Auger et al., 2010) and spirals (e.g. Bershady et al., 2010).

In Section 2.5.1.2 we made a preliminary comparison between our dynamical measures of the stellar (M/L) and the predictions of colour–(M/L) relations. Unfortunately, in edge-on galaxies, the use of colour as a probe of stellar populations is of limited utility because of the uncertainties introduced by the very significant dust content along the line of site of the disk.

Two approaches are available to minimize this problem, both of which we are pursuing at the time of writing. The first is to adopt the (M/L) of the SSP-equivalent populations derived in Chapter 5. The SSP-equivalent populations are constrained by

absorption line strengths, which are almost unaffected by dust (MacArthur, 2005). This approach is sufficient in spectra that are well-described by a single stellar population (e.g. Cappellari et al., 2006).

The second approach is to find SSP templates that best describe the complete spectrum. This method uses the full information in the 2000 pixel spectrum to constrain the stellar populations, rather than reducing it to six absorption line strengths. Crucially, with the increased information available to constrain the stellar populations, it is possible to fit using a linear superposition of several SSP spectra rather than searching for the one SSP spectra that best matches the observed spectrum. This more general approach is better able to capture the multiple populations and ongoing star formation expected in spirals. This is particularly important, because the SSP-equivalent approach described above is biased towards younger stars, and can yield a (M/L) that is extremely unrepresentative of the mass-weighted (M/L) in a given spectrum (MacArthur, González & Courteau, 2009). The multi-population approach allows the determination of a mass-weighted (M/L) directly from the weights assigned to the SSP spectra used in the fit.

Once the stellar population (M/L) of each spectrum is derived using one of the two methods described above, we must adopt a global average in order to make meaningful comparisons to the dynamical stellar (M/L) derived for the galaxy. The stellar population (M/L) can be recalibrated for a given IMF using a simple multiplicative scaling. It may by difficult to distinguish between effects of a varying IMF and the baryonic contraction of the halo, but we should be able to exclude an IMF if there is no evidence for its variation.

6.2.2 *Measuring Lick indices using high S/N template spectra*

We have investigated measuring Lick/IDS absorption indices on the best-fitting continuum spectrum found by GANDALF/PPXF, rather than on the observed spectrum. Assuming the template describes the data well, this template spectrum is a very high S/N version of the observed spectrum. In essence, an observed spectrum of moderate

S/N can be used to bootstrap a physically motivated process whose product is a nearly noiseless version of the original spectrum.

Of course the crucial assumption in the above paragraph is that the model is a good fit to the data. This is meant not only in the sense that the mean residuals of the fit should be zero, but also in the sense that there are not systematic differences between the model and data on the scale of individual absorption features, i.e. template mismatch.

In the case of our galaxies and template library, a crucial sanity check of this is passed with flying colours, as is shown in Figs. 6.1 and 6.2. By eye, the Lick indices measured on the observed spectrum (cleaned of emission), look like those measured on the best-fitting continuum spectrum with the addition of observational noise.

However, a more rigorous demonstration that includes a quantification of the effects of template mismatch is required. We propose to attempt this by measuring Lick indices on the residuals or 'mismatch spectrum'. If the model describes the data well in the senses described above, then (1) The Lick indices of the mismatch spectrum should be zero within the uncertainties on the Lick indices of the observed spectrum, typically $\lesssim$ a few tenths of an Å. (2) There should be no systematic variation of the Lick indices of the mismatch spectrum with galaxy properties or, crucially, with spatial position within the galaxy. The first of these tests is merely a quantitative version of the sanity check described above. The second looks for systematic template mismatch, i.e. a failure of the template library to capture physically meaningful features of the spectra in the sample. It is particularly important that mismatch of this kind not vary spatially, since that would introduce artificial population gradients.

Our results will only hold for the specific case of our galaxies and our template library, but the method is sufficiently simple that it may be it may be repeated easily in future work. The potential advantages of line strength measurements at increased effective S/N are wide-ranging. Two specific examples relevant to the present work are (1) more prominent breaks in radial profiles and (2) significantly reduced uncertainties on the measurement of Δ[Z/H]. This latter prospect is of interest because it raises the possibility of measuring the *intrinsic* scatter of Δ[Z/H], which is a testable prediction of models of galaxy formation (e.g. Spolaor et al., 2009), rather than the total scatter,

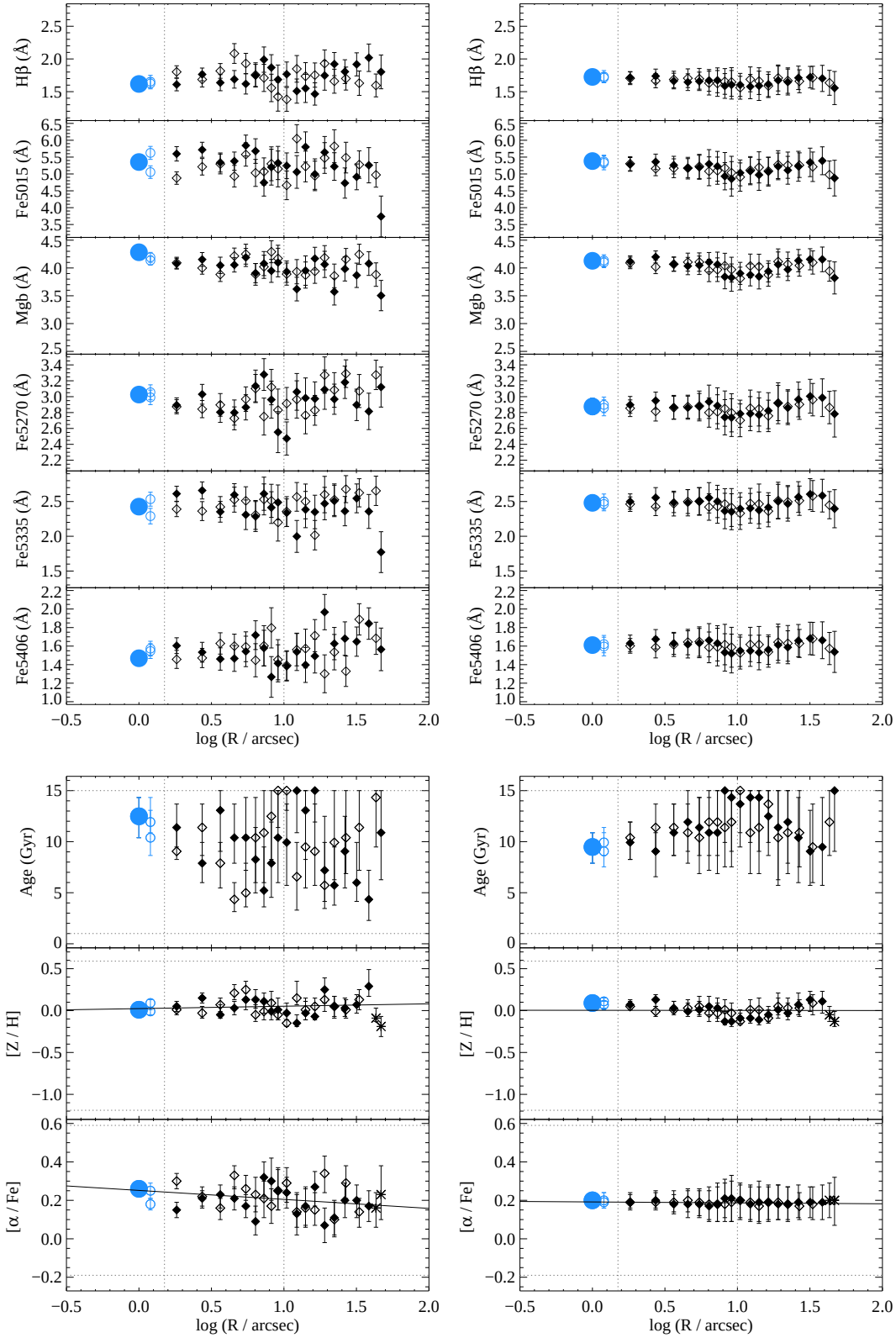

Figure 6.1: *Left:* Lick indices and SSP-equivalent populations of the observed spectrum of NGC 1381 as a function of log R. Symbols are as in Section 5.A. *Right:* The same measured on the best-fitting model spectrum.

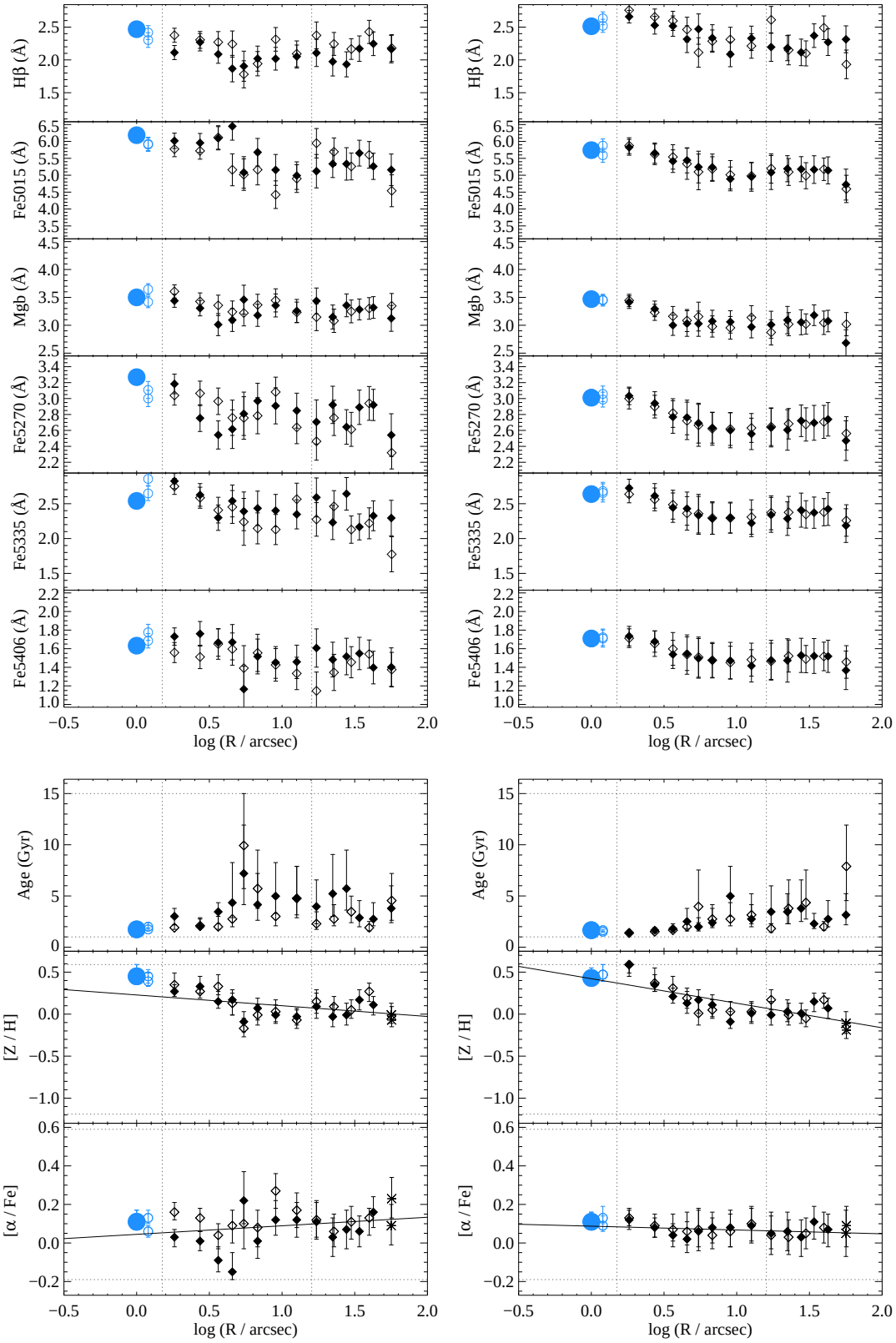

Figure 6.2: As Fig. 6.1 but for NGC 2310

which is dominated by measurement uncertainties in the present work.

6.3 FUTURE WORK

6.3.1 Explaining the S0 TFR

In Chapter 3 we demonstrated that S0s are systematically fainter than spirals of the same rotational velocity. This observation is consistent with the interpretation of Bedregal, Aragón-Salamanca & Merrifield (2006) and others that S0s are faded spirals that are dynamically similar to their progenitors. If correct then, in the absence of transformational major mergers, the aging and consequent fading of stars in spirals means that S0s are the end point of the evolution of galaxies like the Milky Way.

However, we further showed that (1) the amount by which they are fainter is difficult to reconcile with models of passive fading and the observed evolution of the fraction S0s galaxies, and (2) the offset in luminosity persists in stellar mass and dynamical mass. We therefore proposed the possibility that S0s are dynamically different to spirals, perhaps because of an environmental or secular process that lead to the build up of a massive and dominant bulge rather than a diffuse and/or small pseudobulge, or perhaps because their host dark halo contracted more efficiently than in spirals.

Discriminating between these competing scenarios is observationally challenging. Bedregal, Aragón-Salamanca & Merrifield (2006) showed using a small sample of 8 galaxies that the distance of individual S0s from the spiral TFR is correlated with their stellar age. This observation is consistent with the fading interpretation, and should hold generally for all disk galaxies, with young galaxies found above the luminosity–velocity relation, and old galaxies below.

However, the scenario cannot explain the offsets of S0s from the stellar mass and dynamical mass spiral TFR observed in Chapter 3. This suggests that part (or all) of the explanation may be given by the second scenario, in which S0s are smaller or more concentrated for a given dynamical mass due to an unknown mechanism. If

this is true then the residuals of disk galaxies from the mean spiral TFR should be correlated with the structural properties of their dynamical mass distribution. To seek such correlations requires a physical model of the mass distribution of each galaxy, in which the halo model is as general as possible.

To this end, I have begun a collaboration with Remco van den Bosch (MPIA) and Anne-Marie Weijmans (Toronto) to collect integral field spectroscopic observations of a sample of S0 galaxies. We are using the VIRUS-P spectrograph, which has advantages over both the long-slit data used in this thesis and Bedregal, Aragón-Salamanca & Merrifield (2006), and the integral field observations of the SAURON sample of early-types. Firstly, because it collects data in two spatial dimensions, it has the potential to formally break the disk–halo degeneracy, rather than sidestepping it by inserting motivated assumptions about the halo shape as we did in Chapter 2. Secondly, it has field of view approximately 10 times larger in area than SAURON, so can make observations of the disks of nearby S0s. This is crucial because, without disk spectroscopy, you cannot measure the age of the stellar disk (which may correlate more tightly with the residuals of the TFR than the bulge age), and, crucially, you cannot measure the maximum velocity and therefore cannot place S0s on the Tully-Fisher relation.

Our sample currently stands at six field S0s observed in August 2010, and we intend to collect observations of a further 6–12 galaxies in the Virgo cluster. We will also take advantage of the VENGA survey of local star-forming spiral galaxies observed with the same instrument (Blanc et al., 2009), which we will use as a control sample.

6.3.2 *The populations of boxy bulges in SDSS*

Drory & Fisher (2007) showed that the global colours (as measured by SDSS) of galaxies which host pseudobulges are systematically bluer than those of galaxies which host classical bulges. They defined pseudobulges as those that have nuclear star formation, so this was perhaps not surprising, but they further demonstrated that

Figure 6.3: Global optical colour of bulges hosting nuclear star formation, i.e. pseudobulges (blue) and classical bulges (red) as a function of Sérsic index. Open symbols are S0s, filled symbols are spirals. Figure taken from Drory & Fisher (2007), ommited here for copyright reasons.

their pseudobulges have small Sérsic indices (see Fig. 6.3). That is to say, a structural parameter of the bulge of the galaxy is a good predictor of whether it will fall in red sequence or the blue cloud of the colour-magnitude diagram (e.g. Strateva et al., 2001; Balogh et al., 2004; Baldry et al., 2004; Driver et al., 2006).

As emphasized in Chapter 1, there is an apparent connection (and indeed some confusion) between pseudobulges (thought to be the products of bar-driven inflow) and boxy/peanut-shaped bulges (vertical protuberances thought to either simply be bars, or to be created by bars). In an attempt to illuminate this, I will make a similar comparison to Drory & Fisher (2007) for boxy and peanut-shaped bulges in the SDSS dataset. There are two samples I can draw from. Firstly, Lütticke, Dettmar & Pohlen (2000) classify the shape of the bulges of ≈1200 large nearby edge-on galaxies using photographic DSS images. About 300 of this sample are in SDSS, and 45% are boxy or peanut-shaped. Secondly, the Galaxy Zoo 2 database provides a much larger sample of edge-on galaxies at $z \lesssim 0.07$. The bulges of these galaxies can be classified as boxy/peanut-shaped or round either by expert visual inspection, or using the collective classification of non-expert Galaxy Zoo users. Either method will significantly increase the sample of known boxy/peanut-shaped bulges, and the

classification may be more robust than the Lütticke, Dettmar & Pohlen (2000) sample because of the higher quality imaging.

Global colours are reddened by dust in edge-on spirals, so I will investigate measuring colours within a central aperture that encloses the boxy bulge but in which the disk has been masked. Using the central SDSS fibre spectra for each galaxy, I will repeat the analysis of Section 5.5 of this thesis, i.e. examine the central stellar populations of barred galaxies to look for evidence of differences between their central stellar populations and those of classical bulges and ellipticals. This will improve over the analysis in this thesis both in the wavelength coverage of the spectra used to constrain the populations and the size of the sample, which will be 1–2 orders of magnitude larger.

REFERENCES

Aaronson M., Mould J., 1983, ApJ, 265, 1

Abadi M. G., Navarro J. F., Fardal M., Babul A., Steinmetz M., 2010, MNRAS, 847

Aguerri J. A. L., Debattista V. P., Corsini E. M., 2003, MNRAS, 338, 465

Aguerri J. A. L., Méndez-Abreu J., Corsini E. M., 2009, A&A, 495, 491

Arnouts S., et al., 2007, A&A, 476, 137

Athanassoula E., 1992, MNRAS, 259, 345

—, 2005, MNRAS, 358, 1477

Athanassoula E., Bureau M., 1999, ApJ, 522, 699

Athanassoula E., Misiriotis A., 2002, MNRAS, 330, 35

Auger M. W., Treu T., Gavazzi R., Bolton A. S., Koopmans L. V. E., Marshall P. J., 2010, ArXiv e-prints

Babusiaux C. et al., 2010, A&A, 519, A77

Baldry I. K., et al., 2004, ApJ, 600, 681

Balogh M. L., Baldry I. K., Nichol R., Miller C., Bower R., Glazebrook K., 2004, ApJ, 615, L101

Banerjee A., Jog C. J., 2008, ApJ, 685, 254

Barway S., Wadadekar Y., Kembhavi A. K., Mayya Y. D., 2009, MNRAS, 394, 1991

Baugh C. M., 2006, Reports on Progress in Physics, 69, 3101

Bedregal A. G., Aragón-Salamanca A., Merrifield M. R., 2006, MNRAS, 373, 1125

Bedregal A. G., Aragón-Salamanca A., Merrifield M. R., Cardiel N., 2008, MNRAS, 387, 660

Bell E. F., de Jong R. S., 2001, ApJ, 550, 212

Bell E. F., McIntosh D. H., Katz N., Weinberg M. D., 2003, ApJS, 149, 289

Bender R., 1990, A&A, 229, 441

Bender R., Burstein D., Faber S. M., 1993, ApJ, 411, 153

Bendinelli O., 1991, ApJ, 366, 599

Benson A. J., Bower R. G., Frenk C. S., Lacey C. G., Baugh C. M., Cole S., 2003, ApJ, 599, 38

Bershady M. A., Verheijen M. A. W., Swaters R. A., Andersen D. R., Westfall K. B., Martinsson T., 2010, ApJ, 716, 198

Bertola F., Cinzano P., Corsini E. M., Rix H., Zeilinger W. W., 1995, ApJ, 448, L13+

Bertola F., Pizzella A., Persic M., Salucci P., 1993, ApJ, 416, L45

Bettoni D., Galletta G., 1994, A&A, 281, 1

Bigiel F., Leroy A., Walter F., Brinks E., de Blok W. J. G., Madore B., Thornley M. D., 2008, AJ, 136, 2846

Binney J., Petrou M., 1985, MNRAS, 214, 449

Binney J., Tremaine S., 2008, Galactic Dynamics: Second Edition. Princeton University Press

Blanc G. A., Heiderman A., Gebhardt K., Evans N. J., Adams J., 2009, ApJ, 704, 842

Blanton M. R., Moustakas J., 2009, ARA&A, 47, 159

Blanton M. R., Roweis S., 2007, AJ, 133, 734

Blumenthal G. R., Faber S. M., Flores R., Primack J. R., 1986, ApJ, 301, 27

Blumenthal G. R., Faber S. M., Primack J. R., Rees M. J., 1984, Nature, 311, 517

Bolton A. S., Treu T., Koopmans L. V. E., Gavazzi R., Moustakas L. A., Burles S., Schlegel D. J., Wayth R., 2008, ApJ, 684, 248

Borriello A., Salucci P., Danese L., 2003, MNRAS, 341, 1109

Bottinelli L., Gouguenheim L., Paturel G., Teerikorpi P., 1995, A&A, 296, 64

Bournaud F., Elmegreen B. G., Elmegreen D. M., 2007, ApJ, 670, 237

Brough S., Proctor R., Forbes D. A., Couch W. J., Collins C. A., Burke D. J., Mann R. G., 2007, MNRAS, 378, 1507

Bruzual G., Charlot S., 2003, MNRAS, 344, 1000

Bullock J. S., Kolatt T. S., Sigad Y., Somerville R. S., Kravtsov A. V., Klypin A. A., Primack J. R., Dekel A., 2001, MNRAS, 321, 559

Bureau M., Aronica G., Athanassoula E., Dettmar R.-J., Bosma A., Freeman K. C., 2006, MNRAS, 370, 753

Bureau M., Athanassoula E., 1999, ApJ, 522, 686

—, 2005, ApJ, 626, 159

Bureau M., Freeman K. C., 1999, AJ, 118, 126

Bureau M. et al., 2011, MNRAS, submitted

Burstein D., Bertola F., Buson L. M., Faber S. M., Lauer T. R., 1988, ApJ, 328, 440

Burstein D., Davies R. L., Dressler A., Faber S. M., Stone R. P. S., Lynden-Bell D., Terlevich R. J., Wegner G., 1987, ApJS, 64, 601

Burstein D., Faber S. M., Gaskell C. M., Krumm N., 1984, ApJ, 287, 586

Burstein D., Ho L. C., Huchra J. P., Macri L. M., 2005, ApJ, 621, 246

Cappellari M., 2002, MNRAS, 333, 400

—, 2008, MNRAS, 390, 71

Cappellari M. et al., 2006, MNRAS, 366, 1126

Cappellari M., Emsellem E., 2004, PASP, 116, 138

Cappellari M. et al., 2007, MNRAS, 379, 418

Cappellari M., McDermid R. M., 2005, Classical and Quantum Gravity, 22, 347

Cappellari M., Neumayer N., Reunanen J., van der Werf P. P., de Zeeuw P. T., Rix H.-W., 2009, MNRAS, 394, 660

Cappellari M., et al., 2011, MNRAS, submitted

Cardelli J. A., Clayton G. C., Mathis J. S., 1989, ApJ, 345, 245

Carlberg R. G., 1984, ApJ, 286, 403

Carollo C. M., Scarlata C., Stiavelli M., Wyse R. F. G., Mayer L., 2007, ApJ, 658, 960

Chabrier G., 2003, PASP, 115, 763

Christlein D., Zabludoff A. I., 2004, ApJ, 616, 192

Chung A., Bureau M., 2004, AJ, 127, 3192

Chung A., Koribalski B., Bureau M., van Gorkom J. H., 2006, MNRAS, 370, 1565

Cinzano P., Rix H., Sarzi M., Corsini E. M., Zeilinger W. W., Bertola F., 1999, MNRAS, 307, 433

Ciotti L., 1991, A&A, 249, 99

Cole S., Aragon-Salamanca A., Frenk C. S., Navarro J. F., Zepf S. E., 1994, MNRAS, 271, 781

Combes F., Debbasch F., Friedli D., Pfenniger D., 1990, A&A, 233, 82

Combes F., Sanders R. H., 1981, A&A, 96, 164

Conselice C. J., Bundy K., Ellis R. S., Brichmann J., Vogt N. P., Phillips A. C., 2005, ApJ, 628, 160

Corsini E. M. et al., 1999, A&A, 342, 671

Courteau S., Dutton A. A., van den Bosch F. C., MacArthur L. A., Dekel A., McIntosh D. H., Dale D. A., 2007, ApJ, 671, 203

Courteau S., Rix H.-W., 1999, ApJ, 513, 561

Courtois H. M., Tully R. B., Fisher J. R., Bonhomme N., Zavodny M., Barnes A., 2009, AJ, 138, 1938

Cretton N., Rix H., de Zeeuw P. T., 2000, ApJ, 536, 319

Crook A. C., Huchra J. P., Martimbeau N., Masters K. L., Jarrett T., Macri L. M., 2007, ApJ, 655, 790

Croton D. J. et al., 2006, MNRAS, 365, 11

Davies R. L., Efstathiou G., Fall S. M., Illingworth G., Schechter P. L., 1983, ApJ, 266, 41

Davies R. L., Sadler E. M., Peletier R. F., 1993, MNRAS, 262, 650

de Blok W. J. G., McGaugh S. S., 1997, MNRAS, 290, 533

de Blok W. J. G., McGaugh S. S., Rubin V. C., 2001, AJ, 122, 2396

de Lorenzi F., Debattista V. P., Gerhard O., Sambhus N., 2007, MNRAS, 376, 71

De Rijcke S., Zeilinger W. W., Hau G. K. T., Prugniel P., Dejonghe H., 2007, ApJ, 659, 1172

de Souza R. E., Dos Anjos S., 1987, A&AS, 70, 465

de Vaucouleurs G., 1948, Annales d'Astrophysique, 11, 247

—, 1959, Handbuch der Physik, 53, 275

de Vaucouleurs G., de Vaucouleurs A., Corwin H., Buta R., Paturel G., Fouqué P., 1991, Third Reference Catalogue of Bright Galaxies (RC3). Springer-Verlag, Berlin

de Zeeuw P. T. et al., 2002, MNRAS, 329, 513

Debattista V. P., Sellwood J. A., 2000, ApJ, 543, 704

Dekel A., Stoehr F., Mamon G. A., Cox T. J., Novak G. S., Primack J. R., 2005, Nature, 437, 707

Devereux N., Hriljac P., Willner S. P., Ashby M. L. N., Willmer C. N. A., 2009, in Galaxy Evolution: Emerging Insights and Future Challenges, arXiv:0902.0778, Jogee S., Hao L., Blanc G., Marinova I., eds., ASP Conf. Ser., Astron. Soc. Pac., San Francisco

Devereux N. A., Becklin E. E., Scoville N., 1987, ApJ, 312, 529

Djorgovski S., Davis M., 1987, ApJ, 313, 59

Dressler A., 1980, ApJ, 236, 351

Dressler A., Lynden-Bell D., Burstein D., Davies R. L., Faber S. M., Terlevich R., Wegner G., 1987, ApJ, 313, 42

Dressler A., et al., 1997, ApJ, 490, 577

Driver S. P., et al., 2006, MNRAS, 368, 414

Drory N., Fisher D. B., 2007, ApJ, 664, 640

Dutil Y., Roy J., 1999, ApJ, 516, 62

Dutton A. A., 2009, MNRAS, 396, 121

Dutton A. A., van den Bosch F. C., Dekel A., Courteau S., 2007, ApJ, 654, 27

Edvardsson B., Andersen J., Gustafsson B., Lambert D. L., Nissen P. E., Tomkin J., 1993, A&A, 275, 101

Eggen O. J., Lynden-Bell D., Sandage A. R., 1962, ApJ, 136, 748

Eke V. R., Navarro J. F., Steinmetz M., 2001, ApJ, 554, 114

Elmegreen D. M., Elmegreen B. G., Hirst A. C., 2004, ApJ, 604, L21

Emsellem E. et al., 2004, MNRAS, 352, 721

Emsellem E., Monnet G., Bacon R., 1994, A&A, 285, 723

Emsellem E., et al., 2007, MNRAS, 379, 401

Englmaier P., Gerhard O., 1999, MNRAS, 304, 512

Erwin P., 2005, MNRAS, 364, 283

Eskridge P. B. et al., 2000, AJ, 119, 536

Faber S. M., Friel E. D., Burstein D., Gaskell C. M., 1985, ApJS, 57, 711

Falcón-Barroso J. et al., 2006, MNRAS, 369, 529

—, 2004, MNRAS, 350, 35

Fasano G., Poggianti B. M., Couch W. J., Bettoni D., Kjærgaard P., Moles M., 2000, ApJ, 542, 673

Fioc M., Rocca-Volmerange B., 1997, A&A, 326, 950

Fisher D., Illingworth G., Franx M., 1994, AJ, 107, 160

Flores H., Hammer F., Puech M., Amram P., Balkowski C., 2006, A&A, 455, 107

Förster Schreiber N. M. et al., 2009, ApJ, 706, 1364

Franx M., 1993, in IAU Symposium, Vol. 153, Galactic Bulges, H. Dejonghe & H. J. Habing, ed., p. 243

Freeman K. C., 1970, ApJ, 160, 811

—, 2008, in IAU Symposium, Vol. 245, IAU Symposium, M. Bureau, E. Athanassoula, & B. Barbuy, ed., p. 3

Friedli D., 1998, in Astronomical Society of the Pacific Conference Series, Vol. 147, Abundance Profiles: Diagnostic Tools for Galaxy History, D. Friedli, M. Edmunds, C. Robert, & L. Drissen, ed., p. 287

Friedli D., Benz W., Kennicutt R., 1994, ApJ, 430, L105

Gadotti D. A., dos Anjos S., 2001, AJ, 122, 1298

Ganda K. et al., 2007, MNRAS, 380, 506

Gentile G., Salucci P., Klein U., Vergani D., Kalberla P., 2004, MNRAS, 351, 903

Gerhard O., Kronawitter A., Saglia R. P., Bender R., 2001, AJ, 121, 1936

Gerssen J., Kuijken K., Merrifield M. R., 2003, MNRAS, 345, 261

Gnedin O. Y., Kravtsov A. V., Klypin A. A., Nagai D., 2004, ApJ, 616, 16

Gunn J. E., Gott J. R. I., 1972, ApJ, 176, 1

Häring N., Rix H., 2004, ApJ, 604, L89

Heald G. H., Rand R. J., Benjamin R. A., Bershady M. A., 2007, ApJ, 663, 933

Hernquist L., 1990, ApJ, 356, 359

Hinz J. L., Rieke G. H., Caldwell N., 2003, AJ, 126, 2622

Hinz J. L., Rix H.-W., Bernstein G. M., 2001, AJ, 121, 683

Hopkins P. F., Cox T. J., Dutta S. N., Hernquist L., Kormendy J., Lauer T. R., 2009a, ApJS, 181, 135

Hopkins P. F., Kereš D., Ma C., Quataert E., 2010, MNRAS, 401

Hopkins P. F., Lauer T. R., Cox T. J., Hernquist L., Kormendy J., 2009b, ApJS, 181, 486

Howard C. D., et al., 2009, ApJ, 702, L153

Hubble E. P., 1936, Realm of the Nebulae. Yale University Press

Jablonka P., Gorgas J., Goudfrooij P., 2007, A&A, 474, 763

Jarrett T. H., Chester T., Cutri R., Schneider S., Skrutskie M., Huchra J. P., 2000, AJ, 119, 2498

Jarrett T. H., Chester T., Cutri R., Schneider S. E., Huchra J. P., 2003, AJ, 125, 525

Jarvis B., 1990, in Dynamics and Interactions of Galaxies, Wielen, R., ed., Springer, p. 416

Jarvis B. J., 1986, AJ, 91, 65

Jeans J. H., 1922, MNRAS, 82, 122

Jensen J. B., Tonry J. L., Barris B. J., Thompson R. I., Liu M. C., Rieke M. J., Ajhar E. A., Blakeslee J. P., 2003, ApJ, 583, 712

Jeong H. et al., 2009, MNRAS, 398, 2028

Jorgensen I., Franx M., Kjaergaard P., 1996, MNRAS, 280, 167

Karachentsev I. D., Karachentseva V. E., Parnovskij S. L., 1993, Astronomische Nachrichten, 314, 97

Kassin S. A., de Jong R. S., Weiner B. J., 2006, ApJ, 643, 804

Kassin S. A. et al., 2007, ApJ, 660, L35

Kauffmann G., White S. D. M., Guiderdoni B., 1993, MNRAS, 264, 201

Kaviraj S., Schawinski K., Devriendt J. E. G., et al., 2007, ApJS, 173, 619

Kennicutt, Jr. R. C., 1998, ARA&A, 36, 189

Kent S. M., 1988, AJ, 96, 514

Kobayashi C., 2004, MNRAS, 347, 740

Koen C., Lombard F., 2009, MNRAS, 395, 1657

Komatsu E., et al., 2009, ApJS, 180, 330

Koopmans L. V. E., Treu T., Bolton A. S., Burles S., Moustakas L. A., 2006, ApJ, 649, 599

Kormendy J., Bender R., 1996, ApJL, 464, L119

Kormendy J., Drory N., Bender R., Cornell M. E., 2010, ApJ, 723, 54

Kormendy J., Fisher D. B., Cornell M. E., Bender R., 2009, ApJS, 182, 216

Kormendy J., Illingworth G., 1982, ApJ, 256, 460

Kormendy J., Kennicutt, Jr. R. C., 2004, ARAA, 42, 603

Kormendy J., Westpfahl D. J., 1989, ApJ, 338, 752

Krajnović D., Cappellari M., Emsellem E., McDermid R. M., de Zeeuw P. T., 2005, MNRAS, 357, 1113

Kranz T., Slyz A., Rix H.-W., 2003, ApJ, 586, 143

Kuhlen M., Strigari L. E., Zentner A. R., Bullock J. S., Primack J. R., 2005, MNRAS, 357, 387

Kuijken K., Merrifield M. R., 1995, ApJL, 443, L13

Kuntschner H., 2000, MNRAS, 315, 184

Kuntschner H. et al., 2006, MNRAS, 369, 497

Kuntschner H., et al., 2010, MNRAS, 408, 97

Larson R. B., 1974, MNRAS, 166, 585

Larson R. B., Tinsley B. M., Caldwell C. N., 1980, ApJ, 237, 692

Laurikainen E., Salo H., Buta R., Knapen J. H., 2009, ApJ, 692, L34

Levine E. S., Heiles C., Blitz L., 2008, ApJ, 679, 1288

Lintott C. J. et al., 2008, MNRAS, 389, 1179

Lütticke R., Dettmar R.-J., Pohlen M., 2000, A&AS, 145, 405

MacArthur L. A., 2005, ApJ, 623, 795

MacArthur L. A., González J. J., Courteau S., 2009, MNRAS, 395, 28

Macciò A. V., Dutton A. A., van den Bosch F. C., 2008, MNRAS, 391, 1940

Magorrian J., Ballantyne D., 2001, MNRAS, 322, 702

Magorrian J. et al., 1998, AJ, 115, 2285

Maraston C., 2005, MNRAS, 362, 799

Marigo P., Girardi L., 2007, A&A, 469, 239

Marinova I., Jogee S., 2007, ApJ, 659, 1176

Marinova I. et al., 2009, ApJ, accepted, 698, 1639

Markwardt C. B., 2008, in Astronomical Data Analysis Software and Systems XVIII, Bohlender, D., Dowler P., Durand D., eds., Astronomical Society of the Pacific Conference Series

Martin P., Roy J., 1995, ApJ, 445, 161

Masters K. L. et al., 2010, MNRAS, in press, arXiv:0910.4113

Masters K. L., Springob C. M., Huchra J. P., 2008, AJ, 135, 1738

Mathieu A., Merrifield M. R., Kuijken K., 2002, MNRAS, 330, 251

Mayer L., Governato F., Kaufmann T., 2008, Advanced Science Letters, 1, 7

McGaugh S. S., de Blok W. J. G., Schombert J. M., Kuzio de Naray R., Kim J. H., 2007, ApJ, 659, 149

McGaugh S. S., Schombert J. M., Bothun G. D., de Blok W. J. G., 2000, ApJ, 533, L99

Mehlert D., Thomas D., Saglia R. P., Bender R., Wegner G., 2003, A&A, 407, 423

Mei S., et al., 2007, ApJ, 655, 144

Méndez-Abreu J., Corsini E. M., Debattista V. P., De Rijcke S., Aguerri J. A. L., Pizzella A., 2008, ApJL, 679, L73

Merrifield M. R., Kuijken K., 1999, A&A, 345, L47

Merrifield M. R., et al., 2010, in Hunting for the Dark: The Hidden Side of Galaxy Formation, Debattista V. P., Popescu C. C., eds., AIP Conf. Ser.

Monnet G., Bacon R., Emsellem E., 1992, A&A, 253, 366

Moore B., Katz N., Lake G., Dressler A., Oemler A., 1996, Nature, 379, 613

Moorthy B. K., Holtzman J. A., 2006, MNRAS, 371, 583

Morelli L. et al., 2008, MNRAS, 389, 341

Moster B. P., Somerville R. S., Maulbetsch C., van den Bosch F. C., Macciò A. V., Naab T., Oser L., 2010, ApJ, 710, 903

Mould J. R. et al., 2000, ApJ, 529, 786

Napolitano N. R. et al., 2005, MNRAS, 357, 691

Navarro J. F., Frenk C. S., White S. D. M., 1997, ApJ, 490, 493

Neistein E., Maoz D., Rix H.-W., Tonry J. L., 1999, AJ, 117, 2666

Neto A. F. et al., 2007, MNRAS, 381, 1450

Nimoy L., 1987, *Three Men and a Baby*. Touchstone Pictures, Burbank, California

Noguchi M., 1999, ApJ, 514, 77

Noordermeer E., van der Hulst J. M., Sancisi R., Swaters R. S., van Albada T. S., 2007, MNRAS, 376, 1513

Noordermeer E., Verheijen M. A. W., 2007, MNRAS, 381, 1463

Noordermeer E., et al., 2008, MNRAS, 384, 943

Norris M. A., Sharples R. M., Kuntschner H., 2006, MNRAS, 367, 815

Oosterloo T., Fraternali F., Sancisi R., 2007, AJ, 134, 1019

Palunas P., Williams T. B., 2000, AJ, 120, 2884

Paturel G., Petit C., Prugniel P., Theureau G., Rousseau J., Brouty M., Dubois P., Cambrésy L., 2003, A&A, 412, 45

Paudel S., Lisker T., Kuntschner H., Grebel E. K., Glatt K., 2010, MNRAS, 405, 800

Peletier R. F., Balcells M., Davies R. L., Andredakis Y., Vazdekis A., Burkert A., Prada F., 1999, MNRAS, 310, 703

Peletier R. F. et al., 2007, MNRAS, 379, 445

Peletier R. F., Willner S. P., 1993, ApJ, 418, 626

Pérez I., Sánchez-Blázquez P., Zurita A., 2007, A&A, 465, L9

—, 2009, A&A, 495, 775

Persic M., Salucci P., Stel F., 1996, MNRAS, 281, 27

Pfenniger D., Friedli D., 1991, A&A, 252, 75

Pipino A., Matteucci F., 2004, MNRAS, 347, 968

Pizagno J. et al., 2007, AJ, 134, 945

Pizzella A., Corsini E. M., Vega Beltrán J. C., Bertola F., 2004, A&A, 424, 447

Poggianti B. M. et al., 2001, ApJ, 563, 118

Pohlen M., Trujillo I., 2006, A&A, 454, 759

Proctor R. N., 2003, PhD thesis, University of Central Lancashire

Proctor R. N., Sansom A. E., 2002, MNRAS, 333, 517

Proctor R. N., Sansom A. E., Reid I. N., 2000, MNRAS, 311, 37

Prugniel P., Soubiran C., 2001, A&A, 369, 1048

Puech M., et al., 2008, A&A, 484, 173

Puglielli D., Widrow L. M., Courteau S., 2010, ApJ, 715, 1152

Raha N., Sellwood J. A., James R. A., Kahn F. D., 1991, Nature, 352, 411

Ratnam C., Salucci P., 2000, New Astronomy, 5, 427

Reda F. M., Proctor R. N., Forbes D. A., Hau G. K. T., Larsen S. S., 2007, MNRAS, 377, 1772

Renzini A., 2006, ARA&A, 44, 141

Roberts M. S., 1978, AJ, 83, 1026

Romanowsky A. J., Douglas N. G., Arnaboldi M., Kuijken K., Merrifield M. R., Napolitano N. R., Capaccioli M., Freeman K. C., 2003, Science, 301, 1696

Rothberg B., Saunders W., Tully R. B., Witchalls P. L., 2000, ApJ, 533, 781

Rowley G., 1988, ApJ, 331, 124

Roy J., Walsh J. R., 1997, MNRAS, 288, 715

Rubin V. C., Burstein D., Ford, Jr. W. K., Thonnard N., 1985, ApJ, 289, 81

Rusin D., Kochanek C. S., Keeton C. R., 2003, ApJ, 595, 29

Sackett P. D., 1997, ApJ, 483, 103

Sakai S., et al., 2000, ApJ, 529, 698

Sánchez-Blázquez P., Forbes D. A., Strader J., Brodie J., Proctor R., 2007, MNRAS, 377, 759

Sánchez-Blázquez P., Gorgas J., Cardiel N., González J. J., 2006a, A&A, 457, 787

Sánchez-Blázquez P. et al., 2006b, MNRAS, 371, 703

Sandage A., 1961, The Hubble Atlas of Galaxies. Washington: Carnegie Institution, 1961

—, 2005, ARAA, 43, 581

Sarzi M., et al., 2006, MNRAS, 366, 1151

—, 2010, MNRAS, 402, 2187

Schawinski K. et al., 2009, MNRAS, 396, 818

Schlegel D. J., Finkbeiner D. P., Davis M., 1998, ApJ, 500, 525

Schulz A. E., Mandelbaum R., Padmanabhan N., 2009, ArXiv e-prints

Schwarzschild M., 1979, ApJ, 232, 236

Scott N. et al., 2009, MNRAS, 398, 1835

Sellwood J. A., Wilkinson A., 1993, Reports of Progress in Physics, 56, 173

Sérsic J. L., 1968, Atlas de galaxias australes. Cordoba, Argentina: Observatorio Astronomico, 1968

Shapiro K. L., Gerssen J., van der Marel R. P., 2003, AJ, 126, 2707

Shapiro K. L., et al., 2010, MNRAS, 402, 2140

Shaw M., 1993, A&A, 280, 33

Shaw M., Wilkinson A., Carter D., 1993, A&A, 268, 511

Shaw M. A., 1987, MNRAS, 229, 691

Shen J., Rich R. M., Kormendy J., Howard C. D., De Propris R., Kunder A., 2010, ApJ, 720, L72

Sheth K., et al., 2008, ApJ, 675, 1141

Silge J. D., Gebhardt K., Bergmann M., Richstone D., 2005, AJ, 130, 406

Singhal A., 2008, PhD thesis, University of Virginia

Skrutskie M. F., et al., 2006, AJ, 131, 1163

Somerville R. S., Hopkins P. F., Cox T. J., Robertson B. E., Hernquist L., 2008, MNRAS, 391, 481

Spitzer L. J., Baade W., 1951, ApJ, 113, 413

Spolaor M., Forbes D. A., Proctor R. N., Hau G. K. T., Brough S., 2008, MNRAS, 385, 675

Spolaor M., Kobayashi C., Forbes D. A., Couch W. J., Hau G. K. T., 2010, ArXiv e-prints

Spolaor M., Proctor R. N., Forbes D. A., Couch W. J., 2009, ApJ, 691, L138

Springel V. et al., 2005, Nature, 435, 629

Stark D. V., McGaugh S. S., Swaters R. A., 2009, AJ, 138, 392

Strateva I., et al., 2001, AJ, 122, 1861

Swaters R. A., 1999, PhD thesis, , Rijksuniversiteit Groningen, (1999)

Swaters R. A., Madore B. F., van den Bosch F. C., Balcells M., 2003, ApJ, 583, 732

Temi P., Brighenti F., Mathews W. G., 2009a, ApJ, 695, 1

—, 2009b, ApJ, 707, 890

Terlevich R., Davies R. L., Faber S. M., Burstein D., 1981, MNRAS, 196, 381

Thomas D., Davies R. L., 2006, MNRAS, 366, 510

Thomas D., Greggio L., Bender R., 1999, MNRAS, 302, 537

Thomas D., Maraston C., Bender R., 2003, MNRAS, 339, 897

Thomas D., Maraston C., Bender R., Mendes de Oliveira C., 2005, ApJ, 621, 673

Thomas J. et al., 2009, MNRAS, 393, 641

Thomas J., Saglia R. P., Bender R., Thomas D., Gebhardt K., Magorrian J., Corsini E. M., Wegner G., 2007, MNRAS, 382, 657

Tonini C., Maraston C., Ziegler B., Böhm A., Thomas D., Devriendt J., Silk J., 2010, MNRAS, submitted, arXiv:1006.0229

Tonry J. L., Blakeslee J. P., Ajhar E. A., Dressler A., 2000, ApJ, 530, 625

Tonry J. L., Dressler A., Blakeslee J. P., Ajhar E. A., Fletcher A. B., Luppino G. A., Metzger M. R., Moore C. B., 2001, ApJ, 546, 681

Trager S. C., Worthey G., Faber S. M., Burstein D., Gonzalez J. J., 1998, ApJS, 116, 1

Tremaine S. et al., 2002, ApJ, 574, 740

Treu T., Auger M. W., Koopmans L. V. E., Gavazzi R., Marshall P. J., Bolton A. S., 2010, ApJ, 709, 1195

Trujillo-Gomez S., Klypin A., Primack J., Romanowsky A. J., 2010, MNRAS, submitted, arXiv:1005.1289

Tully R. B., Fisher J. R., 1977, A&A, 54, 661

Tully R. B., Fouqué P., 1985, ApJS, 58, 67

Tully R. B., Mould J. R., Aaronson M., 1982, ApJ, 257, 527

Tully R. B., Pierce M. J., 2000, ApJ, 533, 744

van Albada T. S., Bahcall J. N., Begeman K., Sancisi R., 1985, ApJ, 295, 305

van Albada T. S., Sancisi R., 1986, Royal Society of London Philosophical Transactions Series A, 320, 447

van den Bergh S., 1990, ApJ, 348, 57

—, 2009a, ApJ, 702, 1502

—, 2009b, ApJ, 694, L120

van den Bosch F. C., 2001, MNRAS, 327, 1334

van den Bosch R. C. E., van de Ven G., Verolme E. K., Cappellari M., de Zeeuw P. T., 2008, MNRAS, 385, 647

van der Kruit P. C., 1979, A&AS, 38, 15

Vazdekis A., Sánchez-Blázquez P., Falcón-Barroso J., Cenarro A. J., Beasley M. A., Cardiel N., Gorgas J., Peletier R. F., 2010, MNRAS, 404, 1639

Vega Beltrán J. C., Pizzella A., Corsini E. M., Funes J. G., Zeilinger W. W., Beckman J. E., Bertola F., 2001, A&A, 374, 394

Verheijen M. A. W., 1997, PhD thesis, PhD thesis, Univ. Groningen, The Netherlands , (1997)

—, 2001, ApJ, 563, 694

Vila-Costas M. B., Edmunds M. G., 1992, MNRAS, 259, 121

Wang L., Li C., Kauffmann G., De Lucia G., 2006, MNRAS, 371, 537

Wechsler R. H., Bullock J. S., Primack J. R., Kravtsov A. V., Dekel A., 2002, ApJ, 568, 52

Weijmans A.-M., 2009, PhD thesis, Leiden University, `http://hdl.handle.net/1887/13970`

Weijmans A.-M., Krajnović D., van de Ven G., Oosterloo T. A., Morganti R., de Zeeuw P. T., 2008, MNRAS, 383, 1343

Weiner B. J., Sellwood J. A., Williams T. B., 2001, ApJ, 546, 931

White S. D. M., Rees M. J., 1978, MNRAS, 183, 341

Whyte L. F., Abraham R. G., Merrifield M. R., Eskridge P. B., Frogel J. A., Pogge R. W., 2002, MNRAS, 336, 1281

Williams M. J., Bureau M., Cappellari M., 2009, MNRAS, 400, 1665

—, 2010, MNRAS, 409, 1330

Willick J. A., 1994, ApJS, 92, 1

Wilman D. J., Oemler A., Mulchaey J. S., McGee S. L., Balogh M. L., Bower R. G., 2009, ApJ, 692, 298

Wolf J., Martinez G. D., Bullock J. S., Kaplinghat M., Geha M., Muñoz R. R., Simon J. D., Avedo F. F., 2010, MNRAS, 406, 1220

Worthey G., 1994, ApJS, 95, 107

Wozniak H., 2007, A&A, 465, L1

Young L. M., Bureau M., Cappellari M., 2008, ApJ, 676, 317

Zaritsky D., Kennicutt, Jr. R. C., Huchra J. P., 1994, ApJ, 420, 87

Zoccali M., Hill V., Lecureur A., Barbuy B., Renzini A., Minniti D., Gómez A., Ortolani S., 2008, A&A, 486, 177